GSI Helmholtzzentrum für Schwerionenforschung

FAIR

Summer Student Program at GSI 2022

HGS-HIRe for FAIR
Helmholtz Graduate School for Hadron and Ion Research

Book of Reports

Darmstadt, Germany 2022

Foreword

Congratulations! To ourselves of course... Congratulations to the organizers of the program for creating incredible opportunities for young aspiring scientists. Congratulations to the summer students for becoming these aspiring scientists by working tirelessly on their projects (mostly). And congratulations to the book editors to working on this thing until 3 am (as every year).
These aspiring scientists of this years program have filled it with strong interaction forces. Strong interactions, friendships and community. Just like the strong nuclear interactions, this force of our community was by no means repelling, instead, it was strongly coupling all of us to create memories which will last beyond the big crunch (I am sorry if this theory is no longer valid by the time you are reading this report).
In a way, our Summer Student program has been unique. We have reached heights by the number of times we have been to the beergarden (and by climbing fences). We have invented the country "Jermany". Beaten the mafia multiple times (reference to the card game). And made the GSI into a cinema to watch House of Dragons (hint for the next summer students: use either conference rooms or the KBW lecture hall, this is just an amazing experience!).
Finally, we would like to thank our most patient and endurant tutors for dealing with the amount of challenges that one summer student can create (probably not even Grahams Number fits to describe the amount!). We thank them not only for teaching us, but for giving us lifelong skills in critical thinking, skills so useful, they will help us wherever we might end up at the end of the day...
Shall this collection of reports be dedicated to the people that made this unique opportunity possible. Thank you.

Organization Brought to a New Level

Not only was the organizational team of the GSI Summer Student Program a new one but also the competitions they faced. With in total three participants either coming or getting physically injured Ralf, Gaby, Arnauld, Jörn and all their helpers had their hands full. And the way they managed to support us is unrivaled. Who else would organize wheelchairs, do dozens of phone calls with parents and hospitals and have the infringed students and their parents stay in the guest house on campus.
For all these and many more things you did to support us, we'd like to express our immense gratitude.
THANK YOU!

Contents

Summer Student Reports

Transverse coupled-bunch instability with empty buckets in SIS100

Thiti Aungcharoen
Prince of Songkla University, kajung1255@gmail.com

This report presents the study of the transverse coupled-bunch instability, driven by the resistive wall impedance, in SIS100 using the PyHEADTAIL simulation framework. The effect of betatron tune, chromaticity, and the number of bunches in the buckets on the coupled-bunch growth rate are studied.

1 Introduction

In the synchrotron simulations, we treat the particle beam as a bunch of macro-particles that move around the accelerator pipe. As the bunches travel along the circumference, the particles in the head of the bunch train can generate forces that will exert on the following particles in the tail end of the bunch train resulting in the oscillation of each bunch. In this study, we focus on oscillation in the transverse direction by considering the structure of the transverse position of each bunch in SIS100. As the turn number increases, without some appropriate mitigation, the oscillation amplitude can grow indefinitely, leading to a loss of beam quality and, ultimately, a loss of particles from the beam [1]. So, this project aims to minimize the growth rate of the coupled-bunch instability by varying betatron tune, chromaticity, and the number of bunches in the buckets. In addition, we also show bunche structure in the case of empty buckets in SIS100.

The rest of this report is organized as follows: transverse coupled-bunch instability and PyHEDTAIL description are described in sections 2 and 3, respectively. The simulation results are shown in section 4. Finally, this report is concluded with a discussion in section 5.

2 Transverse coupled-bunch instability

Consider the particle accelerator containing equally spaced bunches. As a beam travels along the accelerator pipe, transverse coupled-bunch instability occurs when particles in the former bunches interact with the machine's structure through the self-generated electromagnetic field in such a way as to produce wake fields that can interact back with particles in the later bunches. Note that the total wake field is the sum of the fields generated by all bunches over all previous turns. As a result, each bunch will oscillate with an exponentially growing amplitude which can limit the efficiency of the accelerator.

In the absence of wake fields, each bunch performs collective betatron motion with frequency ω_β, which means a centroid of each bunch oscillates with the same betatron frequency. In the presence of wake fields, each bunch oscillates with frequency Ω_μ and then performs a sinusoidal structure with an exponentially growing amplitude. The pattern of the sinusoidal structure depends on the mode number which is in the range $0 \leq \mu < n_b$ where n_b is the number of bunches. The betatron frequency, Ω_μ, is obtained by the following equation:

$$\Omega_\mu - \omega_\beta = -i\frac{q^2 n_b N_b \omega_0 c}{8\pi^2 E_0 \nu_x} \cdot \sum_{p=-\infty}^{\infty} Z_1^\perp(\omega_\beta + (\mu - n_b p)\omega_0), \quad (1)$$

where q is the elementary charge, N_b is the number of real particles in each bunch, $\omega_0 = 2\pi\frac{c}{C_0}$ is the revolution (angular) frequency, c is light speed, C_0 is the ring circumference, E_0 is reference energy, $\nu_x = \frac{\omega_\beta}{\omega_0}$ is the betatron tune, and $Z_1^\perp$ is the impedance of the wake field. The real part of Ω_μ gives the betatron oscillation fre-

quency in the presence of wake fields, and the imaginary part of Ω_μ gives the growth or damping rate of the mode amplitude depending on whether it is positive or negative, respectively.

In the particular case of transverse coupled-bunch instability, driven by the resistive-wall wake fields which occur when the accelerator pipe has a finite resistivity, the growth rate of the fastest-growing mode can be obtained by the equation:

$$\gamma = \mathrm{Im}\,\Omega_\mu = \frac{n_b N_b r_0 c}{4\pi^2 \gamma_0 \nu_x b^3} \cdot \sqrt{\left(\frac{4\pi}{Z_0 c}\right)\frac{cC_0}{\sigma}}\,\frac{1}{\sqrt{1-\mathrm{frac}(\nu_x)}}, \quad (2)$$

where r_0 is the classical radius of the particles in the beam, γ_0 is the relativistic factor, b is the beam pipe radius, Z_0 is the impedance of the free space, σ is the conductivity of the accelerator pipe, and $\mathrm{frac}(\nu_x)$ is the fractional part of the betatron tune. Note that the betatron tune depends on the momentum. Changing in the momentum can lead to a change in betatron tune which implies that the growth rate is also changed. The change in betatron tune due to momentum is called chromaticity (ξ) and is defined by

$$\triangle\nu = \xi\frac{\triangle p}{p_0}, \quad (3)$$

where $\triangle p/p_0$ is the momentum deviation relative to the ideal momentum. In other words, chromaticity values can determine whether the motion of the particle beam is stable or unstable. [2]

From Eq.(2) we can see that the growth rate of transverse coupled-bunch instability depends on many parameters such as betatron tune, chromaticity, and the number of bunches. So in this study, we try to decrease the growth rate by varying those parameters and then observe the change in bunch structure.

3 PyHEADTAIL description

PyHEADTAIL is a macro-particle tracking code written in Python, C, and NVIDIA's CUDA for simulating beam dynamics in particle accelerators with collective effects. The tracking routines consist of betatron and synchrotron tracking [3]. In this study, we use PyHEADTAIL to track the transverse position of the bunches that are generated by the generator module, which is implemented in the PyHEADTAIL library. Creating wake fields in the transverse direction can be done by using the ResistiveWall object as a wake source by setting Yokoya_X1 = 1 as an input parameter which means it will construct a wake kick in the x-direction.

4 Results

The effect of betatron tune, chromaticity, and the number of bunches on the growth rate of coupled-bunch instability for SIS100 [4] are studied. Technically we select the number of macro-particle in each bunch equal to 10,000 to get acceptable results and not spend too long simulation time.

4.1 The effect of betatron tune

The result of the dependence of coupled-bunch instability growth rate (γ/γ^*) on betatron tune (Q_x) is shown in Fig.1 for the case fulfilled 10 buckets.

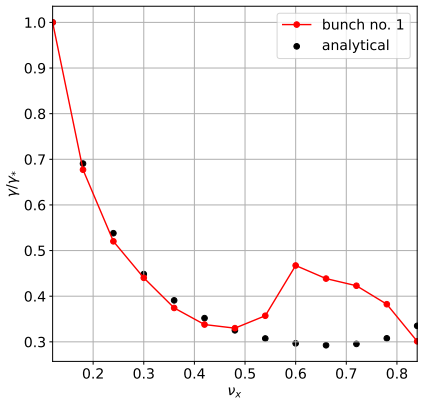

Fig. 1: *Normalized growth rate as a function of betatron tune from simulation results (red) and analytical solution (black)*

It can be seen that the difference in growth rate between simulation results and analytical solutions becomes larger at betatron tune greater than 0.48 because at the low level of betatron tune, bunch structure is solely mode number 1 but at the high level (> 0.48) there is a combination of mode number 0 and 1 so, the growth rate is also the combination of these modes. Note that the analytical solution is obtained by Eq.2 and it is a solution for mode number 1.

4.2 The effect of chromaticity

The results of the dependence of the growth rate (γ) on the chromaticity (ξ) are shown in Figs.2 and 3. Each color of a dot-line in each picture indicates simulation results from the different number of fulfilled buckets. Fig.2 shows the result of varying chromaticity for mode number 1 and Fig.3 for mode number 0.

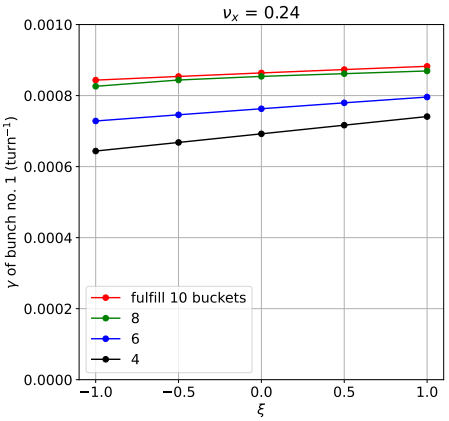

Fig. 2: *Dependence of growth rate on chromaticity for mode number 1 with* $\nu_x = 0.24$

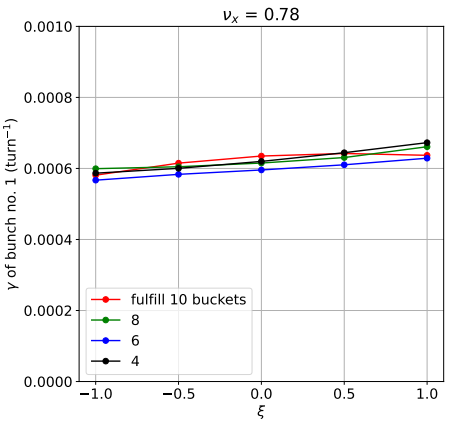

Fig. 3: *Dependence of growth rate on chromaticity for mode number 0 with* $\nu_x = 0.78$

From Figs.2 and 3. It was found that the growth rate has weakly dependent on the chromaticity and also found that varying the chromaticity cannot change the mode number.

4.3 The effect of the empty buckets

The result of the dependence of the growth rate on the number of bunches in 10 buckets is shown in Fig.4

From Fig.4 we see that the growth rate decreases as the number of bunches in 10 buckets decrease. Until there are only 2 bunches in 10 buckets, the growth rate become 0 which means there is no occurrence of coupled-bunch instability because the number of bunches is too low.

Fig.5 illustrates the simulation result of filling 8 bunches into 10 buckets. The y-axis indicates the energy offset and the x-axis indicates the longitudinal position.

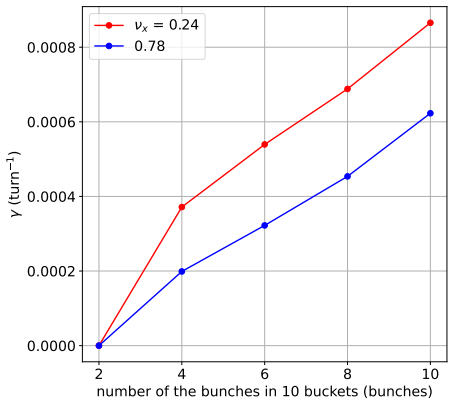

Fig. 4: *Dependence of growth rate on the number of bunches in 10 buckets*

Figs.6 and 7 show bunches structure in the case of filling 10 buckets with 8 bunches with betatron tune equal to 0.24 and 0.78, respectively, after tracking for 10,000 turns.

It can be seen that the bunch structure in Figs.6 and 7 is mode number 1 and 0, respectively. Note that, in this work, it is still not clear that the bunch structure with $\nu_x = 0.24$ is whether mode number 1 or 9 because these modes have the same sinusoidal structure. In addition, it was also found that bunch structure still occupies these modes number as the number of bunches in 10 buckets decreases for both betatron tunes.

5 Conclusions and Discussions

In this report, we show the dependence of the coupled-bunch instability growth rate on betatron tune, chromaticity, and the number of bunches in 10 buckets. We found that at the low level of betatron tune, bunch structure is mode number 1 but at the high value of betatron tune, it is the combination of mode number 0 and 1. We also found that the growth rate weakly depends on the chromaticity, varying the chromaticity cannot change the mode number of

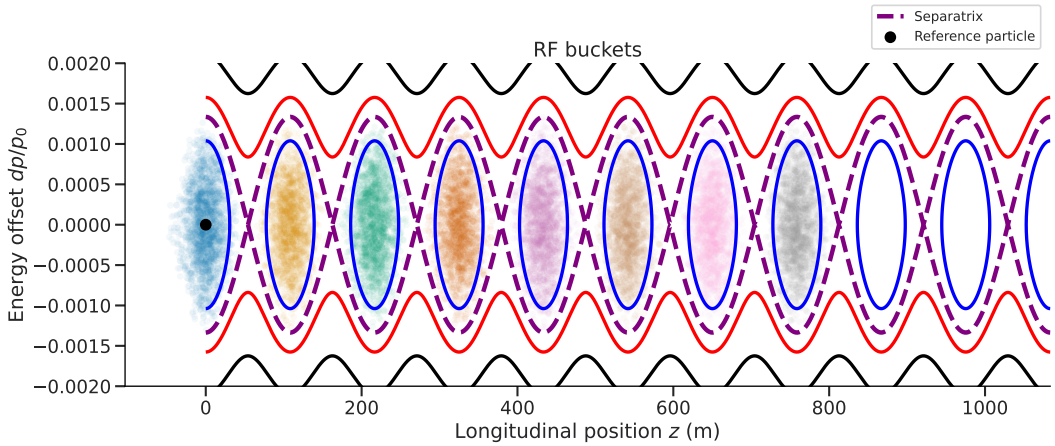

Fig. 5: *Filling 10 buckets with 8 bunches. The separatrix indicates the boundary of the buckets. All macro-particles are filled in these buckets.*

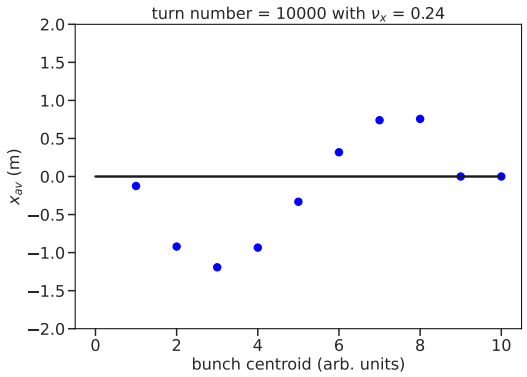

Fig. 6: *Brunch structure for the case 10 buckets with 8 bunches with* $\nu_x = 0.24$

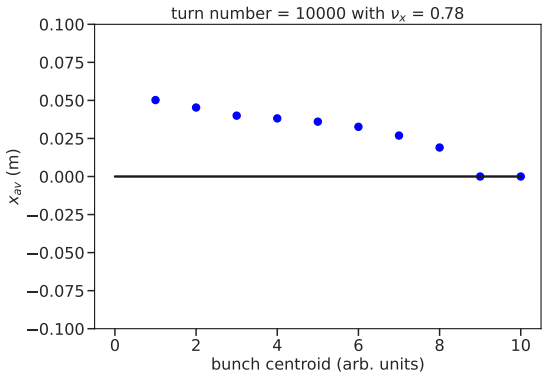

Fig. 7: *Brunch structure for the case 10 buckets with 8 bunches with* $\nu_x = 0.78$

the bunch structure. Moreover, we found that the growth rate decreased as the number of the bunches in 10 buckets decreased, varying the number of the bunches also cannot change the mode number. In work at $\xi_x = 0.24$, it is still not clear whether the mode number is 1 or 9, further study should be done for classifying the mode number.

Acknowledgments

I would like to express my deep appreciation to my tutor, Dr. Vladimir Kornilov for the encouragement and guidance. I would also like to thank Vadim Gubaidulin for his willingness to help and support me during this program. Especially, they give me inspiration about particle accelerator research. Special thanks to the GSI summer student program, which provides us the opportunity to gain experience in particle accelerator research. Lastly, I would like to thank my partner, Pablo García Gil, for supporting me during this summer program.

References

[1] A. Wolski. Beam Dynamics in High Energy Particle Accelerators. IMPERIAL COLLEGE PRESS, Apr. 2014, pp. 512–519. doi: 10.1142/p899 (cit. on p. 1).

[2] D. A. Edwards and M. J. Syphers. An Introduction to the Physics of High Energy Accelerators. Wiley, Jan. 1993, pp. 96–98. doi: 10 . 1002 / 9783527617272 (cit. on p. 2).

[3] A. Oeftiger. An Overview of PyHEADTAIL. 2019 (cit. on p. 2).

[4] O. Boine-Frankenheim and V. Kornilov. "Intensity Thresholds for Transverse Coherent Instabilities During Proton and Heavy-

Ion Operation in SIS100". In: Conf. Proc. C 1205201 (2012). Ed. by V. Suller, pp. 2934–2936 (cit. on p. 2)

Energy loss of hydrogen-like gold (Au^{78+}) ions colliding with a helium target at CRYRING@ESR

Andreas Biniskos
University of Ioannina, anbiniskos@gmail.com

In this work the calculated energy loss using the Bethe-Bloch formula of a stored hydrogen-like gold (Au^{78+}) ion beam at energies of $4.8MeV/u$ and $10.1MeV/u$ is compared to experimental measurements. The energy loss of the ion beam was measured at different helium target area densities. The experiments were performed at CRYRING@ESR in GSI, where the new internal target station has been commissioned. A Schottky detector was used to obtain the energy loss data. Our results seem to be in fairly good agreement with the theory, especially if compared with respect to similar measurements that took place at the Experimental Storage Ring (ESR) [1].

1 Introduction

In the course of the last decades storage rings have been the focus of interest in the exploration of heavy charged particles. Stored and cooled beams of highly-charged ions unlocked fascinating research origins. The CRYRING is a storage ring, at which groundbreaking work was performed for several decades beginning in the late 1980's, in Stockholm. The optimal ion energy operation of the CRYRING ranges from $14MeV/u$ down to $300keV/u$. Since the early 1990's the ESR is located in GSI for the investigation of the heaviest ions in the highest charge-states. The ESR can provide ions with a big variety of charge states (up to bare Uranium) and energies ranging from $4MeV/u$ to $500MeV/u$. CRYRING@ESR currently is located in GSI and in combination with the ESR and cyclotron SIS18 represents a unique machine, which is expected to provide hitherto unprecedented experimental opportunities. CRYRING@ESR is the only experimental apparatus in the world that will be able to provide ion beams with such a big bandwidth of energies and charge states at low energies [2].

CRYRING@ESR will provide opportunities for novel experiments in the fields of atomic physics, nuclear astrophysics, material sciences etc. In many cases the experiments require the use of an internal gas target for the investigation of collision processes. Molecular beam techniques are utilized for the production of internal target beams. They offer the ability of unique studies of cooled ion beams colliding with matter under single collision conditions. A novel internal target station design is used at the CRYRING@ESR. Scientists performing experiments at the internal target of CRYRING@ESR need to know a precise value for the internal target area density. Usually, the increase in the dump chamber of the internal target station is used for calculating the target area density. The area density can also be obtained by measuring the energy loss of the ion beam interacting with the target by means of a Schottky detector and comparing it to theoretical predictions of the Bethe-Bloch formula. In the course of the commissioning process of the new internal target station, both methods are utilized in order to assess their validity.

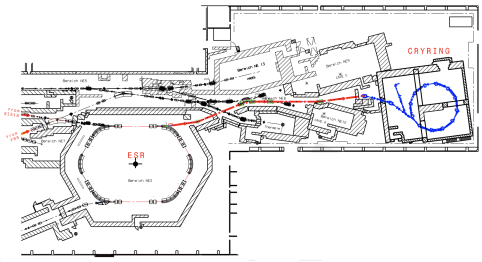

Fig. 1: *The new storage ring topology at GSI with CRYRING@ESR inside the former Cave B in the Target Hall of GSI.*

2 Experimental Procedure and the Internal Gas Target Set-Up

2.1 Experimental Procedure

In order to start the measurements the target had to be prepared accordingly. In the beginning the target source was set to the desired area density. After the ion beam had been injected the internal Schottky detector device [4] of the CRYRING@ESR initiated the measurement of the revolution frequency spectra. With the deactivation of the electron cooler the Schottky detector recorded a decline of the average ion beam frequency due to the energy loss (see Fig. 2). The Schottky detector kept recording for some seconds before the remaining ions were removed. The same procedure was repeated for multiple times in order to improve the statistics. Also, during the experimental procedure background measurements were obtained. In order to do that the valve of the interaction chamber was closed and the electron cooler was switched on.

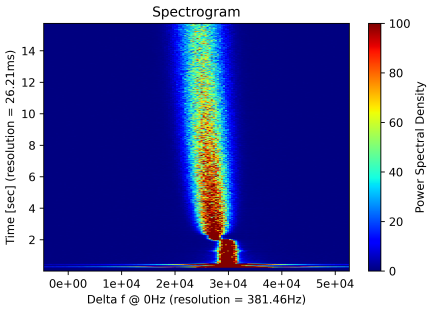

Fig. 2: *Typical Schottky frequency spectrum recorded during the energy loss measurement of a* Au^{78+} *beam at* $10.1 MeV/u$.

2.2 Internal Gas Target Set-Up

The most important components of the target station are the cryostat and the nozzle. At the CRYRING@ESR internal target a pinhole orifice nozzle with a diameter of $5\mu m$ was used. A closed-cycle cryostat (see Fig. 4) with a nominal cooling power of 1.5W@4.2K was used to reduce the temperature of the nozzle down to $7K$ for the measurements. The helium backing pressure at the nozzle was set to values between 18 and 42 bars.

At cryogenic temperatures, the pinhole orifice nozzle was capable of producing target beams

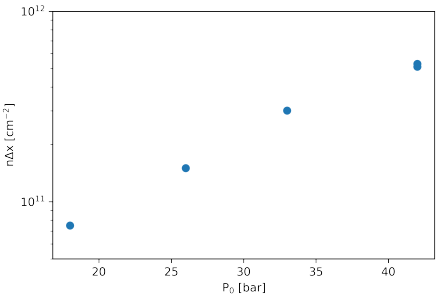

Fig. 3: *Target area density as a function of the helium backing pressure. The nozzle temperature was set to* $T_0 = 7K$.

with area densities of up to $5.3 \times 10^{11} cm^{-2}$ (see Fig. 3).

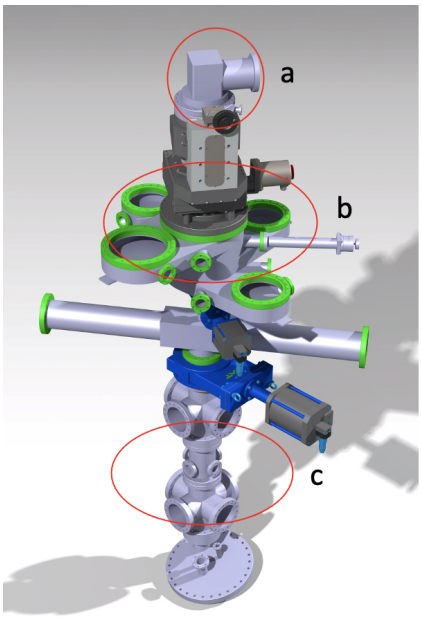

Fig. 4: *3D CAD of the CRYRING gas jet target. a) Cryostat cold head. b) New inlet chamber. c) CRYJET dump chamber.*

The inlet chamber is composed of four differential pumping stages (see Fig. 5). The turbomolecular pumps are mounted headfirst on the lateral wings visible. This configuration reduces the distance between the skimmer and the interaction point to 41cm [3]. The separation of the four differential stages is achieved with the use of circular metal plates. At the center of each plate a skimmer is placed (see Fig. 5). The aperture sizes of the skimmers are 0.2, 0.3, 0.8 and $1.0mm$ at the first, second, third and fourth stage, respectively. The aperture of the first two

skimmers is important due to the fact that they determine the interaction length Δx of the target.

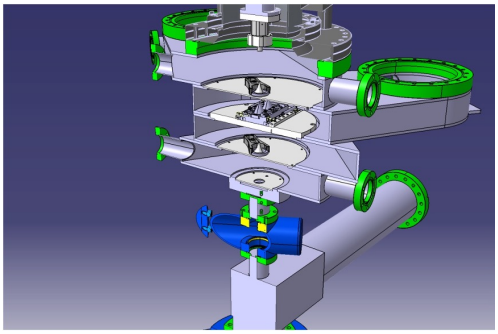

Fig. 5: *3D CAD of the CRYRING@ESR gas jet target in which the 4 differential pumping stages are shown.*

Only the pressure in the last differential pumping stage is important in order to ensure good vacuum conditions in the ring. Without differential pumping, the vacuum condition in the nozzle chamber would negatively affect the vacuum in the ring and target operation would not be possible. Differential pumping is therefore crucial for an internal target station.

3 Results and Discussion

In Fig. 2 a typical Schottky frequency spectrum recorded during the energy loss measurement is shown. The precise number of averaged spectra depends on the initially chosen recording time during the measurement. The mean value of the frequency distribution was determined for every spectrum and plotted as a function of time as shown in Fig. 6.

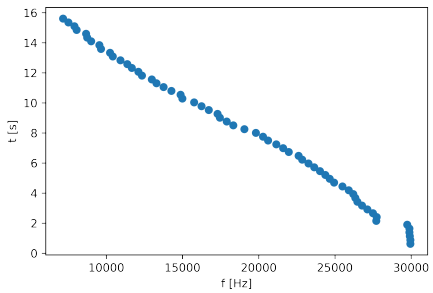

Fig. 6: *Time evolution of the mean revolution frequency obtained from the Schottky spectra.*

In Fig. 6 we can see a linear decline of the mean revolution frequency, which can be represented by:

$$f(t) = f_0 - f't, \tag{1}$$

where f' is the frequency shift rate and f_0 the initial revolution frequency of the cooled ion beam. The energy loss of the ion beam per cycle is related to the frequency shift by Eq. 2

$$\Delta E = \left(\frac{1+\gamma_0}{\gamma_0}\right)\frac{1}{\eta}\frac{E_0}{{f_0}^2}f', \tag{2}$$

where E_0 is the initial energy of the cooled ion beam and $\eta = {\gamma_0}^{-2} - {\gamma_{tr}}^{-2}$ is the frequency slip factor and depends on the Lorentz factor γ_0 of the ion beam and the transition energy γ_{tr}. The transition energy for the CRYRING@ESR was measured and has a value of $\gamma_{tr} = 2.42$ [2]. Two reasons for a non-linear decline of the revolution frequency are the emittance growth and the non-zero dispersion at the target section, which induces a horizontal ion beam displacement.

We can also calculate the expected energy loss using the Bethe-Bloch formula:

$$-\frac{dE}{dx} = \frac{Z^2e^4}{4\pi{\epsilon_0}^2 m_e}\frac{n_e}{{\beta_0}^2c^2}\left\{\ln\left[\frac{2m_ec^2{\beta_0}^2}{I(1-{\beta_0}^2)}\right] - {\beta_0}^2\right\}, \tag{3}$$

where m_e is the electron mass, e is the elementary charge, ϵ_0 is the vacuum permittivity, n_e is the electron number density in the target ($n_e = 2n$ for He), Z is the ion charge number and I is the mean ionization potential of the target atoms. The results for the beam energy loss of the gold ion beam are shown in Fig. 7.

As expected, the energy loss is higher for the ion beams with lower energies. We can also see that there is a good agreement between the experimental values and the theory, even if a discrepancy by a factor of around 2 is observed. Measurements performed at the ESR showed a similar discrepancy, which could be explained if certain effects were taken into account [1]. One effect is the pressure increase in the interaction chamber, which can be increased by up to two orders of magnitude during target operation. Another effect is the incomplete overlap between the target beam and the ion beam due to the fact that the ion beam size does not match the target width at the interaction point. The difference between the two becomes even larger after the electron cooler is switched off, which leads to an almost immediate emittance growth

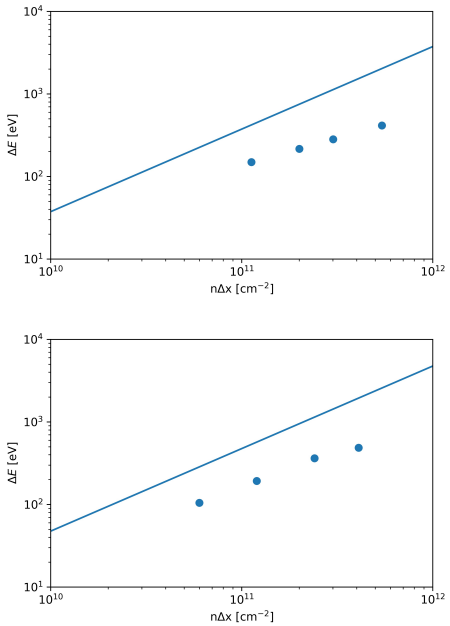

Fig. 7: *Measured ion energy losses as a function of the measured target area density for hydrogen-like gold* Au^{78+} *at energies of* $10.1MeV$ *(top) and* $4.8MeV$ *(bottom).*

of the ion beam. Those effects were not addressed in the analysis and results of the present work.

4 Conclusions

In the present work we measured the energy loss of hydrogen like gold beams with energies of $4.8MeV/u$ and $10.1MeV/u$ for various He target area densities. We also compared our data with the theoretical values that were obtained from the Bethe-Bloch formula. The final results show a fairly good agreement between the experimental and the theoretical values, considering previous measurements that showed a similar discrepancy, which is attributed to certain effects.

Acknowledgments

I would like to thank my tutor Dr. Nikolaos Petridis for the trust he has shown me and the support he has given me, and without his guidance the completion of this work would be impossible.

References

[1] N.Petridis, "The Internal Multiphase Target for Storage Ring Experiments", *PhD Thesis* (2014).

[2] M.Lestinsky, "Physics book: CRYRING@ESR", *The European Physical Journal Special Topics* (2016).

[3] N.Petridis, Prototype internal target design for storage ring experiments, *Phys. Scr.* **T166**, 014051 (2015).

[4] F. Caspers, Schottky signals for longitudinal and transverse bunched-beam diagnostics, *CAS - CERN Accelerator School: Beam Diagnostics*, (2009).

ZnO-based radiation-hard fast scintillators investigation

Darko Brunet
University of Novi Sad, brunet.darko@gmail.com

This paper discusses the application of different ZnO-based ceramics as radiation-hard scintillation detectors for heavy-ion beam diagnostics. The paper describes the data analysis process of obtaining ionoluminescence spectra of different ZnO-based ceramics irradiated with high-energy heavy ions for their mutual comparison.

1 Introduction

Scintillators are materials that exhibit luminescence properties when they are excited by ionizing radiation. When struck by a particle, these materials absorb their energy and re-emit it in the form of light. If they are coupled with an electric light sensor such as a photomultiplier tube (PMT), photodiode, or a silicon photomultiplier, these materials can be used as scintillation detectors in nuclear and accelerator physics, beam diagnostics as well as High Energy Physics (HEP) [1]. At the GSI accelerator facility, where heavy-ion beams from proton up to uranium are accelerated and extracted from SIS-18 synchrotron at energies above 150 MeV per nucleon, scintillation detectors are used as a part of particle detector combination (along with secondary electron monitors and ionization chambers) [2]. Scintillation detectors are used as an invasive tool to measure beam intensities provided by SIS-18. Therefore, the detector's active area is directly subjected to a heavy-ion impact. Each particle that passes through the detector's active area creates a light pulse which is then detected using a photomultiplier tube, where each particle corresponds to a separate PMT signal which is analyzed. Future HEP and accelerator physics experiments at the energy and intensity frontiers require faster scintillators with excellent radiation hardness. Radiation hardness becomes especially critical when irradiation with heavy ions takes place. At GSI, for absolute beam intensity and micro-spill structure measurements, a BC400 plastic scintillator is used. Due to the low radiation hardness of this material, alternative inorganic scintillators such as pure ZnO, ZnO(Ga) and ZnO(In) are currently being investigated. ZnO exhibits two emission bands, a narrow band located near the absorption edge of the crystal (NBE, Near Band Edge emission), which is characterized by an ultrafast luminescence with a decay time below one nanosecond. This short-wavelength band is of an exciton nature. The second band is rather broad and comes from native defects present in the material (frequently referred to as DL band, deep-level emission band). Its maximum intensity is around the green light spectral region, and its decay time is in order of milliseconds. For the purpose of suppressing the DL emission band and better utilization of the fast NBE, previous studies have shown that pure ZnO can be doped with Ga or In [3–7]. Due to a lack of the ZnO-based scintillators' performance at high-energy heavy-ion irradiation, a comprehensive investigation of these materials is required.

2 Experimental setup

Beams of ^{40}Ar, ^{209}Bi, and ^{238}U with energies ranging from 250 MeV/u up to 500 MeV/u were used for measurements. The beam extracted from the SIS-18 synchrotron passed through a set of detectors in a vacuum chamber: SEM (Secondary Electron Monitor) and IC (Ionization Chamber), which were used for beam tuning (see Figure 1). The beam exits the vacuum chamber through a stainless steel window and further travels towards the experimental setup placed in air. The beam on its way to the target passes through a collimator, which is used for beam shaping, and then enters a second IC

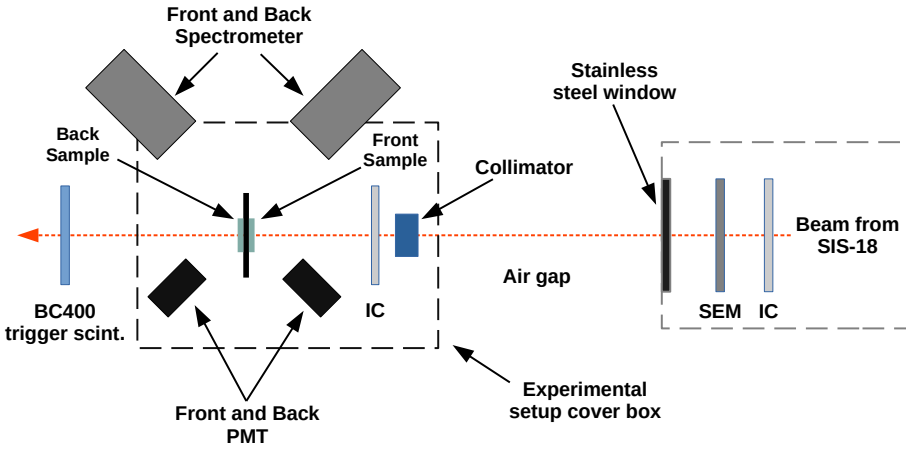

Fig. 1: *Schematic view of the experimental setup used for in-situ ionoluminescence spectra characterization*

mounted inside the experimental setup. This IC was used for determining the number of ions per spill during ionoluminescence spectra acquisition. After the IC, the beam hits samples placed on the front and back sides of a target holder. In this project, we investigated: (i) indium- and gallium-doped zinc oxide transparent ceramics produced by uni-axial hot pressing in vacuum; (ii) indium- and gallium-doped zinc oxide ceramics (samples (i)) subjected to a thermal treatment in H_2/Ar atmosphere (further in the text referred as "thermal"); (iii) pure ZnO single crystal; (iv) BC400 plastic scintillator. Samples (i) and (ii) were produced by the Joint Stock Company "Research and Production Corporation S.I. Vavilova" (Russia). Samples (iii) and (iv) were purchased from Crystal GmbH (Germany) and Saint-Gobain Crystals (USA), respectively. Samples that were used in this work had different sizes and shapes. ZnO-based and BC400 plastic reference samples had thicknesses of 0.5 and 1 respectively. Due to the high energies used within the studies, ion beams could go through the entire sample thickness and homogeneously deposit the energy inside samples. Scintillation produced with irradiation of the sample was recorded with two different spectrometers facing the front and back sample. The spectrometers consist of a HORIBA CP 140-202 spectrograph with a digital camera attached to it. In this project, PCO.1600 and PCO SensiCam QE cameras were used for reading spectra images from HORIBA spectrograph output for front and back samples, respectively. The PCO camera images provided an output that is the integral function of intensity over different wavelengths. Energy losses of heavy ions in the investigated samples were calculated using ATIMA, a program developed at GSI for calculating various physical quantities characterizing the slowing down of protons and heavy ions in a matter for energies ranging from 1 keV/u to 450 GeV/u, such as stopping power, energy loss, range, mean projectile range etc. The calculated energy loss values are shown in Table 1.

Tab. 1: *Energy losses of various ion beams in ZnO when irradiating front and back of the samples*

Sample location	Ion species	Energy [MeV/u]	Energy loss $\left[\frac{MeV}{mg/cm^2}\right]$
Front	^{40}Ar	250	0.95
	^{209}Bi	300	19.58
	^{238}U	300	24.01
Back	^{40}Ar	250	0.97
	^{209}Bi	300	20.43
	^{238}U	300	25.14

3 Data analysis

3.1 Reading the spectrum

For the acquisition of raw ionoluminescence spectra PCO.1600, and PCO SensiCam QE camera were connected to HORIBA CP 140-202 spectrograph. Both cameras have a CCD (Charged Couple Device) chip, which is used as a light-sensitive circuit that converts photons to electrons. A CCD sensor breaks the image elements into pixels that are then converted into an electrical charge whose intensity is re-

lated to the intensity of light captured by that pixel. An example of the image recorded with PCO SensiCam QE camera is presented in Figure 2. X-coordinates of the camera image correspond to different wavelengths, and a median projection in a horizontal plane of the camera image is acquired to extract a light spectrum line.

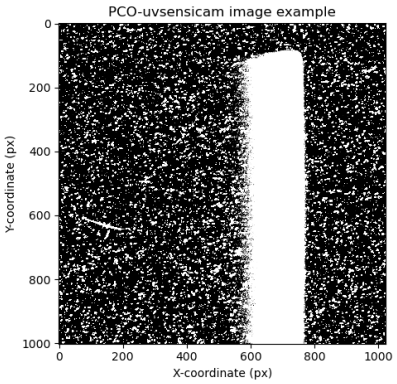

Fig. 2: *An example of the image recorded with PCO SensiCam QE attached to HORIBA CP 140-202 spectrograph.*

3.2 Spectra normalization

Each spill extracted from SIS-18 has a different number of ions per spill, which is why spectra normalization needs to be applied. An ionization chamber is placed in front of the sample in order to get a measurement of the number of ions per spill. The number of counts in the raw spectrum depends on the number of ions that hit the sample during acquisition. Therefore we perform normalization by beam intensity to have average information on spectral counts per unit of beam intensity.

3.3 Spectra calibration

In order to correlate camera pixel x-coordinates with wavelength, the application of wavelength calibration is required. Calibration is performed by reading camera pixel x-coordinates of peaks recorded from Ocean Optics HG-2 calibration light source, which is used as a reference spectrum. The samples used in the experiment were sometimes placed on different target holders. This difference in target holder placement impacts the spectra' comparison, meaning that a specific scaling factor should be applied.

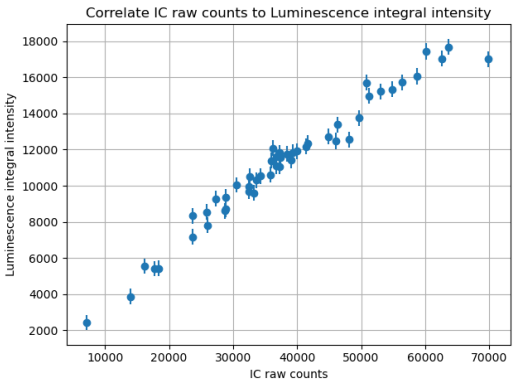

Fig. 3: *Correlation of raw spectra area to IC intensity counts in ZnO(Ga) sample irradiated with ^{238}U @300 MeV/u*

Measurements were performed for the reference BC400 plastic scintillation detector on all three target holders, and the scaling was calculated relative to the first target holder. Quantum efficiency correction was extracted and taken from the user manual for PCO cameras. All spectra were scaled relative to the BC400 spectrum recorded with ^{238}U at 300 MeV/u for easier comparison.

4 Results

Figure 4 compares samples prepared by different manufacturing methods. Doping ZnO with In or Ga resulted in a major light intensity output increase compared to pure ZnO. Results have shown that ZnO(In) yields a slightly greater intensity than samples doped with Ga. The suppression of DL emission by In and Ga doping has been observed in all of the doped samples. It agrees with the results of previous studies (photoluminescence and x-ray luminescence characterization) [6, 8]. After applying thermal treatment, the intensity of the spectra increased by roughly 45%, while the broadness of the spectra remained unchanged. The maximum intensity of the spectra of samples doped with In remained higher than the spectra for Ga, thus leaving thermally treated ZnO(In) as the best candidate for radiation-hard replacements of plastic scintillators for beam diagnostics application.

Recorded spectra of the same materials, when irradiated with ^{40}Ar and ^{238}U, have shown that the intensity of ^{238}U spectra is approximately an order of magnitude higher than spectra with

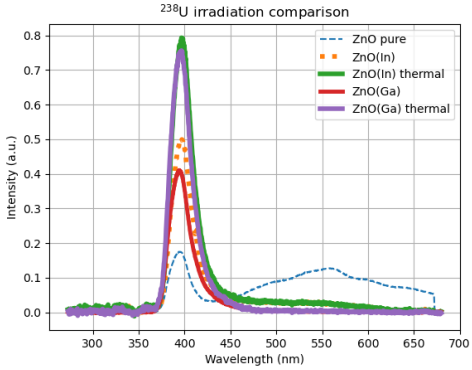

Fig. 4: *Ionoluminescence spectra of pure ZnO, as well as ZnO(Ga) and Zn(In) before and after thermal treatment when irradiated with ^{238}U @300 MeV/u*

^{40}Ar, while irradiation with ^{209}Bi has resulted in intensities that are roughly 90% of ^{238}U spectra. Figure 5 shows spectra maximum intensities as a result of ^{40}Ar and ^{238}U irradiation. For all the samples currently being investigated, it has been recorded that as energy loss increases, the maximum intensity of the spectrum changes in a linear manner. Despite having the lowest maximum intensity of the spectrum, ZnO(Ga) has been noted to have the highest increase in intensity maxima with increased energy loss. Thermally treated ZnO(In) exhibits the highest maximum intensity of any of the samples investigated, while the minimal change of maxima has been noted for initial ZnO(In).

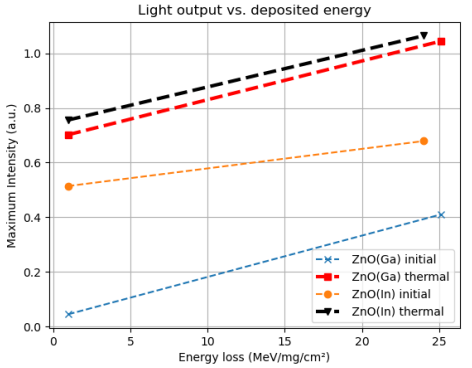

Fig. 5: *Maximum intensities of different materials vs. deposited energy*

Conclusion

In this work, experiments were conducted for the purpose of measuring the intensity of the light emission from scintillations of ZnO based ceramics. The spectra were compared with spectra of BC400 plastic scintillator, currently in use at GSI. Results have indicated that thermally treated ZnO(In) yields a greater light intensity output than that of a BC400 spectrum, while being a fast scintillator and possessing radiation hardness. However, these measurements were performed for samples that were previously never irradiated with heavy-ion irradiation, thus further studies should be conducted on these samples after heavy-ion irradiation.

Acknowledgments

I would like to thank my tutor Maxim Saifulin for the help and guidance he has given me in carrying out my project at GSI during this program. I am also grateful to Ralf Averbeck and everyone who helped organise the International Summer Student Program 2022.

References

[1] C. Kim et al., *Crystals* **11**, 6 (2021), pp. 669 (1–19).

[2] P. Forck, T. Hoffmann, and A. Peters, *in Proc. DIPAC'97, Frascati, Italy* (1997), pp. 165–167.

[3] E.Gorokhova et al., *J. Opt. Technol.* **78**, 11 (2011), pp. 753–760.

[4] E.Gorokhova et al., *J. Opt. Technol.* **82**, 12 (2015), pp. 837–842.

[5] E.Gorokhova et al., *J. Opt. Technol.* **85**, 11 (2018), pp. 729–737.

[6] K. Cherenko et al., *IEEE Trans. Nucl. Sci.* **65**, 8 (2018), pp. 2196–2202.

[7] P. Boutachkov et al., *in Proc. IBIC'19, Malmö, Sweden* (2019), pp. 71–73.

[8] P. Rodnyi et al., *in Proc. EExPolytech'19, St.Petersburg, Russian Federation* (2019), pp. 197–200.

Particle detection on slow atomic collisions at CRYRING

Aina Cabrer Tortajada
UIB (Spain), aina.cabrer2@estudiant.uib.cat

In this project, a new particle detector has been implemented and brought to high vacuum at CRYRING@ESR. The particle detection has been tested using a source for α-particles. The setup is based on a YAP:Ce scintillator with photomultiplier readout.

1 Introduction

CRYRING@ESR is a low-energy storage ring at the GSI-FAIR facility able to store, cool and decelerate heavy, highly charged ions at low energies. Ions can be injected into CRYRING either from a small 300 keV/u RFQ accelerator or from the GSI accelerator complex and injected through ESR. These ions are used to study atomic process and nuclear reaction and the main installations for experiments presently are the electron cooler for precision spectroscopy and the gas-jet target for atomic collisions experiments. [1,2] An overview of the arrangement of CRYRING@ESR is shown in fig. 1.

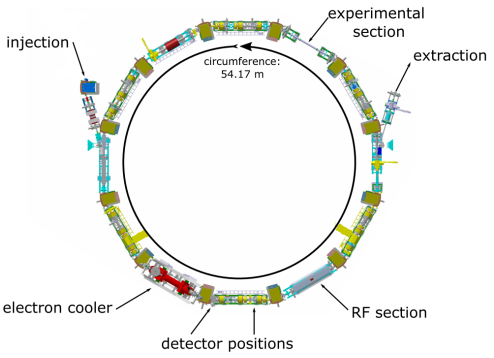

Fig. 1: *Overview of the arrangement of sections at CRYRING@ESR.*

At the gas-jet target station, a stream of cold atoms or molecules are produced to study atomic or nuclear collisions in the stored ions. The low energy range where CRYRING is operating is covering ideally a very interesting domain where the projectile ion is slowly approaching a target atom and the electronic wave functions have a long time to adjust to a two-center combined system. Observing such atomic collisions is of high interest in the strong fields of highly charged ions. Similarly, the available beam energies in the ring are covering a very important range for studying nuclear reactions as they play a role in the nucleosynthesis in astrophysical objects (the so-called "Gamow-window"). Experiments provide a detailed understanding of the processes of how stars are producing ions in different stages of their lifetime.

The circulating stored ions interact with the target and can change their charge state through ionization or through electron capture, or they undergo a nuclear reaction through which the number of nucleons is changed. The product of these reactions are daughter ions with a changed charge to mass ratio and possibly even changed momentum and will be deflected off from the parent ion beam in the next main dipole magnet of the ring. The product ions can be counted using small, movable detectors which can be installed in a position which is specific for each product ion. The detector count rate is used to derive the cross section σ for the particular reaction being studied in each experiment.

In this project, a previously existing detector setup at the gas-jet target has been modified and measurements using an α-source were performed to characterize the new detector configuration. The purpose of this measurement is to identify an optimum working point and also to obtain reference data for analyzing long-term aging effects of the detector head through many years of use.

The detector is identified by the GSI/FAIR nomenclature name 'YR09DD1AS'. The detector mount was installed to a position where it

is sensitive to electron capture reactions at the gas-jet target and for primary ion beams with charge states $1 \leq q_i \leq 20$. The detection principle is a scintillation detector with photomultiplier readout. The detector head is a slightly modified variant of a setup at a different section of CRYRING (YR03DS1HA) and the modifications include a new light shielding and by installing a holder for a weak radioactive source emitting α particles. The detector assembly is designed to fulfill the strict ultra-high vacuum conditions of CRYRING.

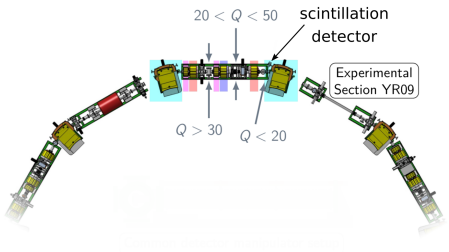

Fig. 2: *Schematic positions of planned or existing particle detectors for beam-like products produced in the gas-jet region YR09 of CRYRING@ESR.*

2 Detector and Setup

The detector is based on a scintillator setup. It uses a YAP:Ce crystal (Yttrium-Aluminium-Perovskit with very low Cerium doping) as scintillating material. This scintillator consists of a slab of 20 mm x 20 mm x 0.5 mm where the product particles will impinge. The impacting ions deposit its full kinetic energy into the crystal, creating a large number of electron-hole pairs. [3] The Cerium-doping acts as impurity center, capturing the electrons and holes, and emitting fluorescent photon in their capture. A light-flash is emitted by the crystal, transmitted from the vacuum side of the detector through a light guide and window flange to the air side where it is recorded with the photomultiplier assembly (PMT), whose function is to convert the incident photons into a measurable electrical signal. The PMT assembly itself consist of a PMT model Hamamatsu R8619 which is embedded into a Mu-metal tube for shielding of external magnetic fields. In front of the PMT there is an optional bandpass filter (Edmund Optics model Techspec 86-982) to block anything but the light from the scintillator and a short cylindrical plastic light guide to allow a further recessed installation of the PMT into the Mu-metal tube for improved magnetic shielding.

The process of conversion of the photons to an electrical signal starts when the photons strike the photocathode of the PMT and by the photoelectric effect the electrons of the surface are ejected. These photoelectrons are directed by the focusing electrode toward the cascading array of dynodes, where through secondary electron production, an ever increasing avalanche of electrons is started. The electron cloud is transported from one dynode to the next stage by electrical fields which are optimized for high

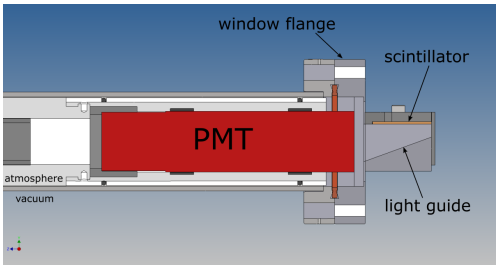

Fig. 3: *Schematic of the scintillator detector.*

yield in secondary electron production. Typically, for one incident photon, about $\approx 10^8$ electrons are produced, converting a small number of photons into measurable quantities of electrical current.

In order to carry out the test measurements, the α particle source that has been used is 241-Am. In its decay process, in addition to generating alpha decay, gamma rays are also obtained, although in a much smaller proportion.

241-Am has two main decay channels through α-decay. The α particles have nearly the same kinetic energies of 5.486 MeV at 85% branching ratio and 5.443 MeV for 13% of the time. The α decay of 241-Am leads to an excited Neptunium (237-Np) nucleus, which consecutively emits a secondary γ quant. For the γ-rays, the predominant energy is 59.5409 keV [4, 5].

The source is a commercial product where the α emitter has been applied to the surface of a thin steel plate in an open design. The nominal activity of the source is 5 kBq. The steel plate is installed into the vacuum system of the detector setup on a new source holder and the scintillator crystal can be moved in front of the source with ≈ 45 mm the closest distance. Considering the solid angle coverage of the scintillator crystal

from the source, we expect a count rate of about 90/s on the detector.

3 Results

First, the raw photomultiplier output signal for the detector in front of the α source is directly measured by an oscilloscope. A characteristic trace of the output signal is given in fig. 4. The raw pulse straight has a height of $\sim 90mV$ when the detector is in front of the α source and we find a signal rise time $(10-90\%)$ of about 5 ns and 50 ns for the decay, which is characteristic for YAP:Ce [6]. Since Am-241 emits nearly monoenergetic α particles, only one characteristic peak height is expected and the shown signal is a good example of the detector performance.

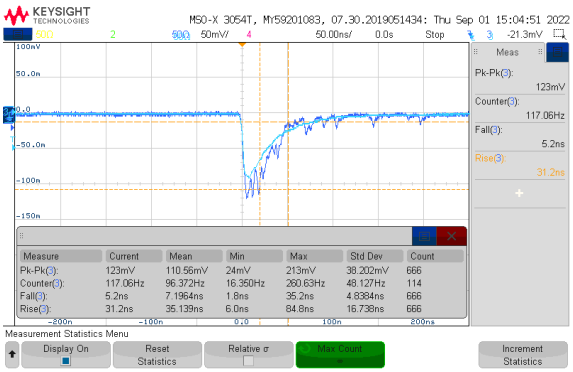

Fig. 4: *Signal shown in the osciloscope when an alpha particle reaches the detector*

In the next step, a Multichannel Analyzer (MCA) shall characterize the detector signal quantitatively. The MCA analyzes the input peaks for maximum peak height, converts the peak height analog value into a digital number, and counts the signals in a histogram. Each bin of the histogram corresponds to a narrow range of input voltages and after a certain amount of time, the count rate in each bin contains the number of occurrences of each input voltage in the time period. Ideally, the histogram x-axis scales linearly with particle impact energies.

The very fast detector signal needs to be matched to the expected input characteristics of the MCA. Therefore, a shaping amplifier (Ortec 671) stretches, inverts and amplifies the PMT signal. The oscilloscope trace for one example pulse (red line) is shown in fig. 5. In the following, the results from MCA measurements are discussed for different configurations.

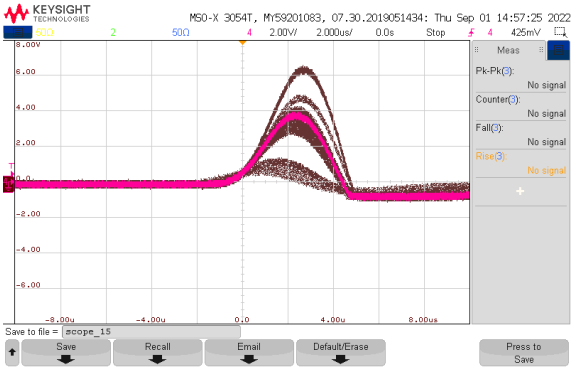

Fig. 5: *Signal received by the MCA. The shaded curves represent the different signals that have been collected in a given period of time.*

It was observed that small changes in the PMT configuration provided very different results, as can be seen in fig. 6. In the first subpanel, the filter and light guide were installed and the results obtained are surprisingly poor, as the found signal is very broad and impossible to confidently discriminate from the background. For the second subimage, the PMT was installed without filter and without light guide and a dramatic improvement of the spectrum was found, as now the alpha line is prominently visible and easy to separate. In the third subpanel, the filter remained removed from the setup but the light guide was installed between the vacuum window and the PMT with only a slight visible degradation from the previous case. The degrading effect of the filter on the transmission of scintillation light is unexpected. In consequence, the filter was left out from the setup from all following measurements.

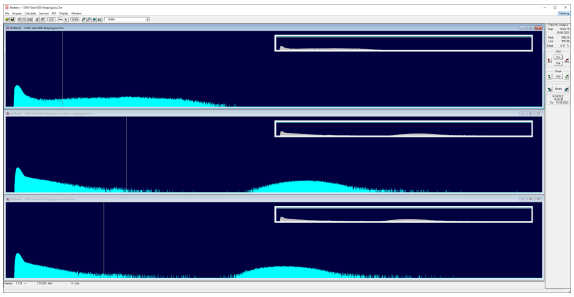

Fig. 6: *Output received from the MCA.*

To identify the ideal working point of the Photomultiplier (PMT), detector spectra were recorded with the MCA setup for different PMT voltage settings. In total, a range of 850 to 1300 V bias voltage was measured where we

analyzed the relative line width and the findings are shown in fig. 7. We find systematically

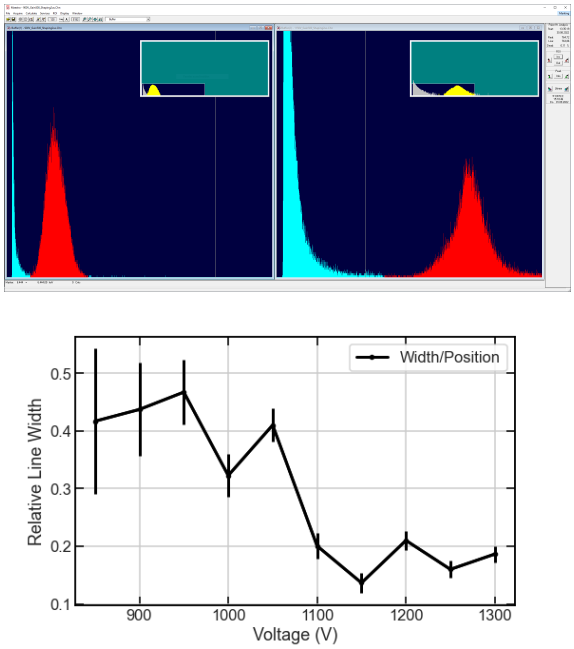

Fig. 7: *Top: Example spectra for PMT at 900 V and 1150 V respectively. Bottom: Relative line width of the 5.4 MeV α radiation as function of the Photomultiplier operating voltage.*

for increasing PMT bias voltages, the lines are shifting to higher MCA channels, while the line width is nearly constant. From the curve in fig. 7 we find that voltage settings around 1150 V produce a clearly distinguishable, narrow line (FWHM $\approx$ 15%) which is well separated from the low-energy background noise. This allows for a confident setup of a discriminator threshold in future particle counting experiments.

4 Conclusion and Outlook

The results of this project have been satisfactory. It has been possible to improve on the PMT assembly; without the filter, the expected results are obtained. For the future, it might be interesting to characterize this filter on a optical bench in order to understand its degrading influence of the overall performance.

Thanks to the various tests carried out, it has been possible to obtain reference data on the detector's performance. These data will allow us to track the YAP:Ce crystal's aging throughout future beamtimes. Also, significantly optimized conditions for its operation were identified and the performance significantly improved.

Moreover, measurements were also taken with exactly the same parameters but distinguishing between the cases in which the cave light was on and off, although no measurable differences were obtained. The latter is a very positive factor since possibly when the whole ring is working, there could be some external light sources that should not affect the detector performance. It was found though, that internal light sources (e.g. vacuum gauges or ion pumps) are strongly affecting the detector's performance. At the present detector's position, operation in experiments with all such internal light sources turned off is a possible remedy but an improved design of the light shielding should be considered in the future.

Acknowledgments

First of all I would like to show my most sincere thanks to my tutor Michael Lestinsky, for all his help and above all for always having time to answer all my doubts. I would also like to thank Esther and Mircea for their support and involvement in the project, and to all the summer students for making this experience unforgettable. Finally, thanks to my family, for always supporting me in all my decisions and encourage me every day to give my best.

References

[1] "TDR: Low energy Storage Ring LSR". In: (2011).

[2] M. Lestinsky, Y.Litvinov, and T.Stöhlker. "Physics book: CRYRING@ESR". In: *The European Physical Journal Special Topics* (2016)

[3] C.Hahn et al. "A scintillator-based particle detector for CRYRING@ESR". In: *X-Ray Spectrometry*(2020).

[4] Richard B. Firestone and Virginia S.Shirley, eds. *Table of Isotopes*. Eighth edition. John Wiley and sons, Inc., 1996.

[5] url: https://en.wikipedia.org/wiki/Americium-241.

[6] V.G. Baryshevsky et al. "YAlO3:Ce-fast-acting scintillators for detection of ionizing radiation." *In: NIM B* 58 (1991), p. 291.

Particle tracks interactions featuring radiation chemistry evolution

Lorenzo Castelli
University of Pisa, l.castelli3@studenti.unipi.it

This project concerns the use of the Monte Carlo track structure code TRAX and its chemistry version TRAX-CHEM for the study of the evolution of radiation damage in a water volume. After presenting the major features of these algorithms, simulation results concerning the radicals and molecules produced by different beam qualities will be discussed. Special emphasis will be placed on the effects of track interactions at the chemical stage of radiation damage.

1 Introduction

The first step in the process of radiation damage is the energy transfer of the primary particle and the secondary electrons to the surrounding medium, via ionization or excitation of the target molecules. Damage to biologically relevant compartments occurs either directly by these processes or indirectly due to the formation of radicals which diffuse and react with the biomolecules. The most sensitive target for sustainable damage of tissues is the DNA within the cell nucleus. Not only it contains all genomic information, which is transmitted to daughter cells during mitosis, but it is also the basis of protein expression, fundamental for the entire cell functionality.

Monte Carlo (MC) codes, thanks to their capability to reproduce the stochastic nature of radiation interactions with a target material, are appropriate tools to describe this fenomena. The events featuring radiation damage currently simulated by MC algorithms can be divided and studied in different stages, ranging from 1 fs to 1 μs: physical($\sim fs$), pre-chemical ($fs - ps$) and chemical (up to the μs). Within the physical stage, water molecules - major target of radiation - are ionized and excited, and at the same time secondary electrons are produced. On the other hand, the pre-chemical stage consists in the formation of radiolityc species by dissociation processes of ionized and excited water molecules and in the thermalization and hydration of the sub-excitation electrons. At this point the new chemical species diffuse and react with themselves and with the solvent until reaching an equilibrium (cf. Fig 1). TRAX [1] is an example of a MC code developed at GSI, with the intent of simulating the passage of electrons and ions through different materials. Ionization, excitation and elastic interactions caused by primary radiation and secondary electrons within the target are described event by event, computing all their positions and energy depositions after each interaction. Recently [2] the code has been extended to simulate the pre-chemical and chemical stages (TRAX-CHEM). Moreover, a new feature has been introduced, to allow for the study of chemical species interaction generated by different tracks. In this way it is possible to study which are the effects of different

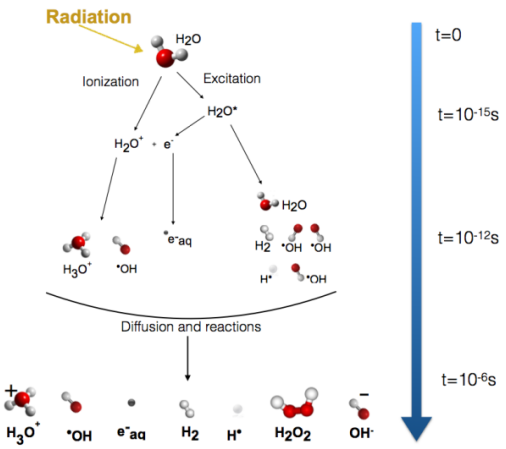

Fig. 1: *Time scales of radiobiological events featuring water radiolysis*

beam qualities, energies (and LET, linear energy transfer), target oxygenation at a chemical level, with the possibility of application to different scenarios. An example is FLASH (ultra high dose rates), where multiple pulses are delivered in a very short time, making it necessary to take into account possible intertrack interactions.

2 Methods

The physical stage of radiation damage in liquid water simulated with the TRAX code considers cross sections for shell specific ionization and excitation events. For water target the cross section set includes five ionization shells and eight excitation states [2]. Additionally, elastic interaction cross sections for electrons and the production of Auger electrons are included as well, in order to obtain a spatially realistic pattern and subsequent distribution of chemical species (electrons are always present either as primary particles or as secondaries). The tracks of incident projectile are followed event by event until reaching a cutoff value corresponding to the lower electronic excitation energy of $7.4eV$.
After the completion of the physical stage, the spatial distribution of all the shell specific ionization and excitation events are provided, as well as the position of all the sub-excitation electrons. Different radiation qualities, i.e. radiation type and energy, vary in their energy deposition patterns. A first simulation using the classic TRAX code was carried on in order to visualise these differences, in both the physical and chemical stages. Three beam qualities were studied: electrons at $500keV$, protons $100MeV$ and carbon ions $40MeV/u$. These are originated from a point-like source and directed towards a water volume (cylinder with $5\mu m$ radius and $1\mu m$ depth). The simulations followed the process up to the end of the chemical stage.

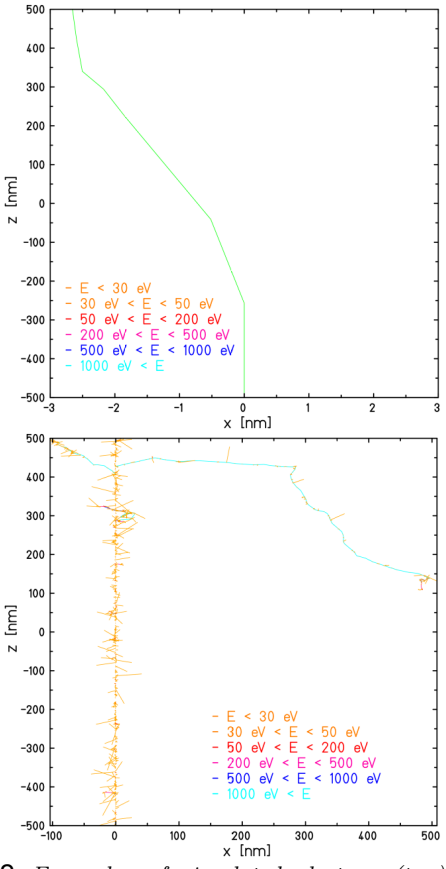

Fig. 2: *Examples of simulated electron (top) and carbon ion (bottom) tracks produced by the TRAX code.*

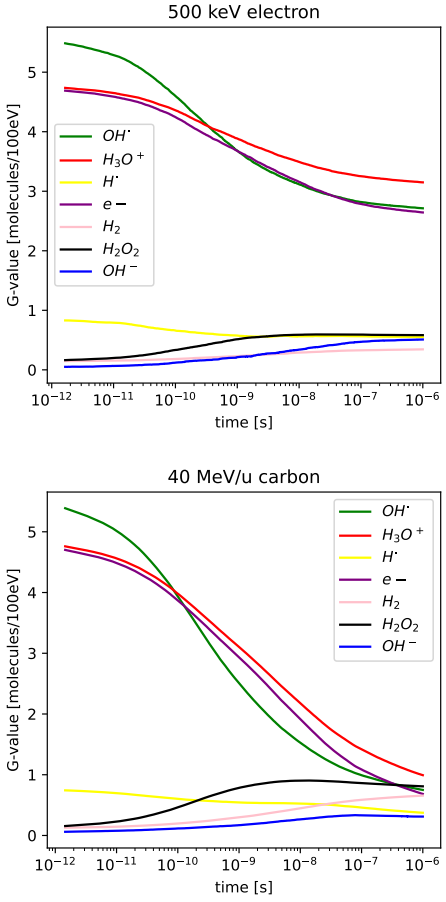

Fig. 3: *G-value curves induced by electron (top) and carbon ion (bottom) tracks.*

The differences in LET are strikingly visible

in Figure 2 (here only the extreme cases featuring electrons at low LET and carbon ions at high LET are presented). From one side, the carbon beam is characterised by a high ionization density around its track, with also few delta electrons which deposit energy far from the primary ion (Fig. 2). On the other side, low LET electrons are featured by low density tracks, resulting from more sparsely ionization/excitation events [3]. The pre-chemical phase is characterized by dissociation and thermalization of all the products generated during the physical stage. Here radicals are formed and thermalized within a ps and few nm. Afterwards, the radiolytic products start to diffuse and interact with each other until the track evolution is concluded (also this stage is described with a step by step approach). The interaction follows a distance criterion based on the definition of a proximity parameter a_{AB}, so that the interaction takes place if the distance between reactants (A and B) is smaller than a_{AB} [2]. As a consequence, a difference in the physical behaviour of the primaries, resulting in turns into different relative locations of their chemical species, implies huge changes in the final amount of radicals/molecules. The respective G-value curves(number of molecules produced for every $100eV$ released) of the physical tracks presented in Figure 2 are shown in Figure 3. At the end of the pre-chemical stage ($\sim ps$) the number of molecules produced is almost the same, but once they start interacting, the radicals produced by the carbon beam are consumed at a faster rate, due to the close proximity between each other (high ionization density). Taking for instance the two radicals $OH^{\cdot}$ and e^{-}_{aq}, their amount at $1\mu s$ is different when comparing the two primaries (for carbon and electrons respectively $(0.80\text{vs}.2.66)e^{-}$ and $(0.75\text{vs}.2.72)OH^{\cdot}$). As a consequence, also the amount of produced molecules changes (e.g. H_2 and H_2O_2).

3 Results

3.1 Intertrack effect from a point-like source

For this study the intertrack option has been enable, leaving the simulation setup identical to the previous case with cylindrical geometry, point-like source and electrons ($500keV$) or carbon ions ($40MeV/u$) as primary particles. Here, the physical and pre-chemical phases do not change with respect to the case without intertrack, because at this early times particles do not interact between each others, and consequently the amount of decay/thermalization events per track remains unaltered. In fact the G-value at $1ps$ is equal in every simulation the ratio between the G-value curves from simulations with and without intertrack at $1ps$ is always one. However, the evolution in time strictly depends on number of particles simulated simultaneously, as well as on the LET of primaries. For each radiation type 3 cases have been explored: 2, 3 and 6 simultaneous particles (repeated to have enough statistics to smooth the curve). In Fig.6-7 it is evident that by increasing the number of primary tracks there is a

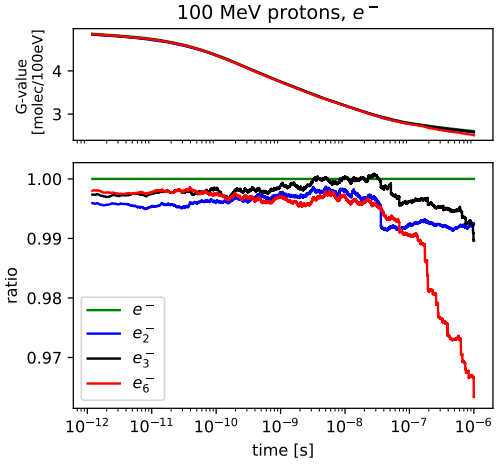

Fig. 4: e^{-}_{aq} *G-values for* $100MeV$ *protons*

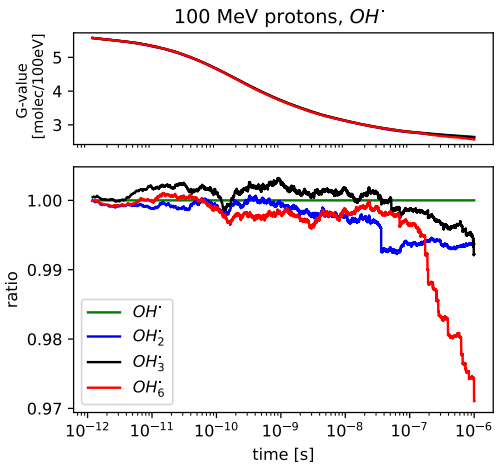

Fig. 5: $OH^{\cdot}$ *G-values for* $100MeV$ *protons*

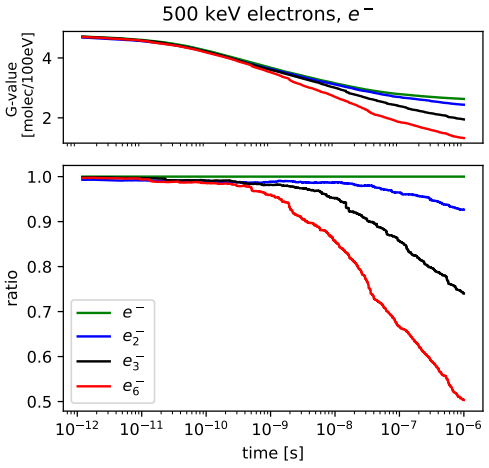

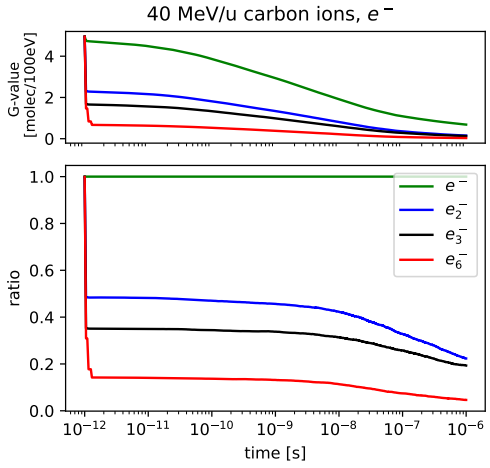

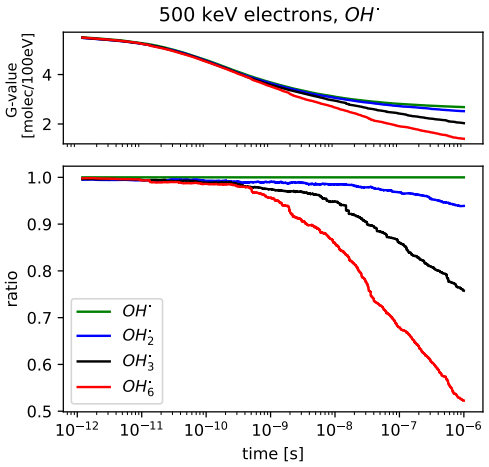

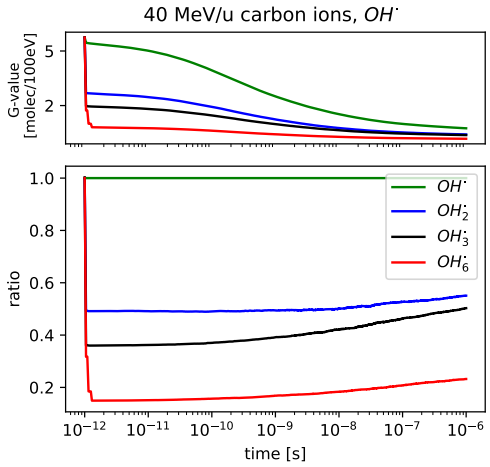

Fig. 6: e^-_{aq} *and* $OH^\cdot$ *G-values for* $500keV$ *electrons*

Fig. 7: e^-_{aq} *and* $OH^\cdot$ *G-values for* $40MeV/u$ *carbon ions*

decrease in the G-value. For the carbon ions case the process is faster because as already mentioned high LET radiation implies high ionization density. Radicals are indeed generated at distances lower than the interaction parameter a_{AB}, inducing them to interact almost completely within $1.3ps$. After this brief phase the ratio for 2 carbon ions is ~ 0.5, because given the same number of molecules produced, they are twice as likely to react (it is possible to move the same argumentation for the cases featuring 3 and 6 particles). G-values for electrons show a strong decrease at $1\mu s$ (almost 50% for 6 particles) with values close to carbon ions without intertrack. Being produced from a low LET radiation, these species are more sparsely distributed, and therefore more affected by intertrack interactions at a longer times.

3.2 Intertrack effect from a 3D source

In this section the simulation setup consisted of two coaxial parallelepipeds (5 x 5 x $0.4\mu m$) and a water cube of $5\mu m$ side irradiated uniformly on one surface by a $100MeV$ proton source. The two parallelepipeds are placed one before and one after the cube (all coaxial) to account for forward and backward scattered secondary electrons. The source simulated is a parallelepiped square ($5x5\mu m$) with $1nm$ depth. Similar to Sec. 3.1 three different cases have been analyzed; 2, 3 and 6 particles simultaneously generated in the volume of the source. Furthermore, to provide the ratio, another simulation without intertrack and with the same geometry (target and source) was made. Protons at $100MeV$ are low LET particles and since they can be generated far from each other $\sim \mu m$, due to the

conformation of the track the intertrack effect is less intense with respect to the previous simulations. As shown in Fig.4- 5 the cases of 2 and 3 tracks are similar even though a little variation from no-intertrack simulation is visible at $1\mu s$ (not relevant $< 1\%$). On the other hand, for 6 particles it is possible to spot a discrepancy, which starts from a tenth of μs and approaches a 3% difference with the no-intertrack case at $1\mu s$.

4 Conclusions

Our results showcase that intertrack-related reactions affect the G-value of radicals and molecules within the target, in particular for $OH^{\cdot}$ and e^{-}_{aq}. The intensity of the effect depends on the particle LET and on the reciprocal position of the primaries. This has been elucidated for setups considering protons, electrons and carbon ions delivered simultaneously.
New simulations can be carried out with the purpose of exploring more deeply the differences between intratrack and intertrack effects, i.e. high vs. low LET (e.g. C vs. $3He$) or even by varying the initial distribution of primaries. Also, by changing the particle rate [4], it is possible to investigate complex fenomena like the FLASH effect where chemical interactions between tracks play a role.

Acknowledgments

I would like to thank my tutor Michael Krämer for giving me the opportunity to work in an interesting research project. It has been a fruitful experience. I am also very grateful to Martina Fuss and Gianmarco Camazzola for their support and their kindness in helping me whenever I had problems with my work. I would like to thank also the other members of the Biophysics group and all the organizers of the Summer Student Program.

References

[1] Kraft G., Krämer M. in *Linear energy transfer and track structure*, Adv. Radiat. Biol., **17** :1-51 (1993)

[2] D. Boscolo, M. Kramer, M. Durante, M.C. Fuss, E. Scifoni in *TRAX-CHEM: A pre-chemical and chemical stage extension of the particle track structure code TRAX in water targets*, Chemical Physics Letters **698** (2018) 11–18

[3] Barbara Drossel, David J. Brenner, Harald Paganetti in *Biophysical modeling of effects of ionizing radiation and associated uncertainties*

[4] J. Ramos-Mèndez, N. Domìnguez-Kondo in *LET-Dependent Intertrack Yields in Proton Irradiation at Ultra-High Dose Rates Relevant for FLASH Therapy* (RADIATION RESEARCH **194**, 000–000 (2020))

Measurement of Ξ_c^0 production in p–Pb collisions at $\sqrt{s_{NN}} = 5.02$ TeV with the ALICE experiment

Fabrizio Chinu
University of Turin, fabrizio.chinu@edu.unito.it

The measurement of the production of prompt Ξ_c^0 baryons in proton–lead collisions at the centre-of-mass energy per nucleon pair of $\sqrt{s_{NN}} = 5.02$ TeV with the ALICE detector at the LHC, is reported. The differential production cross section is measured at mid-rapidity ($|y| < 0.8$) as a function of transverse momentum ($p_{\rm T}$) in the interval $2 < p_{\rm T} < 12$ GeV/c.

1 Introduction

The ALICE experiment at the CERN Large Hadron Collider is optimised to study proton-proton (pp), proton-lead (p–Pb) and lead-lead (Pb–Pb) collisions at ultrarelativistic energies.
Charmed baryons production is a hot topic in the field since recent studies [1] showed an enhancement in the production of charmed baryons in pp and p–Pb collisions with respect to e^+e^- ones, which is yet to be fully understood. This enhancement is related to hadronisation phenomena, therefore studying charmed baryons can lead to a better understanding of how charm quarks hadronise and are confined into hadrons.
In this report feasibility studies for the measurement of the production of Ξ_c^0 baryons in p–Pb collisions with the data collected at the LHC in Run 2, reconstructed in the fully-hadronic decay chain

$$\Xi_c^0 \rightarrow \Xi^-\pi^+ \rightarrow \Lambda\ \pi^-\pi^+ \rightarrow \mathrm{p}\ \pi^-\pi^-\pi^+,$$

with a branching ratio (BR) of $(0.9 \pm 0.2)\%$ (Tab. 1 for details), are presented.

Decay	$\Xi_c^0 \rightarrow \Xi^-\pi^+$	$\Xi^- \rightarrow \Lambda\ \pi^-$	$\Lambda \rightarrow \mathrm{p}\ \pi^-$
BR	$(1.43 \pm 0.32)\%$	$(99.887 \pm 0.035)\%$	$(63.9 \pm 0.5)\%$

Tab. 1: *Branching ratios of the decays studied in this analysis*

Ξ_c^0 baryons are short lived particles (decay length $\approx 46\ \mu m$), so they cannot be detected directly (since the closest detector, the Inner Tracking System, is 3.9 cm away from the interaction point [2]); instead, they have to be reconstructed from the tracks of their decay products. Furthermore, the decay length is so short that it is not possible to reconstruct the decay vertex of Ξ_c^0 baryons with the ALICE apparatus, thus making these particles very difficult to be reconstructed. In order to improve the reconstruction of the complex decay topology, the Kalman Filter (KF) Particle Finder package [3] is used, while to improve the selection efficiency of Ξ_c^0 baryons, machine learning (ML) algorithms are used in this analysis.

2 Kalman Filter Particle Package

To reconstruct the decay topology of this short-lived particle the KFParticle Package was used. It is based on the Kalman Filter algorithm [4], which produces estimates of hidden variables based on inaccurate and uncertain measurements and can predict the future system state based on precedent estimations.
Particles are parameterised as the state vector

$$\mathbf{r} = (x, y, z, p_x, p_y, p_z, E, s)^T\ ,$$

where $(x, y, z)^T$ is the position of the particle, $(p_x, p_y, p_z)^T$ is its momentum, E is its energy and s is the length of the trajectory in the laboratory system l normalised to the particle momentum p, $s = l/p$.
The KF estimates the state vector of the mother particles in 3 steps: at the beginning of the algorithm an approximation of the state vector of the daughters and their covariance matrix is

given; next, for each measurement, the estimate of the state vector of the daughters is extrapolated, taking into account the errors on the measurement; finally, the daughters are transported along their trajectories to reconstruct the decay vertex.

3 Machine learning

The term machine learning comprehends a set of algorithms which allow machines to learn without being explicitly programmed to do so. In this analysis, supervised learning algorithms are used. They are trained by feeding them with examples containing the desired output. The models then adjust their weights until the example data is fitted appropriately. Supervised learning algorithms can be used to solve very common problems in particle physics, such as separating the interesting signal from a large combinatorial background.

4 Data analysis

The data analysed comes from LHC Run 2. Loose preselections were applied on the data, in order to obtain a cleaner dataset. Since the decay topology might differ a lot when studying different $p_{\mathrm{T}}^{\Xi_c^0}$ ranges, the analysis was carried out in different p_{T} intervals: [2-4], [4-6], [6-8] and [8-12] GeV/c. In order to obtain an higher signal-to-background ratio, some selection criteria were applied on the p_{T} (π from Ξ_c^0), which was not used to train the model, as shown in Table 2.

p_{T} (GeV/c)	[2-4]	[4-6]	[6-8]	[8-12]
π p_{T} (GeV/c)	> 1.6	> 1.2	> 1.0	> 1.0

Tab. 2: *Selection criteria on the p_{T} of the bachelor π from Ξ_c^0 decay*

4.1 Training the model

In order to train the ML model, signal and background examples are needed. The former comes from Monte Carlo (MC) simulations, the latter comes from the data obtained by the experiment. Since no signal should be included in the background examples, only data coming from the mass invariant distribution range of M $<$ 2.39 GeV/c^2 or M $>$ 2.55 GeV/c^2 ($M^{\Xi_c^0} = (2.47044 \pm 0.00028)$ GeV/c^2 [5]) are included in the background dataset.

Each candidate is described by an array of physical variables:

- **PA (Ξ^- to PV)**: Pointing Angle of Ξ^- to PV, i.e. the angle between the momentum of the reconstructed Ξ^- and the line connecting the Ξ^- production vertex to primary vertex (PV)
- **Ξ^- mass**
- **χ^2_{topo} (Ξ^- to PV)**, describing how well the Ξ^- track fits the PV
- **nσ_{TOF} (π from Ξ_c^0)** and **nσ_{TPC} (π from Ξ_c^0)**, particle identification information of the pion coming from the Ξ_c^0 provided by the Time Projection Chamber (TPC) and by the Time Of Flight (TOF) detectors, which proved to be the best variables to separate signal from background
- **Normalised decay length** Ξ^-, i.e. the decay length divided by its uncertainty
- **DCA$_{xy}$ ($\pi^+$from Ξ_c^0)**, i.e. the Distance of Closest Approach in the transverse plane of the $\pi^+$from Ξ_c^0

These variables are mainly related to the Ξ^- topology.

The model learns how to separate the signal from the combinatorial background by recognising patterns within the data. It can then exploit the differences between the signal and background variables distributions to make predictions on candidates it has never seen before. The ML algorithm makes predictions by assigning to each candidate a score related to the probability of that candidate being signal.
To study how well the model has learnt to classify the data, output score distributions can be studied. As shown in figure 1, the background distributions peak at low probabilities, in accordance to what is expected. The signal distributions instead do not peak at high probabilities. This is a consequence of the fact that it is not possible to reconstruct the Ξ_c^0 decay vertex and to use decay's topology variables and shows the level of difficulty of the analysis.

In order to quantitatively understand how well the model has learnt to classify signal from background, Receiver Operating Characteristic (ROC) curves are studied. ROC curves plot the

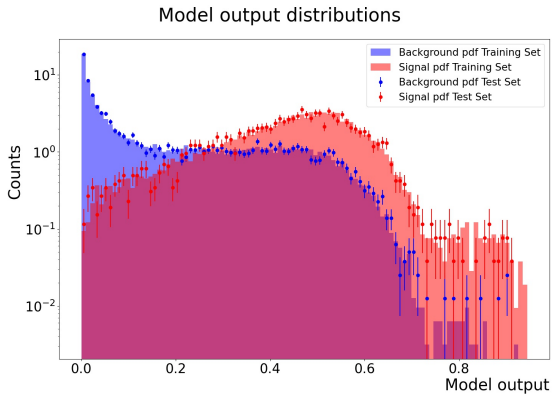

Fig. 1: *Distributions of the probability scores for background (blue) and signal (red) for training and test sets in the* $2 < p_{\mathrm{T}} < 4$ *GeV/c interval*

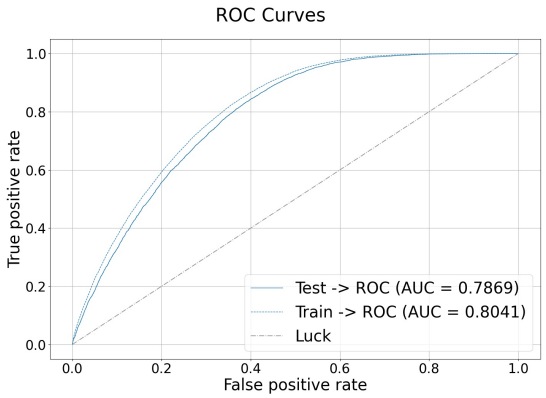

Fig. 2: *ROC curves for train and test datasets in the interval* $4 < p_{\mathrm{T}} < 6$ *GeV/c*

true positive rate, i.e. the signal selection efficiency, vs the false positive rate, which is related to the background selection efficiency, for various threshold values on the model output. The ROC AUC (Area Under the Curve) is then evaluated, giving a quantitative description on the model's performance; ROC AUC value of 0.5 corresponds to a random classifier, while ROC AUC of 1 corresponds to a perfect classification of the two class samples. The ROC curves obtained in this analysis for the train and test sets in the interval $4 < p_{\mathrm{T}} < 6$ *GeV/c* are shown in figure 2. It is important to compare the train and test ROC curve: a big difference between the two curves suggests *overfitting*, i.e. the model has only learnt how to classify the training data and cannot generalise on the test set. The model trained in this analysis obtained a good ROC AUC on the testset (0.7869), with a small gap between train and test ROC curves, suggesting it has learnt how to classify signal from background and that it is not overfitting.

4.2 Working point

Once the model is trained, a working point has to be chosen. The working point is a threshold value on the model output such that every candidate that obtained a score greater than the threshold will be selected as a possible signal. It is chosen in a blind way, without looking at the data, in order not to introduce any biases in the working point choice.
In order to choose the working point, the following quantities were estimated for several threshold values on the ML output scores:

1. **Efficiency**, which is the fraction of produced Ξ_c^0 being actually reconstructed and selected as Ξ_c^0. It was evaluated on the MC fraction used for testing the model as:

$$\varepsilon = \frac{\#\Xi_c^0 \ selected}{\#\Xi_c^0 \ in \ test \ set} \cdot \frac{\#\Xi_c^0 \ reconstructed}{\#\Xi_c^0 \ generated} \ ,$$

   where the first fraction corresponds to the model selection efficiency, while the second takes into account the reconstruction efficiency and the acceptance of the detector

2. **Background**, which was estimated by fitting the invariant-mass distribution of the selected candidates and then integrating the background fitting function in the region under the peak. A quadratic function was used to describe the background in the $2 < p_{\mathrm{T}} < 4$ *GeV/c* region, while an exponential function was used in the $4 < p_{\mathrm{T}} < 12$ *GeV/c* region

3. **Expected signal**, estimated using the cross section measured in proton-proton collisions at $\sqrt{s} = 5.02$ TeV [6], scaled by the number of nucleons in Pb nuclei (208):

$$N^{\Xi_c^0,\overline{\Xi}_c^0}_{raw,exp} = 2{\cdot}208 \left.\frac{\mathrm{d}^2\sigma}{\mathrm{d}p_{\mathrm{T}}\mathrm{d}y}\right|_{pp} {\cdot}\Delta p_T \Delta y {\cdot}\varepsilon {\cdot} BR {\cdot} \mathcal{L}_{int}$$

   Where $\mathcal{L}_{int}$ is the integrated luminosity: $\mathcal{L}_{int} = (302 \pm 10)\mu b^{-1}$, Δp_T is the p_{T} bin width, Δy is the rapidity bin width and the factor 2 takes into account the fact that both particles and antiparticles are measured

4. **Pseudo-significance**, defined as

$$\frac{N^{\Xi_c^0,\bar{\Xi}_c^0}_{raw,exp}}{\sqrt{N^{\Xi_c^0,\bar{\Xi}_c^0}_{raw,exp} + background}} \ ,$$

is the leading factor in choosing the working point: the threshold value is selected in order to maximise the pseudo-significance.

The chosen threshold values are reported in table 3:

p_{T} (GeV/c)	[2-4]	[4-6]	[6-8]	[8-12]
Score threshold	0.25	0.15	0.15	0.15

Tab. 3: *Working points chosen for the different p_{T} intervals*

These selection criteria are very loose and lead to a very high efficiency and background rejection.

4.3 Raw yield, efficiency and cross section

Once the working point is chosen, the raw yields S (i.e. the number of candidates that are reconstructed and selected as signal in the analysis sample) are extracted. They are obtained by fitting the invariant-mass distribution of the candidates that pass the working point selection with a gaussian function and then integrating it. The background (B) is obtained by integrating the background fitting function in the region under the peak. Significance is then evaluated as $S/\sqrt{S+B}$.

A significance greater than 3 was achieved in every p_{T} bin of the analysis.

Efficiency are also evaluated after choosing the working point. The total efficiency can be factorised in 3 parts:

- Reconstruction efficiency, i.e. the efficiency of reconstruction of the Ξ_c^0 baryons of the ALICE apparatus
- Preselections efficiency, which is the ratio of the number of Ξ_c^0 after applying the preselections to the number of Ξ_c^0 before applying those selection criteria
- BDT model efficiency, i.e. the ML model efficiency of selection of the Ξ_c^0

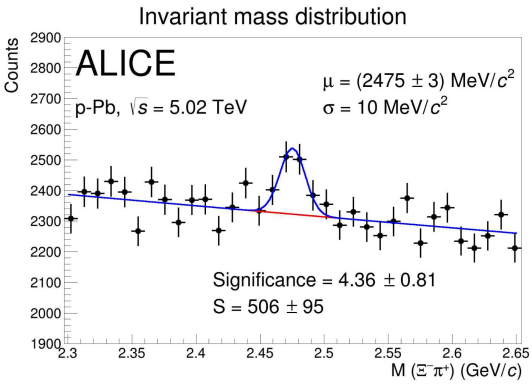

Fig. 3: *Invariant mass distribution fit of the candidates that pass the selection in the $6 < p_{\mathrm{T}} < 8$ GeV/c interval*

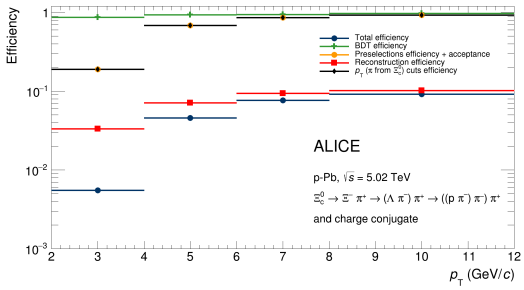

Fig. 4: *Comparison of total efficiency (blue) vs reconstruction efficiency (red) vs preselection efficiency (yellow) vs p_{T} (π from Ξ_c^0) selection efficiency (black) vs ML model efficiency (green)*

As shown in figure 4, the ML model efficiency is very high (≈ 1), while the main contribution to the efficiency drop is due to the reconstruction efficiency. The comparison also shows that the main contribution to the preselections efficiency comes from the selection criterion on the p_{T} (π from Ξ_c^0).

5 Results and discussion

Once the raw yields (now referenced as $N^{\Xi_c^0,\bar{\Xi}_c^0}_{raw}$) and the efficiency are extracted, the cross section is evaluated through the formula:

$$\frac{\mathrm{d}^2\sigma}{\mathrm{d}p_{\mathrm{T}}\mathrm{d}y} = \frac{N^{\Xi_c^0,\bar{\Xi}_c^0}_{\mathrm{raw}}}{2 \cdot \Delta p_{\mathrm{T}} \Delta y \cdot \varepsilon \cdot \mathrm{BR} \cdot \mathcal{L}_{\mathrm{int}}} \ ,$$

and is compared with the production of Ξ_c^0 in pp collisions [6] scaled by 208 and with the production of D^0 mesons in both pp [7] (scaled by 208) and p–Pb [8] collisions. The results obtained are reported in figure 5, while in figure 6

the ratio of the production cross section of Ξ_c^0 in pp and p–Pb collisions to the D^0 one in pp collisions is shown.

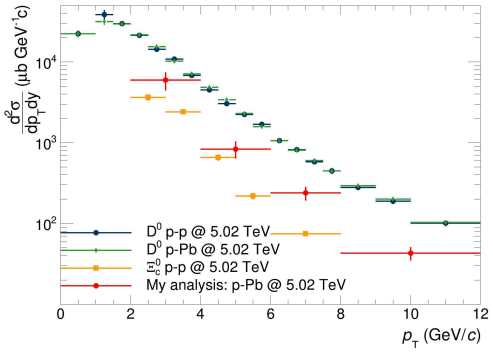

Fig. 5: *Production cross-section of Ξ_c^0 baryons in p–Pb collisions at 5.02 TeV (red) compared with Ξ_c^0 production in pp collisions (yellow), D^0 production in p–Pb collisions (green) and D^0 production in pp collision (blue)*

The production cross section of Ξ_c^0 obtained in this analysis is larger than the one obtained in pp collision by a factor of approximately 2. The reason behind this difference has yet to be understood and will be studied in the future.

6 Summary

The p_T-differential production cross sections of Ξ_c^0 baryons in p–Pb collisions at a centre-of-mass energy of $\sqrt{s_{NN}} = 5.02$ TeV was reported. The measurement was performed at mid-rapidity ($|y| < 0.8$) in the transverse-momentum range $2 < p_T < 12$ GeV/c with the data collected by the ALICE detectors. The results obtained in this analysis are unexpectedly larger of a factor of approximately 2 from the results of the Ξ_c^0 analysis in pp collisions. In the future this difference will be studied in detail and will be compared to the results obtained with LHC Run 3 data, which will provide more accurate results due to the larger statistics available.

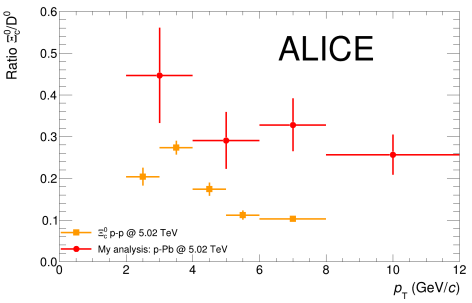

Fig. 6: *Ratio of the Ξ_c^0 production cross section in p–Pb collisions (red) and in pp collisions (yellow) to the D^0 production cross section in pp collisions*

Acknowledgments

I would like to thank my supervisor Andrea Dubla for the help he has given me in carrying out my project at the GSI facility and for all the useful suggestions he gave me during these two months. Many thanks to the ALICE group for the interesting insights into the working environment, for their support, their kindness and their availability at any time. Working with them has always been pleasant and enjoyable. Lastly, I would also like to thank Francesco Prino for his help in entering into this program.

Thanks!

References

[1] The ALICE Collaboration, "Charm-quark fragmentation fractions and production cross section at midrapidity in pp collisions at the LHC" doi: 10.1103/PhysRevD.105.L011103

[2] The ALICE Collaboration, “The ALICE experiment at the CERN LHC” , doi: 10.1088/1748-0221/3/08/s08002

[3] The KF Particle Finder package for short-lived particles reconstruction for CBM - GSI-SR2012-PHN-NQM-EXP-50

[4] Kalman Filter Tutorial, url: https://www.kalmanfilter.net/default.aspx

[5] R.L. Workmanet al.(Particle Data Group), Prog.Theor.Exp.Phys.2022, 083C01 (2022)

[6] The ALICE Collaboration, "Measurement of the production cross section of prompt Ξ_c^0 baryons at midrapidity in pp collisions at $\sqrt{s}$ = 5.02 TeV", doi: 10.1007/jhep10(2021)159

[7] The ALICE Collaboration, "Measurement of D^0, D$^+$, D^{*+}, and D$_s^+$ production in pp collisions at $\sqrt{s_{NN}}$ = 5.02 TeV", doi: 10.1140/epjc/s10052-019-6873-6

[8] The ALICE Collaboration, "Measurement of prompt D^0, D$^+$, D^{*+}, and D$_s^+$ production in p–Pb collisions at $\sqrt{s_{NN}}$ = 5.02 TeV", doi: 10.1007/jhep12(2019)092

Assessing the expansion model dependence of the r-process reaction network

Raquel Nicolás del Álamo
University of Sevilla, raquelnicolasdelalamo@gmail.com

Chen, Heng Hao
National Tsing Hua University, ajordan510409@gmail.com

Neutron star mergers have been identified as possible r-process production sites. Simulating the operation of the r-process reaction network requires knowing the thermodynamic evolution of the material ejected from the merger. Present limitations in hydrodynamic calculations enforce the use of an extrapolation scheme in order to follow the evolution of the ejected material at times $\gtrsim$ 30 ms. We have analysed the model dependence of the network calculations adopting two different expansion prescriptions. Moreover, we have studied how the expansion model can influence the production of the fissioning isotope $^{254}_{98}$Cf.

1 Introduction

Big-bang nucleosynthesis and the various stages of stellar burning are the responsible mechanisms for the production of elements up to iron. However, the observed solar abundance pattern is not yet fully understood, and the comprehension is even poorer when it comes to the heavy element region.

The fast neutron capture process, or r-process, is the mechanism responsible for the synthesis of the heavy neutron-rich elements. It consists of a succession of neutron captures and β decays taking place close to the neutron drip lines requiring a neutron-rich environment in order to proceed [1].

The astrophysical site where the r-process takes place is still a matter of debate. The need of high neutron densities arises neutron stars (NS) as suitable neutron reservoirs. Following the detection of the first gravitational wave coming from a NS-NS merger, GW17081 [2], and its electromagnetic (EM) counterpart AT 2017gfo [3], neutron star mergers (NSM) were identified as feasible sites for r-process production.

At late times after the merger ($\sim$ days), the EM emission could be dominated by the decays of a limited set of species. $^{254}_{98}$Cf decays through fission and has a lifetime of 60.5 days [4], similar to that of $^{56}_{27}$Co ($t_{1/2}$ = 77.236 d [5]) in the $^{56}_{28}$Ni to $^{56}_{27}$Co chain dominating supernovae emissions [6]. Consequently, it is believed that $^{254}_{98}$Cf might be one of the main contributors to the EM signal following the merger [7]. Identifying signatures of heavy isotopes, such as $^{254}_{98}$Cf, in the observed EM signal would provide evidence for the presence of elements produced via the r-process in NSM.

Uncertainties in the r-process modelling come both from the astrophysical environment conditions and from the nuclear data input. Simulating the dynamics of the material ejected from the merger implies cumbersome hydrodynamic calculations which are computationally expensive. Besides, a vast amount of nuclear information is needed to model the r-process path. In particular, information on the masses, neutron separation energies and beta decay half-lives must be provided for nuclei far away from stability for which there is no available experimental data, and thus one relies strongly on theoretical predictions [8]. Furthermore, fission comes into interplay when heavy nuclei are produced. Precise knowledge on the fission yields is hence required for an accurate modelling of the reaction network [9].

In our study, we have simulated the operation of the r-process reaction network within

the material ejected from a binary NSM. Due to present limitations on the hydrodynamic calculations, at late times the expansion dynamics cannot be solved precisely and the density evolution is extrapolated following some analytical model left to choice. The use of different models leads to differences in the results and in the final abundance pattern. We have explored two different expansion scenarios, aiming to understand how sensitive the reaction network calculation is to changes in the thermodynamic evolution. In addition, we have studied how the $^{254}_{98}$Cf production is affected by modifications in the expansion model.

2 Hydrodynamic calculations and nuclear input

The reaction network calculations depend on astrophysical conditions such as density, temperature, entropy, etc. In our calculation, the initial conditions ($t \lesssim 30$ ms) of the NSM have been established from a trajectory of an ejected fluid element based on a smoothed, three-dimensional particle hydrodynamics code. The code solves the Einstein equations approximately by imposing conformal flatness in the three-dimensional space. The calculations start with a NS binary system in quasi-equilibrium, a few orbits before the merger, where matter is assumed to be at zero temperature, in equilibrium and neutrinoless. The gravitational masses of both stars are $1.35 M_\odot$, and the equation of state (EoS) used to model nuclear matter is TM1 [10]. The initial composition is determined from the trajectory data assuming nuclear statistic equilibrium (NSE), implying balance among all the nuclear species.

The network contains data on the masses, half-lives, neutron separation energies and reaction rates for more than 7300 nuclei, which have been derived in accordance with the finite range droplet model (FRDM). The processes included are charged particle reactions, neutron captures, photodissociations, β and α decays and fission.

Although the trajectory dynamics depends mainly on the astrophysical conditions, it has been corrected consistently with the reheating due to the energy released in the nuclear reactions. The EoS used by the code takes into account 3 contributions: a Boltzmann ideal gas of nuclei, a Fermi-Dirac ideal gas of electrons and an ideal gas of photons. Defining the specific heat per nucleon at a constant volume as $c_V = d\varepsilon/dT$, the expansion scale $\tau_n = \rho\, dt/d\rho$ and $\dot{q}$ being the energy generated by nuclear processes, one can calculate the temperature evolution using:

$$\frac{dT}{dt} = \frac{1}{c_V}\left[\dot{q} - \frac{1}{\tau_n}\left(\frac{P}{\rho} - \rho\frac{d\varepsilon}{d\rho}\right)\right]. \qquad (1)$$

The entropy is calculated at each time-step using the relation:

$$\frac{ds}{dt} = \frac{\dot{q}}{k_B T} - \left[\sum \eta_i \frac{dY_i}{dt} + \eta_e \frac{dY_e}{dt}\right] \qquad (2)$$

with [1]

$$\eta_i = \ln\left[\frac{\rho}{m_u}\frac{Y_i}{g_i}\left(\frac{2\pi\hbar^2}{A_i m_u k_B T}\right)^{3/2}\right], \qquad (3)$$

$Y_i = n_i m_u/\rho$ the abundance of each nuclear species and g_i the partition function.

3 Expansion model

Due to numerical instabilities in the code solving the full hydrodynamic evolution, the precise calculations are limited to a time of ~ 30 ms. Afterwards, the expansion is determined by assuming some parametrization of the density as a function of time, $\rho(t)$ [10].

It is expected that, at late times, the gravitational attraction becomes negligible and the ejected material reaches a constant velocity.

In the one hand, imposing mass conservation inside a spherical volume expanding at a constant velocity, often recalled as an *homologous expansion*, implies that the quantity ρr^3 must remain constant over time. This leads to the relation:

$$\rho(t) = \rho_0\left(\frac{t_0 + \Delta}{t + \Delta}\right)^3,$$

where ρ_0 and t_0 are the density and time coordinates corresponding to the last step of the full hydrodynamic simulation and $\Delta = r_0/v - t_0$.

On the other hand, flux conservation along an expanding spherical shell imposes that $\rho r^2 v$ must be a conserved quantity. Hence, the density evolves as:

$$\rho(t) = \rho_0\left(\frac{t_0 + \Delta}{t + \Delta}\right)^2.$$

[1] Comes from the chemical potential assuming Boltzmann statistics.

The mass conservation argument seems more reasonable at late times after the merger but, however, one cannot yet argue which prescription holds better for an early-time description of the dynamics ($t \lesssim 1$ s).

As seen in Section 2, the changes on the density evolution affect also the way temperature and entropy evolve. This fact leads to changes on the reaction rates, modifying the way the r-process follows, and leading to significant differences in the final mass abundance pattern.

4 Results

Figure 1 shows the thermodynamic evolution of both expansion scenarios. As discussed above, the different density evolution affects the way the r-process operates, leading to differences in the abundances of the nuclear species all along the calculation (see Figure 2).

The hydrodynamic code provided the thermodynamic evolution of the system up to 37 ms. The evolution afterwards is computed using the models introduced in Section 3. The increase of the temperature up to $\sim$ 1 GK at times $\sim$ 30 ms is due to the reheating by nuclear reactions.

As expected, the density remains higher in the $\rho \sim t^{-2}$ with $\Delta = r_0/v - t_0$ (blue line) case, making the temperature remain remarkably higher than in the $\rho \sim t^{-3}$ with $\Delta = r_0/v - t_0$ (red line) and lowering the entropy. Additionally, we observe that the neutron-to-seed ratio reaches a value of $\sim$ 1 at a later time in the cases where the density is kept higher. The instant when this happens is know as *freeze-out* and plays a crucial role in the determination of the final abundance pattern. After freeze-out, due to the low availability of free neutrons in the environment, neutron capture reactions slow down. From then on, generally, no heavier material is produced, beta decays start to dominate and the material decays to stability.

We have run an additional calculation in order to highlight the major role played by the evolution up to the freeze-out. For this, we have imposed the homologous expansion model adjusting the Δ value so that the densities of this new calculation and the blue curve match at freeze-out. Comparing the abundances of the nuclear species at $t = 1$ Gyr (see Figure 2), we observe that the results resemble much more the ones obtained with the $\rho \sim t^{-2}$ model, highlighting the dominating role of the early time evolution in the late time results.

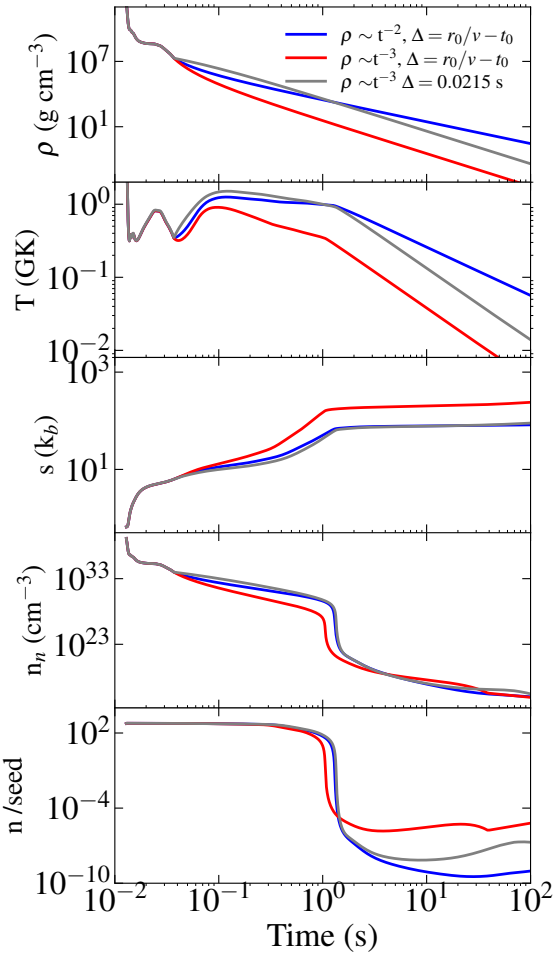

Fig. 1: *Evolution of the more relevant thermodynamics variables as a function of time for the late-time expansion models introduced in Section 3.*

4.1 Study of the $^{254}_{98}Cf$ region

As explained in Section 1, analysing the $^{254}_{98}$Cf yield is relevant for the understanding of the EM emission following the merger, and might help identify nuclear species produced by the r-process in NSM.

In our calculation, the maximum $^{254}_{98}$Cf abundance is observed at $t \sim 10^4 - 10^6$ s (see Figure 4). As seen in Figure 3, at $t = 1$ day important differences in the abundances of the heavy nuclei appear. The peak in the $A \in [220, 255]$ region is broader in the $\rho \sim t^{-3}$ case.

When plotting the abundance of the $A = 254$ isobars as a function of time, we have observed that there are also significant differences between both expansion scenarios. Whereas at

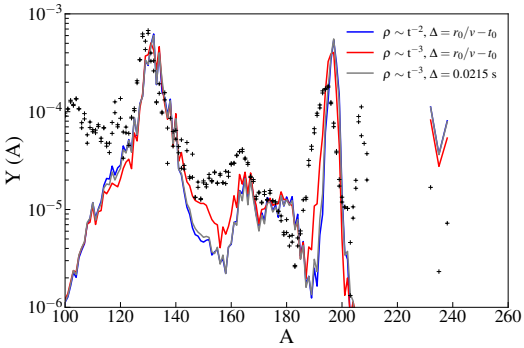

Fig. 2: *Final mass abundance pattern obtained for the r-process network calculations using the three density evolution prescriptions shown in Fig. 1. Observational data from the r-process solar abundance pattern is provided for reference [11, 12].*

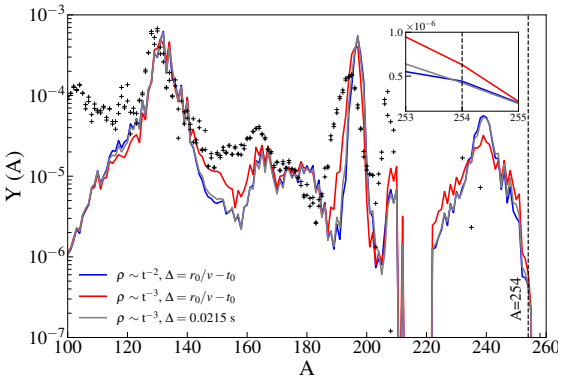

Fig. 3: *Mass abundance pattern at $t = 1$ day for the r-process network calculations using the three density evolution prescriptions shown in Fig. 1. The heavy element region peak is broader in the case corresponding to the red line, although the maximum is lower than in the other cases. The abundance of $^{254}_{98}Cf$ (note the dashed line and the zoomed plot) is higher for the red line prescription, and very similar for the gray and blue.*

early times the abundance of the $A = 254$ isobars is higher within the $\rho \sim t^{-2}$ prescriptions, the $\rho \sim t^{-3}$ expansion favours the production of nuclei with $A = 254$ and, in particular, of $^{254}_{98}$Cf at late times.

We have tried to identify the reaction mechanism responsible for the observed differences in the $A = 254$ abundances. This is not a simple task as one should analyze the competition between all the different reactions channels taken into account in the network calculation. In Ref. [9] neutron induced fission was identified as the main responsible mechanism for the destruction of the $A = 254$ isobars.

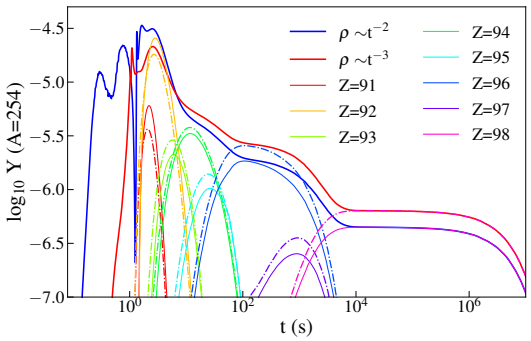

Fig. 4: *Abundances of the $A = 254$ isobars as a function of time. The blue an red lines represent the total abundance of the $A = 254$ isobars for the $\rho \sim t^{-2}$ and $\rho \sim t^{-3}$ expansion scenarios, respectively. The rest of the lines represent the abundances of each element with $A = 254$ as a function of time. The continuous line corresponds to the $\rho \sim t^{-2}$ model, whereas the dashed line shows the results obtained within the $\rho \sim t^{-3}$ prescription. The production of $^{254}_{98}Cf$ is favored by the $\rho \sim t^{-3}$ (homologous) expansion model.*

In order to be able to compare the rates of the different channels, one should calculate the reaction fluxes. We have computed the fluxes for neutron captures, beta decays and photodissociations after freeze out, at $t \gtrsim 2$ s.

Photodissociation rates decrease fast as the temperature drops. As the temperature in the $\rho \sim t^{-2}$ prescription is still ~ 1 GK at times around freeze out, we observed that contary to the $\rho \sim t^{-3}$ case, in the former case photodissociations dominate over neutron captures. This phenomenon diminishes the formation of the more neutron-rich nuclear species, and hence, the abundance of the heaviest elements is also most likely decreased.

5 Conclusions

Different expansion scenarios of the ejected material from NSM lead to significant differences in the r-process path and the final isotopic abundance pattern. We expect, out of the two models considered, that the homologous expansion ($\rho \sim t^{-3}$) makes a more realistic description of the physics of the system at late times, due to

mass conservation arguments. However, at early times there is in principle yet not enough knowledge to favor one or another model.

As the final abundance pattern and the whole r-process dynamics depend strongly in the thermodynamic evolution at early times (in particular, at times around freeze out, ~ 1 s), further improvement of the codes solving the full hydrodynamic equations is required in order to find a more complete solution of the thermodynamic evolution.

Moreover, we have observed significant supression of the ^{254}Cf production within the $\rho \sim t^{-2}$ scheme, presumably due to the role played by photodissociations, preventing the formation of more neutron-rich material and suppressing the formation of heavier nuclei. This fact remarks the major role played by the competition among the different reaction channels in tracing the r-process path. Nonetheless, we have not been able to fully understand the reaction dynamics in the region of interest, and further work should be made in order to identify the dominating reactions in the production of ^{254}Cf. In addition, the code neglects photon induced fission. Due to the importance of the role played by photodissociations when the temperature is kept high at early times, we believe this processes should be also included in the network calculation.

Finally, we would like to point out that r-process reaction network studies could be used in parallel with NSM hydrodynamic calculations. They could provide information on the reheating due to nuclear reactions, and be used to correct the thermodynamic evolution of the purely hydrodynamic calculations where nuclear processes are neglected.

6 Acknowledgements

We would like to thank the people that made possible for us to participate in the GSI Summer School Programme, providing us with valuable experience for our forthcoming professional career. In particular, thank you to the organisers and to our tutor, Gabriel Martínez Pinedo, and Zewei Xiong for their excellent guidance and very helpful advice. We would also like to express our gratitude to the GSI Theory group for giving us the opportunity to take part in the many interesting group discussions and welcoming us in their everyday working life.

References

[1] J. J. Cowan et al. in *Rev. Mod. Phys.* **93**, 015002 (2021).
[2] B. P. Abbott et al. (LIGO Scientific Collaboration and Virgo Collaboration) in *Phys. Rev. Lett.* **119** (2017).
[3] B. P. Abbott et al. 2017 in *ApJL* **848** L12 (2017).
[4] B. Singh in *Nucl. Data Sheets* **156**, 1 (2019).
[5] Huo Junde et al. in *Nucl. Data Sheets* **112**, 1513 (2011).
[6] Meng-Ru Wu et al. *Phys. Rev. Lett.* **122**, 062701 (2019).
[7] Y. Zhu et al. in *ApJL* **863** L23 (2018).
[8] M. Arnould, S. Goriely and K. Takahashi in *Phys. Rept*, **450:** 97-213 (2007).
[9] S. A. Giuliani et al. in *Phys. Rev.* C **102**, 045804 (2020).
[10] J. J. Mendoza-Temis et al. in *Phys. Rev.* C **92**, 055805 (2015).
[11] J. J. Cowan et al. in *Phys. Rep.* **208**, 267-394 (1991).
[12] S. Goriely (1999) in *Astron. & Astrophys.* **342**, 881–891 (1999).

SIS100 Laser beam path simulation

Simona Di Costanzo
University of Naples Federico II, dicostanzo.simona@hotmail.com

Laser cooling is an innovative technique to obtain high-quality ion beams. That is especially true for relativistic ion beams, which will be accelerated in the SIS100. Established ion beam cooling methods(electron cooling and stochastic cooling) are less effective and difficult to implement. For my project, I have simulated the laser beam path going in the SIS100 for laser cooling experiments.

1 Introduction

1.1 Laser Cooling

Many atomic and nuclear physics experiments benefit from having high-quality ion beams (e.g. with a low momentum spread $\Delta p/p$) which is achieved using ion beam cooling techniques. For low-energy storage rings ($\gamma \sim 1$), electron cooling is suitable and commonly used. However, when the ion energy becomes higher, the electron cooler is not the best choice in terms of cooling times (see e.g. [1]) and costs. In particular, the cooling time increases as $\tau_e \propto \gamma^{2/3}$ [2]. Especially for cooling high-energy few-electron ions, laser cooling represents a smart and convenient alternative to electron cooling. Its principle is the fast photon absorption by ions and successive fast emission of fluorescence [3]. Naturally, the ions only absorb the incoming photons with a frequency equal to f_0, the cooling transition frequency in the ion rest frame. Since the photons and the ions have to move towards each other, for laser cooling to work, the frequency of the laser photons f in the rest frame has to be Doppler shifted:

$$f = f_0\gamma(1-\beta) \tag{1}$$

The Lorentz factor γ can be expressed in terms of the magnetic rigidity of the accelerator(Bρ) and the properties of the ion:

$$\gamma = \sqrt{\left(\frac{B\rho Q}{Mc}\right)^2 + 1} \tag{2}$$

where Q is the charge of the ions multiplied by the elementary charge e and M is the atomic weight multiplied by u, the atomic mass unit. The magnetic rigidity determines the maximum velocity, and therefore the maximum kinetic energy at which the ions can be stored in the ring. Once the ion has absorbed the photon, it emits fluorescence. However, since this happens randomly in all directions, the recoil momenta average out to zero.

The net effect is a decelerating force on the ion. Besides the laser force, a counter-balancing force is required to achieve laser cooling. This force is provided by a moderate bunching of the stored ion beam and is created by exciter electrodes, which are simple parallel plates carrying an RF-current [4]. The bunching frequency is determined by the ion revolution frequency f_{rev} and by the number of bunches h, so $f_{bunching} = hf_{rev}$.

There is a potential bucket where bunched ions oscillate (Fig. 8); the ones with the highest oscillation amplitude should be in resonance with the laser. Afterwards, the laser frequency has to be adjusted to be in resonance with ions with the second highest oscillation amplitude. The laser light must always be red-detuned, else heating (instead of cooling) occurs. The minimum red-detuning is about half the laser linewidth.

In contrast to the electron cooling force, the laser cooling force does not become weaker as the ions' energy increases; it rather becomes stronger. Indeed, the laser cooling force scales with γ^3, meaning really short cooling times (of the order of seconds) even for high energy particles [5]. Apart from the higher "efficiency" at higher energy, just the possibility of working at high energies is an advantage itself. At FAIR SIS100, many different species of ions can be laser-cooled [6].

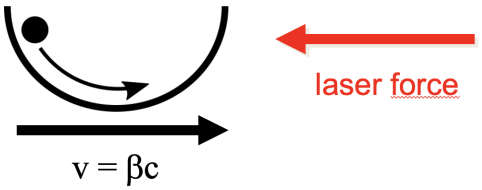

Fig. 1: *The bunched ions oscillate in the RF bucket with different amplitudes. The ions with the highest amplitude are in resonance with the laser. (With the kind permission of Sebastian Klammes.)*

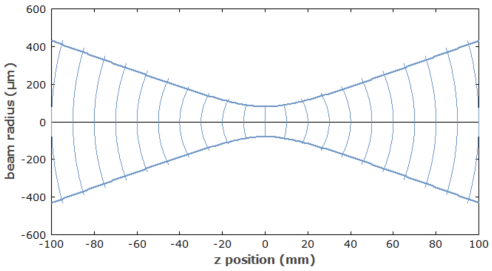

Fig. 2: *Gaussian beam radius versus the distance of propagation. The waist (at z=0) is about 0.2 mm. [7].*

Laser cooling experiments took place at the ESR in the past years, first using narrow-band cw laser systems and recently using a broad-band pulsed laser. New laser cooling experiments are planned for the SIS100, which is the heavy-ion synchrotron being built as the heart of the FAIR facility. As written in the name, the SIS100 has a magnetic rigidity Bρ = 100 Tm, in contrast to the ESR, which has Bρ = 10 Tm.

2 Laser beam Properties

For laser cooling at the SIS100, the laser beam must be overlapped(anti-collinearly) with the ion beam. Therefore, the laser beam must travel a large distance($\sim 50m$) from the laser lab to the accelerator.
To understand completely the SIS100 laser beam path simulations, a good knowledge of the properties of a Gaussian beam was needed. For a deeper understanding of the topic, I have also done M^2 test measurements in the laser laboratory.

2.1 Gaussian laser beams

A Gaussian beam is a light beam where the transverse(to the beam axis) electric field profile can be described with a Gaussian function [7]. The radius of a Gaussian beam is the distance from the beam axis where the intensity drops to $1/e^2$ of the maximum value.
Due to the phenomenon of diffraction, the beam radius is not constant as the light propagates through the space(Fig. 2). On the contrary, it varies along the propagation direction z and it can be described mathematically as :

$$w(z) = w_0\sqrt{1+\left(\frac{z}{z_R}\right)^2} \qquad (3)$$

where w_0 is called *beam waist* or *focus* and it is the beam radius in z = 0, where it reaches a minimum; z_R is the Rayleigh length and determines the length over which the beam can propagate without diverging significantly.
The Rayleigh length is expressed in terms of w_0, the wavelength and the M^2 factor as

$$z_R = \frac{\pi w_0^2}{\lambda M^2} \qquad (4)$$

where the M^2 factor is a common measure of the beam quality of a laser beam [8].
Indeed, the closer a beam's M^2 factor is to 1, the tighter is the focus, meaning more energy in a single spot.

2.2 M2 measurement of a laser beam

Having understood the importance of the M^2 factor of a beam, I have set up an experiment to measure it (Fig. 3).

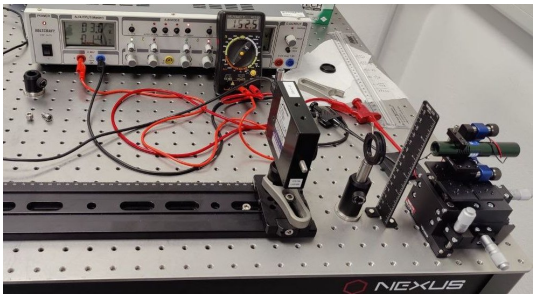

Fig. 3: *Experimental setup for the M^2 test measurements. It consists of a green laser diode ($\lambda = 532nm$), a camera with a CCD detector inside, an optical rail to move the camera on, a power supply and two irises to align the laser beam path.*

Using the BeamMic app, connected to the camera, the laser beam profile was acquired for different laser-camera distances z, going from 15

cm to 60 cm. For each profile, the program computes the D4σ, which represents the diameter of the laser beam, and its relative error.
Afterwards, the diameter of the beam was plotted as a function of z. From this graph, the position of the focus z_0 and the waist of the beam could be found. Figure 4 shows beam diameter versus the relative distance z-z0. The red line is a fit of Eq. (3) to the data.

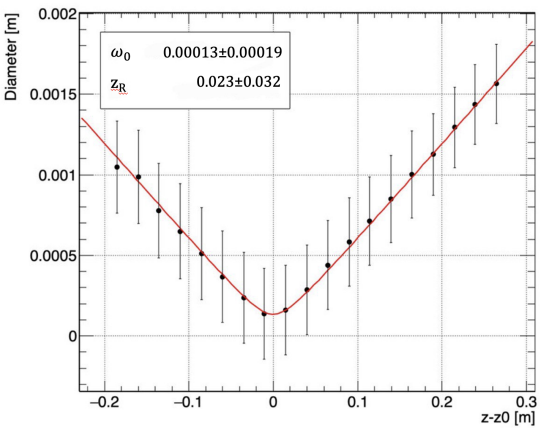

Fig. 4: *Beam diameter vs $z - z_0$ fitted with Eq. 3. The waist function fits optimally to the experimental data into the error bars.*

Since the diameter is twice the radius, the ω_0 obtained by the fit has to be divided by two before calculating the M^2 factor.
Using Eq. 4, the M^2 results equal to 1.08, meaning that the laser beam emitted in a pure Gaussian mode.

3 Simulations of SIS100 laser beam path

The main focus of this study is the simulation of the SIS100 laser beam path, for which the use of the program GaussianRay CAD, developed by the TU Darmstadt, was chosen.

3.1 The program

GaussianRay CAD is a Gaussian beam simulator, where the user interface allows to change the features of the beam (wavelength, waist radius and position, Rayleigh distance) and to insert propagation spaces and lenses made of different materials. Concerning the lenses, it is also possible to customize them by changing the wavelength and focal length. Furthermore, there is the possibility to design a new optical element(like mirrors and ducts) by changing the ABCD matrix elements.
The program can be used only for single mode (Gaussian) beam simulations (with an $M^2 factor$ close to 1), which is why the $M^2 factor$ is fixed and cannot be changed in the program.

3.2 Mirror box configuration

The whole laser beam path (Fig. 5) had to be simulated in GaussianRay CAD, starting from the lenses on the optic table in the laser lab and ending in the SIS100 accelerator, where there is an overlap of the ion beam with the laser beam.

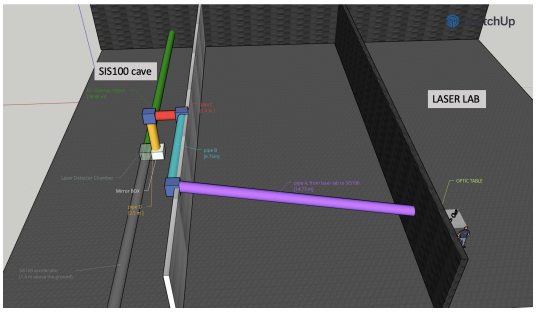

Fig. 5: *SIS 100 laser beam path, made up of pipe A (purple) going from the laser laboratory to the accelerator cave, pipe B (light blue) and pipe C (red) along the ceiling, pipe D (yellow) from the ceiling to the mirror box. Via the detector box, the laser beam enters the accelerator pipe e-f (green), which is the overlap region. The grey pipe in the picture represents the SIS100, which is 1.4m above the ground.*

The mirror box shown in Fig. 5 is a 50 cm diameter stainless steel box in which a vacuum will be created and in which the lenses will be positioned.

The UV light that will enter the SIS100 is obtained starting from an infrared laser (1029 μm) using a set of lenses and crystals to change the frequency of the laser light. The two crystals are the LBO (*Lythium triborate*) and the BBO (*Barium borate*); after each crystal the frequency is doubled, obtaining a final wavelength $\lambda = 257nm$. This configuration of lenses was then implemented in GaussianRay CAD in collaboration with the laser team at TU Darmstadt.

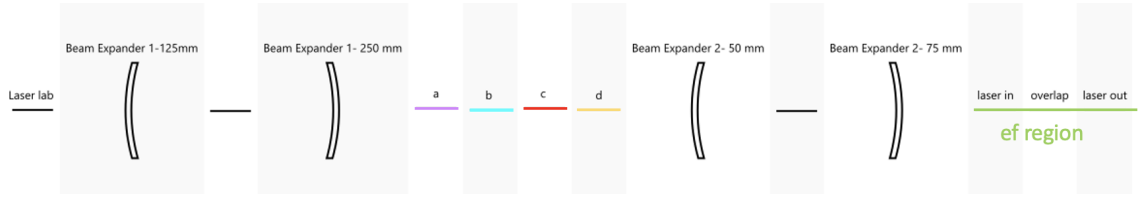

Fig. 6: *The first beam expander is placed in the laser laboratory and it was made of two lenses, a plano-convex of focal length $f_1 = 125mm$ and a plano-concave of focal length $f_2 = -250mm$, which are 375mm apart. The second lens system is placed in the mirror box, the plano-convex lens has $f_3 = 50mm$ and the plano-concave lens $f_4 = -75mm$, separated from each other by 125 mm.*

After that, two beam expanders were placed to obtain at most a laser beam radius equal to 1 cm (Fig. 6). The focal lengths of the lenses were chosen from the available lenses on the market (Thorlabs, Newport, CVI laser optics).
By varying the distance between the lenses the focus can be moved over the entire overlap region, i.e. a 20 m long region inside the e-f pipe. (Fig. 7)

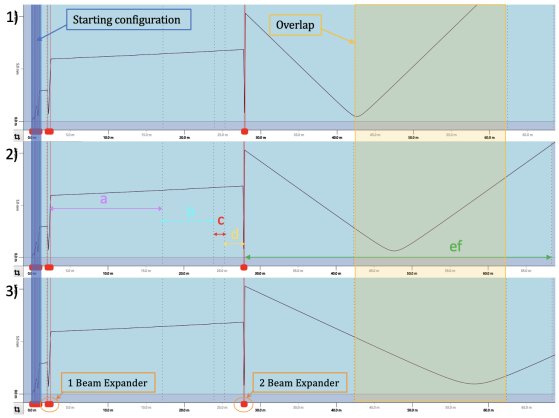

Fig. 7: *The focus position by changing the distance. 1) Focus 14.7 m from the ef-region, distance between lenses:125.4mm, waist radius: 464.93μm; 2)Focus 19.7 m from the ef-region, distance between lenses:125.3mm, waist radius: 627.42μm; 3)Focus 31.2 m from the ef-region, distance between lenses:125.2mm, waist radius: 963.73μm.*

4 Conclusion

This work showed that the laser beam path presented here could be suitable for the SIS100 laser cooling experiments. However, the restricted space available in the mirror box limits the possible positions of the focus in the overlap region. Better results (more tunability) could be obtained by a different position of the lenses inside the mirror box, i.e. when they are further apart. This would allow to use higher focal length lenses resulting in a better control of the position of the focus within the overlap region.

Acknowledgments

I gratefully acknowledge the supervision and the topic of the project by my tutor, Danyal Winters, and the precious help and support of Sebastian Klammes.
Secondly, I would like to thank Markus Becker for his kindness and for making my days in the office seem shorter and lighter. I extend my thanks also to Davide for being always supportive and for believing in me.
Finally, I would like to express my gratitude to the organizers of the summer student program for the opportunity they gave me.

References

[1] Poth H 1990 Phys. Rep. **196** 135.
[2] A.H. Sørensen et al., Nucl. Instr. Meth. Phys. Res. 215, 27 (1983).
[3] D. Winters *et al.*,*Conf Proc IPAC*, **THPMY040**, (2016).
[4] D. Winters *et al.*,*Phys. Scr.*, **T166**, 014048 (2015).
[5] U. Schramm et al., Nucl. Instr. Meth. Phys. Res. A 532, 348 (2004).
[6] U. Schramm, D. Habs, Progr. Part. Nucl. Phys. 53(2), 583 (2004).
[7] Dr. Rüdiger Paschotta, *https : //www.rp − photonics.com/gaussian$_b$eams.html*, accessed on [8/09/2022].
[8] Dr. Rüdiger Paschotta, *https : //www.rp − photonics.com/m2$_f$actor.html*, accessed on [8/09/2022].

Polarity Switching Circuit for Directing the HITRAP Offline Ion Beam

Adam Dockery
Michigan State University, dockery.adam27@gmail.com

Highly charged ions (HCI) are generated by an electron beam ion trap (EBIT) for the commissioning of the HITRAP cooler Penning trap and the associated experimental setups. After production, ions are directed by an electrostatic quadrupole beam deflector (EQBD) to either the cooler trap or the experimental beamlines. The polarity of the EQBD determines the direction of the ion beams, and until now, it has been manually adjusted in order to change the beam direction. An upgrade to the EQBD system is presented, which allows polarity to be changed by a trigger signal. This has enabled users to remotely control the beam direction and reduced the switching time from tens of seconds to under five milliseconds. Beamline components after the EBIT are then retuned to provide current in both directions symmetrically. The design and implementation of the polarity flipping circuit, as well as the results of the switching and retuning, are presented.

1 Introduction

1.1 The HITRAP Decelerator Facility

Heavy, slow HCI such as U^{91+} or U^{92+} are preferred candidates to test the strong-field limit of quantum electrodynamics (QED) theory [1]. For the HITRAP associated experiments (ARTEMIS, SPECTRAP, etc.) to reach necessary statistical precision, the HCI must be delivered at extremely low energies near four Kelvin.

At GSI, HCI are produced by first accelerating heavy ion beams to 11 MeV/u in the UNILAC. Beams are then further accelerated to 400 MeV/u, and reach an intermediate charge state, in the SIS heavy ion synchrotron. The final highly charged states are produced by passing the 400 MeV/u ion beams through a stripper foil. HCI beams can be collimated after the stripper and cooled in the ESR to 4 MeV/u.

The HITRAP linear decelerator is designed to further cool HCI from the ESR to 4K and deliver these ions to attached experimental beamlines. From the ESR, one microsecond HCI bunches are delivered to HITRAP and restructured by a double drift buncher. Deceleration and cooling of the ion bunches then occurs in three stages at the beamline. First, HCI pass through the interdigital H-type structure (IH) and are decelerated to 500 keV/u. A radio frequency quadrupole decelerator (RFQ) further slows the HCI to 6 keV/u, and the ion bunches are finally cooled to four Kelvin by the HITRAP cooler Penning trap. From here, ions can be extracted to the attached experiments.

1.2 The EBIT Offline Ion Source

For commissioning and offline operation of the cooler trap and attached experiments, the beamline is equipped with a dedicated ion source—a Dresden EBIT [2]. The EBIT breeds HCI by stripping successive electrons from trapped particles with an intense electron beam. Charge states up to K^{19+} have been created using this EBIT at HITRAP.

HCI are released from the EBIT in short bunches and an energy on the order of the RFQ output. Therefore, the EBIT is a suitable tool for testing the cooler trap and experimental setups at near on-line conditions.

1.3 The EQBD for Beam Direction

Ion bunches from the EBIT are directed by an EQBD to either the cooler trap or the associated experiments. The internal construction of the

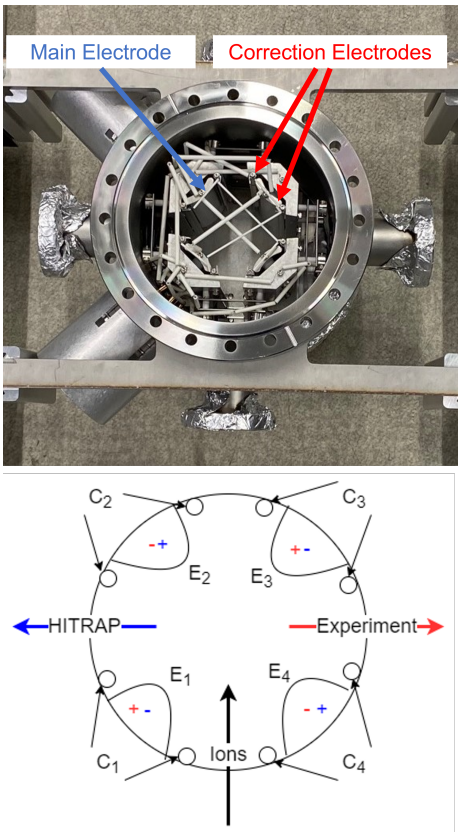

Fig. 1: *The EQBD consists of four main electrodes and eight correction electrodes (two correction next to each main electrode), with a potential of approximately four kilovolts on each. The potential of the diagonal electrodes is fixed to be the same: E_1&E_3, E_2&E_4, C_1&C_3, and C_2&C_4. Correction electrode and main electrode potentials can be varied independently. Consecutive electrodes have the same magnitude of potential and opposite polarity, so $|E_1\&E_3| = |E_2\&E_4|$.*

EQBD is described in Figure 1. The potential on the EQBD is maintained by four separate wires (two positive, two negative) from two high voltage power supplies.

In the configuration where E_1&E_3 is negative, the HCI beam is directed towards the cooler trap. The opposite configuration directs the beam towards the experiments. Before the presented upgrades were installed, the only way to switch between configurations was manually: to decrease the high voltage to zero, switch the positive and negative wires, and ramp the voltage back up.

2 Experimental Setup

2.1 Circuit Design

To decrease the time needed to change beam direction and enable remote switching, a polarity flipping circuit is designed and implemented for the EQBD. The circuit is primarily based around two double pole double throw (DPDT) high voltage relays. One relay is used to switch the main electrode polarities while the other switches the correction electrode polarities. See Figure 2 for a diagram of the circuit.

Each relay is activated by a bias of 12 volts with a current of 0.5 amps. Therefore, the relays are attached in parallel to a 12-volt DC power supply capable of delivering four amps of current. The ground terminal of the relay is attached to a low voltage DPDT relay in the normally open (NO) position. A five-volt DC trigger signal can be sent to activate the low voltage relay and close the NO connection, which grounds the 12-volt circuit to switch the high voltage relays.

In addition, an LED signal circuit was connected to the second switch of the low voltage relay. One LED (left on the circuit box front plate) was attached to the normally closed (NC) position to indicate that the beam is sent to HITRAP, and a second LED (right on the front plate) was connected to the NO position to signal that beam is delivered to the experiments. When the NO LED is activated, the high voltage relays are also activated. The LED circuit is powered by a five-volt DC power supply capable of delivering 1.5 amps of current, and a small resistor is placed in front of the LEDs to act as a voltage divider. This ensures that the specified 2.3 volts are applied to the LEDs. High voltage resistors are attached in series after the high voltage relays in the circuit to limit the current. This prevents HV sparks at the cost of slightly slower switching time.

2.2 Circuit Implementation

The final circuit was built inside a 19-inch rack-compatible high voltage safety box, see Figure 3, which is installed underneath the transport beamline from the EQBD to the HITRAP associated experiments. A Sun Power SPS-035-D1 DC power supply is installed internally to power the 12-volt and 5-volt circuits. This unit was chosen since it can supply two circuits simulta-

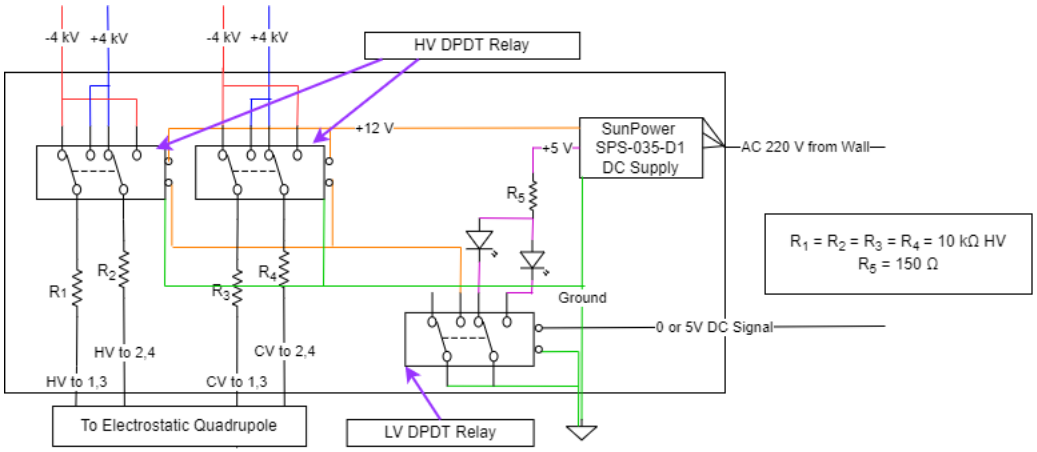

Fig. 2: *The diagram for the EQBD polarity switching circuit. Wires are color coded to the potential that is carried. Blue lines are high voltage wires of positive polarity, while red lines carry a negative polarity high voltage. The orange lines constitute the 12-volt DC circuit, and the pink lines are the 5-volt DC circuit. The green lines are all grounded potentials. Note, the high voltage lines for the main electrodes are labeled 'HV to . . . ' while the correction electrodes are labeled 'CV to . . . '.*

neously at different voltages.

Two G15WPD DPDT high voltage relays are suspended in the box and perform the switching described previously. These feature a 15-kilovolt maximum potential on each relay connection and millisecond range switching time to reduce capacitive discharge.

SHV cables input the high voltage and dedicated high voltage wires and plugs matching the bender feedthrough system are used for the output. Before the present upgrade, the cable adaptation was known to cause sparks. A TTL input is used for the 5-volt switching signal, and the port can be easily attached to the HITRAP control computers in the future.

2.3 Testing Setup

After the construction of the safety box, a series of tests were performed to ensure the proper functioning of the polarity switching circuit. The box was moved to a temporary location and attached to the EQBD. Switching tests were performed from zero up to 4.5 kilovolts potential on each EQBD electrode. The potential of the E_1&E_3 output line was monitored on an oscilloscope with a Testec TT-HVP 2739 high voltage probe.

An Ar^{16+} primary beam was produced by the HITRAP EBIT to perform final tests of the switching circuit. Two Faraday cups were placed in the transport beamline after the EQBD: one along the path towards HITRAP and the other towards the experimental beamlines. A Femto DHPCA-100 amplifier was used to convert the current to a voltage signal (at a ratio of one microamp to one volt), and this voltage signal was recorded with an oscilloscope.

Alternatively, a microchannel plate (MCP) detector was used at the Faraday cup position on the beamline towards the experiments. An MCP was not available for the Faraday cup position towards HITRAP. After testing, the same setup was used to retune the beamline between the EBIT and EQBD.

3 Results / Discussion

3.1 Switching Times

Switching time for the circuit is dependent on the potential applied to the EQBD electrodes. At one kilovolt of potential, switching takes about two milliseconds, while at higher potentials it slows to three or four milliseconds

Voltage jumps are observed during switching (see Figure 4), which is likely caused by the power supply overcoming stored charge in the EQBD. The aberrations in voltage are stronger when polarity is changed from positive to negative than negative to positive. Since the negative power supply provides less current, this difference in behavior is consistent with expectations. This behavior, however, occurs within one millisecond and is not a concern for the purpose of the circuit.

Fig. 3: *Top view of the polarity switching circuit. The upper panel consists of the high voltage elements: red wires are the SHV inputs, white wires are the relay outputs, white rectangular prisms are the resistors, and the relays are attached to the median. The lower panel consists of the two low voltage circuits discussed in the previous section and corresponding power supply. Green wires are the grounds for the HV relays and low voltage circuits.*

In order to provide an ion beam to both HITRAP and the experimental beamlines, switching the EQBD polarity needs to be short and remotely capable. The circuit accomplishes this goal as the full switching process occurs in under five milliseconds.

3.2 Beam Tuning

The Ar^{16+} beam had been previously tuned for delivery to HITRAP. When switching was performed with this beam, a signal of 4.0 volts was observed on the Faraday cup towards HITRAP, and no signal was seen towards the experiments.

The beamline components between the EBIT and Faraday cups were tuned to find a symmetric setting that maximizes an equal magnitude current in both directions. A setting was found that yielded 3.0 volts towards HITRAP and 2.2 volts towards the experiments (Figure 5a). This setting was imaged with the available MCP (towards experiments) and a broad, asymmetric beam was observed.

Further tuning was performed with the MCP image to focus and center the beam. The effort yielded a narrow beam width that was much more symmetric than the previous setting (Figure 5b). However, the ion beam was located off the axis of the Faraday cup. Therefore, no signal was observed towards the experiments, and only a small signal was seen towards HITRAP. Efforts to recenter the beam were hindered by no usable MCP in the HITRAP direction.

4 Conclusion

An upgrade to EQBD after the HITRAP EBIT was designed and implemented to remotely switch ion beams from the HITRAP direction to the experimental beamline direction remotely on user request and in a short time frame. The time needed for the directional change has been decreased from tens of seconds to less than five milliseconds. In addition, the EBIT output beam has been tuned to provide current in both directions under the same settings. A parameter set for high current magnitude was found, but the current is asymmetric between the two directions. The measurement with the MCP revealed a broad width and asymmetric shape. Additional attempts to optimize the beam profile resulted in a more focused image, but this beam is off the central axis and does not register strongly on the Faraday cups. Further work

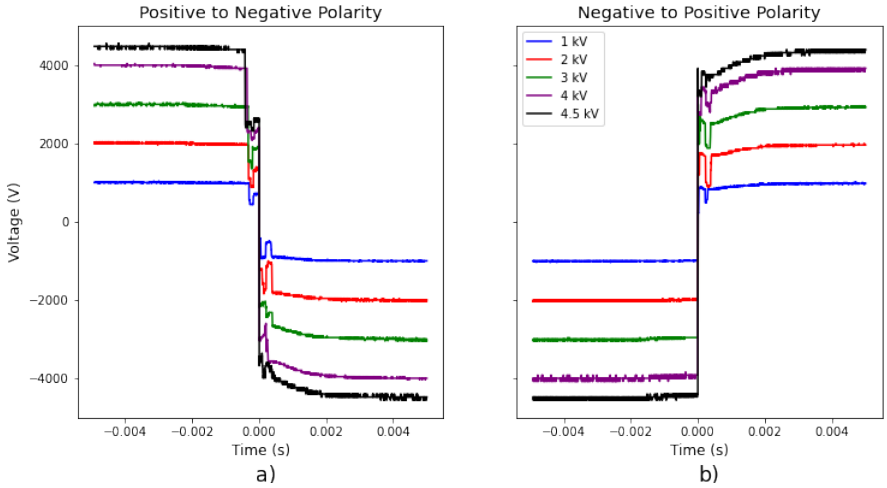

Fig. 4: *The voltage of the E_1&E_3 output line is plotted against time during the switching process. A change from positive to negative polarity is shown in a) and negative to positive polarity in b).*

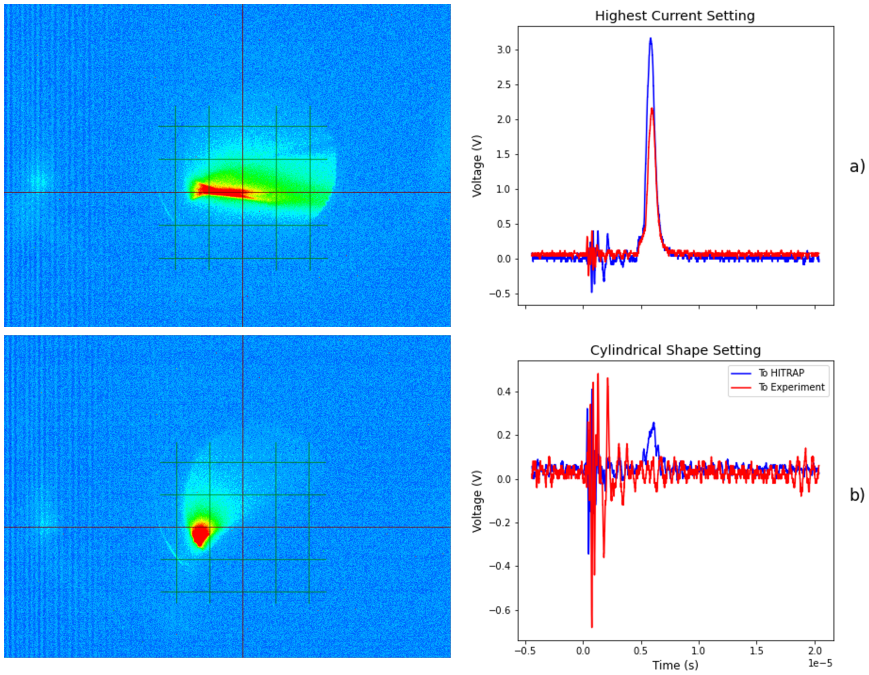

Fig. 5: *Measurements of the ion beam in the tuned configuration for a) highest current settings and b) symmetric shape settings. The left plot shows the image on the MCP towards the experimental beamline, where intensity (current) is color-coded. Red is the highest current and blue is the smallest current in the image. The right plot shows the voltage reading versus time for the Faraday cup towards HITRAP (blue) and towards the experiments (red).*

is necessary to find a setting that achieves high current and a symmetric, narrow beam profile.

Acknowledgments

This work was carried out with the supervision of Nils Stallkamp, and I thank him for his guidance. I would also like to thank Zoran Andelkovic for his advice in adjusting the circuit and beam tuning. Nikita Kotovskiy and Davide Racano built the high voltage box.

References

[1] F. Herfurth et al., *Proceedings of HIAT 2012* 217-221 (2012).
[2] G. Vorobjev et al., *Rev. Sci. Instrum.* **83** 053302 (2012).

Hypertriton Reconstruction in the CBM experiment using PHQMD transport model

Dutta, Kaustav
Johannes Gutenberg University Mainz, kadutta@students.uni-mainz.de

In this report, we present new results from the simulation of fragments and exotic hypernuclei in the CBM experiment using the Parton-Hadron-Quantum-Molecular-Dynamics (PHQMD) transport model. The report especially focuses on Hypertriton (H^3_Λ) decay into ${}^3He^+$ and π^- at an collision energy of $\sqrt{s}$=3 GeV. The reconstruction of multi-strange short-lived particles and hypernuclei have been done using the Kalman Filter Particle Finder (KFPF) which is an excellent tool to reconstruct complex decays within extremely high track densities.

1 Introduction

Hyperons are baryons containing one or multiple strange quarks. A bound state of hyperons, protons and neutrons is called a Hypernuclei. This report focuses on the decays of fragments, single and multi-strange baryons and a hypernuclei, Hypertriton ($^3_\Lambda$H), which was observed by the STAR experiment in Au-Au collisions at $\sqrt{s}$=200 GeV [1]. Experiments reconstruct the invariant mass of the decay products of $^3_\Lambda$H, which are ^{3}He + π^- (2-body decay) or d+p+π (3-body decay) with branching ratios of about 0.25 and 0.40 respectively [3]. This should be equal to the invariant mass of $^3_\Lambda$H, as it is Lorentz-invariant. In the search for $^3_\Lambda$H, the CBM experiment will ensure consistency of earlier findings by experiments like ALICE at TeV ranges and STAR at a few GeVs.

2 CBM Detector Geometry

CBM is a heavy-ion fixed target experiment, which beam energies between 2-11 A GeVs. The Au-Au collision frequencies are extraordinarily high (up to 10MHz), which facilitates the detection of rare decays of hypernuclei. The polar acceptance angle lies between 2.5 and 25 degrees, which is sufficient to cover forward and mid rapidity ranges.

A few cm behind the target lies the Micro-Vertex Detector (MVD), which are Monolithic Active Pixel Sensors (MAPS) specialized in identifying the decay vertices of short-lived particles such as the hyperons. Behind the MVD are positioned the 8 stations of the Silicon Tracking System (STS) within a large superconducting dipole magnet, which measure the momentum of charged particles. After the STS is located the Ring Imaging Cherenkov Detector (RICH), which identifies the lightest particles such as e^-/e^+. In order to compute the energy loss dE/dx of particles, a Transition Radiation Detector (TRD) will be set up. The Time-Of-Flight (TOF) detector measures the time it takes for the charged particles to move a certain distance, which gives an estimate of their masses.

3 Simulation and Reconstruction

3.1 Simulation

The simulation of events in the CBM experiment involves the transport of particles through the detector components, generating the MC points and MC tracks.

3.1.1 PHQMD Transport model

The main focus of this week was to improve upon the transport model of the simulation, more specifically to include the PHQMD approach. This would replace the earlier used UrQMD model, which did not produce fragments like ${}^2H^+$, ${}^3He^+$ and ${}^4He^+$, which is essen-

tial in getting a correct estimate for our background.

The PHQMD model largely focuses on cluster formation, and in turn hypernuclei production, after the beam-target collision (Fig 1). Light clusters with binding energies around 10 MeV cannot survive a temperature of more than T=100 MeV [2], as would be the conditions after the fireball. Hence, it is quite challenging to understand how such weakly bounded systems could exist so early after the collision. If the density of nucleons remains fairly constant in the system, these observed clusters should not be formed very early on as collisions would be frequent and the mean free path of collisions would be very small. Clusters could not possibly have formed much later as the distance between nucleons would have been larger than the strong force range.

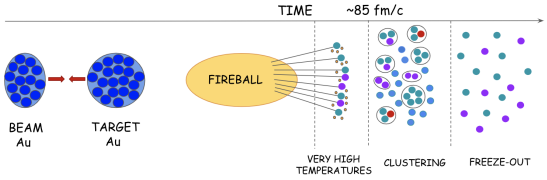

Fig. 1: *Cluster formation in Au-Au central collisions (Lab frame)*

3.1.2 Digitization

The next step consists of the subsequent digitization of these points to simulate actual detector response. The input to the digitization is the output file of the transport simulation. The energy and coordinate information is used by the digitizers to calculate the response of the detector and the behavior of the read-out electronics.

3.2 Reconstruction

3.2.1 Cellular Automaton Track Finder

The search for tracks begin with the Cellular Automaton (CA) track finder which takes as input the digitized hits, which includes their coordinates and time stamps. Hits on adjacent stations are combined into triplets which then form a track. Those triplets which have 2 common hits form part of the same track. A missing hit on one of the stations is tolerated due to the detector inefficiency. These track candidates have to go through a further filtering process which accepts or rejects them based on track length and measures χ^2 value [4].

To speed up this process, the high momentum and primary track are reconstructed at first. The hits belonging to these tracks are then removed from the input and the search for secondary and lower momentum tracks continue. The combinations of hits belonging to these tracks are greatly reduced because of the filtering done after the first step. Whatever hits remain are used to reconstruct remaining tracks. To make sure that the a track belongs to a single particle, the hits should coincide in spatial and time coordinates. Because the estimated time of flight of particles between any of the 2 stations is negligible to the detector time precision, they should coincide within 3σ of the detector time resolution.

3.2.2 Kalman Filter Particle Finder (KFPF)

The Kalman Filter Particle Finder (KFPF) is an excellent and widely accepted algorithm for finding, reconstructing and selecting short-lived particles with an extremely high event rate (order of MHz). As many as 200 decay channels have been implemented.

The particle tracks detected in one of the decay channels are reconstructed back to see if they converge to a single point (vertex), within a certain margin of errors. If a track does not converge, the particle is ruled out for that decay channel. Now, it is checked whether the vertex is the primary vertex. If not, then the tracks are secondary (or tertiary) which are produced in the decay of short-lived particles which have a sufficient life-time to move away from the primary vertex. These particles are usually single or multi-strange hyperons.

4 Results and discussion

4.1 Fragments

We present the first results here for fragments ($^2H^+$, $^3He^+$, $^4He^+$) in the PHQMD model, doing a mass reconstruction based on their time-of-flight through the detector.

In Fig. 2, we observe that all of the bands broaden as we move towards higher momenta p. This is because

$$m^2 = p^2\beta^2\gamma^2 = p^2\beta^2\frac{1}{1-\beta^2} = \frac{l}{c(t_{actual} \pm \Delta t)}$$

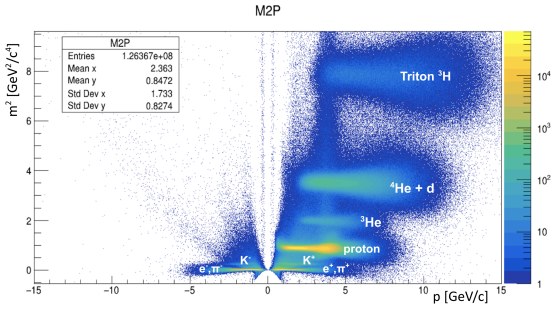

Fig. 2: *m^2 vs p for reconstructed particles and fragments*

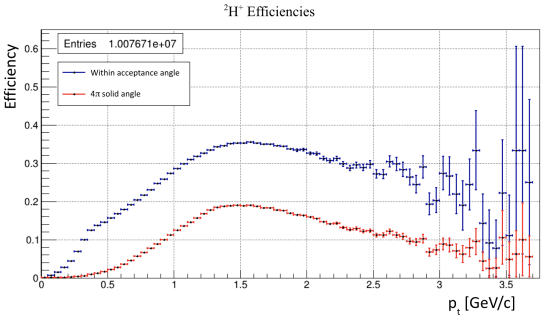

Fig. 4: *Comparison of detection efficiencies for $^2H^+$ within the acceptance region and over 4π solid angle.*

Here, l is the length of the trajectory of the particle inside the detector and t_{actual} is the actual time taken by the particle to travel through the detector. Because of finite time resolution of about 60 ps (due to electronic noise or Gaussian blurring of hits during digitization), the time calculated by the ToF detector might be greater than or less than the actual time. As we move towards higher p, t_{actual} becomes less due to which even a small Δt can result in a significant fluctuation in Δm^2. Because $\Delta m^2 \propto m$, the broadening gradually increases as we move towards higher masses, like in the case of ^{4}He and ^{3}H.

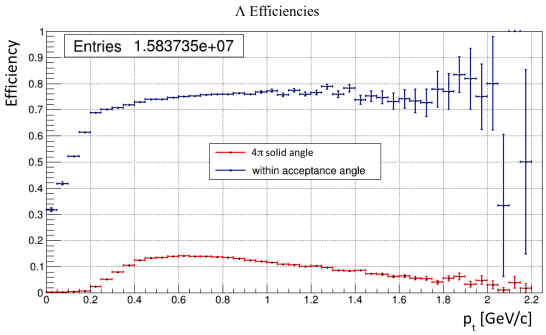

Fig. 5: *Comparison of detection efficiencies for Λ^0 within the acceptance region and over 4π solid angle.*

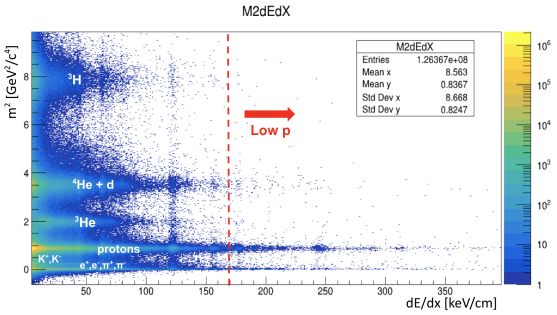

Fig. 3: *m^2 vs dE/dx for reconstructed particles and fragments. Red dotted line only demonstrates that particle with low momenta give high dE/dx.*

The m^2 vs dE/dx spectrum on Fig. 3 shows us the ionizing power of different charged particles. Minimum ionizing particles like e^- and π^- travelling at low momenta show a long narrow peak extending to 350 keV/cm. Thermal protons are also low ionizing and have an equally narrow and high peak. By comparison, ^{3}He, ^{4}He, d and ^{3}H travel at relativistic velocities and have smaller peaks.

Fig. 4 and Fig. 5 show the detection efficiencies of Λ-baryon and $^2H^+$ dN/dy within the acceptance zone and over a solid angle of 4π. This would help us to indirectly understand the detection efficiency of H^3_Λ, which is a bound state of both the systems. The efficiencies are less at low p_t and high p_t because of low statistics. This could be due to non reconstructed events along the beamline (low p_t) and boundary (high p_t) of the detector.

4.2 Hypertriton

We present the results from the H^3_Λ decay into $^3He^+$ and π^- produced by the PHQMD model here. It is important to note that in the following plots, H^3_Λ was forced to decay into $^3He^+$ and π^- with a branching ratio of 100%. Fig. 6 shows the invariant mass spectrum of H^3_Λ, calculated by reconstructing the topology and momentum of its daughter particles.

The fit works quite well as the number of correctly identified signal events (comparing to MC true events) was 1439, which is close to the value predicted by the plot (∼1313). The lower value might be because we only consider signal events

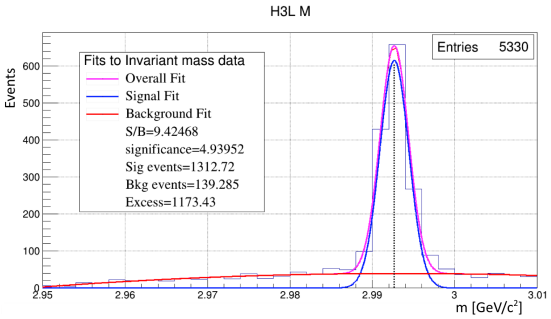

Fig. 6: *Mass spectrum for reconstructed H^3_Λ events*

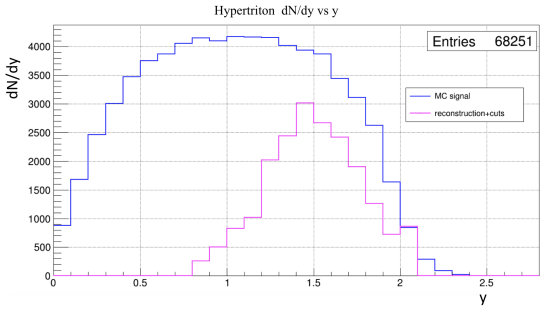

Fig. 8: *Comparison of H^3_Λ dN/dy for MC generated signal and correctly reconstructed signal with mass ID cuts*

within 2σ from the peak of the Gaussian fit, instead of 3σ. Fig. 7 shows the efficiency of reconstructed daughter particles within the acceptance zone and over a 4π solid angle as a function of p. As clearly visible, the efficiency of detection increases to almost twice for events inside the acceptance zone. The efficiency drops at lower p due to multiple scatterings.

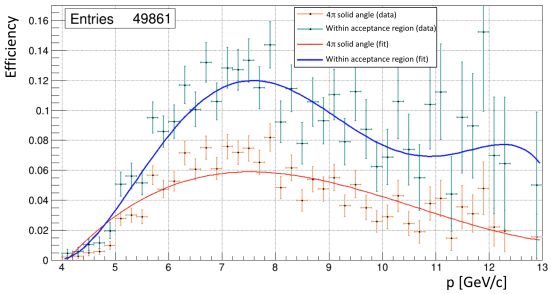

Fig. 7: *Comparison of detection efficiencies for H^3_Λ within the acceptance region and over 4π solid angle.*

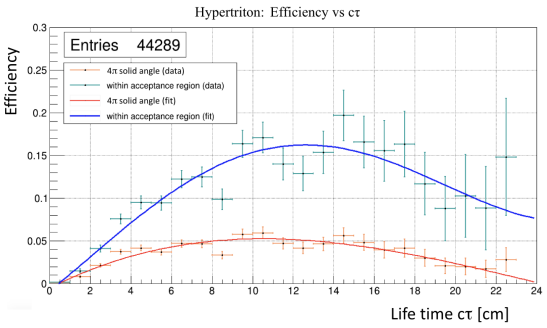

Fig. 9: *Comparison of detection efficiencies vs proper time $c\tau$ for H^3_Λ within the acceptance region and over 4π solid angle.*

Next, Fig. 8 displays the plot of the H^3_Λ yield dN/dy vs y inside the acceptance zone and a comparison with the MC signal. This is again to demonstrate how the yield goes down as we move towards the boundaries of the acceptance zone. Because of reconstruction errors and misidentification, the reconstructed plot has, of course, a much lesser amplitude than the MC signal.

We are also interested in looking at the Efficiency vs life time $c\tau$ for a H^3_Λ (Fig. 9). For very early lifetimes, the detection efficiency is low because of the high density of tracks right after the collision. This makes it hard to reconstruct $^3He^+$ and π^- tracks, and thus to identify H^3_Λ. If the lifetime is too large, then H^3_Λ does not decay while passing through the detector. Thus, we cannot reconstruct the daughter particles and the efficiency drops again. The efficiency reaches a maximum only at intermediate lifetimes, specifically between 12-14 cm.

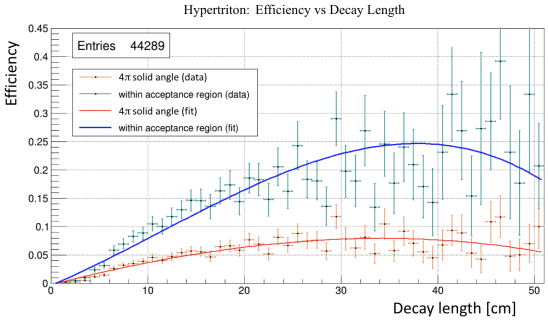

Fig. 10: *Comparison of detection efficiencies vs decay length for H^3_Λ within the acceptance region and over 4π solid angle.*

A similar argument holds for Fig. 10 showing the plot for the Hypertriton Efficiency vs Decay Length. If H^3_Λ decays too early into $^3He^+$ and π^-, there might be reconstruction errors

due to the high density of tracks. If it decays too late, the decay might take place after H^3_Λ has traversed the detector length. In this case, few correct reconstructions of daughter particles will take place and the efficiency drops.

Fig. 11 shows the Hypertriton detection efficiency vs rapidity y, compared for correct reconstructions inside the acceptance region and over a solid angle of 4π. We see that the detection efficiencies for H^3_Λ reach a maximum between rapidities y=1.4 and y=1.6.

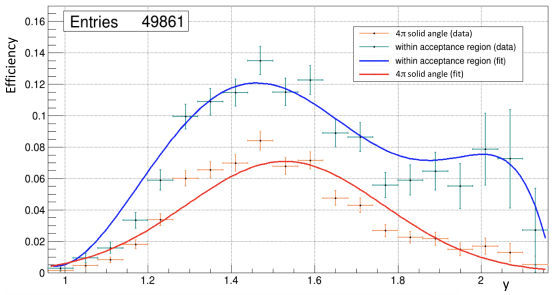

Fig. 11: *Comparison of detection efficiencies vs rapidity y for H^3_Λ within the acceptance region and over 4π solid angle.*

Fig. 12 shows a 2D histogram representing the distribution of transverse momentum p_t of H^3_Λ with the rapidity y. We see that the mean p_t for H^3_Λ is 1.341 GeV/c and the mean y is 1.547. The distribution is localised between y=0.5 and y=2.5, which is within the acceptance region of the CBM detector.

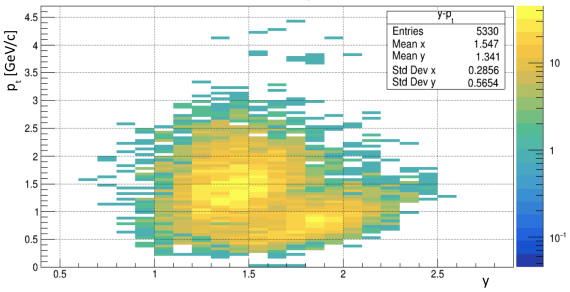

Fig. 12: *H^3_Λ transverse momentum p_t vs rapidity y*

5 Conclusions

This report presents results using the PHQMD model to produce hypernuclei and fragments in Au+Au collisions at $\sqrt{s}$=3 GeV. We now have actual cluster formation and subsequent generation of exotic fragments and single and multi-strange hypernuclei. The KF particle finder also works really well for searching specific decay tracks in a dense track environment. Finally, the collaboration might want to incorporate the changes made in the code regarding the primary vertex position and the time-of-flight calculation.

6 Acknowledgements

I wish to express my sincere gratitude to Prof. Dr. Iouri Vassiliev for providing me with an opportunity to work on this project, and for their valuable suggestions in this work. I am also grateful to Dr. Florian Uhlig and Dr. Susanne Gläßel who spared countless hours in correcting and incorporating the transport code used in this work.

References

[1] Susanne Gl¨aßel, Viktar Kireyeu, Vadim Voronyuk, J¨org Aichelin, Christoph Blume, Elena Bratkovskaya, Gabriele Coci, Vadim Kolesnikov, and Michael Winn. Cluster and hypercluster production in relativistic heavy-ion collisions within the parton-hadronquantum-molecular-dynamics approach. Phys. Rev. C, 105:014908, Jan 2022.

[2] Measurement of the mass difference and the binding energy of the hypertriton and antihypertriton. Nature Physics, 16(4):409–412, mar 2020.

[3] F. Hildenbrand and H.-W. Hammer. Lifetime of the hypertriton. Physical Review C, 102(6), dec 2020.

[4] Ivan Kisel. Event topology reconstruction in the CBM experiment. Journal of Physics: Conference Series, 1070:012015, aug 2018.

Thermal performance of the front-end electronics of the Silicon Tracking System for the CBM experiment

Sergey Konstantin Ermakov
Technische Universität Darmstadt, Germany
sergey.k.ermakov@gmail.com

Leo Christian Flehinghaus
Westfälische Wilhelms-Universität Münster, Germany
l_fleh01@uni-muenster.de

The CBM Silicon Tracking System uses complex custom-designed electronics for the signal read out and data processing. As up to 50 kW *of heat are dissipated within the detector volume, an effective cooling has to be implemented. This report aims to summarize thermal simulations and temperature measurements for the STS front-end electronics. Internal thermometer of the ASIC is used together with the reference measurement with thermal imaging camera; the numerical simulation with the open-source SW is developed for the cross check and validation with the measurements.*

1 Introduction

The Compressed Baryonic Matter (CBM) experiment is one of the major experiments at the future FAIR facility[1]. Using a fixed target in heavy ion collisions, rare isotopes and particles such as multistrange hyperons or charmed particles are expected to be created and detected by the complex detector system. CBM aims to investigate the phase structure of strongly interacting matter and to explore the QCD phase diagram in region of high baryon densities. [1] [2]
The key tracking detector of the CBM experiment is the Silicon Tracking System (STS). Its main task is to reconstruct tracks of charged particles with high efficiency and perform high resolution momentum measurements. That means, it must be able to detect up to 700 charged particles per central Au+Au collision with beam/target interaction rates up to 10 MHz. For this, 896 double sided silicon microstrip sensors are arranged in 8 tracking stations. The apparatus covers a solid angle between 2.5 ° and 25 ° and is placed between 30 cm and 100 cm downstream the target. The entire detector covers a volume of $1.4 \times 2.3 \times 1.3\,\mathrm{m}^3$ and is placed inside a 1 Tm superconducting magnet. Thereby, many challenges arise. As with each detector, particles are being scattered, one must reduce the material budget. Additionally, the detectors are exposed to high radiation during the operation of SIS100, such that the detectors must be radiation tolerant.
Finally, the challenge this paper deals with is proper cooling of the STS electronics. The cooling system must efficiently remove 50 kW of dissipated heat inside the detector box.
Section 2 gives an overview about the used front-end boards with focus on the main components and its heat dissipation. Afterwards, the used experimental setup to study the thermal performance of the STS electronics will be explained in section 3. A description of the measurement results are given in section 4. Numerical thermal simulations of the studied system are shown in section 5

[1] Facility for Antiproton and Ion Research in Europe

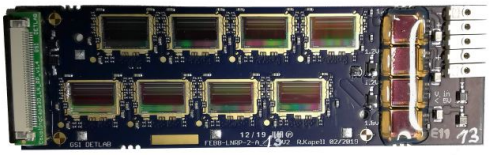

Fig. 1: *Prototype of a front-end board with 8 ASICs (FEB8). The 4 LDOs and the low and high voltage interface are placed on the left side and the connection for data transfer is located on the right side. [3]*

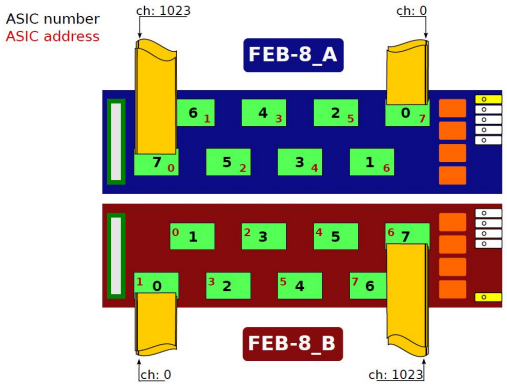

Fig. 2: *Drawing of the two different FEB types with numbering of the ASICs [4].*

2 STS Front-End Electronics

2.1 Signal Acquisition and Processing

Each double-sided silicon strip sensor is connected to two Front-End Boards (FEBs) located inside the detector box at the periphery of the detector. FEBs are responsible for reading the charge aggregated in the detector (see fig. 1). The 1024 stripes of each sensor side are connected via ultralight aluminium-polyimide microcables to 8 custom-designed Application Specific Integrated Circuits (ASICs) with 128 channels each hosting charge sensitive amplifiers (CSA). This ASICs are able to measure the time and amplitude of an incoming signal pulse and transfer the charge into a voltage step. Each amplitude value comes together with a time stamp from the in-built Time to Digital Converter (TDC) in the ASIC. Also, the additional higher level time stamp is given by the data concentrating electronics. In this step, Readout Boards (ROBs) will aggregate data from different FEBs and will guide the preprocessed data with the optical readout interface out of the detector volume. [3]

In the first step of a measurement, the ASICs are synchronized via a full register configuration, where 35496 bits for controlling the Analog Front-End (AFE) and a start of the timestamp counter are set. As the power consumption is dominated by the current in the CSA, it can be tuned with the corresponding registers of the ASIC. The voltage drop at the 1.2 V line, which provides the V_{DDM} voltage to the ASICs, can be taken as a reference whether the ASICs operate properly. Additionally, a thermal probe V_{Temp} as a temperature dependent voltage drop is implemented into the ASIC, which is used as an internal thermometer in the present studies. [3]

2.2 ASIC Power Supply

Powering the ASICs requires two low voltage lines with 1.2 V and 1.8 V, respectively. The analog 1.2 V and 1.8 V potentials are used for the AFE operation while one 1.8 V potential powers the digital part. Thereby, each pole of the 1.2 V line is used to power one row of four ASICs. In contradiction, the 1.8 V lines are used for all ASICs simultaneously.

In order to guarantee a stable value of 1.2 V and 1.8 V at the corresponding supply lines, Low Dropout Regulators (LDOs) are used. In the present studies, the LDOs are supplied with 2.2 V and 2.8 V to account for the voltage drop in the supply lines; the excess power is dissipated to heat. Figure 2 shows a drawing of the FEBs with its major parts. The orange squares represent the LDOs, where the outer LDOs are used for the 1.8 V channels. The remaining power line is used for the high voltage on the sensor and should not be discussed within the scope of this report. [3]

The concept of fixing two FEBs on one cooling fin, which is connected to a channeled liquid-cooled plate, requires a different design for the FEBs on both sides of the detector. As illustrated in fig. 2, one side of the sensor is connected to the blue FEB (A-type), while the other side in connected to the red FEB (B-type). The following measurements will mainly involve one B-type FEB8.

Finally, the structure of the circuit board itself is of interest considering the later thermal simulation. The circuit board is split up into multiple layers. Figure 3 shows a cross section of the circuit board, displaying homogeneous layers with varying thickness (thickness given on

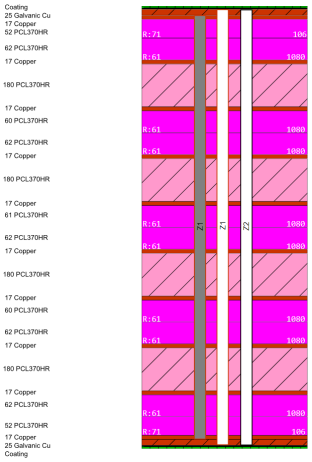

Fig. 3: *Cross section of the circuit board with its different material layers, as well as thermal vias of type Z1, Z2 and Z3.*

the left hand side in μm). While the layers of coating and PCL370HR are homogeneous, as they serve the purpose of shielding from current leakage, the copper layers are in fact, traces of the electrical circuit. For simplicity, in the numerical simulations in section 5, we will consider all these layers as homogeneous. The objects intersecting the board, labelled as Z1, Z2 and Z3 are thermal vias of varying length and different internal material. These serve the purpose of cooling the ASICs and LDOs. Again, to simplify the simulation, one only considers thermal vias of type Z1 (epoxyresin filling and coating).

3 FEB thermal test setup

The core of the test setup are two FEBs as introduced in section 2. In order to guarantee an efficient cooling, both FEBs are glued to an aluminium cooling fin as demonstrated in fig. 4. In future operations, always two FEBs of opposite type will be connected to one cooling fin, which is screwed to an aluminium cooling plate with 4 M3 screws. Putting thermal pads between each connection optimizes the heat transfer.
A water-cooling system is implemented in the aluminium plate with pressed-in copper tubes. Considering the room temperature of about 27 °C and a humidity of up to 50 %, a minimum temperature of about 15 °C may be reached without water condensation on the surface. The maximum temperature on the cooling system was set to approximately 35 °C to avoid overheating.

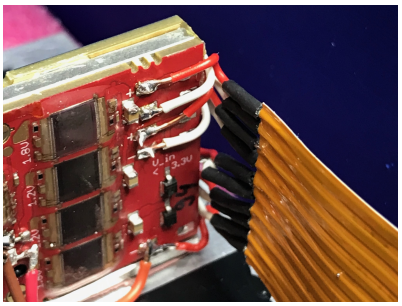

Fig. 4: *Image of the used FEB glued to an aluminium cooling fin. The low voltage lines are soldered to the corresponding contacts.*

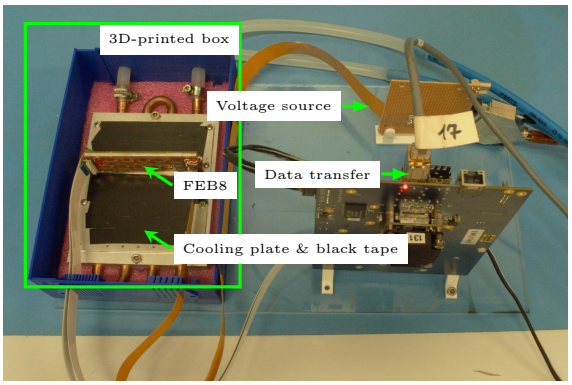

Fig. 5: *Overview to experimental setup. A custom-made box contains a water-cooled aluminium plate connected to two FEBs via an aluminium cooling fin. The* 1.2 V *and* 1.8 V *low voltage channels are supplied from a connector placed on the upper right side. The data of all channels are transferred to a readout board and send to the local network.*

An illustrating image of the test setup is presented in fig. 5. The cooling plate is located in a custom-printed box, which is attached with plastic screws to a portable plexiglas plate. The low voltage lines are supplied with a 8-line 0.5 mm^2 SUMIDA cable. A local computer communicates with the crate to control the voltage and measure the current in order to estimate the power consumption. Since no silicon sensor is connected in this module, it is not necessary to provide the system with a high voltage. The data chain is established with the network-connected EMU board (back-end electronics).
This setup allows to change the three parameters, namely the temperature of the cooling system, the low voltage power supply and the ASIC power consumption. Besides the current of the power supply, the V_{DDM} and V_{Temp} voltage is measured in every individual measurement us-

ing a python script.
Another method to estimate the temperature on the surface of the FEB is given in a Testo infrared camera. As presented in fig. 5, black tape is added on top of the cooling plate in order to decrease the reflectivity of the surface and hence enable a temperature measurement. Using this black tape at different base temperatures, the emissivity set on the infrared camera could be optimized. However, errors in the infrared images could occur due to different thermal emissivities of the ASIC surface. Therefore, some systematic offset of the real temperatures cannot be excluded.

4 Measurement Results

This section aims to summarize the measurement results, divided into two parts for changing the internal power consumption (see section 4.1) and the external temperature (see section 4.2).

4.1 ASIC Power Consumption

As mentioned in section 2, the ASIC power consumption can be controlled by modifying the CSA current. For each CSA current value, the consumed power can be measured in form of the measured V_{DDM} voltage and the provided current by the power supply. By setting a lower power consumption to all ASICs except one, the position of each ASIC number as assumed in fig. 2 could be proven. By increasing the power consumption of all ASICs, a higher temperature can be detected by the infrared camera (see fig. 6). For more quantified results, the V_{DDM} voltage of each ASIC as well as the current of the low voltage supply were measured as a function of the CSA current in fig. 7. The current increases linearly with the CSA current until the limit of the power supply is reached and therefore the curve is flattened. The V_{DDM} voltage stays constant until a CSA current of 20 and then decreases significantly.
Since the V_{DDM} potential can be measured and the 1.8 V line is assumed to provide a stable voltage, the power consumption of each ASIC can be calculated using

$$P = \frac{1}{8}\left(V_{\mathrm{DDM}} \cdot I_{\mathrm{DDM}} + 1.8\,\mathrm{V} \cdot I_{\mathrm{DD}}\right). \qquad (1)$$

Additionally, the ASIC temperature can be estimated by calculating the average value of each

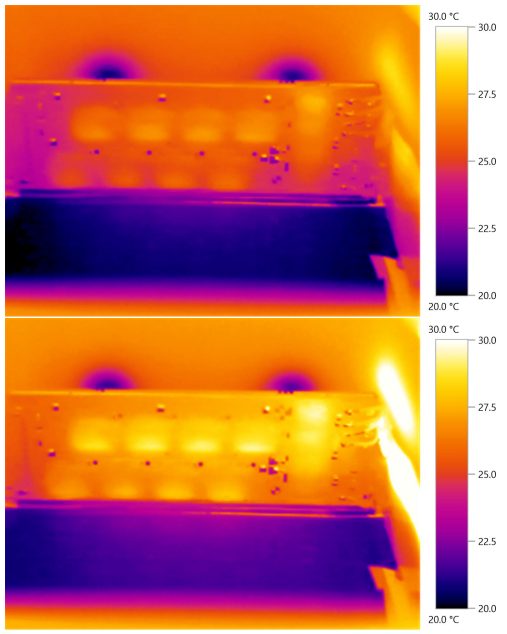

Fig. 6: *Infrared images of the FEB-8 B-type with a low power consumption on each ASIC (top) and with a high power consumption (bottom).*

ASIC surface in the corresponding infrared image. As the edges of the ASICs were not always clearly visible, an uncertainty of $\pm 0.1\,^{\circ}\mathrm{C}$ was estimated by varying the bounders of the ASIC area on the image. Figure 8 presents this measurement with a set temperature of $20\,^{\circ}\mathrm{C}$ at the cooling system and a given low voltage input of 2.2 V and 2.8 V, respectively. As long as the V_{DDM} voltage in fig. 7 is nearly constant, the temperature increases linearly with the ASIC power consumption. However, when the voltage drops down and the power supply is not capable of giving a sufficiently high current, the power consumption starts to decrease. In this region a nearly constant temperature could be observed.

4.2 Calibration of the internal thermometer

The internal thermal probe V_{Temp} is capable of giving a number in arbitrary units corresponding to the voltage drop in each ASIC. This number is assumed to show a linear dependency to the ASIC temperature in a certain range. Thus, a calibration can be done by varying the temperature and fitting the voltage numbers.
The ASIC temperature is varied by changing

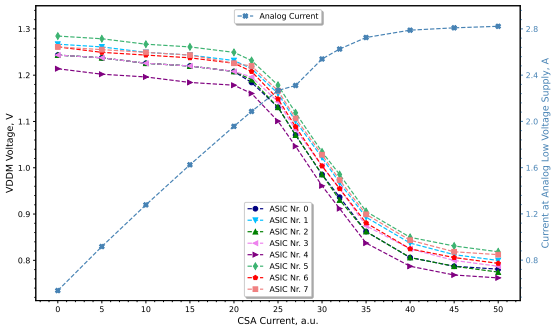

Fig. 7: *The measured voltage of each ASIC and current of the* 1.2 V *power supply as a function of the CSA current in arbitrary units. The current increases linearly with the nominal CSA current at the beginning and then saturates at higher register values. A significant decrease of the* V_{DDM} *potential could be detected at high CSA currents.*

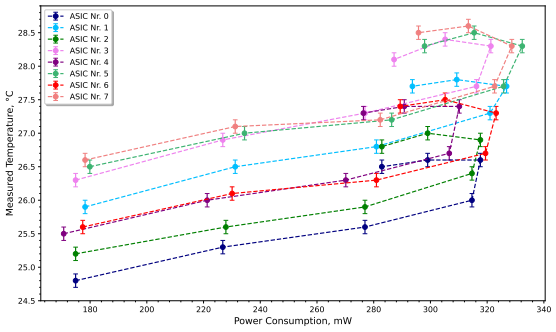

Fig. 8: *From infrared images obtained temperature as a function of the power consumption of each ASIC. The power consumption was calculated from the voltage drop inside the ASIC and the currents at the low voltage supply, which was assumed to be constant.*

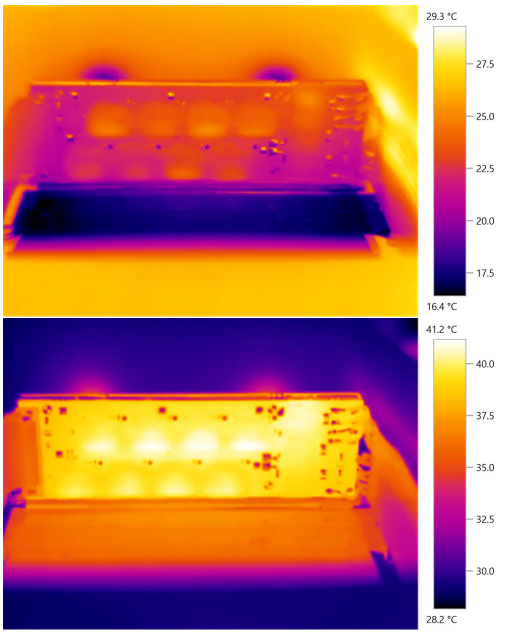

Fig. 9: *Infrared images at two different base temperatures of* 16 °C *and* 34 °C*, respectively.*

ASIC	Slope, °C/a.u.	Offset, °C
0	-3.9 ± 0.3	418.3 ± 31.7
1	-3.5 ± 0.2	390.1 ± 20.0
2	-3.4 ± 0.2	373.8 ± 18.3
3	-3.8 ± 0.3	416.2 ± 32.6
4	-3.8 ± 0.3	398.8 ± 26.8
5	-2.9 ± 0.2	330.7 ± 19.3
6	-3.8 ± 0.3	422.5 ± 32.6
7	-3.9 ± 0.2	428.9 ± 22.2

Tab. 1: *Fit parameter for the temperature calibration*

the temperature of the baseplate, where the coolant temperature changes in a range between 15 °C and 35 °C. The temperature was measured again with the infrared camera in the same way as in the previous section. The infrared images of the two extreme temperatures are attached in fig. 9. Black tape was added on the aluminium plate enabling a reference measurement of the cooling block. After estimating the temperature from the infrared images, the voltage drop at the thermal resistor can be plotted as a function of the temperature in fig. 10. Each ASIC was fitted using a linear function. In this way, the mean calibration function

$$\begin{aligned} T(V_{\mathrm{Temp}}) &= a \cdot V_{\mathrm{Temp}} + b \\ a &= (-3.6 \pm 0.1 \pm 0.1)\ ^\circ\mathrm{C} \\ b &= (397.4 \pm 9.2 \pm 11.6)\ ^\circ\mathrm{C} \end{aligned} \tag{2}$$

can be given, where the first uncertainty is given by the propagation of the fit uncertainties, where the estimated uncertainty of the temperatures is included. The second uncertainty is calculated as the statistical error of the 8 ASICs. The parameter of the calibration functions of each ASIC are presented in table 1. However, it should be noted that a possible uncertainty of the absolute temperature measurement with the infrared camera was not taken into account.

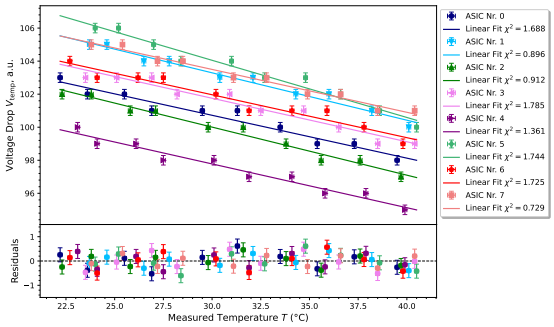

Fig. 10: *Calibration of the internal thermal voltage drop using linear fits.*

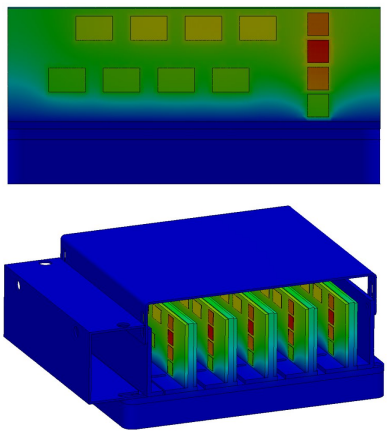

Fig. 11: *The model done in [6] includes the cooling box as well as the FEB itself. The final, equilibrium state of the simulation is displayed.*

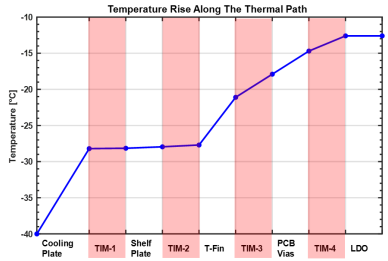

Fig. 12: *Temperatures between each component and thermal interface (TIM) display the temperature gradient across each component.*

5 Thermal Simulations

5.1 Previous Simulations

Simulation of the thermal performance of the STS front-end electronics was previously performed using several assumptions to simplify the calculation [6]. The model involved in that study considers the ASICs and LDOs as well as the average thermal conductivity of the PCB board and array of thermal vias.

There were no explicit volumes representing the glue contact. Instead, thermal interfaces were defined in various regions with a certain thermal resistivity, in order to simulate the effect of the glues without having to mesh it.
The simulation was done in SOLIDWORKS and is based on several assumtions. Each ASIC and LDO has a constant power dissipation. Furthermore, the cooling plate has a constant cooling temperature, which is constant across the entire plate. This cooling temperature was obtained from a previous simulation [6] simulating the flow of the cooling fluid and the consequent temperature field over the entire cooling plate. The highest temperature value was taken as a conservative estimation for the uniformly cold base plate.
The results of this simulation may serve as a first reference for the measurements described above.

5.2 Development of the New Simulation

In order to have a reliable cross-check for the future studies, to validate the observations in section 4, and to address possible systematical uncertainties, we decided to perform a set of numerical simulations of the thermal performance of the STS front-end electronics. In comparison to the former simulation described in section 5.1 the new simulation aims to include further details and therefore give more precise results and therefore account for the systematic errors of the experiments.
The largest uncertainty comes from the glob-top surface absorbing part of the heat radiation, which should be measured by the thermal camera. Additionally, we can see various effects, which by the experimental data alone cannot be fully explained. Hence, the simulation provides not only an explanation for these effects, but additionally, can help estimate the impact of the systematic errors.
As the simulation is supposed to be performed in great detail, only a fraction of the experimental setup is considered. Further details will be discussed in the following chapters.
In the scope of this work, only the geometry construction- and the meshing-process are de-

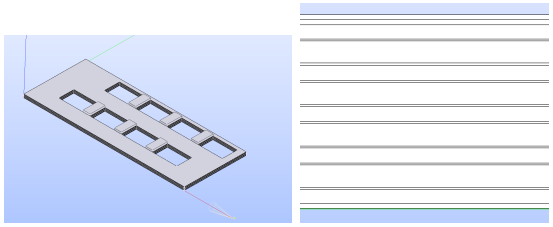

Fig. 13: *The PCB board has holes for the ASIC boxes to later be placed into. Additionally, glob top layers inbetween each ASIC box are visible (left). Additionally, a side view shows the different material layers of the PCB (right).*

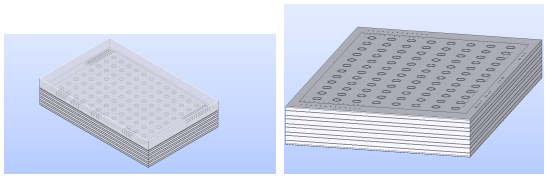

Fig. 14: *Left: the ASIC box with a transparent glob top above the chip. The chip has cut out vias faces, which are in fact not "real" thermal vias, but will rather be used later for meshing purposes. Right: the thermal vias inside the ASIC box.*

scribed. The simulation itself will be performed in future, since the setup of the simulation itself is not yet completed due to the complexity of the mesh.

5.3 Construction of Geometry

The geometry of the experimental setup is simplified to the region of interest for the simulation. This includes the part of the circuit board, which holds the ASICs. However, it is modelled in great detail. This includes the different layers of the circuit board, 8×12 thermal vias under each ASIC, the ASICs themselves, the pins connecting the ASICs to the circuit board, the glue for attaching the ASIC and finally, the glob top (protective epoxyresin coating).
While the different layers of the PCB are considered, circuit tracks are not modelled. Instead, the layers are considered as homogenious. Only thermal vias of type Z1 are considered (coating and epoxyresin filling), to further simplify the material groups considered. The geometry is built in two seperate arrangements, to make calculations and later, meshing, easier with SALOME. The first geometry is the "base plate" (figure 13) and the second geometry presents the "ASIC box" (figure 14).
The base plate includes the circuit board, with holes for the ASIC boxes. Additionally, the glob top inbetween each ASIC is modelled on top.
The ASIC box is a cut-out part of the circuit board itself; it includes the thermal vias underneath the ASIC (figure 14) and the ASIC, connecting pins and glob top on top.

5.4 Meshing with SALOME

Various meshing algorithms are used to producte the final mesh compound for the simulation. The base plate is created through a NETGEN-2D-1D quadrangle dominant algorithm and extruded through each layer (figure 15).The copper layers are split into four pieces across the board, the PCL370HR is split into three and finally, the gold and coating layer are split into two (figure 15). Seperate faces for the glob top inbetween each ASIC are created and then extruded to create a 3D mesh.
The ASIC is meshed in several parts. The glob top has a quadrangle surface, is however, meshed by a NETGEN-3D algorithm on the inside. For the ASIC itself, for the glue and for the bottom part of the ASIC box which includes the thermal vias, an extrusion was created. For this, all the vias caps and topmost faces of the bottom part of the ASIC box have been selected (figure 16) and extruded along the edges of the ASIC and the bottom half of the ASIC box.

The final ASIC mesh is copied multiple times and placed into the holes of the base mesh. These two are then put into a compound mesh, to create the final mesh for the simulation. The groups inside the total mesh were selected by materials and external faces.

6 Conclusion

During this project, the thermal and electrical properties of the front-end electronics of the silicon tracking system of the CBM experiment were investigated.
A test setup was constructed, where in first measurements the V_{DDM} and V_{Temp} voltages were measured. Additional information about the temperature on the surface could be gained with an infrared camera.
A drop of the V_{DDM} voltage could be observed at

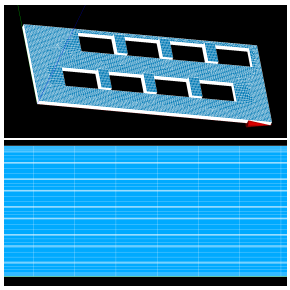

Fig. 15: *The base mesh with the the extruded glob top sections (left). While the number of segments across the board varies in each material layer, the glob top is split up into fifteen pieces across the mesh. A side view (right) shows the separation of each layer into different pieces across the board. The copper layers are split into four, the PCL370HR layers are split into three and the gold and coating layer are split into two layers.*

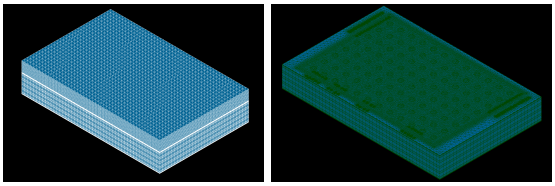

Fig. 16: *The ASIC box is meshed in two parts. While the upper part with chip, pins and glob top epoxy cover (left) is meshed via various algorithms, the lower part (right) is simply extruded from the topmost face.*

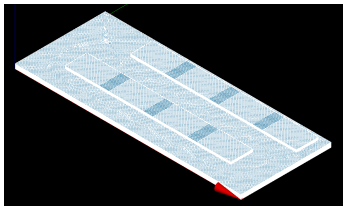

Fig. 17: *The view of the final mesh used for the simulation. It is composed of the meshes discussed before (base mesh and ASIC box).*

higher CSA currents. The reason for this early is still to be investigated. One possible reason might be a partially broken contact due to the thermal cycling of the FEB. To confirm this, further tests are required.
Furthermore, a calibration for the internal thermometer could be given.
Since the numerical simulation was developed for slightly different system, we cannot perform one-to-one comparison with the present measurements. Qualitatively, the simulation and measurements agree. In figure 11 higher temperatures on the upper ASICs can be observed, which corresponds to the measurements taken by the infrared camera (e.g. figure 6). However, measurements show the highest LDO to have the highest temperature, whereas the simulation shows the second LDO (from the top) to have the highest temperature. Additionally, since the ASICs were assumed to disspate power uniformally, the effect of having the highest temperature at the bottom of each ASIC, could not be replicated either.
For the detailed study of the thermal effects in the STS FEBs one certaily needs more detailed investigations. For this reason, the model described in section 5.3 was expanded to include further mechanical details, in particular chip pins and explicit geometries for glue and thermal vias. As they are placed on the lower side of the ASIC, the heat conducted by the pins might create the effect of measuring higher temperatures at the bottom. Additionally, instead of defining thermal interfaces with a thermal resistance, the heat flow through the glues can be observed more accurately. Generally, the result is expected to be more detailed and therefore, to serve as a basis for an explanation of the unknown effects from the measurements. After submitting this work, the simulation will be set up in order to compare the simulation data with the measurement results.

Acknowledgments

We would like to thank the organizers of the Summer Student Program 2022 for this amazing opportunity. Great thanks also to our tutor Dr. Maksym Teklishyn who supported and guided us throughout the entire program. Furthermore, we want to thank the STS group, especially Ilija Elizarov, who guided us through the simulations of this work. Additionally, we would like

to thank Prof. Andronic and Dr. Sven Soff for recommending us to the Summer Student Program.

References

[1] Tomas Balog. Overview of the CBM detector system. Journal of Physics: Conference Series 503 (2014) 012019

[2] P Senger and the CBM Collaboration 2021 Phys. Scr. 96 054002

[3] A.R. Rodríguez. The CBM Silicon Tracking System front-end electronics. Phd. thesis 2019

[4] A.R. Rodríguez, O.M. Rodríguez, J.Lehnert, A. Lymanets. STS module testing protocol v1.0

[5] W. Zubrzycka, K. Kasinski. Biasing Potentials Monitoring Circuit for Multichannel Radiation Imaging ASIC In-system Diagnostics. Conference paper 2017

[6] K. Agarwal. STS Cooling Concept And Design. 37th CBM Collaboration Meeting

Construction of the Baryon Operator for the Λ Octet

Feyer, Tristan
University of Graz, tristan.feyer@edu.uni-graz.at

The baryon operator of Λ_8 is evaluated in the quark model regime.

1 Introduction

The calculation of the hadron spectrum of QCD is a urgent field of research in lattice QCD. This report will focus on the spectrum of the $\Lambda(1405)$ baryon with $J^P = \frac{1}{2}^-$. Precise data has already been experimentally obtained [4]:

$$\begin{aligned} M_\Lambda &= 1405^{+1.3}_{-1.0}\text{MeV}, \\ \Gamma_\Lambda &= 50.5 \pm 2.0\text{MeV}. \end{aligned} \tag{1}$$

Unitarized χPT+ model calculations, however, yield that the situation is more complex, showing two poles in the range of $\mathcal{R} \approx 1400$MeV. There is no generally accepted results in lattice QCD. The CEBAF Large Acceptance Spectrometer (CLAS) observed different line shapes for $\Sigma^-\pi^+$, $\Sigma^+\pi^-$, $\Sigma^0\pi^0$ in [6]. These probably arise from the interference between the $I = 0$ and $I = 1$ amplitudes. In lattice QCD one can work with interpolators with well-defined isospin quantum numbers, where these amplitudes do not mix. Here one can switch of isospin breaking. But in experiment one cannot, which leads to the coupled channel problem.

A first step is the calculation of finite volume energies, where one uses the three quark interpolators as well as $\Sigma\pi$, $N\bar{K}$ - and possibly $\Lambda\eta$ for multihadronic systems. Particularly, it is important to have a diverse basis, to guarantee an efficient variational method. A larger basis helps analyzing the asymptotic behavior of the correlation function. In comparison one now expects a good interpolator with little noise in $\frac{1}{2}^-$, $\frac{1}{2}^+$. For calculation in the moving frame, one needs to get a connection between the finite volume energies one knows how to extract and the scattering amplitude. This is achieved by Lüscher's method. In the moving frame the symmetry of the lattice is reduced. In Lüscher's equation this reduction of symmetry leads to the problem that other continuum quantum numbers appear too. Therefore, one considers the energies of close by states with those quantum numbers. A prominent example is $\Lambda(1520)$ $(\frac{3}{2}^-)$)

In order to treat such high spin states, one has to improve computational methods. Progress has been made in [1] by introducing operators with displacements of the quarks within the baryon operator. Reverence [2], however, uses a completely independent, purely group theoretically evolved set of operators for the same task. This report shall do the groundwork for developing a computationally efficient mapping between these operator sets. This must consist of a linear combination of the used operators. The mere superposition of all, however, is likely to produce too much noise to allow identifying the asymptotics.

2 Correlation functions and lattice interpolators

This chapter as well as much of the notation is based on [5].

Hadron interpolators serve to build creation and annihilation operators by choosing the quantum numbers of interest. One differes between the interpolators of baryons and mesons. This chapter treats systems consisting of 3 valence quarks and neglects all other phenomenologies.

Let be a Hilbert space operator such that

$$\begin{aligned} < O(n_t)\bar{O}(0) > &= \sum_k < 0|\hat{O}|k >< k|\hat{O}\top|0 > \mathrm{e}^{-n_i a E_k} \\ &= A\mathrm{e}^{-n_t a E_H}(1 + \mathcal{O}(\mathrm{e}^{-n_t a \delta E})), \end{aligned} \tag{2}$$

with $A = \text{const}$, the lowest state $|H>$ with corresponding energy E_H and $< 0|\hat{O}|H > \neq 0$. The task is to find an $\hat{O}$ that fits state and quantum numbers.

Λ consists of u,d,s. Thus an interpolator takes the form

$$\begin{aligned} O_\Lambda(n) = \epsilon_{abc}(s_a(n)(u_b\top(n)C\gamma_5 d_c(n))+ \\ +d_a(n)(u_b^\top(n)C\gamma_5 s_c(n))+ \\ +u_a(n)(d_b^\top(n)C\gamma_5 s_c)). \end{aligned} \quad (3)$$

By summing up the color indices with the Levi-Cevita tensor one concludes that the interpolator is a color singlet and also gauge-invariant.

Another quantum number is parity which yields

$$O_\Lambda^P(\mathbf{n}, n_4) = \gamma_4 O_\Lambda(-\mathbf{n}, n_4). \quad (4)$$

This translation of the spatial vector ($\mathbf{n} \to -\mathbf{n}$) can be neglected when projecting to 0 momentum. The parity projectors are

$$P_\pm = \frac{1}{2}(1 \pm \gamma_4). \quad (5)$$

Projection to 0 momentum then simplifies to $P = \pm 1$. One finds

$$\begin{aligned} \bar{O}_\Lambda = \epsilon_{abc}(2(\bar{u}_a\top C\gamma_5 \bar{d}_b)\bar{s}_c P_\pm + \\ +(\bar{u}_a\top C\gamma_5 \bar{s}_b)\bar{d}_c P_\pm - \\ -(\bar{d}_a\top C\gamma_5 \bar{s}_b)\bar{u}_c P_\pm). \end{aligned} \quad (6)$$

Let Γ^A, Γ^B be two matrices such that $(\Gamma^A, \Gamma^B) = (1, C\gamma_5)$. Then

$$\begin{aligned} O_{\Lambda\pm} = \epsilon_{abc} P_\pm \Gamma^A (2s_a(u_b\top\Gamma^B d_c)+ \\ +d_a(u_b\top\Gamma^B s_c)- \\ -u_a(d_b\top\Gamma^B s_c)) \end{aligned} \quad (7a)$$

$$\begin{aligned} \bar{O}_{\Lambda\pm} = \epsilon_{abc}(2(\bar{u}_a\top\Gamma^B \bar{d}_b)\bar{s}_c + \\ +(\bar{u}_a\top\Gamma^B \bar{s}_b)\bar{d}_c - \\ -(\bar{d}_a\top\Gamma^B \bar{s}_b)\bar{u}_c)\Gamma^A P_\pm. \end{aligned} \quad (7b)$$

The corresponding correlator can be computed by

$$< O_{\Lambda\pm}(n)_\alpha \bar{O}_{\Lambda\pm}(m)_\alpha > . \quad (8)$$

3 Symmetry properties of quarks

In this paper we consider a *uds* baryon, Λ that shall be uniquely identified. In order to distinguish baryons from each other it is necessary to introduce quantum numbers. This is done by increasing the representation.

In this chapter the notation of [3] is introduced. For a didactic explanation one starts by considering mesons first, later adding the additional quark.

state 1	state 2	$1 \leftrightarrow 2$ interchange	
u	u	uu	
u	d	$\frac{1}{\sqrt{2}}(ud + du)$	$\frac{1}{\sqrt{2}}(ud - du)$
d	d	dd	
		symmetric	antisymmetric

Tab. 1: *Symmetry states for 2 objects in SU(2).*

state 1	state 2	$1 \leftrightarrow 2$ interchange	
u	u	uu	
u	d	$\frac{1}{\sqrt{2}}(ud + du)$	$\frac{1}{\sqrt{2}}(ud - du)$
d	u		
d	d	dd	
u	s	$\frac{1}{\sqrt{2}}(us + su)$	$\frac{1}{\sqrt{2}}(us - su)$
s	u		
d	s	$\frac{1}{\sqrt{2}}(ds + ds)$	$\frac{1}{\sqrt{2}}(sd - ds)$
s	d		
s	s	ss	
		symmetric	antisymmetric

Tab. 2: *Symmetry states for 2 objects in SU(2).*

3.1 SU(2) representation

Considering solely the u, d quarks and the isospin $I = \frac{1}{2}$, its projection is distinguished between the up state $I_z = +\frac{1}{2}$ for the proton (uud) and d state $I_z = -\frac{1}{2}$ for the neutron (udd).
Let a system consist of two objects in SU(2). Then there are 4 states of how the objects 1 and 2 can arrange that are given in table 1. The sign in the table separates them into a symmetric and an antisymmetric entry. In group theoretical terms this means $2 \otimes 2 \to 3 \oplus 1$. Any number of u and d quarks can be arranged in such a table.

3.2 SU(3) representation

This principle can be expanded to SU(3) by introducing a new flavor s, which yields 27 combinations with 18 entries from $3 \otimes 6$ and 9 from $3 \otimes \bar{3}$ and are denoted in table 2. Expanding by an other state means adding an additional quark in the system, which then gives

$$\begin{aligned} 3 \otimes (3 \otimes 3) &\to 3 \otimes (6 \oplus 3) \\ &\to (10_S \oplus 8_{MS} \oplus (8_{MA} \oplus 1). \end{aligned} \quad (9)$$

The results - without the trivial 10_S are given in table 3. S refers to a symmetric state, MS to a mixed-symmetric, MA to a mixed-antisymmetric and A an antisymmetric.

	ψ_{MS}	ψ_{MA}
P	$\frac{1}{\sqrt{6}}[(ud+du)u-2uud]$	$\frac{1}{\sqrt{2}}(ud-du)u$
N	$-\frac{1}{\sqrt{6}}[(ud+du)d-2udd]$	$\frac{1}{\sqrt{2}}(ud-du)d$
Σ^+	$\frac{1}{\sqrt{6}}[(us+su)u-2uus]$	$\frac{1}{\sqrt{2}}(us-su)u$
Σ^0	$\frac{1}{\sqrt{6}}[s(\frac{du+ud}{\sqrt{2}})+(\frac{dsu+usd}{\sqrt{2}})-$	$\frac{1}{\sqrt{2}}[\frac{dsu+usd}{\sqrt{2})-s(\frac{ud+du}{\sqrt{2}})}$
	$-2(\frac{du+ud}{\sqrt{2})s}$	
Σ^-	$\frac{1}{\sqrt{6}}[(ds+sd)d-2dds]$	$\frac{1}{\sqrt{2}}(ds-sd)d$
Λ^0	$\frac{1}{\sqrt{2}}[\frac{dsu-usd}{\sqrt{2}}+\frac{s(du-ud)}{\sqrt{2}}]$	$\frac{1}{\sqrt{6}}[\frac{s(du-ud)}{\sqrt{2}}+\frac{usd-dsu}{\sqrt{2}}-$
		$-\frac{2(du-ud)s}{\sqrt{2}}$
Ξ^-	$-\frac{1}{\sqrt{6}}[(ds+sd)s-2ssd]$	$\frac{1}{\sqrt{2}}(ds-sd)s$
Ξ^0	$-\frac{1}{\sqrt{6}}[(us+su)s-2ssu]$	$\frac{1}{\sqrt{2}}(us-su)s$
	ψ_A	
Λ_1^0	$\frac{1}{\sqrt{6}}[s(du-ud)+(usd-dsu)+(du-ud)s]$	

Tab. 3: *MS, MA, A symmetry representations for octet states of the 3 quark system.*

4 Group theory on the lattice

4.1 Octahedral group

One generally considers a cubic lattice. Here rotational symmetry applies which is broken by the finite octahedral group O. O consists of 24 elements by which the system can be rotated with respect to a point or a point on the lattice can be rotated with keeping the coordinate system fixed, which are equivalent arguments.

The irreducible representations (irreps) play an important role because the states of the continuum angular momentum can be described by the states we find in specific patterns of the irreps. For finite groups there is an equivalience between the number of irreps and that of conjugacy classes. Therefore O has 5 single-valued irreps. Their number is calculated by the equality of the number of squared dimensions and the number of group elements. We find 1,1,2,3,3 dimensions. Mulliken convention calls the corresponding irreps A_1, A_2, E, T_1, T_2.
In quantum physics the patterns of these groups, correspond to the rotational symmetry group SU(2) with spin J. Diverse connections of irreps provide different quantum numbers J as listed in the table below.

4.2 Double octahedral group

Since baryons are half-integer particles, the irreps need double-value. This is accieved by the introduction of new generators. The new irreps

J	Λ
0	A_1
1	T_1
2	$E \oplus T_2$
3	$A_2 \oplus T_1 \oplus T_2$
4	$A_1 \oplus E \oplus T_1 \oplus T_2$

Tab. 4: *Angular momentum and corresponding irrep. for O.*

J	Λ
$\frac{1}{2}$	G_1
$\frac{3}{2}$	H
$\frac{5}{2}$	$H \oplus G_2$
$\frac{7}{2}$	$G_1 \oplus H \oplus G_2$

Tab. 5: *Angular momentum and corresponding irrep. for O^D.*

G_1, G_2 have irrep dimension 2 and H has dimension 4.

5 Construction of the baryon operator

First of all one wants to reduce the number of quark labels by symmetry argumentation. Baryons are color singlets. Thus they allow solely antisymmetric combinations of the colors of the involved quarks. Secondly, the baryon operator will also need to be antisymmetric under the exchange of any quark-pair, which is automatically fulfilled because they are constructed by Grassmann algebra, which anticommutes. Consequently, there are three remaining quark-

labels (flavor, spin, spatial projection).

Let $\{x, y, z\}$ be a set of three quarks and $\{\phi_1, \phi_2, \phi_3\}$ the corresponding generic three-quark operator. $\mathcal{F}_{\Sigma_f}$ is the flavor, $\mathcal{S}_{\Sigma_s}$ the Dirac spin and $\mathcal{D}_{\Sigma_D}$ the spatial projection operator. The sums in the suffix indicate the symmetry combinations they allow. Then we can define an operator

$$B = (\mathcal{F}_{\Sigma_f} \otimes \mathcal{S}_{\Sigma_s} \otimes \mathcal{D}_{\Sigma_D})\{\phi_1\phi_2\phi_3\}. \tag{10}$$

For simplicity the spatial projection will furthermore be neglected as is done in local and quasi-local operators.
Since bosons have symmetric wavefunctions, the final B operator needs to be symmetric too. Thus the operators need to fulfill the symmetry property

$$\{1\}_S\{2\}_S = \{1,2\}_S \tag{11a}$$

$$\{1\}_A\{2\}_A = \{1,2\}_S \tag{11b}$$

$$\frac{1}{2}(\{1\}_{MS}\{2\}_{MS} + \{1\}_{MA}\{2\}_{MA}) = \{1,2\}_S, \tag{11c}$$

where 11c guarantees the overall symmetry. The labels 1 and 2 represent spin and flavor respectively in this particular example.
This shows that the task of the construction of the baryon operator can be split into the Dirac spin and the flavor (and spatial projection) part.

5.1 Dirac spin

Let ρ, s be two different spinors with two different spin orientations each labeled $+$, -, representing spin up and down states. The symmetries of the spinors direct product $\rho \otimes s$ are listed in table 4.

Plugging this into the previous table and applying the direct product $\left|\begin{matrix}\rho_1 & \rho_2 & \rho_3\\ s_1 & s_2 & s_3\end{matrix}\right\rangle = |\mu_1, \mu_2, \mu_3>$ yields to Table 6 and thereby verifies [1]. Here the shorts read $\left|\begin{matrix}+ & \cdots\\ + & \cdots\end{matrix}\right\rangle = |1, \cdots>$, $\left|\begin{matrix}+ & \cdots\\ - & \cdots\end{matrix}\right\rangle = |2, \cdots>$, $\left|\begin{matrix}- & \cdots\\ + & \cdots\end{matrix}\right\rangle = |3, \cdots>$, $\left|\begin{matrix}- & \cdots\\ - & \cdots\end{matrix}\right\rangle = |4, \cdots>$. With f_i being the flavor of the ith smeared quark q in the baryon the first line of the table reads

$$\begin{aligned} -2(q_3^{f_1}q_3^{f_2}q_2^{f_3} + q_3^{f_1}q_2^{f_2}q_3^{f_3} + \\ q_2^{f_1}q_3^{f_2}q_3^{f_3}) + q_3^{f_1}q_4^{f_2}q_1^{f_3} + \\ q_4^{f_1}q_3^{f_2}q_1^{f_3} + q_3^{f_1}q_1^{f_2}q_4^{f_3} + \\ q_4^{f_1}q_1^{f_2}q_3^{f_3} + q_{f_1 q_3^{f_2} q_4^{f_3}} + \\ q_1^{f_1}q_4^{f_2}q_3^{f_3} \end{aligned} \tag{12}$$

5.2 Flavor

In this review the example of a Λ_8 baryon is considered, which is a flavor octet with

$$\begin{aligned} \phi_{MS} &= \frac{1}{\sqrt{2}}(|sud>_{MS} - |uds>_{MS}) \\ \phi_{MA} &= \frac{1}{\sqrt{2}}(|uds>_{MA} - |uds>_{MA}) \end{aligned} \tag{13}$$

5.3 Baryon operator

Thus 10 becomes

$$\begin{aligned} B = &\frac{1}{2}((|\rho>_S\,|s>_{MS} + \\ &\frac{1}{\sqrt{2}}(-|\rho>_{MS}\,|s>_{MS} + |\rho>_{MA}\,|s>_{MA})) \\ &(|sud>_{MS}\,|uds>_{MS}) + \\ &(|\rho>_S\,|s>_{MA} + \\ &\frac{1}{\sqrt{2}}(|\rho>_{MS}\,|s>_{MA} + |\rho>_{MA}\,|s>_{MS})) \\ &(|sud>_{MA} - |uds>_{MA})) \end{aligned} \tag{14}$$

6 Conclusion and Outlook

This report verifies the results of [1]. The construction of [2] was followed till the MAPLE program. A next step for understanding was to request this program. Then the mapping between the displacement operators and the solely mathematically constructed operators can be performed.

References

[1] S. Basak et al. in *Clebsch-Gordan Construction of Lattice Interpolating Fields for Excited Baryons*,arxiv:hep-lat/0508018v1, (2005).

[2] S. Basak et al. in *Group-theoretical construction of extended baryon operators*

in lattice QCD , arxiv:hep-lat/0506029v2, (2005).

[3] F. E. Close, *An Introduction to Quarks and Partons*, (Academic Press, London, 1979).

[4] J. Beringer et al. (Particle Data Group), PR D86, 010001 (2012) (URL: http://pdg.lbl.gov).

[5] C. Gattringer and C. Lang in *Quantum Chromodynamics on the Lattice*, (Soringer Verlag, Berlin, 2010).

[6] K. Moriya et al. in *Differential Photoproduction Cross Sections of the* $^0(1385)$*,* $\Lambda(1405)$*, and* $\Lambda(1520)$, arxiv:1305.6776, (2013).

symmetry	embedding	$\rho \otimes s$
S	1	$\frac{1}{\sqrt{2}}(\|\rho>_{MS}\|s>_{MS}+\|\rho>_{MA}\|s>_{MA})$
	1,2	$\|\rho>_S\|s_>S$
MS	1,2	$\|\rho>_S\|s>_{MS}$
	3	$\frac{1}{\sqrt{2}}(-\|\rho>_{MS}\|s>_{MS}+\|\rho>_{MA}\|s>_{MS})$
MA	1,2	$\|\rho>_S\|s>_{MA}$
	3	$\frac{1}{\sqrt{2}}(\|\rho_{MS}>\|s>s_{MA}+\|\rho>_{MA}\|s>_{MS})$
A	1	$\frac{1}{\sqrt{2}}(-\|\rho>_{MS}\|s>_{MA}+\|\rho>_{MA}\|s>_{MS}$

Tab. 6: *Dirac spin symmetry and direct product of Dirac spinors for $\frac{1}{2}$ spin*

	symmetry	$\|J,m>$
S	$\|+++>$	$\|\frac{3}{2},\frac{3}{2}>$
	$\frac{\|++->+\|+-+>+\|-++>}{\sqrt{3}}$	$\|\frac{3}{2},\frac{1}{2}>$
	$\frac{\|+-->+>-+->+>--+>}{\sqrt{3}}$	$\|\frac{3}{2},-\frac{1}{2}>$
	$\|---->$	$\|\frac{3}{2},-\frac{3}{2}>$
MS	$\frac{1}{\sqrt{6}}(2\|++->-\|+-+>-\|-++>)$	$\|\frac{1}{2},\frac{1}{2}>$
	$-\frac{1}{\sqrt{6}}(2\|--+>-\|-+->-\|+-->)$	$\|\frac{1}{2},-\frac{1}{2}>$
MA	$\frac{1}{\sqrt{2}}(\|+-+>-\|-++>))$	$\|\frac{1}{2},\frac{1}{2}>$
	$\frac{1}{\sqrt{2}}(\|+-->->-+->)$	$\|\frac{1}{2},-\frac{1}{2}>$

Tab. 7: *S, MS, MA combinations for quantum states $|J,m>$.*

Λ	k	λ	S Dirac indices μ_1, μ_2, μ_3
G_{1g}	1	1	-2(332+323+233)+341+431+314+413+134+143
	2	1	2(144+414+441)-234-342-423-243-324-432
	2	2	-2(223+232+322)+214+124+241+142+421+412

Λ	k	λ	MS Dirac indices μ_1, μ_2, μ_3
G_{1g}	1	1	2(112)-121-211
	1	2	-2(221)+212+122
	2	1	2(332+314+134)ä341-323-143-431-413-233
	2	2	2(441 + 423 + 243) + 432 + 414 + 234 + 342 + 324 + 144
	3	1	2(332 + 413 + 143) + 323 + 233 + 134 + 314 + 341 + 431
	3	2	2(441 + 324 + 234) 414 144 243 423 432 342
G_{u1}	1	1	2(114 + 132 + 312) 123 141 321 213 231 411
	1	2	-2(223 + 241 + 421) + 214 + 232 + 412 + 124 + 142 + 322
	2	1	2(334) 343 433
	2	2	-2(443) + 434 + 344
	2	1	2(332+314+134)-341-323-143-431-413-233
	2	2	-2(441+423+243)+432+414+234+342+324+144
	3	1	-2(332+413+143)+323+233+134+314+341+431
	3	2	2(441+324+234)-414-144-243-423-432-342
G_{1u}	1	1	2(114+132+312)-123-141-321-213-231-411
	1	2	-2(223+241+421)+214+232+412+124+142+322
	2	1	2(334)-343-433
	2	2	-2(443)+434+344
	3	1	2(114+231+321)-141-411-312-132-123-213
	3	2	-(8223+142+412)+232+332+421+241+214+124

Λ	k	λ	MA Dirac indices μ_1, μ_2, μ_3
G_{1g}	1	1	121-211
	1	2	122-212
	2	1	143-233+323-413+341-431
	2	2	144-234+324-414+341-432
	3	1	-233+323+134-314-341+431
	3	2	-414+144-243+423+432-342
G_{1u}	1	1	123-213+141-231+321-411
	1	2	124-214+142-232+322-412
	2	1	343-433
	2	2	344-434
	3	1	-141+411-312+132+123-213
	3	2	232-322+421-241+214

Tab. 8: *List of Dirac indices for given symmetry groups Λ, and embeddings.*

GPU Simulations of Nonlinear High-current Beam Dynamics

García Gil, Pablo
University of Vigo (Spain), pablogarciagil16@gmail.com

The aim of this project is to obtain a new tracking simulation for the heavy-ion synchrotron SIS100 based on the recent xsuite library. With this we intend to obtain a new more universal simulation that can run on more devices thanks to the use of OpenCL instead of CUDA as a communication API to the GPU, allowing computation on Nvidia and AMD graphics cards as well as on CPUs.

1 Introduction

The tracking simulation of a synchrotron consists of the update of the position and momentum coordinates of particles as they pass through every element of the accelerator. This process is known as tracking the lattice, the set of accelerator elements. In addition to this lattice tracking, the space charge effects should be added. These effects consist of the Coulomb repulsion force between particles because of their charge and is simulated by adding between the elements of the lattice a new element called space charge node (SC node).
The stable version of the simulation uses the library SixTrackLib [**?**] for the lattice tracking and the library PyHEADTAIL [**?**] for the space charge effects. PyHEADTAIL uses CUDA as GPU communication API which only allows the use of Nvidia cards for computing. The aim is to develop a new version of the simulation using the xsuite [**?**] library that gives the same results as the stable version. Switching to xsuite would provide greater versatility by allowing the use of any type of GPUs and CPUs thanks to the use of OpenCL as API. This change allows to run simulations on the new cluster of 400 AMD Radeon Instinct MI100 available at GSI with great computational power. The original simulation script has been developed to analyse the space-charge limit of the FAIR synchrotron SIS100 [**?**].

2 Results comparison

It is necessary to compare both codes to make sure that both give the same results. The space charge effects and lattice tracking have been analysed independently and are finally put together in one single script. This way it is easier to locate and measure the differences found.

2.1 Tracking effects

This script has as a starting point the files generated for MAD-X [**?**] that define the accelerator lattice. From these we have to import to xsuite the set of elements that represent as faithfully as possible the accelerator. Both simulation scripts have the same MAD-X files to ensure that both lattices are exactly equal. The same particle beam distribution was used in both codes, which were found to be identical before tracking.

2.1.1 Difference in the definition of the longitudinal coordinate ζ between codes

Xsuite uses from version 0.14 on-wards a ζ variable that represents the particle longitudinal position which has a different definition from the ζ found in SixTrackLib. The definition of the variables are

$$\zeta_{stl} = s - \beta ct \tag{1}$$

$$\zeta_{xsuite} = s - \beta_0 ct \tag{2}$$

where s is the absolute position in the accelerator, c is the speed of light and β represents the particle velocity divided by the speed of light while β_0 represents the reference velocity of the bunch divided by the speed of light. This change must be taken into account using the following conversion

$$\zeta_{stl} = \frac{\beta}{\beta_0}\,\zeta_{xsuite} \tag{3}$$

2.1.2 Comparison between tracking codes

The positional coordinates and moment coordinates after every lattice element in both codes have been compared to look for differences in the tracking of any element.
The figure 1 shows the difference of results in the x-coordinate of a random bunch particle over one complete revolution and the position in x of the same particle at the different points calculated by tracking. As it can be seen in the figure, the difference is negligible. The relative difference is on the order of magnitude of 10^{-30}, which is even less than double floating point machine precision, so it has been demonstrated that both codes perform equivalent tracking. The maximum difference found was 3.312×10^{-29}.

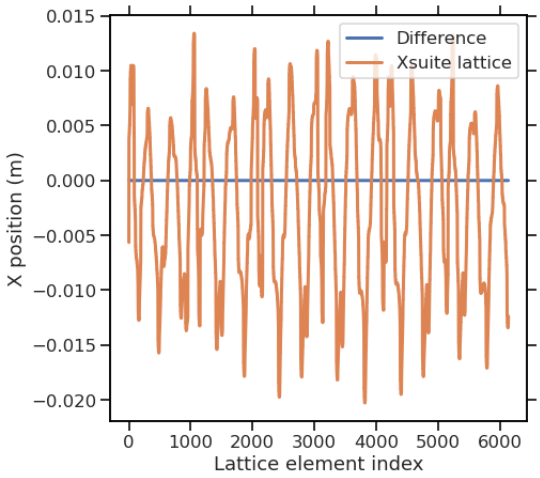

Fig. 1: *Tracking differences along the lattice*

2.2 Space charge interactions

There are different algorithms to apply the space charge effects in the simulation. These simulations use the PIC (particle-in-cell) algorithm. PIC gives results more similar to real behaviour but is more computationally expensive.

It must be taken into account that in the creation of the mesh needed for PIC algorithm PyHEADTAIL places a cell boundary at the origin where xsuite places a cell center. This generates a change in the mesh that could mean a small change in the results, especially in this testing phase where we are working with few particles to speed up the program. To remedy this we need to subtract the distance of a cell to the right in xsuite to counteract this internal effect.

With this consideration it is possible to achieve the same mesh for the calculations. This gives the same conditions to both codes. This difference in definition does not mean that one code is less reliable than the other. The fact of forcing the same mesh is to ensure that the rest of the algorithm is the same. Comparing the results the maximum difference found was $2,233 \times 10^{-06}$ which represents an error of 0.09%. This difference may be caused by the way the two codes interpolate onto the mesh but does not make a substantial difference.

2.3 Tracking and SC interactions integration

In the development of the complete final script some modifications were made to obtain a better performance. Xsuite proposes the application of the space charge interactions by the PIC method by first applying nodes of a different method and then replacing them with PIC nodes. This method also creates a node for each location which implies generating the same mesh for all nodes as many times as there are space charge nodes. This can be a waste of computational power creating many nodes replicating the same mesh multiple times.

The solution that has been proposed to this problem consists of a function that searches for the appropriate locations for each node. It then places directly on the nodes a new object that we have called SpaceChargeWrapper which contains the desired length of the SC node and the SC node object itself which is common to all. This object has a track function that changes the length of the PIC SC node and calls the track function of this object. This allows to do the usual tracking of the SC nodes with a single object for different distances. A small flowchart of all this is shown in figure 2.

3 Run times comparison

In this section the run times of both codes on different platforms are compared in order to understand in which situation it is better to use each code. It is also analysed which part of each code is the slowest.
To monitor execution times we use the python function cProfile which allows us to obtain detailed times for each function and instruction.

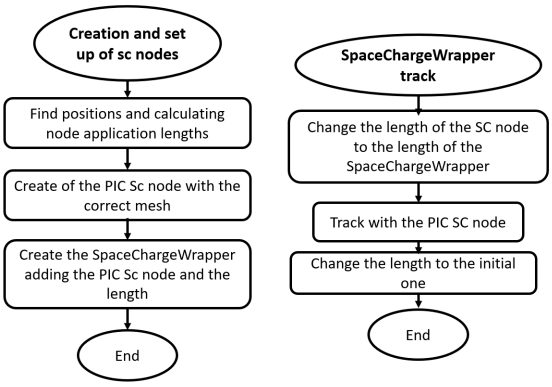

Fig. 2: *SpaceChargeWrapper creation and tracking*

3.1 Computing time of the main parts of the code

The execution times of the main functions of the code have been compared in order to find out which are the most time-consuming. It has been observed that even with a low number of turns, tracking takes most of the time. Already in a simulation of only 10 turns for a million particles and a thousand SC nodes it has been observed that in both libraries the tracking exceeds 70% of the total run time. It is most logical as a measure of the speed of the codes to focus on the time it takes for a turn around the accelerator lattice. The difference in these two time values will be noticeable in simulations with a high number of turns, where time is crucial.

3.2 Time measurement

We have obtained the times for different number of turns for each code in a set of platforms and we have seen that there is a clear linear relationship between the number of turns, as expected. From a linear fit we have obtained the time versus the number of laps so that we can compare the slope of these straight lines which represents the cost in time of a turn without taking into account the setup preparations. The slope and the R^2 of the linear fits are shown in the table below and a graphic representation is shown in the figure 3.
Simulation times as reported in Table 1 were taken for one million particles and 1000 SC nodes. The hardware devices used to obtain the results were the GPUs NVIDIA GeForce RTX 2080 Ti and the AMD Radeon Instinct MI50 as well as the CPU AMD Ryzen Threadripper 1950X. The GPUS have run the code with either CUDA or openCL while the CPU has run on a single core.

Tab. 1: *Timing linear fits*

Code - device	**Time/turn(s)**	R^2
Pht+stl - RTX	9.130	0.999
Xsuite - RTX	12.719	0.999
Xsuite - MI50	21.448	1.000
Xsuite - CPU	728.736	1.000

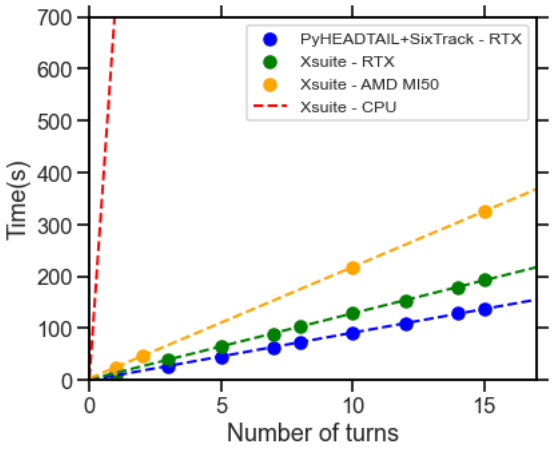

Fig. 3: *Different codes and devices timing*

As a first conclusion, GPU usage is much faster than CPU usage, as expected. This is due to the fact that the GPU allows parallelisation of computation and in the case of the type of operations needed for the simulation it is possible to take a big advantage of this.
The second point is that comparing both codes in the same device (the NVIDIA GeForce RTX 2080 Ti) the stable versión of the simulation performs better than the new xsuite one with a difference of more than 3 seconds per turn. Also the new code on the AMD MI50 gets slower results than using the Nvidia with a relatively big difference.

3.3 Timing of the difference between tracking lattice and space charge effects

The execution times of a lap on different platforms have been taken to analyse the times of the sub-processes in the different platforms. Simulation times were also taken for one million particles and 1000 SC nodes. The devices

used were the same like in the previous section, adding the GPU NVIDIA Tesla V100. The results are shown in figure 4.

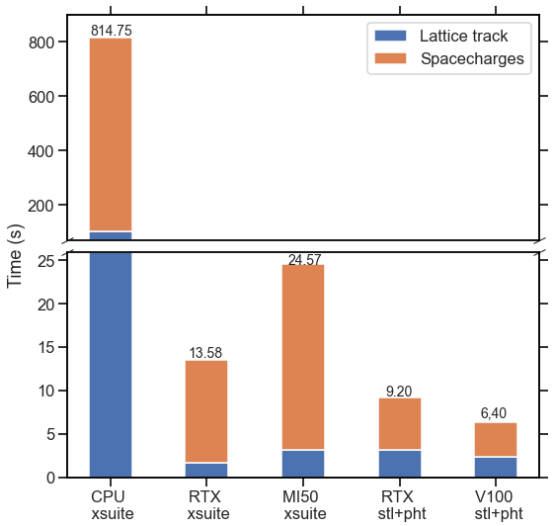

Fig. 4: *Tracking parts timing*

What can be observed in this graph is that in the case of stable code, the percentage of space charge effects time is lower than in the case of new code. This means that the xsuite space charge effects code appears less efficient than PyHEADTAIL. Furthermore, once again it is observed that AMD cards perform slower than Nvidia cards in the new code. However, the time difference is small enough that exploiting the AMD GPU cluster is still a big advantage.

4 Conclusions

The goal of establishing a new simulation script for SIS100 running on AMD GPU cards has been achieved. Using xsuite provides greater versatility and now allows to use the AMD GPU cluster at GSI for future simulation studies. However, it is clear that there is room for improvement in performance: the xsuite based script is up to a factor 4 slower on high-end GPUs when comparing to the stable version of PyHEADTAIL and SixTrackLib, especially the PIC algorithm for space charge computations.

5 Script and complementary information

The simulation script as well as the different scripts and jupyter notebooks of the main tests are available at the following github project:

https://github.com/pgarciagil/xsuite$_b$*enchmarks*$_a$*nd*$_c$*ode*

Acknowledgments

I would especially like to thank my tutor Adrian Oeftiger for all the help and time spent and for giving me this opportunity to learn and be curious about every detail. I must also give special thanks to Conrad Caliari, Dmitrii Rabusov and Vadim Gubaidulin for all the help and patience. You have made this project an even better experience. Last but not least I want to thank my partner Thiti Aungcharoen for all the support. I will never forget this great experience.

Treatment planning on a mouse microCT with stable and radioactive carbon ion beams

Itzel Viridiana González Badillo
National Autonomous University of Mexico, itzel.gonzalez@ingenieria.unam.edu

The clinical outcomes of particle therapy can be enhanced by image guidance techniques with positron emission tomography (PET) that can reduce the errors associated with range predictions. However these techniques are limited since ^{12}**C** *is not a* β^+ *emitter, but the signal is generated by a fraction of its fragments, leading to low intensity signals to be detected. Therefore,* β^+ *emitter beams and their preclinical application are being studied within the BARB project, which benefits from the intensity upgrade of the SIS-18 synchrotron and using a fragment separator FRS in the FAIR in Darmstadt to produce a secondary* ^{11}**C** *beam from a standard* ^{12}**C** *beam, so different characteristics are expected. Since the BARB aims to treat animals in the next years, it is necessary to have a proper realistic beam description for treatment planning. In this work, the* ^{11}**C** *beam data, including the dose-depth distributions and spectra files are calculated with FLUKA Monte-Carlo simulation for energies corresponding to a range in water from 80 to 220 MeV/u with a 3 mm ripple filter. Subsequently, the treatment plans using both* ^{11}**C** *and* ^{12}**C** *beams are simulated with TRiP98 for a study mouse micro computed tomography (microCT). This is a first attempt of treatment planning with a radioactive beam on a microCT to get a first impression on the dose distribution in the upcoming experiment on the animal back tumor treatment.*

1 Introduction

Radiotherapy is the best treatment for cancer only after surgical resection, which can be discarded if the tumor is considered inoperable mainly due to the presence of critical organs in its proximity. Heavy ions have shown a remarkable performance compared to photons because of their favorable depth-dose profile: the Bragg Peak. This implies a much higher dose deposit just before stopping, which is used to set the favorable energies to cover the tumor avoiding as possible the surrounding tissue.

Nowadays, the number of heavy ion radiotherapy facilities is increasing since the use of protons or carbon ions offer great physical advantages for treating tumors [3,8]. Their main benefit is the decreased lateral scattering and the increased relative biological efficiency (RBE) by up to a factor of 3, which makes them better suited for treating more radioresistant, e.g., hypoxic tumors [8].

Image guidance radiotherapy delivery systems with positron emission tomography (PET) represent a major improvement since it helps to overcome the problem of range uncertainties by monitoring the dose delivery. These uncertainties are mainly associated with the conversion of the patient CT in Hounsfield Units to water-equivalent path lengths (WEPL). Other factors affecting the ranges such are the CT quality and physiological changes such as inflammation, accumulation of gas, fluids, etc. In other words, these systems aim to ensure the delivery of prescribed dose to the whole target volume. [7]

A direct β^+ emitting beam enhances the signal increasing it by an order of magnitude and shall also reduce the shift between measured activity and dose and mitigate the washout blur of the image with short-lived isotopes and in-beam acquisition, eventually leading to sub-mm resolution. In figure 1 is noticeable that the peak in the activity from the isotopic projectile fragments is visualized upstream of the Bragg peak, because such fragments, lighter than the projectile, have shorter ranges at the same velocity of the primary ion [2].

After the successful pilot project with pa-

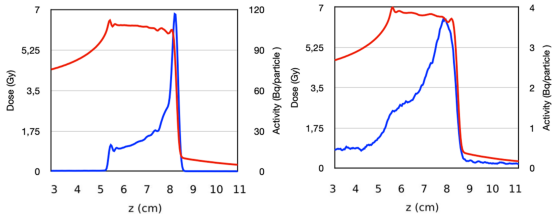

Fig. 1: *Dose (red curve) and activity (blue curve) distribution along the beam for ^{11}C (left) and ^{12}C (right) showing the shift between dose and activity when stable ions are used. [2]*

tients in GSI (Darmstadt, Germany) from 1997 to 2008, nowadays the project Biomedical Applications of Radioactive ion Beams aims to study the performance of a β^+ emitting beam on image guidance techniques with PET. The β^+ emitting beams extraction is possible following the upgrade of the intensity of the SIS-18 synchrotron, using a fragment separator FRS in the FAIR, an active beam scanner and a spherical setting of detectors for a mouse in Cave M. [2]

The final goal of the BARB is to set a treatment of an animal tumor with radioactive beam with a reduced margin. This is the motivation to set a base data describing the characteristics of this secondary, non-standard ^{11}C beam and thus make a first attempt treatment plan in a mouse geometry acquired with a µCT.

2 Methods

The general sequence to achieve the mouse microCT radiotherapy treatment planning was the following.

1. Production of ^{11}C base data in terms of depth dose distributions and energy dependent fragment spectra at different depth in water with FLUKA Monte-Carlo simulations. [1, 9]. The parameters used for producing these base data were measured in previous experimental campaign.

2. Hounsfield lookup table rescaling for the microCT measurements.

3. Tumor and spine segmentation in 3D Slicer [4].

4. Radiotherapy planning with TRiP98 [5] with the above described ^{11}C and the standard clinically validated ^{12}C beam models with similar plan parameters (target contours, beam angle, optimization requirements).

For the beam calculation in FLUKA, a set of energies corresponding to a range in water from 80 to 220 MeV/u with a step of 10 MeV/u were considered as well as capabilities of GSI facility: a full width at half maximum of 12 mm for the ^{11}C beam and 5 mm for ^{12}C. A comparison between the beam-spot sizes and depth dose distribution for the used ^{11}C and ^{12}C beam used in this study are shown respectively in figures 2 and 3.

Following the standards of TRiP98, for every primary beam energy, the energy dependent fragment spectra have been calculated at 77 depth in water [6], essential for the dose plan optimization, specially the biologically-weighted one. These parameters were measured in previous experimental campaign. A Ripple Filter (RiFi) of 3 mm is implemented in order to slightly broaden the Bragg peak to ensure a more homogeneous dose distribution in the target.

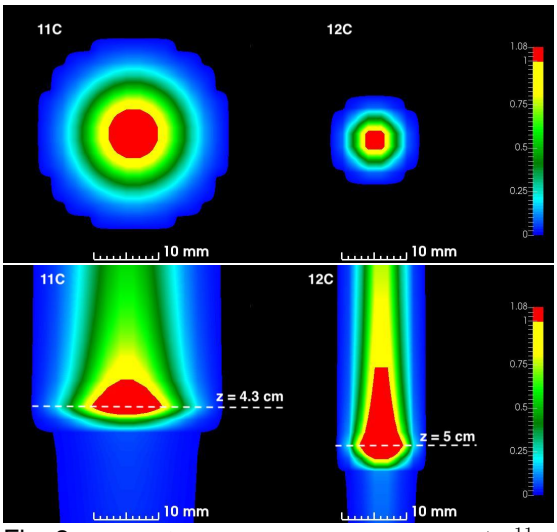

Fig. 2: *Top: Axial view of the 150 MeV/u ^{11}C (left) and ^{12}C (right) pencil beams. Bottom: sagittal view of the ^{11}C (left) and ^{12}C (right). Dashed lines indicate the positions of the respective Bragg peaks. The colorset describes the relative dose deposited by the beam.*

Since the patient of study is a mouse of approximately 3 cm region scanned with a microCT (micro computed tomography), it is important to account the differences in the

Hounsfield units for the soft tissues, organs and bones between the microCT and clinical patient CTs. Therefore a new lookup table was produced by scaling the existing TRiP table (see table 1). The WEPL (water equivalent path length) and Mouse columns were used as actual entries for the mouse treatment planning.

Tumor and cervical region of the spine were considered, since the second one is an organ at risk. These volumes were manually and threshold segmentation contoured respectively with 3D Slicer. The general treatment setting used in TRiP98 is one field orthogonal to the target for a physical dose of 3 Gy. This same treatment was optimized for both ^{11}C and ^{12}C beams.

Tissue	Human	Mouse	WEPL
Air	-1000	-1000	0.001
Lung	-798	-798	0.244
Lung	-750	-750	0.297
Fat	-108	-108	0.943
Fat	-75	-75	0.977
Water	0	0	1
Brain	32	83	1.033
Liver	55	130	1.049
Liver	67	170	1.065
Bone	262	700	1.095
Bone	1974	5500	1.778

Tab. 1: *Hounsfield lookup table produced to account the tissue differences between the mouse microCT and clinical patient CTs.*

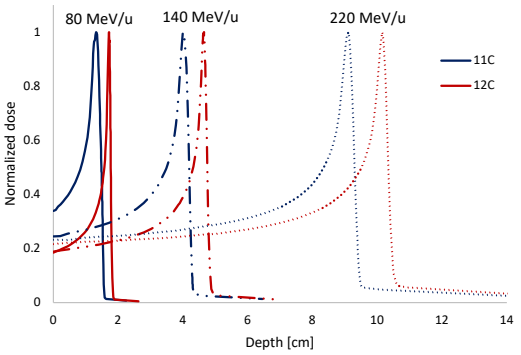

Fig. 3: *Normalized depth-dose distributions for ^{11}C and ^{12}C of 80, 140, and 220 MeV/u in water. The different momentum spread in the case for the ^{11}C and ^{12}C causes an additional enlargement of the Bragg peak to the one caused by the RiFi.*

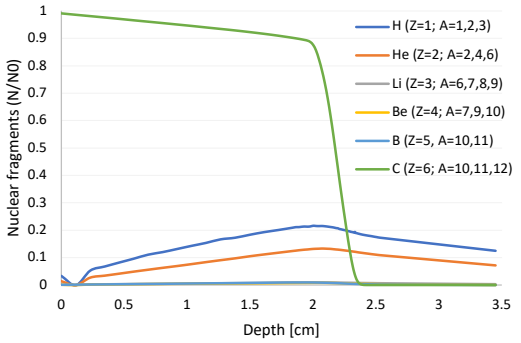

Fig. 4: *Buildup of secondary fragments produced by 100 MeV/u ^{11}C beam slowing down in water. The data is produce with FLUKA Monte-Carlo simulation.*

3 Results

3.1 Beam calculation using FLUKA

The FLUKA results represent a useful basic repository for setting the ^{11}C beam. Figure 3 compare the water depth dose distribution curves for 3 energies with both beams and figure 4 shows the fluence of primary ^{11}C beam at 100 MeV/u as a function of the depth in water. The different momentum spread in the case for the ^{11}C and ^{12}C causes an additional enlargement of the Bragg peak to the one caused by the RiFi; 0.94% in the case of ^{11}C and nominally less than 0.01% for ^{12}C.

3.2 Treatment planning on a mouse microCT

Both plans were optimized for the physical dose of 3 Gy. The resulting raster files contain 7 energies for each ion, in the ranges of 92 to 105 Mev/u for ^{12}C and 101 to 108 MeV/u for ^{11}C. The total numbers of particles are 6.5×10^7 ^{12}C and 1.5×10^8 for ^{11}C. In the actual experiment the doses will be higher (10 or 15 Gy) and thus to give the estimation of the irradiation time, the respective numbers of particles can be scaled. Assuming the planned dose of 15 Gy and 1×10^7 particle per second for the ^{11}C and 1×10^8 particle per second for the ^{12}C, the delivery time will be 75 s and 3.25 s respectively.

A sagittal view of the dose distributions of ^{11}C and ^{12}C on a mouse back (black contour)

are shown in figure 5 and a dose-volume histogram comparison is shown in figure 6. It is important to remark the small size of the patient.

The results confirm the functionality of the beam simulation. With the same plan settings, the dose distribution of ^{11}C, being comparable to the one of ^{12}C, is slightly less homogeneous in the target area and extends further laterally. The latter fact might lead to the stronger damage to the spinal cord; however, it can be protected during the actual experiment.

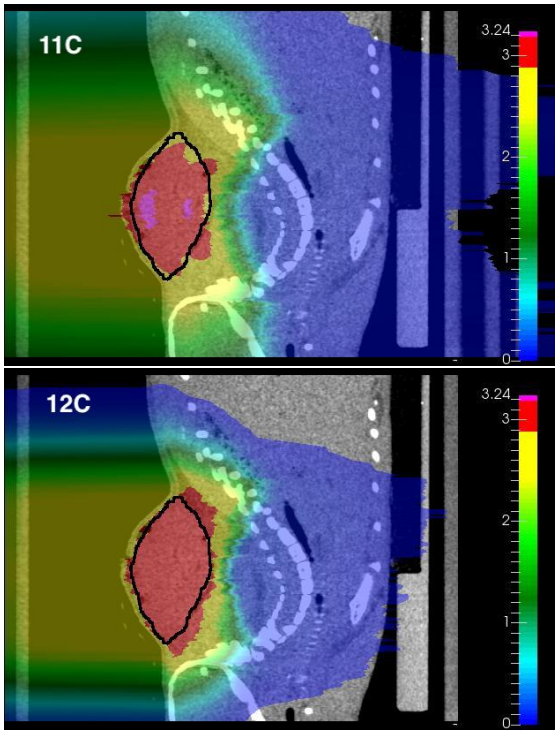

Fig. 5: *Sagittal view of the treatments with ^{11}C (top) and ^{12}C (bottom), color-scale for the deposited dose in MeV/u. The black contour represents the tumor, which is located on the back of the animal.*

4 Conclusions

The new base data produced for ^{11}C beams for the GSI settings was successful as well as the first attempt of treatment planning for a small mouse tumor, since it provides relevant information plan the required field size and the dose distribution in both the target and the spinal cord, which will be tried to be spared by adding a bolus or compensator to the back of the mouse to limit the field only to the tumor area.

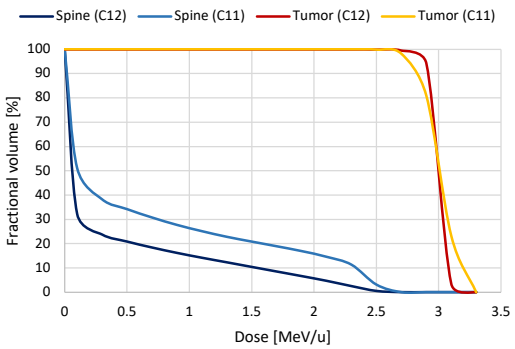

Fig. 6: *Dose volume histogram comparison for the ^{11}C and ^{12}C treatment plans optimized on a mouse microCT. Data is shown both for the tumor and the spine (organ at risk).*

5 Future work

These plans were optimized assuming the same tumor contours for both ions. In the BARB the experiment, the tumor contours will be slightly expanded for ^{12}C plans, assuming the ranges cannot be monitored precisely and thus need some safety margin for that to ensure the uniform tumor irradiation.

Acknowledgments

I would like to thank my tutor Marco Durante for giving me the opportunity to take part in this Summer School in the BARB, and my supervisors Olga Sokol and Daria Boscolo for their caring, close support. It is a wonderful experience to learn from such wise people in an incredible work climate where the commitment and love for their activities is evident and contagious.

Last but not least, I would like to thank my home university tutor Antonio Ortiz for giving me the opportunity to lead the Particle Therapy Masterclass in my Mexico City and Paolo Giubellino, for encouraging me to apply to this wonderful program in GSI.

References

[1] Giuseppe Battistoni et al. “Overview of the FLUKA code”. In: *Annals of Nuclear Energy* 82 (Aug. 2015), pp. 10–18. ISSN: 0306-4549. DOI: 10.1016/J.ANUCENE.2014.11.007

[2] Daria Boscolo et al. “Radioactive Beams for Image-Guided Particle Therapy:

The BARB Experiment at GSI". In: *Frontiers in Oncology* 11.August (2021), pp. 1–15. ISSN: 2234943X. DOI: 10.3389/fonc.2021.737050.

[3] Particle Therapy Co-Operative Group. *Particle therapy facilities in clinical operation (last update: (August 2022)*. 2022. URL: https://www.ptcog.ch/index.php (visited on 09/01/2022).

[4] Ron Kikinis, Steve D. Pieper, and Kirby G. Vosburgh. "3D Slicer: A Platform for Subject-Specific Image Analysis, Visualization, and Clinical Support". In: *Intraoperative Imaging and Image-Guided Therapy* (2014), pp. 277–289. DOI: 10.1007/978- 1-4614-7657-3$_1$9.URL : $https$: $//link.springer.com/chapter/10.1007/978 - 1 - 4614 - 7657 - 3$

[5] M. Krämer et al. "Ion beams in radiotherapy - From tracks to treatment planning". In: *Journal of Physics: Conference Series* 373 (2012), pp. 1–9. ISSN: 17426596. DOI: 10.1088/1742-6596/373/1/012017.

[6] K. Parodi et al. "Monte Carlo simulations to support start-up and treatment planning of scanned proton and carbon ion therapy at a synchrotron-based facility". In: *Physics in Medicine and Biology* 57.12 (2012), pp. 3759–3784. ISSN: 13616560. DOI: 10.1088/0031-9155/57/12/3759.

[7] Katia Parodi. "PET monitoring of hadrontherapy". In: *Nuclear Medicine Review* 15.SUPPL.C (2012), pp. 37–42. ISSN: 15069680.

[8] Walter Tinganelli and Marco Durante. "Carbon Ion Radiobiology". In: *Cancers* 12.10 (Oct. 2020), pp. 1–43. ISSN: 2072-6694. DOI: 10.3390/CANCERS12103022. URL: https://pubmed.ncbi.nlm.nih.gov/33080914/.

[9] V. Vlachoudis. "Flair: A powerful but user friendly graphical interface for FLUKA". In: *American Nuclear Society - International Conference on Mathematics*, Computational Methods and Reactor Physics 2009, M and C 2009 2 (2009), pp. 790–800.

Pressure and temperature logging and control systems for SHIPTRAP

Briain Drew Hartigan
University of Groningen, b.d.hartigan@student.rug.nl

For high-precision mass measurements of heavy nuclei at the SHIPTRAP mass spectrometer, monitoring and controlling of parameters such as temperature and pressure are required. In this work several applications were designed which monitor vacuum and temperature, and control gas flow and heating power. Data storage was migrated to a time-series database to facilitate the monitoring of these parameters.

1 Introduction

Precision mass measurements with uncertainties on the order of 10^{-7} to 10^{-10} can provide information on the nuclear shell structure of atomic nuclei or inputs to nucleosynthesis calculations among other motivations [1]. Penning traps are one such tool that can be used to measure the mass of short lived isotopes with $t_{\frac{1}{2}} \approx 0.1$ s [2]. At GSI/FAIR in Darmstadt the mass of superheavy elements such as ^{257}Rf, which can only be produced in fusion-evaporation reactions, can be measured using the mass spectrometer SHIPTRAP. SHIPTRAP is located downstream from the in-vacuum separator SHIP, which separates the fusion-evaporation fragments produced from the interaction of a wheel target and an ion beam from UNILAC. The selected ions from this interaction are then transported to a cryogenic buffer gas cell where they are slowed from MeV to eV energies. From there the ions are extracted through a nozzle, using the fast gas flow and a radiofrequency quadrupole (RFQ). The ions are then sent to a purification Penning trap where the background can be further reduced before finally being sent to the measurement Penning trap.

A Penning trap is a series of electrodes defining a 3D quadrupolar electrostatic potential. Combined with a homogeneous magnetic field usually generated by by a superconducting coil kept below T_{crit} using a liquid helium bath to confine ions axially and radially. The ions perform a periodic motion whose frequency is

$$\nu_c = \frac{1}{2\pi}\frac{q}{m}B. \tag{1}$$

Here q is the charge of the ion, m is its mass and B is the applied magnetic field. Therefore, measuring the cyclotron frequencies of the ion of interest (IoI) and a reference ion (Ref) with a well-known mass enables the determination of the ion of interest's mass with a very high precision, since

$$\frac{\nu_c^{Ref}}{\nu_c^{IoI}} = \frac{q_{Ref}m_{IoI}}{q_{IoI}m_{Ref}} \tag{2}$$

When the Penning trap's electrostatic field is added, the resulting motion can be expressed as a combination of three independent components: two in the radial plane and one in the axial direction as depicted in figure 1. If the alignement of the magnetic and electric fields are almost perfect ν_c can be oTTained using the sum of the frequencies of the two radial motions [3]:

$$\nu_c = \nu_+ + \nu_-.$$

To determine the mass of isotopes to a high precision a technique known as phase-imaging ion-cyclotron resonance (PI-ICR) has been developed in the last decade and makes use of the above relation. PI-ICR measurements use a position sensitive detector placed outside of the magnetic field; this detector images the position of the trapped ion at the time of ejection. By ejecting the ion at different times the phase acquired can be measured, allowing for the respective motional frequency to be calculated [2]. A requirement for mass spectrometry using Penning traps is that the magnetic field must be

stable during the course of the measurements. The magnetic field intensity is sensitive to environmental conditions. For example, the frequency of the reference ion ^{133}Cs can vary by about 200 mHz/K with the trap temperature and by 8 mHz/mbar with the liquid helium vessel's pressure. Therefore, stabilisation of these parameters is required to attain the required precision. In contrast to other facilities, SHIPTRAP has rather long measurement campaigns, with single measurement campaigns lasting several hours.

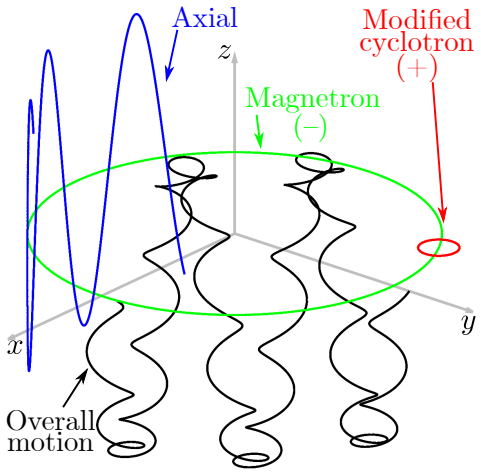

Fig. 1: *The path of the ion is shown in black. The motion consists of three independent components, shown in red, blue and green. Using appropriate burst of RF an independent component can be probed [1]*

This is due to the extremely low production cross-section of the heaviest nuclei, and leads to the daily fluctuations of environmental parameters being a significant source of measurement error. To mitigate this, previous works have implemented a PID temperature control system, reducing the magnet temperature fluctuations to ±10 mK [4].
The purpose of this project was to create several applications that would log and control some of the various pressure gauges, flow controllers and temperature probes. In particular the trap temperature stabilisation system of SHIPTRAP was redesigned to improve stability. In addition the data logging system was migrated to an InfluxDB database.

2 Methodology

2.1 InfluxDB

InfluxDB is an open source time-series database. It allows for the collection, storage, processing and visualisation of time-stamped data. The timestamped data is stored in a bucket, which is a data container with a set retention period. Each data point is labeled using tags, which are indexed to improve searching performance [5]. An advantage of InfluxDB is that it stores information so that it is easily searchable, and its retention policy ensures that the data can be downsampled and deleted appropriately.
Once the data has been stored an interactive visualisation web application such as Grafana can query the database and then display the data. Correlations between PI-ICR measurements and experimental parameters can then be easily identified.

2.2 LabVIEW

LabVIEW is a graphical programming software that has a multitude of functions to log data and allow for the easy interaction of physical devices [6]. Instead of traditional text coding functions, it makes use of objects called Virtual Instruments (VIs). Each VI has a certain function. These VIs are connected together in a block diagram to visually design systems and objects that can be interacted with. The created objects, such as indicators, graphs, and controls are interacted with via the User Interface (UI). The code can be executed directly as an interpreted language would, or compiled into an executable. Devices were connected through a General Purpose Interface Bus (GPIB) or a serial port. Functions from several instrument libraries were then used to send/interpret signals to/from the different devices .
Two VIs had been previously made by the SHP group specifically for using InfluxDB. One to convert the readings received from the various instruments into an InfluxDB friendly format and another to group and send the readings to the database. The OpenG Library was used within these VIs.

3 Results and discussion

3.1 Vacuum monitoring and gas flow control

Two separate applications were designed; one for monitoring the vacuum at various sections of the experiment and another to control the gas flow at various points of the setup. Vacuum monitoring (VM) is performed using several different pressure gauges (depending on vacuum conditions) connected to one of three Pfeiffer TPG 256 Maxi Gauges. This Maxi Gauge communicates with the computer using a serial port.
The designed LabVIEW application can communicate with any of these Maxi Gauges and sends the pressure values from the appropriate pressure gauge to the InfluxDB database. The name of the pressure gauge being monitored can be selected using a drop down menu, as seen in figure 2. If there are issues no value will be sent to the database and a message will appear notifying the user of the error code and meaning. By default values are collected and sent to the database every 3 s. A fast acquisition option can be activated e.g. during pumping or gas injection, which will send information to the database every 0.5 s.

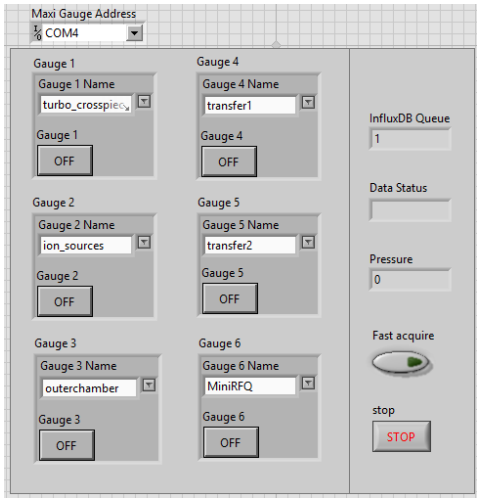

Fig. 2: *UI of the VM application. The name of the pressure gauge can be selected and monitoring is turned on using a button.*

Gas flow to various parts of the system is controlled using several Pfeiffer RVC 300 flow controllers. An application was designed using an event structure, to handle several commands that could be sent to the flow controllers. These commands are 'read actual flow', 'set flow to x mbar' and 'stop gas flow'. In figure 3 the UI of the application can be seen. The name of the flow controller (indicating its location) can be chosen and a maximum flow rate should be selected. This is to ensure that accidental changing of the gas flow rate won't result in damage to the experiment. The actual flow rate value is sent to the database.

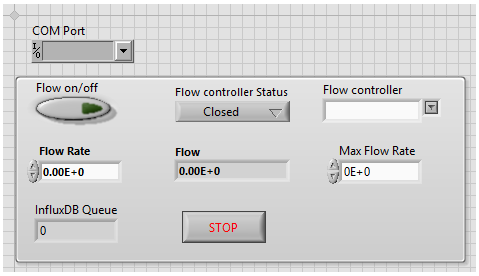

Fig. 3: *The UI of the gas flow control application. A flow and maximum flow limit can be set, and gas flow can be turned off using a button.*

3.2 Temperature monitoring and control

The trap Temperature (TT), environmental temperatures, and the pressure of the liquid helium are monitored using a Keithley 2700 multimeter. The TT is stabilised using a heater attached to a Keithley 2303 power supply, and a PID. Similar to the pressure logging and flow control system, two applications were designed for temperature monitoring and control. These two applications run in parallel, with the temperature monitoring (TM) application sending TT values to the temperature control (TC) application.

The TM application (figure 4) checks the TT, environmental temperatures and liquid helium

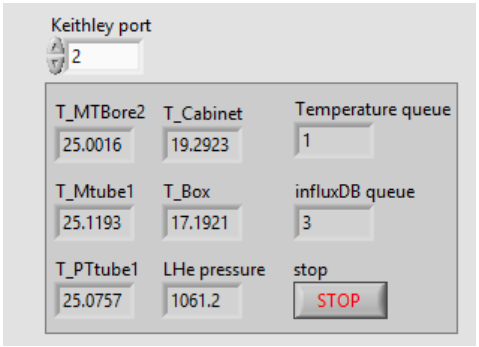

Fig. 4: *UI of the TM application for the superconducting magnet.*

pressure over 8 s, and queues the TT values to be read by the TC application. It sends all of the collected values to the InfluxDB database.

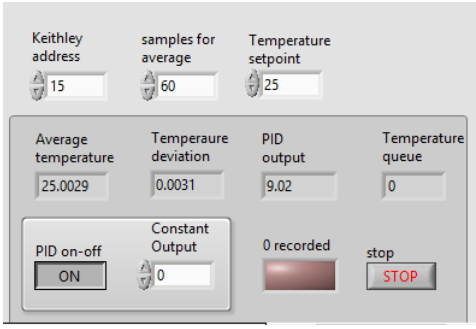

Fig. 5: *UI of the TC application for the superconducting magnet.*

Once the TT values have been sent to the TC application, they are added to a running average. This running average is continuously fed into a PID function which adjusts the voltage to ensure that the system remains at a temperature set by the user. Using a running average reduces the effect of instrument noise. Looking at figure 5 there is also an option to turn off the PID and set the voltage provided to the heater to a constant value.
Testing over a 6 hr period shows a trap temperature stability of ± 10 mK as can be seen in figure 6. Several errors from the previous control system concerning starting of temperature control, storage of data and warning messages from the power supply were solved, improving the system stability. Some possible improvements to the application could be implemented, such as shortening the VM stopping time or making a more straightforward method to turn off the TC heating.

4 Conclusion and future outlook

Monitoring and control of the environmental and systematic factors of SHIPTRAP are crucial for precise mass measurements of the low production yield ions. The vacuum throughout the system can now be easily monitored using InfluxDB, as well as the temperature of the superconducting magnet. The gas flow into the different parts of the setup can now be remotely controlled and monitored, and the temperature of the superconducting magnet is well stabilised. In the future, the ion position and time-of-flight to the detector could also be stored in the InfluxDB database. This would make it easier to verify the measurement conditions and to check for correlations.

Acknowledgments

I would like to thank Manuel Gutiérrez for his support and guidance during this project. Due to a missing appendix, this article would not have been completed without his help. I would also like to thank Francesca Giacoppo and the RADRIS team for the help and our conversations in the lab. Finally, I am grateful to everyone who participated and organised the summer school for making this amazing experience.

References

[1] J. Dilling et al, *Annu. Rev. Nucl. Part. sci.* **68**, 45-74 (2018)
[2] S. Eliseev et al, *Appl. Phys* B **114**, 107-128 (2014)
[3] G. Gabrielse, Int. J. Mass Spectrom. 279, 107 (2009)
[4] C. Droese et al, *Nucl. Instrum. Methods Phys. Res.* B **632**, 157-163 (2011)
[5] InfluxData, *InfluxDB* v**2.1**, https://docs.influxdata.com/InfluxDB/v2.1/ [accessed: 06-09-22]
[6] National Instruments, *LabVIEW SP1* 2019, https://www.ni.com/nl-nl/shop/labview.html [accessed: 06-09-22]

Fig. 6: *Realtime visualisation of the TT , PID output voltage, environmental temperatures and the liquid helium pressure over a 6hr period using Grafana.*

template.aux

Setup for the Radioactive Sources Characterization

Yonatan Kehat
Tel Aviv University, keaht.yonatan@gmail.com

The FRS Ion Catcher group in GSI Helmholtz institute is known for it's high resolution radioactivity measurements using their precise detecting procedure. In order to carry out these precise measurements there is a need for an independent measurement outside the procedure to get a good estimation for the measured quantities involved. This report outlines the measurements of the isotope ^{148}Gd in a different setup before placing it in the precise detecting procedure facility.

1 Introduction

The FRS Ion Catcher experiment in GSI Helmholtz institute specializes in high accuracy mass and radioactivity measurements, from both beam lines and static radioactive sources. For the purpose of beam line measurements, the setup of the system includes a stopping cell which contains high pressure Helium and stops the incoming ions of the beam by collisions between the ions and the Helium molecules. This procedure allows a precise mass and activity measurements for the ions that comes from the beam line. Since the static radioactive sources are placed in the stopping cell as well, there is a certain amount of chemical loss for the radioactive yields due to paring to the Helium or to other gasses that accidentally happened to be in the cell. In order to account for these losses, and other ones which are not mentioned here, we need to have a precise independent measurement of the sources before placing them in the stopping cell. The following measurements of ^{148}Gd were done in a different setup before more accurate measurements carried out in the stopping cell. The properties of the different setup are detailed in the following section.

2 Experimental Setup

The experimental setup consists of 2 Vacuum pumps, vacuum chamber, silicon detector, amplifier, an oscilloscope, a multichannel buffer and the Maestro interface program. A sketch of the system is presented in figure **??**.

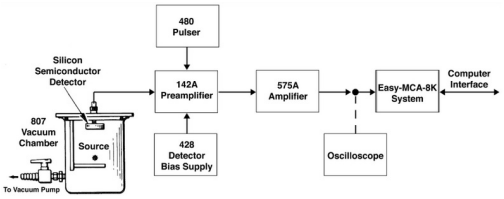

Fig. 1: *Sketch of the system*

The vacuum operation consist of the following pumps: an Agilent IDP3 Pump and Pfeiffer TCP Turbo Pump. The vacuum pumps induced a pressure of 10^{-6}_{mbar}, in order to reduce the background noise inside the chamber as much as possible. The vacuum chamber was used to hold the source and the detector in a constant distance for the entire time of each measurement. That was done using the upper part of the chamber, as shown in figure **??**. There were three different heights for the entire experiment: 5 cm for the calibrators measurement, 10.6 cm for the first measurement and 2.5 cm for the second measurement. The silicon detector that was used was placed on top of the vacuum chamber and was used to detect the alpha particles coming from the source. The silicon detector was connected to the ORTEC142 Amplifier which was connected to the ORTEC 926 ADCAM Multichannel Buffer from the other side. The MCB was connected to the Maestro Program that was installed on the computer which functioned as the interface of the data acquisition procedure. The energy resolution of the detection was about $\approx 10_{keV}$. During the measurements

95_V bias voltage was used for the silicon detector. A broader explanation about the way of operation and detection of the silicon detector could be found in [**?**].

3 Data Analysis

3.1 Calibration

Before the measurements of the ^{148}Gd a calibration measurement was done. The calibrators that were used and their suitable alpha particle energy are detailed in table **??**. The calibration was done by the Maestro program as it assumes a linear relation between the silicon ionization voltage of the detector and the energy of the in coming alpha particles:

$$E = a \cdot channel + b \tag{1}$$

Where channel is a standard name for the value of the voltage of the detector. In order to verify the calibration of the system, firstly only 2 calibrators were set to the appropriate energy values, which decides a certain a and b parameters for the linear relation between the energy and the channel from Eqn. **??**. Afterwards the energy value of the third calibrator's peak was examined. After achieving a good calibration of at most 1% error for the third calibrator's peak, the calibration measurement was finished and system assumed as calibrated.

Isotope	Emitted Alpha Energy [keV]
$239Pu$	5156
$241Am$	5485
$244Cm$	5804

Tab. 1: *Alpha energies for 3 alpha calibration source*

3.2 Energy Measurement Analysis

After calibrating the system the measurements of the ^{148}Gd source has started and the energy peak of the ^{148}Gd was examined to make sure the appropriate alpha kinetic energy is witnessed. From prior database given in [**?**] the ^{148}Gd value is $Q_\alpha = 3271\,\text{keV}$. according to that the expected alpha kinetic energy was calculated:

$$E_{\alpha the} = \frac{q_\alpha}{1 + \frac{m_\alpha}{m_{Gd}}} = 3182\,\text{keV} \tag{2}$$

The experimental value of the alpha particle kinetic energy was witnessed directly from the Maestro program after the calibration measurement was done successfully.

3.3 Activity Measurement Analysis

The value of the activity of the ^{148}Gd source was given by the manufacturer with the value of $A_{manu} = 4.318\,\text{kBq}$ From that value and the activity loss of the ^{148}Gd source the expected value of the activity measurement was calculated:

$$\lambda(t) = \lambda_0 \exp^{-\lambda_0 t} \tag{3}$$

Where $\lambda(t)$ is the activity of the source after time t and λ_0 is the activity at time 0. After placing the appropriate numbers from Eqn. **??** we got the expected value for the activity:

$$\lambda_{the} = 4.135\text{keV} \tag{4}$$

The detector was considered to have 100% efficiency, as stated in [**?**], so the only efficiency that was considered for the activity measurement of the ^{148}Gd source was the geometrical one. In other words, in purpose of calculating the entire activity of the ^{148}Gd source two steps were taken. Firstly, the activity for a certain solid angle covered by the detector was measured. Secondly this value was divided by probability of the alpha particles to arrive in this specific solid angle. The probability distribution for an alpha decay assumed to be isotropic so the efficiency was calculated by the simple equation:

$$\eta_i = \frac{\theta_i}{4\pi} \tag{5}$$

Where θ is the solid angle calculated for each measurement separately. From that value for the geometrical efficiency the experimental activity of the source was calculated:

$$\lambda_{exp_i} = \frac{cps}{\eta_i} \tag{6}$$

Where cps stands for counts per second measured by the detector and i takes the values 1 and 2 for each measurement separately.

3.4 Error Analysis

The errors that were accounted for in the experiments has two parts:

a. The error of the counts per second
b. The error for the solid angle

The first error is coming from the miss or over counts by the data acquisition procedure. This error was calculated by The Maestro program and is noted here as Δcps. Further details about this error calculation can be found in [**?**].

The second error is due the calculation of the solid angle that is used for the activity calculation. The solid angle calculation assumed a point source where in fact the source is a circular source with a 5mm diameter. In order to account for this error a simulation was done in the Giant4 program. The simulation simulated 10^6 events of alpha particles coming from the 5mm diameter circular source with uniform distribution, to a 10mm diameter circular detector for the 2 different distances of the 2 measurements. The errors for the 2 measurements were taken from this simulation and their values were:

$$\Delta\theta_1 = 1\% \tag{7}$$

$$\Delta\theta_2 = 7\% \tag{8}$$

The total error of the activity measurements was calculated using Eqn.(**??**,**??**,**??**) by the following calculation:

$$\Delta\lambda_{exp} = 4\pi\sqrt{\left(\frac{\Delta cps}{\theta}\right)^2 + \left(\frac{cps\Delta\theta}{\theta^2}\right)^2} \tag{9}$$

4 Results

4.1 Calibration

Before the calibration, 3 alpha source was measured by the voltage of the detector, the results are shown in figure **??**. After getting reasonable measurements a linear fit was performed according the procedure explained in subsection 3.1. The linear fit was made by the two right peaks which assumed to be the isotopes: $241Am$ and $244Cm$, and afterwards the calibration of the left peak was examined, namely $239Pu$.

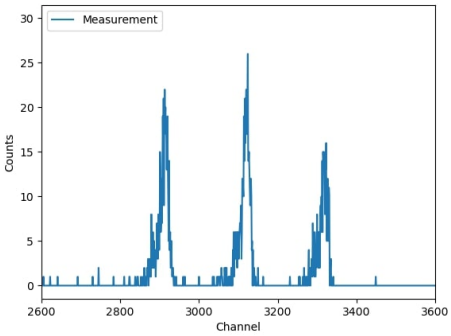

Fig. 2: *Before calibration: 3 alpha source*

The linear fit of the first two calibrators yield the following relation between the channel and the energy of the alpha particles:

$$E_\alpha = 1.6 \cdot channel + 268 \tag{10}$$

From that result the accuracy of the third peak was examined. The energy difference between the examined peak and the known value from table **??** were $\approx 0.1\%$ and from that point on the system was considered calibrated.

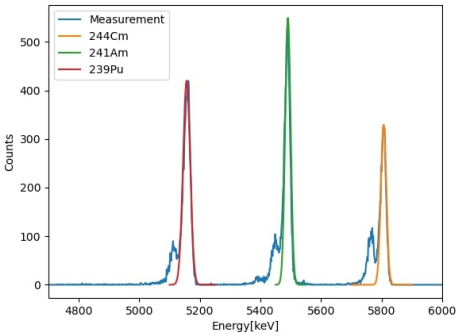

Fig. 3: *After calibration: 3 alpha source*

4.2 148Gd Measurements

After calibrating the system two measurements were taken. The first for $d = 10.6$ cm and the second for $d = 2.5$ cm, each measurement lasted 5000sec and a Gaussian fit was made for each one. The energy of the alpha particles for each measurement were taken from the Gaussian fit and the activity outcome was calculated using Eqn. **??**.

For the first measurement the results are presented in figure **??**. the value for the energy was 3183 keV, meaning less then 0.1% then theoretical one calculated from Eqn.**??**.

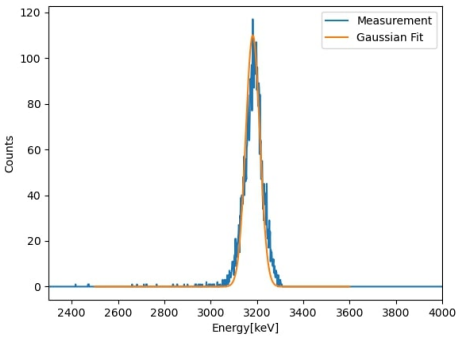

Fig. 4: *First measurement of the 148Gd source, with distance* 10.6cm

The outcome for the activity:

$$\lambda_{exp1} = 3.63 \pm 0.040\text{kBq} \tag{11}$$

With relative errors of:

$$\frac{\Delta\lambda 1}{\lambda 1} = 1.1\% \tag{12}$$

For the second measurement the results presented in figure **??**. The calculations for the required quantities were exactly similar to the first measurement. The value of the energy peak yield 3200 keV which is less than 1% difference from the theoretical value. For the activity the result was:

$$\lambda_{exp1} = 3.45 \pm 0.340\text{kBq} \tag{13}$$

With relative error of:

$$\frac{\Delta\lambda 1}{\lambda 1} = 10\% \tag{14}$$

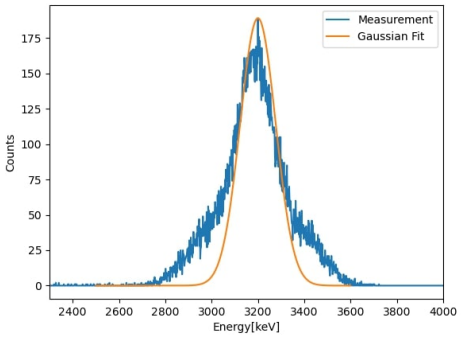

Fig. 5: *Second measurement of the 148Gd source, with distance* 2.5cm

4.3 Discussions and outlook

The second measurement was taken mostly in order to see the behavior of the resolution and the errors grow relatively to the first measurement. It is indeed behaves as expected. we can also see that the fit is worse then the first measurement. The cause for that is probably the error of the solid angle which is much larger for this measurement. Another indication for the consistency of the results are the values of two activity measurements. they are within error bar of each other, which means that they verify the value we got for the activity of the source. After the expected behavior of the two measurements was achieved, the value of the first measurement was considered the final outcome of the experiment.

Another important result to notice is the relative errors. The relative errors of both the cps and the solid angle were very small, around 1%. Therefore the activity also had a relative error of the same order of magnitude. That lead to the conclusion that there was an under estimation of the errors along the experiment. The under estimation of the solid angle is more probable to be higher because than the cps error which is determined by the Maestro program which is reliable.

Although the results of both measurements are consistent, further investigations must be done in order to verify the activity of the ^{148}Gd source since there is a gap of $\approx 8\sigma$ between λ_{the} and λ_{exp}. The difference is an outcome of either the detector damaged, the source is damaged or the activity of the manufacturer is wrong. For the purpose of deeper and more precise study of the ^{148}Gd isotope in the stopping cell, further investigations should include activity measurement of a well known source with the same setup. In that way we could determine the reason for our unexpected activity outcome and check the validity of the setup.

5 Conclusions and Outlook

The activity of the isotope ^{148}Gd was measured in two different distances. The results yield unexpected values by 10-15% off and $\approx 8\sigma$ and therefore further investigations are necessary. For further outlook The same system should measure a well known activity source to determine whether the source is damaged, the detector is damaged or the manufacturer measurements are not precise enough.

Acknowledgements

I would like to thank the FRS Ion Catcher research group and especially my tutor Jianwei ZHao for giving me the opportunity to work in an interesting research project and get hands on accurate radioactivity measurements. It has been a fruitful experience. Many thanks also GSI Helmholtz institute for allowing me to be involved in such an incredible research facility and let me take part in the GSI Summer Student Program.

References

[1] https://www.ortec-online.com/products/radiation-detectors/silicon-charged-particle-radiation-detectors.
[2] https://www.nndc.bnl.gov/nudat3/
[3] https://www.ortec-online.com/-/media/ametekortec/manuals/a/a65-mnl.pdf?la=enrevision=f2f3ed3f-fa2d-4185-9301-7d480b0a6955

Developments at the CRYRING@ESR Electron Cooler

Surawadee Khammee
Chiang Mai University, surawadee.khm@gmail.com

We present two ongoing developments at the electron cooler of CRYRING: potential removal of the compensation solenoid and addition of a trapped-ion clearing region to the electron beam line. Considering potential removal of the solenoid, we provide a comparison of the cooler performance in terms of longitudinal cooling force and transverse cooling rates, finding no significant difference in both cases. By numerical studies of the space charge potentials, we show that addition of clearing electrodes is possible by modification of an existing drift region at the exit of the cooler section.

1 Electron Cooling

1.1 Introduction

CRYRING@ESR is a relatively new addition to the GSI/FAIR accelerator complex, complementing the previously existing facilities by a dedicated low-energy storage ring [1]. This report presents two ongoing developments around the electron cooler of CRYRING.

Electron cooling is an important beam preparation technique in experimental heavy-ion storage rings [2]. The ion beam is overlapped with a cold electron beam at equal average velocity. By repeated collisions with the colder electrons, any ion motion of velocity $\vec{V}$ relative to the comoving frame of the cooler beam is damped by a stopping force $\vec{F}(\vec{V})$, decreasing the velocity spread of the ion beam in all degrees of freedom.

1.2 Theory Model

We can describe the cooling force $\vec{F}(\vec{V})$ by the semi-empirical model proposed by Parkhomchuk [3], where any component of the stopping force F_i is expressed as

$$F_i = -\frac{4e^4 n_e Z^2}{(4\pi\epsilon_0)^2 m_e} \frac{V_i}{(\sqrt{V_i^2 + V_{\text{eff}}^2})^3} \times L_c. \quad (1)$$

The Coulomb logarithm L_c is expressed as

$$L_c = \ln \frac{\rho_{\max} + \rho_{\min} + \rho_{\text{L}}}{\rho_{\min} + \rho_{\text{L}}} \quad (2)$$

n_e , ρ_L, and m_e are the electron density, Lamor radius and mass, respectively, and Z is the charge-state of the ion in the storage ring. V_{eff} is the effective electron velocity spread, usually different for the longitudinal and transverse components of $\vec{F}$. It is related to the effective electron temperature $T_{\text{eff}} = m_e V_{\text{eff}}^2 / k_{\text{B}}$. The range of impact parameters of electron-ion scattering is constrained by $\rho_{\min} \equiv Ze^2/[(4\pi\epsilon_0 m_e) \times (|\vec{V}|^2 + V_{\text{eff}}^2)]$ and $\rho_{\max} \equiv |\vec{v}_i|/(1/\tau_{\text{tof}} + \omega_p)$ where τ_{tof} is the time-of-flight of the ion in the cooler, v_i its velocity in the lab frame, and ω_p is the plasma frequency of the electrons.

In the late stages of *transverse* electron cooling, the ion velocity V_i (with $i \in x, y$) is much smaller than the electron velocity spread V_{eff}. Eq. (1) then simplifies to

$$F_i = -\frac{4n_e Z^2 e^4}{(4\pi\epsilon_0)^2 m_e} L_c \frac{V_i}{V_{\text{eff}}^3} = -2\lambda m_i V_i. \quad (3)$$

This means the friction force leads to an exponential decrease of all betatron oscillation amplitudes at the transverse cooling rate λ.

1.3 Electron space charge

The intense electron beam creates a space-charge potential ϕ_{SC}. Together with the acceleration voltage U_{acc}, the latter defines the kinetic energy of electrons in the cooler beam: $E_e = e(U_{\text{acc}} - |\phi_{\text{SC}}|)$. For a cylindrical beam of radius R and homogeneous density n_e, propagating along the axis of a grounded vacuum chamber of radius R_0, ϕ_{SC} can be calculated

analytically as

$$\phi_{\mathrm{SC}}(r) = \frac{e n_e R^2}{4\epsilon_0} \begin{cases} 1 - \frac{r^2}{R^2} + 2\ln\frac{R_0}{R} & \text{for } r \leqslant R, \\ 2\ln\frac{R_0}{r} & \text{for } r > R, \end{cases} \tag{4}$$

where r is the radial position relative to the common chamber and beam axis.

2 Analysis of electron cooling experiments

2.1 Motivation: Solenoid removal

CRYRING contains a solenoid magnet to counter coupling of betatron motion of the ions induced by the electron cooler magnetic guiding field [4]. Removal of that compensation solenoid could make room for additional experimental installations. However, removal of the compensation solenoid could also make optimal set-up of electron cooling more difficult. Hence, a comparison of the cooler performance in both cases is of interest.

2.2 Longitudinal cooling force

In June 2022, prior to the here-reported work, the longitudinal component of the electron cooling force $F_{\parallel}$ was measured for both configurations of cooler and compensation solenoid via the bunched-beam phase shift method [5]. For the tests, a beam of D^+ was stored and cooled in CRYRING at an energy of 2 MeV/u and at various electron current densities. Within the frame of this work, that data was analysed to check for any differences in cooling performance.

In Fig. (1) we plot the relation between the relative electron-ion velocities and the measured drag forces for both configurations together with fits of Eq. (1) to the data. The effective temperature T_{eff} is the free parameter. We found that the effective temperature without compensation of betatron coupling is 14.1±0.4 K and with compensation is 13.7±0.2 K.

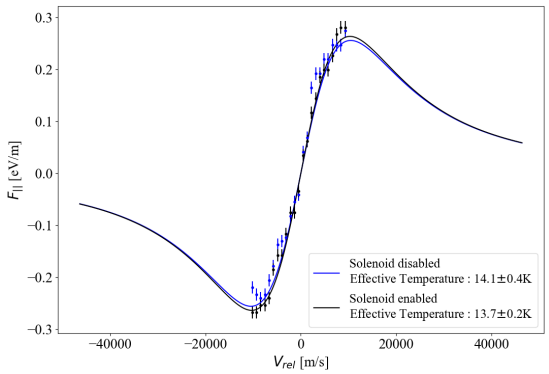

Fig. 1: *Longitudinal cooling force fits with and without compensation solenoid.*

2.3 Transverse cooling rates

Transverse cooling performance was quantified by analysis of the evolution of the beam envelopes during storage, also measured prior to this work, in June 2022. According to Eq. (3) the RMS beam size, measured via ionisation beam profile monitors (IPMs), is expected to shrink exponentially as a function of time in the late stages of electron cooling. Various electron densities and initial beam excitiations were probed. The period of exponential damping needs to be identified "by eye", which limits the precision of the analysis. In the selected period time, we fit the datasets via the equation

$$\sigma(t) = A\exp(-t\,\lambda_{\mathrm{exp}}) + \sigma_{\infty} \tag{5}$$

to obtain the cooling rate λ_{exp} and the final beam sizes σ_{∞}, as shown in Fig. (2). Neither the fitted cooling rates λ_{exp} nor the final beam sizes σ_{∞} exhibit significant difference between the measurements with compensation solenoid disabled or enabled. As the ions interact with the cooler electron beam only for a fraction of their revolution period in the ring, λ_{exp} is related to λ from Eq. (3) via $\lambda_{\mathrm{exp}} = \lambda L_{\mathrm{cool}}/C_{\mathrm{ring}}$, where $L_{\mathrm{cool}}/C_{\mathrm{ring}}$ is the ratio of cooler length and ring circumference.

2.4 Summary

We conclude that the cooling performance with and without compensation of betatron coupling

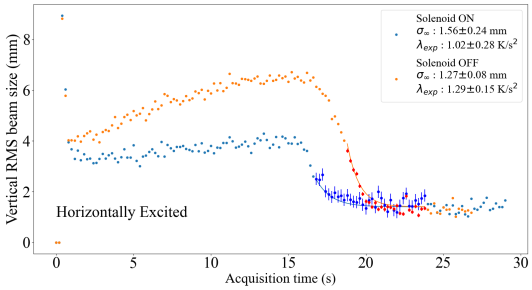

Fig. 2: *Transverse cooling fits with and without solenoid.*

is practically identical, explicitly, with regard to the longitudinal cooling force and transverse cooling rates.

3 Prossible addition of a trapped-ion clearing region

3.1 Trapped-ion clearing

As stated above, the space charge potential of the cooler beam affects its kinetic energy. Direct measurements of the electron energy in past CRYRING beamtimes have repeatedly shown that Eq. (4) overestimated the magnitude of the true space charge potential. A possible explanation is trapping of cations, produced by impact-ionization of the residual gas, in the electron beam. Such ions partly cancel the electron space charge, effectively lowering the value of n_e in Eq. (4). The amount of trapped ions is difficult to estimate but likely depends on the cooler voltage, current and vacuum conditions. Additionally, the ion population may not be stable in time, leading to unwanted changes of the electron energy. The electron beam can be cleared of the trapped ions by a transverse electric field strong enough to accelerate them out of the electron space-charge potential well. Not to disturb the electron beam in the interaction section of the cooler, such clearing electrodes are best added to the collector section of the cooler.

3.2 Numerical Poisson solver

The analytic formula Eq. (4) for the space charge potential is only valid in the case of an electron beam centered in a cylindrically-symmetric drift tube. When the beam is out of center, or when the symmetry of the boundary condition is broken via addition of clearing electrodes, the space charge potential needs to be computed numerically. Within the frame of this project, we developed a numerical Poisson solver in Python 3. The program solves the Poisson equation

$$\Delta\phi(x,y,z) = \frac{\rho_e(x,y,z)}{\epsilon_0} \tag{6}$$

on a 3-dimensional grid of $h \times h \times h$ spatial resolution and for arbitrary electron charge density distributions ρ_e and boundary potential geometries. The solver relies on the relaxation method [6] and converges to a solution via the iteration

$$\begin{aligned}\phi_{k+1}(x,y,z) =& \frac{1}{6}[\phi_k(x-h,y,z) + \phi_k(x+h,y,z) \\ &+ \phi_k(x,y-h,z) + \phi_k(x,y+h,z) \\ &+ \phi_k(x,y,z-h) + \phi_k(x,y,z+h) \\ &- h^2\rho_e(x,y,z)/\epsilon_0].\end{aligned} \tag{7}$$

Convergence of the Python program turned out to be slow for 3-dimensional volumes with many grid points, hence a multigrid method is applied to make the program faster. First, a rough estimate for ϕ is found by running the solver on a coarse $9 \times 9 \times 9$ mm^3 grid. Then we refine the grid to $3 \times 3 \times 3$ mm^3, interpolating the previously found solution for the rough grid accordingly. Finally, the relaxation is repeated in all points on the finer grid, using the interpolated coarse estimate of ϕ as staring point in the iteration. As a result, the overall CPU time for reaching conversion on the $3 \times 3 \times 3$ mm^3 grid is much reduced.

To check the validity of our results, we compare the our numerical solution for a centred electron beam in a cylindrical, grounded drift tube with the analytic solution of Eq. (4). As shown in Fig. (3), the two agree to within 10%. The small deviation in absolute value arises from the relatively coarse approximation of the cylindrical shapes of electrodes and electron beam on the cubic grid and is irrelevant for the purpose of computing equipotential surfaces in the proposed clearing region.

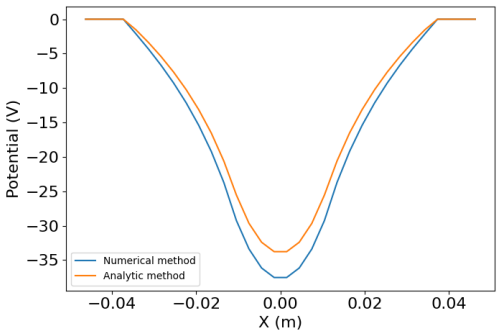

Fig. 3: *Analytic vs. numerical solution of the Poisson equation (Eq. (6)) for centered beam.*

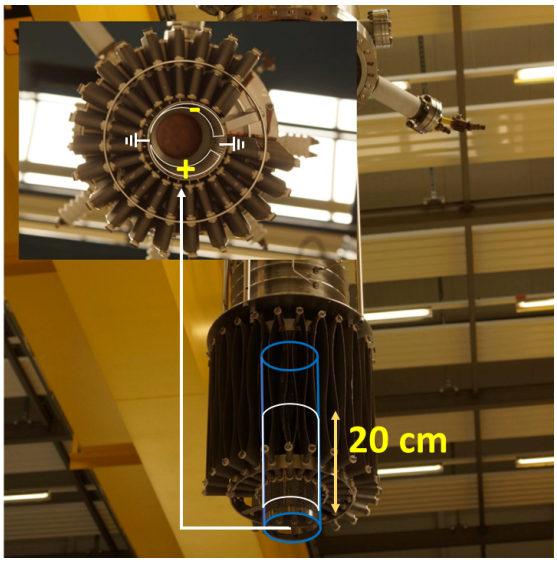

Fig. 4: *The existing drift electrode at the electron collector (dismounted from the cooler) and the proposed clearing electrode geometry.*

3.3 Case study: clearing at collector drift tube

An existing drift-tube at the entrance to the collector section of the CRYRING cooler could be segmented in the way shown in Fig. (4). This yields two ~ 20 cm long clearing electrodes while keeping the electric potentials near the collector cup electrodes unchanged compared to the present configuration. To find out what electrode voltages are required at that new clearing region, we first needed to identify a good test-case for the electron beam size and density. We evaluated the space-charge potential inside said drift-tube for several electron beam configurations that had actually been used in past CRYRING beamtimes. We found the strongest potential gradients to have occurred in case of a high-density ($n_e = 1.7 \times 10^7 \mathrm{cm}^{-3}$) electron beam of relatively small beam radius ($R =$ 1.15 cm, expansion 33.3) that had been used for cooling of U^{91+} at 10.3 MeV/u in 2021.

As visible in Fig. (5), even in this case, an electrode voltage of the proposed new clearing region of only $\pm$ 60 V is sufficient for accelerating trapped ions out of the electron beam, if the latter is co-axial with the clearing region.

Furthermore, we considered electron beam positions shifted laterally with respect to the center of the clearing region. We found that when the beam shifted within the symmetry plane between the two electrodes, or is shifted toward the negative electrode, beam clearing still works with unmodified voltage. However, if the beam position is shifted toward the positive electrode (as shown in Fig. (6), for the example of a shift of $X = 2$ cm) the trapped ions cannot be cleared anymore. This can be seen from the closed equipotential lines at e.g. $Z > 5$ cm. To make sure beam clearing will work in all beam positions, we recommend to use bipolar HV-supplies on both electrodes so that the direction of the clearing field can be changed flexibly.

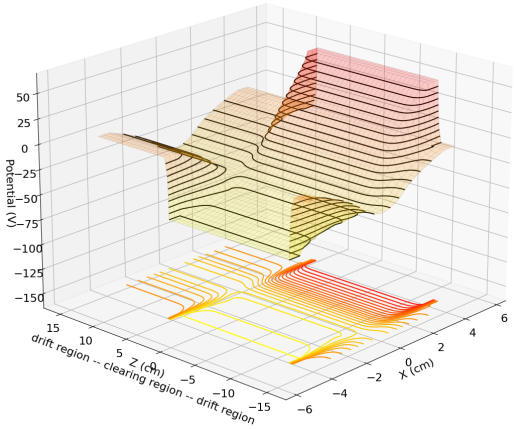

Fig. 5: *Electric potential in the y=0 cm plane of the clearing region, for a centred electron beam.*

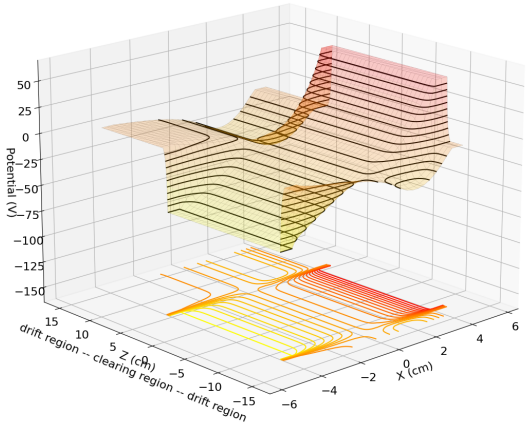

Fig. 6: *Electric potential in the y=0 cm plane of the clearing region, for an electron beam shifted towards the positive electrode ($X > 0$).*

4 Conclusion

We investigated two ongoing developments at CRYRING, namely removal of the electron

cooler solenoid and clearing of trapped ions from the electron beam. The cooling performance in terms of beam quality, longitudinal cooling forces and transverse cooling rates, with disabled and enabled solenoid is found to be practically identical, indicating that removal of the solenoid magnet could be possible, though other aspects of beam dynamics also need to be considered. Our numerical studies have shown that addition of a clearing region is feasible by modification of an existing drift electrode in the collector section of the cooler. We find that only moderate voltages are required, making practical realization straightforward.

Acknowledgments

I could not have undertaken this journey without my tutor, Claude Krantz, who generously provided knowledge an expertise. I owe also many thanks to the summer student program and The Information Technology Foundation under the Initiative of Her Royal Highness Princess Maha Chakri Sirindhorn for supporting.

References

[1] Lestinsky et al., Eur. Phys. J. Special Topics 225 (2016) 797–882.
[2] H. Poth, Nature 345 (1990) 399–405.
[3] V. V. Parkhomchuk, Nucl. Intrum. Methods Phys. Res., Sect. A 441 (2000) 9–17.
[4] S. Peggs, IEEE Trans. Nucl. Sci. 30(4) (1983) 2460–2462.
[5] H. Danared, Nucl. Instrum. Methods Phys. Res., Sect. A 391 (1997) 24–31.
[6] W. H. Press, S. A. Teukolsky, W. T. Vetterling, B. P. Flannery, “Numerical Recipies in C - The Art of Scientific Computing", 2nd Edition, Cambridge University Press, 1992.

Lappo/Lidka.aux

RPC Calibration

Lidia Lappo
Warsaw University of Technology, lidia.lappo@gmail.com

The RPC is a new detector introduced in the R^3B collaboration which was proposed to measure the ToF of the forward emitted protons in inverse kinematic reactions. As a timing detector it is very important to know precisely the position of the detecting plane in the laboratory frame, as a few centimeters of uncertainty can have a big impact in the time measurement, as the protons travel at relativistic speeds. The main goal of this summer internship was to develop a software that allowed to convert a signal in the RPC (X_{RPC},Y_{RPC}) into coordinates in laboratory frame (X_{LAB},Y_{LAB},Z_{LAB}). The developed software can be found in https://github.com/lidka-lappo/RPC_ GSI.

1 Introduction

1.1 Reaction with Relativistic Radioactive Beams

The R^3B collaboration has designed and built what will be the high energy branch of the NUSTAR collaboration at FAIR. This setup allows a complete characterization of the particles involved in the reactions under study. The reactions with radioactive beams will be performed in inverse kinematics. In Fig. 2 you can see, among other detectors, the electromagnetic calorimeter CALIFA, the neutron ToF Wall NeuLAND, or the superconducting magnet GLAD. Here, the collaboration proposed to measure Short Range Correlations (SRCs)[1,2] in radioactive isotopes for the first time. This experiment occurred in May 2022 and then the RPC detector was introduced to CAVE C setup.

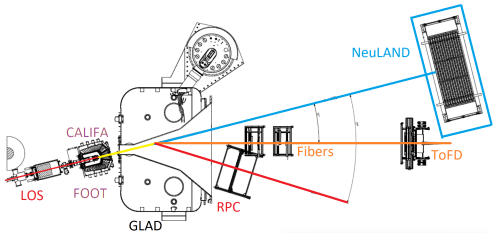

Fig. 1: *R^3B collaboration, CAVE C setup. Courtesy of Daniel Koerper*

1.2 Resistive Plate Chamber (RPC)

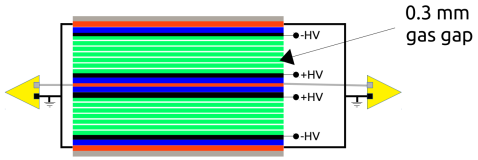

Fig. 2: *Sketch of the internal structure of the of RPC detector, taken from [3]*

Restive Plate Chamber (RPC) is a gaseous parallel plate avalanche detector with electrodes implemented from highly resistive material. The high voltage that is applied to electrodes leads to a uniform electric field between them. The gas gaps between plates are filled with a gas mixture based on $C_2H_2F_4$ and SF_6. The RPC used in R3B consists of two modules with six gas gaps with the readout in the middle of them. The charged particle travels through the gas and creates free charge carriers, which are drifted towards the anode and multiplied by an electric field. The RPC readout consist of 41 parallel horizontal copper strips, which transport electrical signal to both sides of the detector, where the signal is then read by FEE (front-end electronics) [3].

The RPC used in the R^3B Collaboration is a high-precision timing detector with a $\sigma = 50ps$.

The proton's momentum can be calculated by using the Time of Flight (ToF) between the start detector (LOS) and the RPC. Protons measured

in this experiment moved at a relativistic speed, so an error of 5cm in RPC position will lead to approximately 160 ps error in time measurement. This will completely dominate the 50 ps of timing resolution given by the RPC. This makes it imperative that we know the position of the RPC with the utmost precision.

To guarantee this several measurements with a laser where done in order to position the RPC frame in the laboratory frame. They are marked with letters from A to I (Fig.4). To add to this measurement, a source ^{137}Cs was used to irradiate the detector at points named with numbers from 1 to 10 (Fig.4). This was done to correlate the measured data with the detector frame. Source was used with collimator. One background measurement without a source was done. A measurement was made with a source position far away to irradiate whole detector.

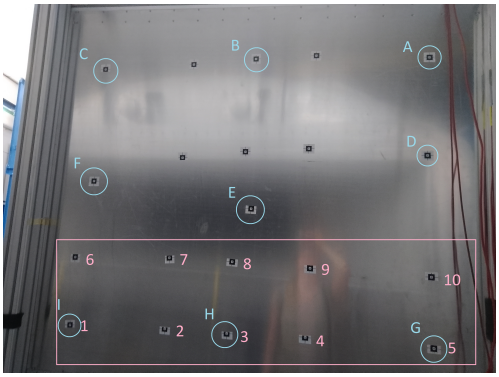

Fig. 3: *Positions of stickers on RPC. Stickers with numbers 1-10 are marking points that were irradiated and cardinal points measured by laser in laboratory frame are marked with letters from A to I*

2 Calibration

2.1 Data processing

Raw data is unpacked and calibrated using R3BRoot, a software developed by the R^3B collaboration, and is written in root format. The calibrated data for the RPC at the moment consist of the time of flight (ToF), the position in X, the strip number, which gives the position in Y, and the time over the threshold (ToT).

2.2 Aligning

It was clear when plotting the 2D hit map that the strips were not properly aligned (Fig. 5). This mismatch comes from the fact that the wires that connect the strips to the FEE and from the FEE to the TDCs have different lengths and it takes different time for signal to travel through.

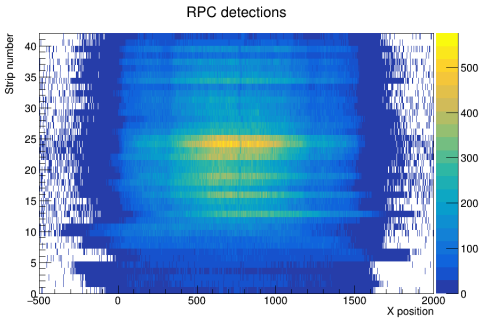

Fig. 4: *Hit map with source placed far away. Width of RPC detector is 1500 mm however here wider range was used to show disalignment of strips*

This is somewhat corrected in the R3BRoot calibration, but as is visible in (Fig. 5) some improvements can still be made. In Fig. 5 it is possible to see a drop in counts in the middle of RPC for every strip. This is caused by a metallic wire used to apply the HV. It is also possible to see a shadow cast by two scintilator bars that were placed in front of the RPC.

All of this drops in counts can be used to calculate an offset that will align every strip. Due to being a sharper and much better defined drop the shadow of the wire was chosen.

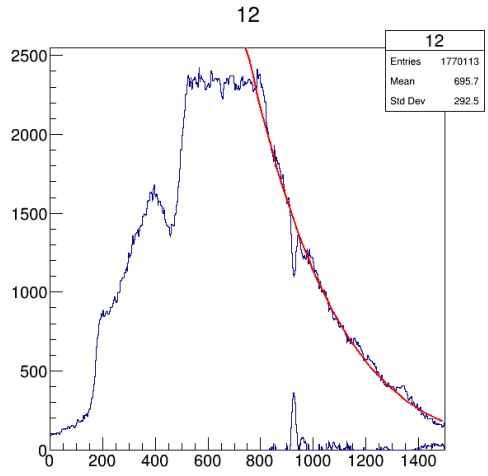

Fig. 5: *Example of one of the strip histograms with fit and subtracted histogram*

To find the position of this wire, we fitted a

function to half of the histogram of each strip. By subtracting the fit function from the histogram the Wire drop is now a peak, which is easier to find (Fig. 6) using a peak finder algorithm. This was done for every strip and

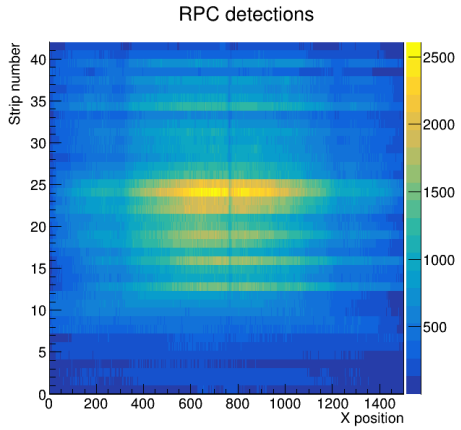

Fig. 6: *Hit map with source placed far away and with aligned strips*

a parameter file was created. Precision of offset was estimated at 1 mm using different measurements. The same calibration was then applied to different data, since a single calibration should align all of the data sets, which was the case. In Fig. 7 a 2D plot of the hit map of the rpc can be seen, strips are all aligned, horizontal and vertical wires are clearly visible and the shadows from the two scintillator bars too.

2.3 Finding source position

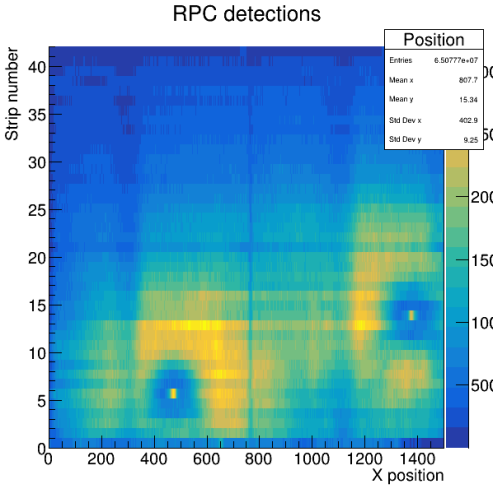

Fig. 7: *Collective Hit map of two distinct data sets with the source position in different points*

When the histogram is aligned, the signal from the radioactive source is now clearly visible. The shape of this signal consists of a sharp peak corresponding to the hole in the collimator, surrounded by a circle of low counts, where the collimator was blocking radiation, and then a halo of high counts, from radiation that didn't traveled through collimator.

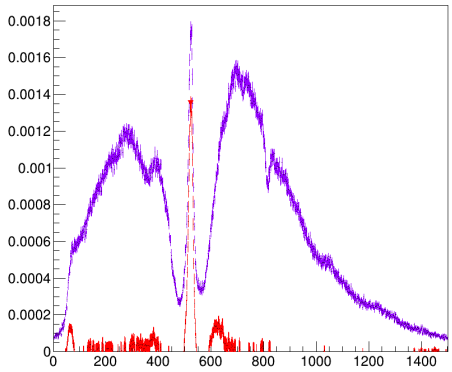

Fig. 8: *Histogram of detections on strip 6 (violet) and histogram of detection in strip 6 with strip 5 subtracted from it (red)*

To locate the peaks, first all the strip x projection histogram were normalized (Fig. **??**, violet), after this, starting on the second strip, the histogram from the previous strip is subtracted removing the background and making the peak of the source more visible and easy to locate (Fig. **??**, red).

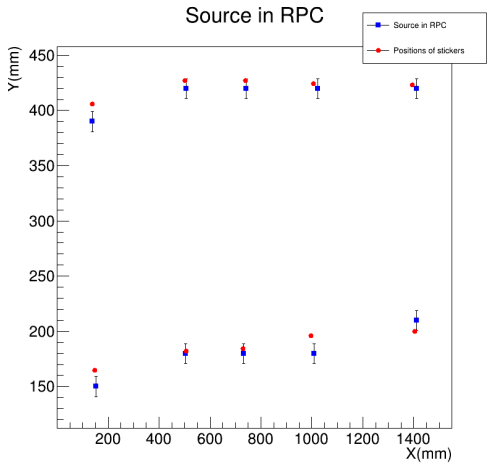

Fig. 9: *Comparison of point measured by RPC and sticker positions*

Measured position of source and position of

peaks in RPC are really similar. The resolution of the Y_{RPC} position is worse than that of X_{RPC}, because copper strips are placed every 30mm, $\sigma(Y_{RPC}) = \frac{30}{\sqrt{(12)}} = 9mm$. Uncertainty of the source peak is $\sigma(X_{RPC}) = 8mm$

2.4 Conversion of RPC coordinates to laboratory frame

Laboratory reference is (X_{LAB},X_{LAB},Z_{LAB}) coordinates, where point (0,0,0) is the bending point of the GLAD magnet. Points marked from A to I were measured in laboratory reference. Using coordinates of those points a plane was created. Knowing that position of irradiated points 1,3,5 are the same as I, H and G I created an algorithm to convert coordinates from RPC to laboratory reference. A root macro is available in the GitHub repository https://github.com/lidka-lappo/RPC_GSI. It was used to calculate laboratory reference coordinates with respect to the source positions measured by the RPC. The positions of the irradiated end cardinal points in laboratory reference are displayed on Fig. **??**.

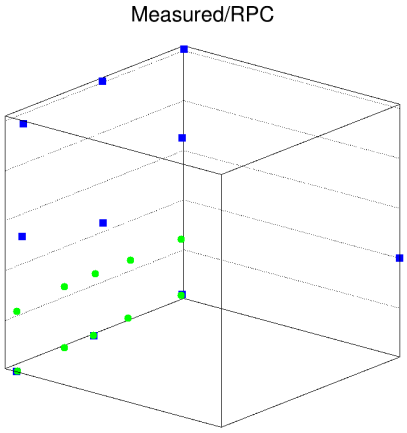

Fig. 10: *Positions of irradiated (green) and cardinal (blue) points in laboratory reference*

3 Conclusion

Very precise alignment of strips was achieved. The positions of the irradiated spots measured by RPC are similar to those of the stickers measured on RPC. For X_{RPC} positions it is really accurate, however Y_{RPC} measurement not always fit in uncertainty. Software for conversion of (X_{RPC},Y_{RPC}) to (X_{LAB},Y_{LAB},Z_{LAB}) was made. And can be used for further data analysis. It was shown that this approach for measuring distance to RPC detector is effective. For future even better calibration will be achieved by measuring every sticker visible on Fig. **??** in laboratory frame and also irradiating every point.

Acknowledgments

I would like to express my deep appreciation to my tutor Manuel Xarepe for the interesting task, guidance and a lot of patience during the editing work. I feel gratitude to Leandro Milhomens da Fonseca for taking care of me at the beginning of workshop. I would like additionally thanks both of them for having a tour in CAVE C for our friends from Summer Program. Many thanks for the very kind attitude to all the members of R^3B collaboration who I had the pleasure to meet. I am also grateful to all organizers of the GSI Summer Student Program for this great scientific experience.

References

[1] The CLAS Collaboration *Probin high-momentum protons and neutrons in neutron- rich nuclei*, (NATURE, VOL 560, AUGUST 2018).

[2] M. Patsyuk, J. Kahlbow, G.Laskaris in *Unperturbed inverse kinematics nucleon knockout measurements with a carbon beam*, (Nature Physics, VOL 17, JUNE 2021).

[3] A. Blanco, F.Clemencio, P.Fonte et al. in *The SHiP timing detector based on MRPC*, (XV Workshop on Resistive Plate Chambers and Related Detectors, 2020, University of Rome tor Vergata, Rome, Italy).

[4] C. Lippmann in *Detector Physics of Resistive Plate Chambers*, (Frankfurt am Main, 2003).

Modelling Rotational Bands in the Nilsson Model

Timothy H. Lees
Heriot-Watt University, Edinburgh, United Kingdom, thl3@hw.ac.uk

Energy levels inside the atomic nucleus shift when the nucleus is deformed and rotating. The Shell, Nilsson and particle rotor models are necessary to make sense of these energy shifts and are explained. Furthermore, it is shown that the Coriolis effect, analogous to the classical Coriolis effect, further shifts energy levels in the strong coupling limit when the projection of the total angular momentum of the orbiting nucleon $\Omega = 1/2$ *and when the decoupling parameter* $a \neq 0$*. This energy shift is compared to the collective rotational energy levels where the Coriolis effect is negligible.*

1 Introduction

1.1 Background

Nuclear physics has, in many ways, shaped the 20th century and continues to influence the 21st. From providing electricity through fission and hopefully, sooner or later, through fusion, to providing medical benefits like radiation therapy, and building fierce destructive weapons, the applications are broad and have left their mark on the world around us.

The structure of the nucleus plays a central role in nuclear physics. Unlike other fields, nuclear physics has no single theoretical framework to describe all observed phenomena, and so the nuclear structure is often described phenomenologically. Through decades of research, it is now understood that the atomic core is not merely a static collection of protons and neutrons, but rather a dynamic system in which nucleons move about inside the nucleus and are made up of a collection of quarks [1]. This entire configuration can rotate and vibrate and is held together by the strong force which behaves differently for different nuclear spin orientations [2]. Thus, the need for a simplified description of the atomic nucleus arises when a sufficient number of nucleons are present and a consideration of all nucleons individually becomes unfeasible. In the case of a few nucleons, properties describing the nuclear core can still be calculated analytically. An undertaking that is, quite simply, not possible for larger nucleon numbers. A new approach is needed.

1.2 Shell Model

The shell model provides the above-mentioned new approach and, although it is an oversimplification, still provides valuable insights into the nuclear structure. The nucleons are bound inside the nucleus by the strong force. On small scales ($\sim 10^{-15}$ m) the strong force overpowers the repulsive force between protons provided by the Coulomb force. In the shell model, it is assumed that nucleons move about the nucleus in orbits of well-defined energy and angular momentum through an averaged potential [2]. In atomic physics, only the valence electrons are responsible for observed atomic properties. A closed shell is present when the electron orbit is filled with electrons, which then gives particularly stable atomic configurations.

An analogous picture holds for the nuclear case. In the shell model, only the "valence" nucleons are responsible for observed nuclear properties. Similarly, it can be experimentally measured that for a certain number of nucleons the total binding energy of the nucleus is considerably higher than for other numbers of nucleons. The nucleon numbers that characterise closed shells in the nuclear case are called "magic numbers". Nucleons occupy different energy levels. The Pauli exclusion principle prevents nucleons with four equal quantum numbers, N (principle quantum number), l (orbital angular momentum), m (magnetic quantum number) and s (spin), from occupy the same energy level. The total spin of a nucleon is given by j which is the sum of the orbital angular momentum l and the spin s. In order to distinguish different nucleon

orbits, a labelling convention is used. For example, an orbit could be labelled as $1d_{3/2}$, where $n = 1$ (counts number of levels), $j = 3/2$ and $l = d = 2$. The naming convention for the angular momentum l is as follows. For $l = 0$ an s orbital is given, $l = 1$ describes a p orbital, $l = 2$ gives a d orbital, $l = 3$ gives a f orbital. l values higher than 3 obey alphabetical ordering, continuing from f (g, h, i,...). The parity of the orbital angular momentum l is denoted by π (i.e. if $l = 0, 2, 4, ..$ it is even parity and $\pi = +$, if $l = 1, 3, 5, ...$ we have an odd parity and $\pi = -$).

Even though the shell model, was and still is, very successful in describing nuclei with a magic number of either protons or neutrons (or both), the model is less successful in predicting energy levels for nuclei that are far away from the magic numbers. For these cases a modification to the shell model is necessary.

1.3 Nilsson Model

The previous discussion centred around a spherical nucleus. However, the majority of nuclei are not spherical but deformed. As mentioned above, this is usually the case when a nucleus has a nucleon number that is far away from a magic number. The result is a shift in the energy levels of an orbiting nucleon. The Nilsson model, developed in the 1950s by Sven Gösta Nilsson, accounts for this shift [3]. This comparably simple model has had remarkable success in describing the behaviour of hundreds of single-particle deformed nuclei. Additionally, it is easy to extend the model for different situations such as vibrations and rotations of the nucleus (see Section 1.4).

The deformation of the atomic core manifests itself as either a prolate deformation (like a rugby ball) or an oblate deformation (like a lentil) and is characterised by the deformation parameter δ. A $\delta > 0$, indicates prolate deformation, while a $\delta < 0$ describes oblate deformation ($\delta = 0$ gives a sphere). Only the binding force between one nucleon and the averaged binding forces between all the other nucleons are considered. The problem is reduced to a two-body interaction consisting of a nucleon orbiting around the core of the nucleus. For a given total angular momentum j, multiple orbital orientations are possible. This means that nucleons cannot be distinguished solely by examining their j values and thus, j is no longer a good quantum number. A good quantum number is instead given by the projection of the total angular momentum j onto the symmetry axis z of the deformed nucleus. This projection is denoted by Ω as can be seen in Fig. 1. The symmetry axis is the axis on which the deformed nucleus is axially symmetric. The number of orbital orientations is dictated by j. If j, for example, has a value of $\frac{(2M+1)}{2}$, for some arbitrary integer M, then [1] the projection onto the symmetry axis Ω can take on values of $\frac{(2M+1)}{2}, \frac{(2M+1)-2}{2}, \frac{(2M+1)-4}{2}, ..., \frac{1}{2}$. Thus, for $j = 7/2$, four orbital orientations are possible. Orbits corresponding to $\Omega = 1/2$ have the most equatorial orbits for prolate deformation. An equatorial orbit will have a different average distance from the nuclear core compared to a nucleon orbit that is tilted more heavily towards the poles of a deformed nucleus (larger Ω). Therefore, the strong force will have a different magnitude for different orbital orientations and energy levels in a deformed nucleus are shifted compared to a spherical nucleus.

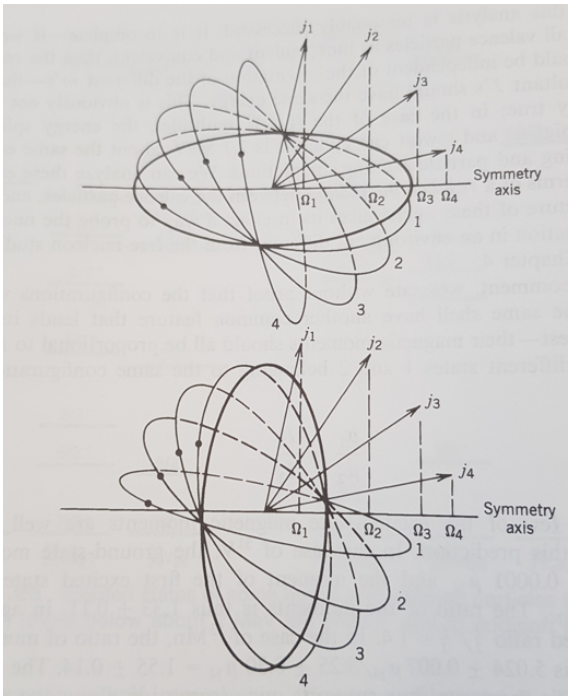

Fig. 1: *Dependent on* j, *multiple orbital orientations with different projection* Ω *are possible. This is shown for an oblate (top) and prolate (bottom) deformation. Fig. taken from [4].*

A given nucleon orbit is labelled as

[1] j will always be a half odd integer since j=l+s, and l is an integer while $s = \pm\frac{1}{2}$

$$\Omega^{\pi}[Nn_z\Lambda]$$

where π is the parity of the orbital angular momentum l, N is the shell number, n_z is the number of nodes in the wave function along the symmetry axis and Λ is the component of the orbital angular momentum along the symmetry axis. Λ is fixed by N and n_z. When N is even, $n_z + \Lambda$ must be even and when N is odd $n_z + \Lambda$ must be odd.

1.4 Particle Rotor Model

An extension of the Nilsson model is the particle rotor model, where it is assumed that the deformed nucleus has an internal rotational motion. Since quantum mechanically a perfect sphere cannot rotate, it necessarily means that all rotational spectra are exhibited by deformed nuclei. In the case of pure collective rotation, nuclear energy levels are given by [5]

$$E_I = \frac{\hbar^2}{2\mathcal{J}} I(I+1) \tag{1}$$

where $\mathcal{J}$ is the moment of inertia and I is the total spin, consisting of the spin of the orbiting nucleon j and the overall spin of the nucleus R as can be seen in Fig. 2. For low Ω values and high spins I, a Coriolis effect analogous to the classical case takes effect and causes further shifts in the energy levels. This occurs as a result of the spin of the orbiting nucleon j being coupled to the spin of the core R. Selection rules require that only $\Omega = 1/2$ values contribute towards the Coriolis effect. A further simplification takes place when the total angular momentum j points most strongly along the symmetry axis. In this limit, called deformation alignment or the strong coupling limit, Ω is roughly constant and thus, remains a good quantum number. For $\Omega = 1/2$ the Coriolis effect must be accounted for and the energy levels are adjusted according to [5]

$$\begin{aligned} E_{I\Omega} =& E_\Omega + \frac{\hbar^2}{2\mathcal{J}}(I(I+1) - \Omega^2 \\ &+ \delta_{\Omega\frac{1}{2}} a(-1)^{j-\frac{1}{2}}(I+\frac{1}{2})) \end{aligned} \tag{2}$$

where E_Ω is the energy of the lowest energy band, $\delta_{\Omega\frac{1}{2}}$ is the Kronecker delta, which is one if $\Omega = 1/2$ and zero otherwise and a is the decoupling parameter given by [5]

$$a = \sum_{Nj} (-1)^{j-\frac{1}{2}}(j+\frac{1}{2}) |a^{\nu}_{Nlj\frac{1}{2}}|^2 \tag{3}$$

where $a^{\nu}_{Nlj\frac{1}{2}}$ are the coefficients of the Nilsson wavefunctions describing the nucleons.

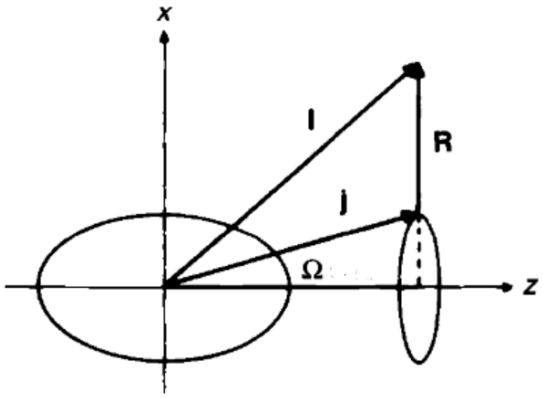

Fig. 2: *In the strong coupling limit* j *points along the symmetry axis z such that* Ω *remains a good quantum number. The total spin of the nucleus* I *is given by the vector sum of the total angular momentum* j *and the collective spin of the core* R. *Fig. taken from [5].*

2 Method

The decoupling parameter a changes with deformation δ. Thus, the energy levels $E_{I\Omega}$ shift for each δ value according to Eqn. 2. Data describing a as a function of δ is retrieved from Ref. [6]. Using the data it is possible to determine the energy shifts for different spin states I, for a range of deformations δ and thus, for different decoupling parameters a in the strong coupling limit. The energy shift due to the Coriolis effect can be plotted for states with $\Omega = 1/2$ and compared to states with $\Omega \neq 1/2$. This analysis is performed for a deformation of $\delta \in [0.5, -0.5]$ for all nucleon orbits with $\Omega = 1/2$ from shells $N = 1$ up to $N = 7$.

3 Results and Discussion

From Fig. 3 it can be seen how the energy levels for different spin states I are affected when $\Omega = 1/2$ as opposed to $\Omega \neq 1/2$ for the $1/2^-[640]$ orbit. The red line represents projections of $\Omega > 1/2$ where the Coriolis effect is negligible. Due to the $\delta_{\Omega\frac{1}{2}}$ term in Eqn. 2,

states with $\Omega \neq 1/2$ experience no Coriolis effect and the situation is essentially reduced to Eqn. 1, which describes a collective rotation of nucleons. Another possibility for Coriolis effect suppression occurs when $a = 0$. This is the case when the sum in Eqn. 3 cancels. The magnitude of the shift away from $\Omega = 1/2$, is proportional to the absolute value of the decoupling parameter $|a|$. From Eqn. 3 it can be seen that a depends linearly on j. Therefore, the energy shift due to the Coriolis effect will be larger for higher spins I, since I=j+R, as is observed in Fig. 3.

Furthermore, the alternating sign in Eqn. 3 causes spin levels to be alternatingly pushed up and down in energy.

Note that, at $\delta = 0$ a spherical nucleus is described. However, no rotational spectra or Coriolis effects are exhibited as quantum mechanically a sphere cannot rotate.

4 Conclusion

Using the particle rotor model, which builds upon the shell and Nilsson models, it has been shown how the Coriolis effect acts on nucleon orbits with $\Omega = 1/2$ states in the strong coupling limit. The Coriolis effect is suppressed, when either $\Omega \neq 1/2$ or when the decoupling parameter $a = 0$. The decoupling parameter is responsible for the magnitude of shift and whether it is an upwards or downwards shift in energy, dependent on the total angular momentum of the particle j. Further work on this project could be done by extending the energy level calculations beyond the strong coupling limit for all possible nucleon spin orientations.

Acknowledgment

I would like to thank Dr Kathrin Wimmer for guiding me through this project.

References

[1] E. N. Economou, *A Short Journey from Quarks to the Universe*. (SpringerLink and LINK 2011, Chapter 1, 1st ed. 2011. Berlin, Heidelberg: Springer Berlin Heidelberg. 2011)

[2] A. Kamal, *Nuclear Physics*. (pages 224 & 363, 1st ed. 2014)

[3] S. G. Nilsson, *Binding states of individual nucleons in strongly deformed nuclei*, (Dan. Fys. Medd. **29**, 1955)

[4] K. S. Krane, *Introductory Nuclear Physics*. (John Wiley & Sons, Hoboken, 1988)

[5] S. G. Nilsson & I. Ragnarsson, *Shapes and Shells in Nuclear Structure*. (Cambridge University Press, Cambridge, 1995)

[6] K. Wimmer, *Nilsson model calculations. to be finalized*. GitHub code: samehttps://github.com/wimmer-k/Nilsson (2020)

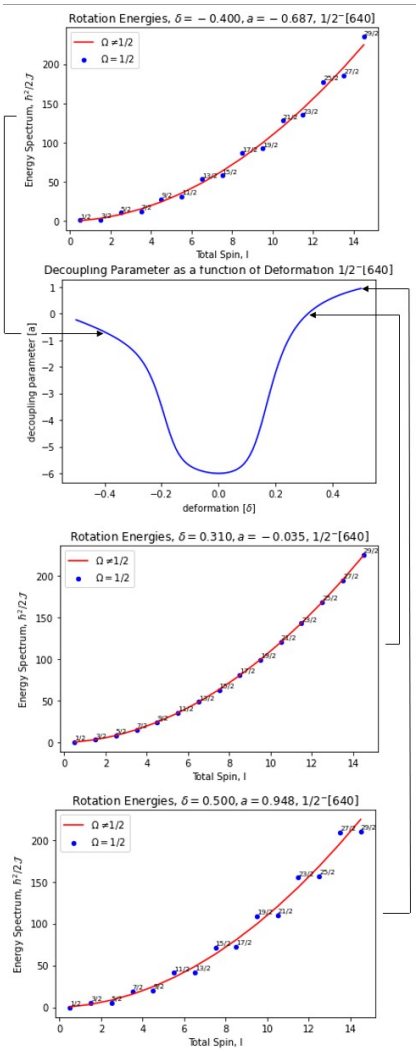

Fig. 3: *Energy shifts in the strong coupling limit in the particle rotor model for nucleon orbit* $1/2^-[640]$. *The energy shift due to the Coriolis effect is apparent for orbits with* $\Omega = 1/2$ *whilst the magnitude of the shift depends on the decoupling parameter* a.

Simulations for the ASY-EOS Experiment

Florentinë Limani
University of Prishtina "Hasan Prishtina", email: florentinab.limani@gmail.com

This work briefly describes a method used to do necessary simulations for the ASY-EOS experiment that will take place at GSI Helmoholtzzentrum. The simulations are done using the R3BRoot software based on the geometrical configuration of neutron detector NeuLAND and fragment detector ToFD placed in Cave C. These simulations are necessary to describe the effect of ToFD as a veto detector for NeuLAND in order to identify neutrons and charged particles. The results show excellent performance of the setup in the separation of neutrons from charged particles.

1 Introduction

The **E**quation **o**f **S**tate (EOS) of nuclear matter plays a key role in determining macroscopic nuclear properties of nuclei in laboratories and in neutron-star crusts [1] as it describes the relation between density, pressure, energy temperature and the isospin asymmetry. Hence, it is important to fully and correctly determine it.

The EOS is divided into a symmetric matter part independent of the isospin asymmetry and an isospin term, also quoted as symmetry energy $E_{sym}(\rho)$,

$$E(\rho,\delta) = E(\rho,0) + E_{sym}(\rho)\delta^2 + o(\delta^4) \quad (1)$$

with $\delta = (\rho_n\text{- }\rho_p)/\rho$, where ρ_n, ρ_p, and ρ are neutron, proton and nuclear matter densities. The behaviour of $E_{sym}(\rho)$ is important to be studied as it will help us to understand and to interpret many astrophysical observations and other phenomena related to nuclei such as drip lines, masses, densities and collective excitation of neutron-rich nuclei [1-3].

Because of its importance, E_{sym}, for many years now, has been at the center of many studies and as such many different theories and experiments have been conducted in order to achieve the goal of determining it. Among the latest ideas, we find the theory of elliptic flow [4] of primary particles in **H**eavy **I**on **C**ollisions (HIC) a very promising tool to study asymmetric nuclear matter. The elliptic flow is related to the angular distribution of emitted particles. All the studies so far show that the distribution of neutrons over protons and other primary charged particles is related to the E_{sym}. In one of the latest experiment done by the FOPI collaboration at the GSI laboratory [5], where different HIC model predictions were used, was concluded that "the value of the so called elliptic flow of protons and charged particles around mid-rapidity is negative at incident beam energies between 0.2 and 5 AGeV, which signifies that matter is squeezed out perpendicular to the reaction plane and shows the strongest sensitivity to the EOS". On the first ASY-EOS campaign constrained E_{sym} using the neutron over proton elliptic flow ratio from Au+Au at 400 AMeV incident energy. The validity of this constraint was up to about 1.5 times the nuclear saturation density. Now, in order to determine the symmetry energy in the region of suprasaturation densities around $2\rho_0$, a new experiment [3] has been proposed in which the elliptic flows ratio of outgoing particles from Au+Au collision in HIC at different energy values (250, 400, 600, and 1000 AMeV) will be investigated.

2 Experimental Setup

To achieve the goal of determining symmetry energy at high densities, based on the flow functions of outgoing particles, the ASY-EOS experiment should take place in Cave C at GSI-FAIR. Inside Cave C, there will be different detectors placed in a unique geometry (Fig.1) in order to have high efficiency and performance. The main protagonists for this project are two detectors from R3B Setup (Reactions with Relativistic Radioactive Beam) [6]: fragment detector ToFD (Time of Flight Detector) [7] and neutron detec-

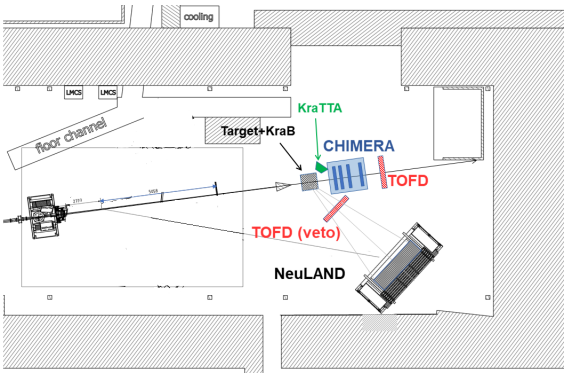

Fig. 1: *Experimental Set-Up in Cave C.*

tor NeuLAND (New Large-Area Neutron Detector) [8]. More information about the other detectors shown in Fig.1 and their importance for this experiment, one can find in [3]. ToFD consists of two frames which have two planes with 44 scintillator paddles each. One of the frames will be used to measure charge and velocity of particles that are emitted at small angles between 1° and 7° in laboratory frame (mainly decay products). The other frame will be placed at a distance of approximately 1.5 m from the target, and it will be used as a veto detector for charged particles detected in NeuLAND. Originally designed as a neutron detector with a high detection efficiency, a high spatial and time resolution, and a large multi-neutron reconstruction efficiency, will be placed 4.5 m away from the target behind the ToFD. It will cover the polar angles between 34° and 62° with the central point at an angle of 50° to the beam line.

3 Simulation of Data

For this project simulations are done using R3BRoot software framework which was developed at GSI and is used for simulations and data analysis of R3B experiments. This software has a modular design with shared libraries, which are loaded on demand. The simulation part is based on the **V**irtual **M**onte **C**arlo (VMC) concept.

In R3BRoot one finds formats that are used for the description of detector geometry, for the input of the simulations, for the event display, particle generating etc. [9]. This work presents the result of simulations for more than 38000 events done with IQMD model [10] for the Au+Au collisions at energies 400 and 1000 AMeV and impact parameter up to 7.5 fm.

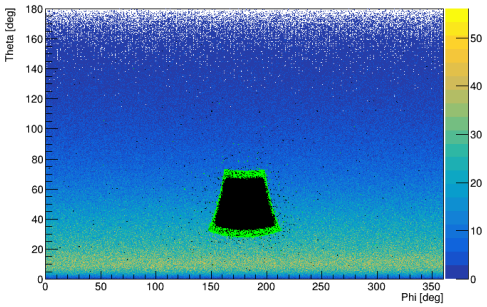

Fig. 2: *Angular distributions of primary particles from Au+Au collisions at 400 AMeV without cuts in full solid angles and those detected in ToFD (green) and NeuLAND (black).*

The codes for achieving this were developed by the R3B Group. Whereas, to generate single particles, the BOX generator which is installed inside the R3BRroot framework was used. Among generated particles we present results for neutrons, protons, deuterons and tritons. Although simulations for the ^{3}He and ^{4}He particles were also done, their results are not shown since their effect is negligible. Fig. 2 represents the angular distribution of primary particles in Au+Au collisions at 400 AMeV and geometrical acceptance of ToFD and NeuLAND. The green dots represent the particles hitting ToFD, while the black ones in this image represent the hits in NeuLAND. One can see the acceptance of ToFD shadows the acceptance of NeuLAND which is necessary for proper vetoing of the charged particles. In Fig. 3 the multiplicity distributions of different particles within the geometrical acceptance are shown. On the average there are several protons and neutrons in each event which have to be identified.

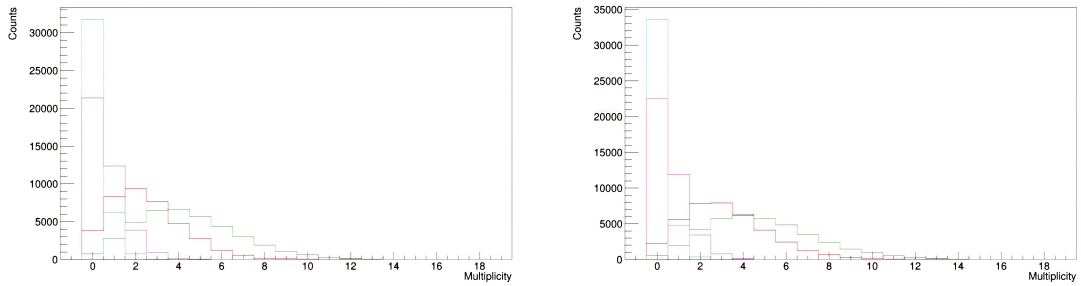

Fig. 3: *Multiplicity distributions of particles from IQMD model for the Au+Au collisions at 400 AMeV (left panel) and 1000 AMeV (right panel). The blue line represents tritons, pink - deuterons, red -protons and green - neutrons.*

3.1 Identification of neutrons and charged particles

One of the main requests during the ASY-EOS experiment is the ability to identify particles in order to get and compare the angular distributions of protons and neutrons. Hence, it is important that the veto detector efficiency for proton detection is much higher than the neutron detection efficiency. The proton and neutron efficiencies in ToFD and NeuLAND are shown in Fig. 4 as functions of kinetic energy. Almost all protons with sufficient kinetic energy to reach the detectors (>40 MeV) will be detected whereas the neutron efficiency is lower. The low neutron detection efficiency in ToFD (3%) is necessary for a good separation of neutrons and charged particles. Another important step is to see the correlations of hits between our detectors as this will help us to identify different particles in multi-particle events. Since the primary particles that are produced in a nuclear reaction will move along straight lines, they will pass through ToFD first and then NeuLAND. The charged particles will react with both detectors and therefore the hit coordinates in them will be correlated. Neutral particles, on the other hand, will pass through ToFD without being detected in 97% of cases, but they will be detected by NeuLAND with a relatively high efficiency of 60-75%. One also can see the X- and Y-correlation 2D histograms in Fig. 5. There is a peak around 0 for charged particles and no peak for neutrons and this is the main condition for the identification of charged particles and neutrons.

The final results are shown in Fig. 6. The histograms show time of flight vs energy depositions of particles detected in NeuLAND with

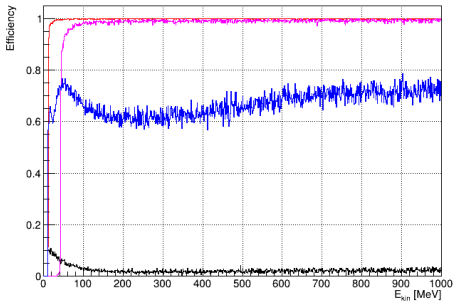

Fig. 4: *Representation of efficiency of detectors: ToFD (red) and NeuLAND (pink); neutrons in ToFD (black) and NeuLAND (blue).*

(left) and without (right) veto condition. Here one can see that typical Bethe-Bloch lines for charged particles are completely removed with veto condition. This together with the 2D histograms in Fig. 5 demonstrate that our experimental setup can efficiently identify neutrons and charged particles. Also different isotopes of hydrogen can be identified as seen in the right panel of Fig. 6. Further analysis is needed to quantify the efficiency of proton detection and contamination of deuterons and tritons.

4 Summary

This report presents some of the results of the simulations done using R3BRoot software for the proposed ASY-EOS experiment, which should take place in 2024-2025 at GSI-FAIR. The aim of the experiment is to determine the E_{sym} of EOS for density around $2\rho_0$ by flow functions of protons and neutrons in HIC of Au+Au reactions. The main challenge was to distinguish neutrons and charged particles

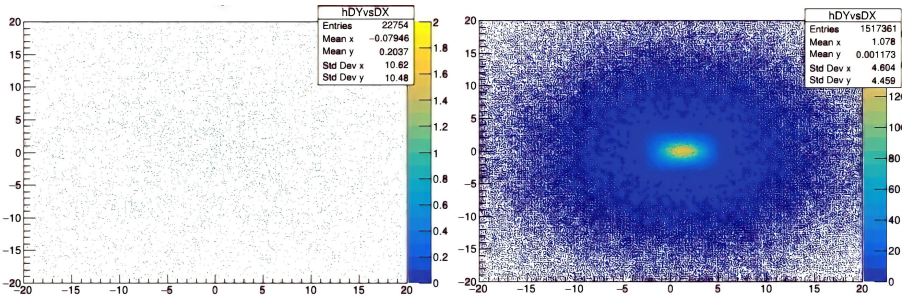

Fig. 5: *Difference in Y coordinate between NeuLAND and ToFD vs difference in X coordinate between NeuLAND and ToFD. Left panel - Neutrons, Right Panel - protons*

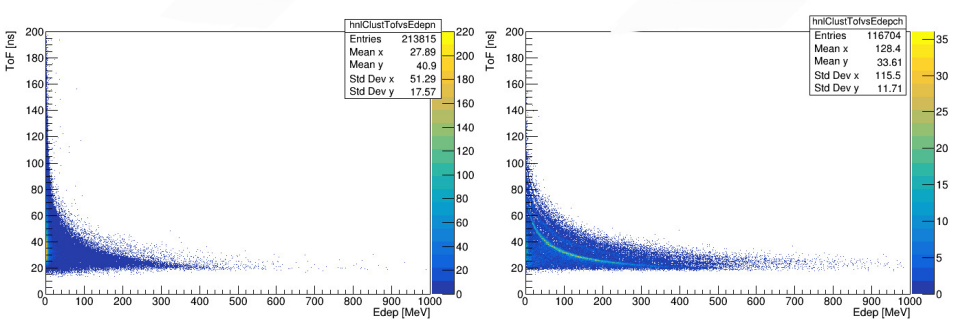

Fig. 6: *Time-of-flight vs deposited energy of particles generated from simulations of Au+Au reactions at 400 AMeV: Left panel - neutrons; Right panel: charged particles.*

that are produced in the collision. Using the R3BRroot software we simulated the response of our experimental setup for reactions Au+Au at 400 AMeV and 1000 AMeV and impact parameter b $<$ 7.5 fm. From the results of these simulations we can conclude that the proposed setup and usage of ToFD and NeuLAND as detectors are the right choice to help us identify neutrons and charged particles.

Acknowledgments

I would like to extend my sincere thanks to my tutor Leandro Milhomens da Fonseca for his full support during this project and many thanks to whole R3B Group at GSI for their help along the way. I would also like to express my deepest appreciation to Igor Gasparic who did not hesitate to help and guide me, and whose work inspired me everyday. At the end, many thanks for A.Le Fèvre, J. Knoll and R. Averbeck for the organization of the Summer School.

References

[1] M. Baldo, G.F. Burgio *arXiv:* 1606.08838 (2016).
[2] S. Huth, et al., *arXiv:* 2107.06229 (2022).
[3] P. Russotto, A. Le Fèvre *arXiv:* 2105.09233 (2021).
[4] P. Russotto et al.Phys. Rev. C 94, 034608
[5] Tsang M.B. et al., Phys. Rev. C 95 (2017) 044614
[6] www.r3b-nustar.de
[7] M. Heil et al, Sci. Report 2014 GSI Report 2015-1
[8] K.Boretzky et al.,*els:*165701 (2021)
[9] *Journ. Phys.* D **331**, 032036 (2011).
[10] P.Russotto (Private Communication, Ag. 2022)

Optimization measurements of JetRIS for laser spectroscopy of heavy elements

Ruxanda Mireanu
University of Bucharest, ruxandamireanu@gmail.com

In this work the transport efficiency of the buffer gas-cell of JetRIS was determined for the ^{219}Rn and ^{215}Po daughters of the ^{223}Ra recoil source, adjusting different parameters of the setup, such as the potential applied on the source, its position, funnel and electrode gradients and position of the PIPS detector.

1 Introduction

In laser spectroscopy studies of heavy elements a high efficiency is essential in order to deal with the low production rates. The element nobelium ($Z = 102$) was recently studied by laser spectroscopy using the RADRIS technique [1]. Here, laser spectroscopy is performed inside of a buffer gas environment, limiting the achievable spectral resolution mainly due to the observed pressure broadening. To overcome this resolution limitation a new experimental high-resolution laser spectroscopy setup, named JetRIS, is being commissioned at GSI, Darmstadt. Here the high pressure region for thermalizing the high energetic recoils after fusion induced reactions is separated from an effusing hypersonic gas jet created by a de Laval nozzle, where laser spectroscopy is performed [2].
This report will conclude characterisation and optimization measuremenets performed with the JetRIS setup in preparation for future beam times. For these measurements an alpha recoil source (^{223}Ra) was placed inside the gas volume, to characterise the gas stopping cell with respect to purity and extraction efficiency.

2 JetRIS

The JetRIS device consists of three main chambers: gas cell, jet cell and detection cell, as schematically sketched in Figure 1. The gas chamber is filled with argon gas at pressure of approximately 80 mbar, which is achieved by a gas flow of 2.45 mbar L/s. The gas cell and the jet cell are connected via a converging-diverging nozzle with a 1 mm orifice to ensure

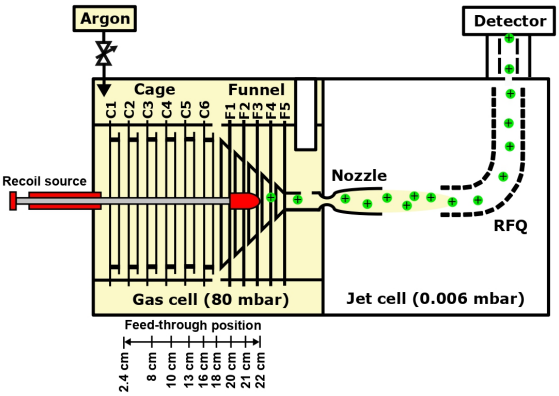

Fig. 1: *Schematic setup of the JetRIS apparatus. The position of the recoil source can be modified by a manual linear feedthrough and placed accordingly between the cage and funnel electrodes. The ions are transported to the nozzle by electrostatic fields produced by the two sets of electrodes, where a gas-jet is formed. The ions are then guided with a 90° bent RFQ towards the detector.*

the formation of a hypersonic gas jet. As the properties like efficiency and spectral resolution of the gas jet are dependent on the pressure ratio between gas cell and jet cell, the jet cell pressure was set to approximately $6 \cdot 10^{-3}$ mbar [3]. An important asset of the setup is the gas purifier (MonoTorr, SAES), which is used for the purification of the argon gas entering the gas cell in order to minimize the impurities in the gas cell, which can lead to neutralization and molecule formation of the isotopes under study.

The radioactive recoil source was mounted on a linear feedthrough manipulator structure,

enabling us to change the position of the recoil source along the middle axis of the gas cell between the positions 2.4 cm, corresponding to a placement between cage 1 and 2, and 22 cm, corresponding to a position between funnel 3 and 4. The position with respect to the cage and funnel structures are indicated in Figure 1.

The recoil ions are guided in the gas cell towards the flow channel and nozzle by electric fields produced by two sets of cylindrical electrodes labeled as cage and funnel. The cage structure consists of six electrodes of identical diameters (C1 to C6). A voltage divider created from five identical resistors is used to apply the voltages to the cage electrodes. The funnel electrodes diameters are decreasing from F1 to F5 in order to guide the ions towards the nozzle, transferring them to the jet cell. In the jet cell, the ions are guided to the detector by a 90° - bent radio frequency quadrupole (RFQ) [3].

3 Recoil source

For the measurements a ^{223}Ra recoil source was used. This isotope has a half-life of 11.435 days, while all daughters in the decay chain to ^{208}Pb feature even shorter half-lives, making this source ideal for characterisation measurements. Members of the decay chain include ^{219}Rn, ^{215}Po and ^{211}Bi whose half-lives are summarized in Table 1.

Tab. 1: *Half-lives, branching ratios and the corresponding literature values of the alpha energies of ^{223}Ra and its nuclides, ^{219}Rn, ^{215}Po, ^{211}Bi.*

Nuclide	Half-life $T_{1/2}$	α-branch ratio %	α Energy (keV)
^{223}Ra	11.435 days	51.2	5716.23
		25.0	5606.73
		8.9	5747.0
		8.9	5539.8
^{219}Rn	3.96 s	79.4	6819.1
		12.9	6552.6
		7.5	6425.0
^{215}Po	1.718 ms	100	7386.1
^{211}Bi	2.14 min	83.45	6622.9
		16.19	6278.2

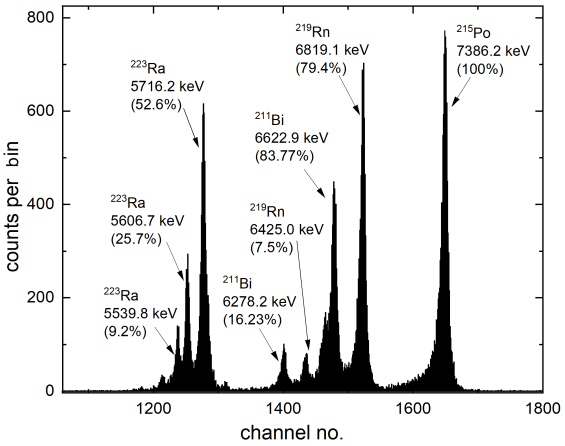

Fig. 2: *Alpha spectrum of the ^{223}Ra recoil source, showing the decay chain of the short-lived daughters, their α energies and branching ratios.*

3.1 Energy calibration

In order to perform an energy calibration of the alpha detector, an alpha spectrum (see Figure 2) of the recoil source was measured at four different relative positions between the recoil source and the silicon detector. In Table 2 the positions are given as the reading on the outside lever of the feedthrough manipulator structure, corresponding to different source positions inside of the vacuum chamber used for calibration. The initial distance between the source and the detector is not known to a suitable precision, but can also be determined from the activity fitting by adding an additional free parameter

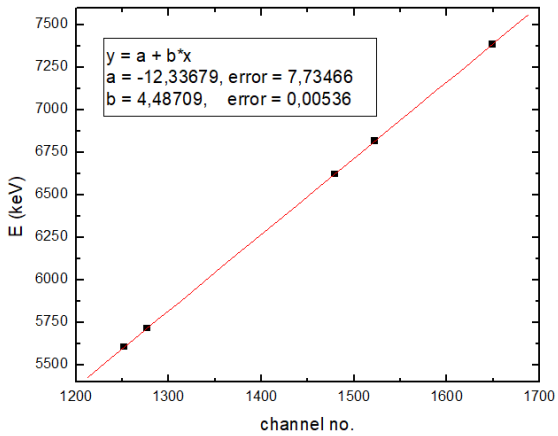

Fig. 3: *Energy calibration of recoil source using the literature values of α energies listed in Table 1 and the corresponding channels.*

(see Figure 4). In the spectrum shown in Figure 2 one can observe the presence of a low energy tailing, which is characteristic to alpha decay measurements due to the energy loss of the alpha particles caused by inelastic collisions.

As the alpha spectrum was recorded in channels or bins, a calibration of the channel to actual decay energy is required. For this the measured peaks were fit with a Gaussian function, thus determining the channel positions of the respective centroid positions. For each obtained centroid, the corresponding alpha energy is associated by comparison with literature values. From a linear dependence between the two parameters the energy calibration was obtained as shown in Figure 3.

3.2 Activity determination

The strength or activity of the used source is crucial for the determination of the transport efficiencies. Thus, the activity was calculated starting from the measured count rates of ^{223}Ra within the spectrum. From the spectrum the peaks corresponding to ^{223}Ra are selected for each relative distance and the counts are calculated. Subsequently, the extracted total counts (N) were divided by the measurement time to obtain the count rates ($R = N/t$).

The count rate is then plotted as a function of distance x as shown in Figure 4. Assuming a point like source in far distance from the detector, the dependence can be described with the formula:

$$R = \frac{\Lambda \cdot 600}{4\pi(x + x_i)^2} \qquad (1)$$

Here, Λ is the activity measured in Bq, 600 mm^2 $= \pi r^2$ is the active area of the detector, with a diameter of $2r = 27.639$ mm, x is the relative position of the source with respect to detector and x_i the unknown distance between source and detector. ^{223}Ra decays via alpha-decay with a branching ratio of 100%. Moreover, the detection efficiency ε is also assumed

Tab. 2: *Measured count rate of ^{223}Ra*

distance (mm)	time (min)	N (counts)	N/t (cps)
50	10	11341	18.9
75	10	6687	11.1
100	10	4241	7.0
150	15	3244	3.6

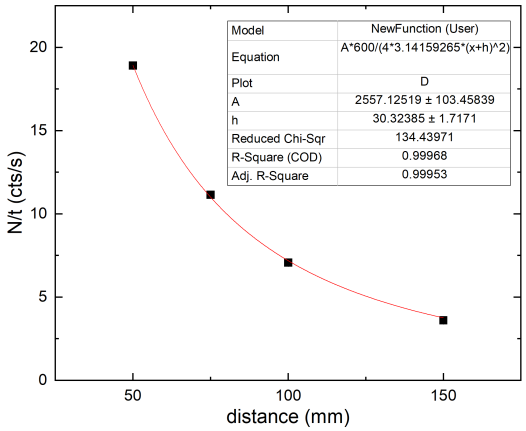

Fig. 4: *Activity of ^{223}Ra source in function of the measured distance between source and detector.*

to be 100%. Fitting equation (1) (see Figure 4), the obtained activity on the 12$^{\text{th}}$ of August was obtained as:

$$\Lambda = 2557 \pm 103 \text{ Bq} \qquad (2)$$

with an offset distance between source and detector of $x_i = 30.3 \pm 1.7$ mm.

3.3 Transport efficiency

Figure 5 shows a spectrum taken at the gas cell setup including the gates used for identifying the count rates. It can be noted that an increased noise level at the gas jet setup deteriorated the recorded alpha signals leading to a decreased resolution. The gates for ^{219}Rn were chosen as channels 1315 and 1415, while for ^{215}Po the

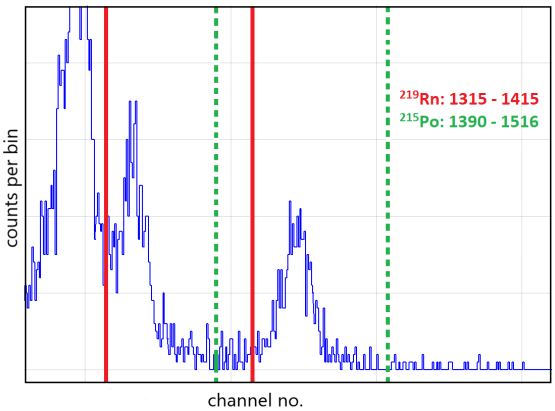

Fig. 5: *Regions of interest of ^{219}Rn (red) and ^{215}Po (green) in the mcpha software.*

gates were chosen to be the channels 1390 and 1516. An overlap is encountered in the region 1390 - 1415, which will slightly overestimate the measured ^{219}Rn count rate, as the software does not allow the selection of gates narrower than 100 channels. In our evaluation we only take the ^{219}Rn peak with the corresponding branching ratio of 79.4% into consideration (see Table 1), which will result in an additional 0.8 factor in the computation of the efficiency.
The ion transport efficiency is defined as the detected rate over the total emitted rate of ^{215}Po or ^{219}Rn from the recoil source [5]. In order to compute the total rates, one must make some assumptions. First, only 50% of the ^{219}Rn recoil ions will be emitted away from the recoil source holder upon the decay of the mother nuclide ^{223}Ra. Second, only 50% of the implanted ^{219}Rn ions will be detected due to the decay in all spatial directions.

$$R_{\mathrm{Rn}}^{\mathrm{tot}} = \frac{1}{2} \cdot \frac{1}{2} \cdot \Lambda(t) = \frac{1}{4}\Lambda(t) \qquad (3)$$

During the decay of the ^{219}Rn ions, only half of the ^{215}Po daughters are implanted in the detector. Similarly, by decaying through emission of alpha particles, 50% of the ^{215}Po will be detected, resulting in a rate of:

$$R_{\mathrm{Po}}^{\mathrm{tot}} = \frac{1}{2} \cdot \frac{1}{2} \cdot \frac{1}{2} \cdot \Lambda = \frac{1}{8} \cdot \Lambda(t) \qquad (4)$$

In the expression of the transport efficiency of ^{219}Rn, a factor of 0.8 must be added as explained before. Thus, one has the following transport efficiencies:

$$\varepsilon_{\mathrm{trans}}^{\mathrm{Rn}} = \frac{R_{\mathrm{Rn}}^{\mathrm{det}}}{R_{\mathrm{Rn}}^{\mathrm{tot}}} = \frac{1}{0.8} \cdot \frac{R_{\mathrm{Rn}}^{\mathrm{det}}}{\frac{1}{4}\Lambda(t)} \qquad (5)$$

$$\varepsilon_{\mathrm{trans}}^{\mathrm{Po}} = \frac{R_{\mathrm{Po}}^{\mathrm{det}}}{R_{\mathrm{Po}}^{\mathrm{tot}}} = \frac{R_{\mathrm{Po}}^{\mathrm{det}}}{\frac{1}{8}\Lambda(t)} \qquad (6)$$

Knowing the activity of the recoil source determined on the 12$^{\mathrm{th}}$ of August, and the half-life of ^{223}Ra to be 11.435 days, we find the activity at the time of the performed measurements using:

$$\Lambda(t) = \Lambda_0 \cdot e^{-\lambda t}, \qquad \lambda = \frac{\ln 2}{T_{1/2}} = \frac{\ln 2}{11.435\ \mathrm{d}} \qquad (7)$$

4 Results and discussion

All electrode potentials were optimized by performing measurements of the count rates as a function of applied voltages. The final parameters for highest efficiency are listed in Table 3. First, the position of the silicon detector biased at -2000 V was optimized by varying the height in respect to the transport electrodes using a feedthrough manipulator structure.
These measurements were performed on 17$^{\mathrm{th}}$ August, when the activity of the source was:

$$\Lambda = 1888.54 \pm 76.07\ \mathrm{Bq} \qquad (8)$$

The resulting transport efficiency in dependence of the position indicated at the feedthrough is shown in Figure 6 with an optimal setting at the position of 115 mm on the feedthrough scale.

Tab. 3: *Parameters after optimization for feedthrough position 22 cm.*

Setting	Value
Source voltage	2 V
Entrance plate	-3 V
RFQ DC Min	-9 V
RFQ DC Max	-10 V
Exit plate	-50 V
Transport electrode 1	-400 V
Transport electrode 2	-1000 V

The first improvement of the setup was done by adding a tantalum shield cut in the shape of a circle and placed right behind the recoil source (see Figure 7). Its role is to act as a deflector, preventing the recoil ions from being attracted by the grounded flange closing the front of the gas cell, which reduced the detected count rates to $\sim$ 1 Hz of ^{215}Po and $\sim$ 1.5 Hz of ^{219}Rn.

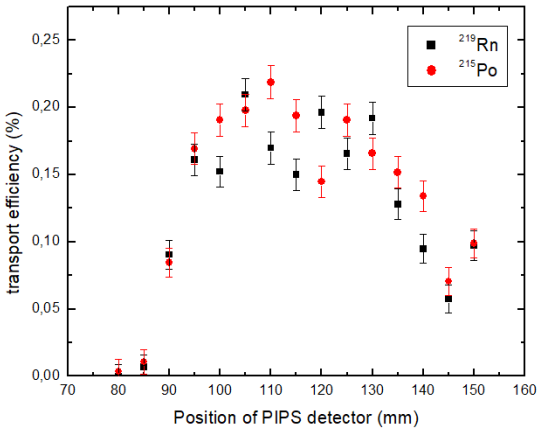

Fig. 6: *Transport efficiency of ^{215}Po and ^{219}Rn as a function of the PIPS detector position in the detector chamber.*

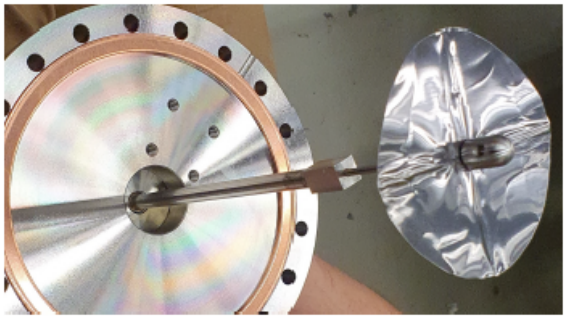

Fig. 7: *Insertion of tantalum shield behind the recoil source [4].*

Adding the tantalum shield led to significantly higher count rates of $\sim$ 5.7 Hz of ^{215}Po and $\sim$ 8.1 Hz of ^{219}Rn.

These sets of measurements were performed on 24$^{\text{th}}$ August. The activity can be calculated from equation (7) and results in:

$$\Lambda \cong 1236.52 \pm 49.77 \text{ Bq} \qquad (9)$$

Table 4 summarizes the values of the source voltage, feedthrough position and ^{215}Po and ^{219}Rn counts for the following applied voltages on the cage and funnel structures: cage high = 30 V, cage low = 22 V, F2 = 20 V, F3 = 15 V, F4 = 10 V and F5 = 5 V.

In the evaluation of the ^{219}Rn count rates we have not taken into account the tailing of ^{219}Rn towards lower energies, whereas we are wrongly counting in the high-energy tailing of ^{211}Bi. This might lead to some discrepancies in the extracted efficiencies of ^{215}Po and ^{219}Rn. Figure 9 shows the dependence of the transport efficiency on the feedthrough position, clearly

Tab. 4: *Optimization of source potential for different positions of the source.*

Source voltage (V)	Fth. dist. (cm)	Pos. in gas cell	^{215}Po rate (cps)	^{219}Rn rate (cps)
13	22	F3 – F4	5.65	8.11
13	22	F3 – F4	5.59	8.06
15	21	F2 – F3	4.79	6.76
16	20	F2 – F3	4.41	6.47
16	19	F1 middle	3.57	4.89
22	18	C6 – F1	3.14	5
22	17	C6 middle	2.32	3.85
22	16	C6 start	1.70	2.58
22	15	C5 – C6	1.19	1.5
22	15	C5 – C6	1.26	2.32
24	14	C5 end	1.13	2.23
24	13	C5 middle	0.64	1.78
25	12	C4 – C5	0.60	1.41
22	10	C4 middle	0.08	0.30
25	10	C4 middle	0.30	1.44
25	8	C3 middle	0.48	1.56
28	2.4	C1 – C2	0.11	0.71
0	2.4	C1 – C2	0.17	0.93
15	12	C5 – C6	0.63	1.09

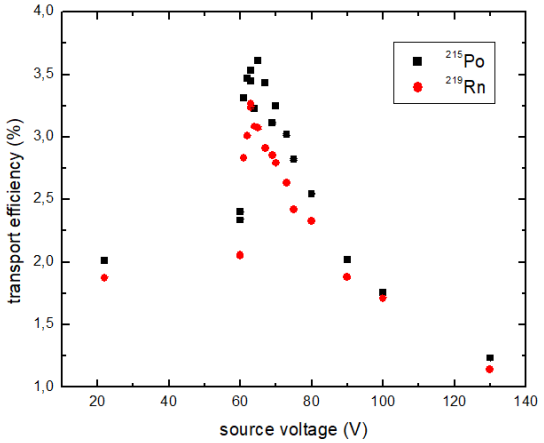

Fig. 8: *Transport efficiency of ^{219}Rn and ^{215}Po as a function of source voltage, when the feedthrough position is 18 cm, corresponding to the position of the recoil source between C6 and F1. Best optimization found for the applied voltage on the source of 63 V.*

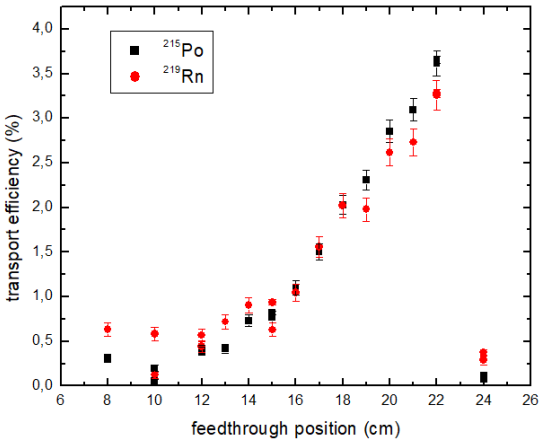

Fig. 9: *Transport efficiency of ^{215}Po and ^{219}Rn as a function of the source position in the gas cell. The applied voltages on the cage and funnel electrodes were: cage high = 30 V, cage low = 22 V, F2 = 20 V, F3 = 15 V , F4 = 10 V and F5 = 5 V.*

indicating a decrease in efficiency upon increasing the distance between nozzle and recoil source.

Further prospects of the JetRIS optimization would be the characterisation of the extraction time from different recoil source positions.

5 Conclusions

In this report measurements were performed with the newly commissioned JetRIS setup in order to characterize and optimize the transport efficiency from the gas cell. In order to do so, the overall efficiency was investigated using a ^{223}Ra recoil source. In the measurements performed in this work the detector position, the voltages applied in all three chamber parts, as well as the recoil source position and potential inside of the gas cell were investigated and optimized on maximum detected count rates of the daughter nuclei ^{219}Rn and ^{215}Po. An important change in the system was the implementation of a tantalum shield behind the recoil source, significantly improving the detected count rates.
In future measurements the extraction times from different recoil source positions in the gas cell should be investigated. Furthermore, the gas purity should be investigated, as the observed count rate was strongly dependent on the argon gas purity.

Acknowledgments

I would like to express my gratitude towards my tutor and scientific coordinator, Sebastian Raeder and thank him for his guidance over the length of the project. I would kindly want to thank the entire team from the laser department at SHIP, especially to Steven Nothhelfer, Jeremy Lantis and Tom Kieck, for their constant help, advice and shared knowledge throughout my project experience in the Summer Student Program.

References

[1] M. Laatiaoui et al., *On laser spectroscopy of the element nobelium (Z=102)*, in The European Physical Journal D **68**, 71 (2014).

[2] Yu. Kudryavstev et al., *The in-gas-jet laser ion source: Resonance ionization spectroscopy of radioactive atoms in supersonic gas jets*, in Elsevier, B **297** (2013) 7-22.

[3] Steven Nothhelfer, *Advances in laser spectroscopy of superheavy elements: Resonance ionization spectroscopy on ^{253,254,255}Es and a new gas-jet based high-resolution spectroscopy setup*, Dissertation, Johannes Gutenberg-Universität Mainz, (2022).

[4] Julian Auler, *Characterization of a gas-jet apparatus for laser spectroscopy of the heaviest elements*, Master Thesis, Johannes Gutenberg-Universität Mainz, (2022).

[5] S. Raeder et al., *A gas-jet apparatus for high-resolution laser spectroscopy on the heaviest elements at SHIP*, in Elsevier, B **463** (2020) 272-276.

[6] Oliver Kaleja, *Mass measurement of ^{197}Au at SHIP and the first on-line test of the novel cryogenic gas stopping cell at SHIP*, Master Thesis, Technische Universität Darmstadt, (2016).

[7] Oliver T. Kaleja, *High-precision mass spectrometry of nobelium, lawrencium and rutherfordium isotopes and studies of long-lived isomers with SHIPTRAP*, Dissertation, Johannes Gutenberg-Universität Mainz, (2020).

[8] F. Lautenschlager et al., *Developments for resonance ionization laser spectroscopy of the heaviest elements at SHIP*, in Elsevier, B **383** (2016) 115-122.

Picosecond Timing Precision of the DiRICH-FEE for the PANDA Barrel DIRC

Davide Panico
University of Naples "Federico II", Italy - panico.davide@outlook.it

Utkarsh Verma*
IIITDM Kancheepuram, India - utkarshverma@protonmail.com

The $\bar{P}ANDA$ experiment at the Facility for Antiproton and Ion Research in Europe (FAIR) will address fundamental questions of hadron physics. Reliable Particle Identification (PID) will be crucial for meeting the objectives of the $\bar{P}ANDA$ experiment. Charged PID will be provided by different DIRC (Detection of Internally Reflected Cherenkov light) detectors: the Barrel DIRC and the Endcapc Disc DIRC. This work describes the improvements in timing resolution we obtained.

1 Introduction

1.1 $\bar{P}ANDA$ Detector

The physics of strong interactions is the area of modern physics dealing with phenomena such as quark confinement and the origin of hadron masses. The $\bar{P}ANDA$ (antiProton ANnnihilation at DArmstadt) experiment which will be installed at the High Energy Storage Ring (HESR) for antiprotons in the future Facility for Antiproton and Ion Research (FAIR) will address these questions and also investigate topics such as:

- Hadron Spectroscopy
- Behaviour of Hadrons in matter
- Nucleon Structure
- Hypernuclei

For more details about the rich physics programs see [1].

To investigate these topics the final detector is subdivided into two parts: the target spectrometer (TS) consisting of a solenoid around the interaction region, and a forward spectrometer (FS) based on a dipole to measure the momentum of the forward-going particles (see Fig. 1) .

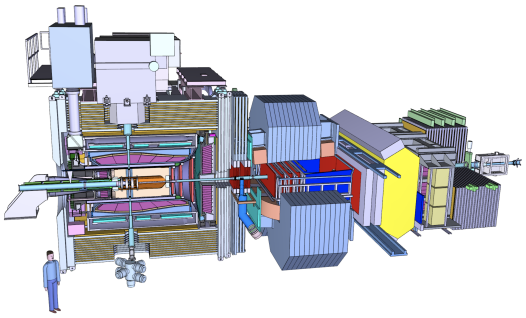

Fig. 1: *The PANDA detector (From [1]).*

The identification of charged particles with good accuracy is one of the key requirements for unveiling many aspects of the physics program of the PANDA experiment. Therefore, the PANDA Detector will be equipped with various dedicated particle identification (PID) systems. This allows the classification of particles over the whole kinematic range with the additional help of $\frac{dE}{dx}$ measurements from tracking and information from the electromagnetic calorimetry.

1.2 Barrel DIRC

Two fast and compact Cherenkov counters (the Barrel DIRC and the Endcap Disc DIRC) will provide PID in the PANDA Target Spectrometer. They are using Detection of Internally Reflected Cherenkov (DIRC) light technology based on the *BABAR* DIRC. In addition, there

*GET_INvolved Student

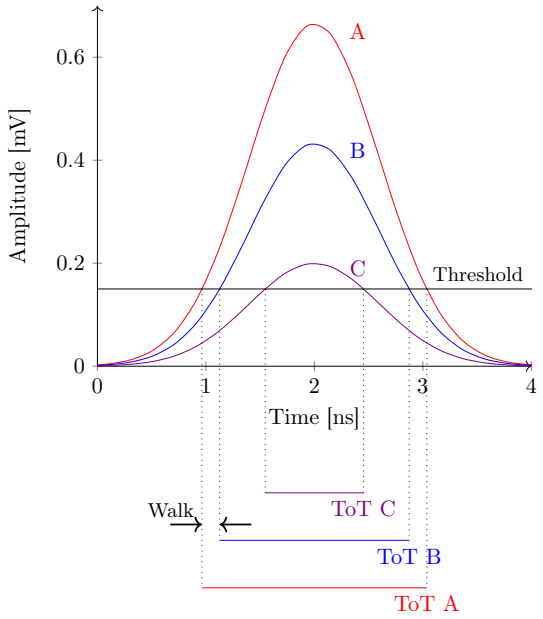

Fig. 2: *Time Over Threshold measurement.*

are major improvements for $\bar{P}ANDA$, such as a focusing lens system, fast timing electronics, and Microchannel-Plate PMTs (MCP-PMTs) for photon detection. In contrast to conventional Ring Imaging Cherenkov (RICH) counters, DIRC detectors use high-precision quartz bars or plates as radiator material to produce and transport the Cherenkov light via total internal reflection. Focusing optics image the Cherenkov photons on arrays of MCP-PMTs and the arrival time of the photons is measured with excellent timing precision. In both DIRCs, the arrival in time and the time-over-threshold of the PMTs signals are recorded.

2 Time Over Threshold (ToT)

The Time Over Threshold (ToT) can provide a meausure for the signal amplitude by using the pulse width of a discriminator logical output as shown in Fig 2. The discriminator compares the signal voltage with a threshold and outputs the digital pulses whose lengths are related to the signal amplitude (Fig 2). The advantage of the ToT technique is that it does not need a costly ADC circuit.

2.1 Time Walk and Jitter

One method to measure the timing precision of a system is to analyse the time difference between two exactly coincident signals. The capability of the system to distinguish small time signals (the timing resolution), usually called *resolving time*,is taken as the RMS of the distribution of time differences.
However this precision is limited by *walk* and *jitter* as explained in great detail in [3].

The *walk* effect is caused by variations in the amplitude (or rise time) of the incoming signals. In fact, higher signals (A in Fig. 2) will cross the discriminator threshold faster than lower ones (C in Fig. 2), thus degrading the timing precision.

Another major contribution to the timing fluctuations is given by noise in both the detector and the electronics. Because of these random fluctuations, two identical signals will cross the discriminator threshold at different points in time dependent on the amplitude of these fluctuations. This effect is usually referred to as *jitter* and can be described by the following formula:

$$\sigma_{time} = \frac{\sigma_n}{\left|\frac{dA_{signal}}{dt}\right|} \tag{1}$$

Where σ_{time} is the timing fluctuation due to jitter, σ_n is the amplitude variation due to noise and dA_{signal}/dt is the slope of the amplitude of the signal. Thus the timing precision strongly depends on signal rise time: the faster the rise time the better the timing precision of the system.

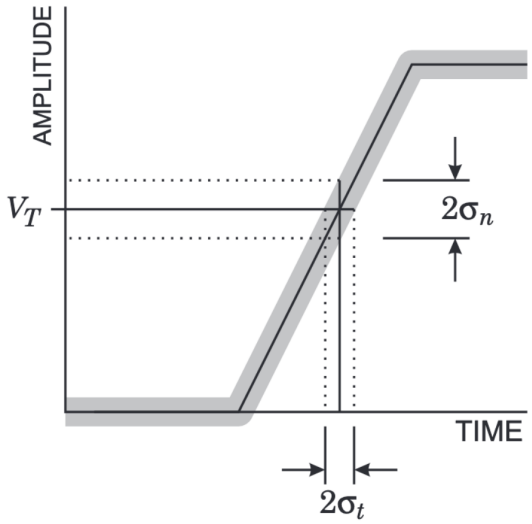

Fig. 3: *Timing Jitter: The timing resolution depends inversely on the slope of the signal at the trigger point. (From [4])*

Thus, in general, the accuracy of any timing measurement is limited by the jitter (caused by noise) and by the time walk (caused by different amplitudes/rise times of incoming signals).

3 Experimental Setup

To measure the timing precision of the system, a Picosecond Laser (PILAS) has been used to generate the single photons for the 64 8mm x 8 mm pixels of the Photonis XP85012 MCP-PMTs and an analog trigger to the front end electronics: the DiRICH boards. The timing precision for each pixel has then been obtained as the RMS of the distribution of the difference between the two coincident signals (the trigger and the photon signal).

Each DiRICH consists of 32 pre-amplifier channels that shape and amplify the raw signals from the MCP-PMTs, and a discriminator implemented in a FPGA. The typical single photon PMT signal is a pulse with a $\approx$ 3 ns width and an amplitude of $\approx$ 5 mV. The input signals are discriminated and digitized, using the differential input line receivers of the FPGA (i.e. the signal on one line and the threshold on the other line) [2].

To measure the timing precision for just the electronics itself, the signal from a fast pulser has been fed into two channels of the DiRICH and then the timing difference between the two has been analyzed as explained before.
In fact, these large signals are only minor affected by noise. The measurements have been carried out in a dark box as shown in Fig.4 by delivering the laser photons via optical fibers.

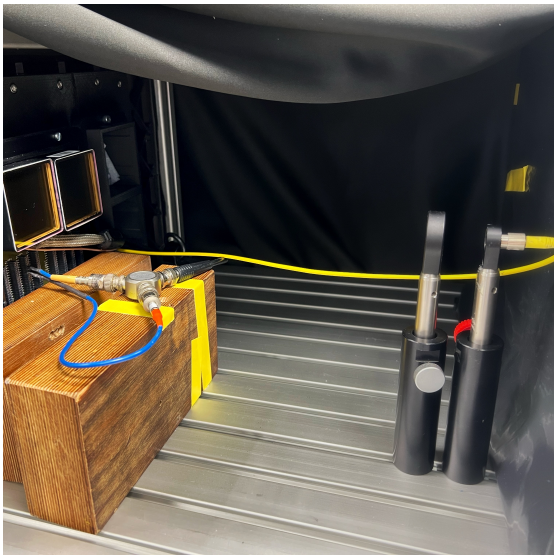

Fig. 4: *Experimental Setup: Two MCP-PMTs are shown on the left side of the picture. On the right side, the laser optic fiber with a diffuser is positioned in front of the MCP-PMTs.*

4 Results

The main result is a significant improvement in the timing precision of the system after the discovery and systematic investigation of the overshoot of the output signal of the DiRICH pre-amplifier(Fig. 5). It was deliberately added by design to increase the steepness of the Trailing Edge signal as explained in [2] and thus to reduce the error on the Trailing Edge timing determination of a signal like in Fig. 5 (as described by Eq.1). Previously, the discriminators were set to negative thresholds. In the case of negative signals (i.e. the MCP-PMTs signals), this simply meant measuring the timing of the overshoot of the signal rather than the actual signal peak.

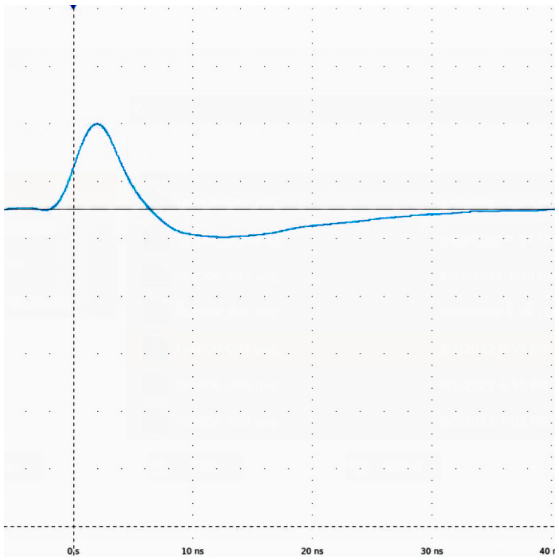

Fig. 5: *Scope view of the output of the DiRICH preamplifier stage of a fast (3 ns) negative pulse input (10 mV). Thus, the positive signal is the amplified signal while the negative one is the overshoot.*

After setting the thresholds to a positive value, it was discovered that to measure the ToT in the right way, the input LVDS signal to the FPGA had to be inverted to account for the inverted discriminator output being fed to the TDC. This ensures the right sequence in time for leading and trailing pulse edges.

These corrections we applied have been validated by multiple experiments performed using a waveform generator.
In particular, the positive threshold setting has been tested by feeding a negative square pulse of 4 ns time width and variable amplitude to the DiRICH inputs in order to analyze the measured TOT as shown in Fig.6.
For testing the TDC inversion, a negative square pulse of 7 mV having variable pulse width has been fed to the DiRICH inputs. The results are shown in Fig.7.
Without TDC inversion the FPGA was measuring ToT in the wrong way (i.e. the difference between the trailing edge and a delayed leading edge). Due to the wrong "polarity" of the output logical signal, this resulted in a decrease in measured ToT for longer pulses. In fact, the trailing edge has to its shallower slope a worse timing precision compared to the steeper leading edge.

To measure the timing precision for just the electronics itself, the Gaussian signal of a 20 mV amplitude and width of 4 ns from a fast pulser has been fed into two channels of the DiRICH and then the timing difference between the two has been analyzed. In Fig. 8 such distribution with a superimposed Gaussian fit (red line) is shown, giving a timing precision of $\sigma_{el} = 9.13 \pm 0.01$ ps.

To measure the timing resolution of the entire system (the MCP-PMT and the electronics) the PILAS has been used. For each channel, the two-dimensional histogram shown in Fig. 9 of the time difference between the MCP-PMT signal and the laser trigger signal vs Time Over Threshold was plotted.
Then the projection of the 2D histogram on the y-axis (Time difference) is cut in a sharp

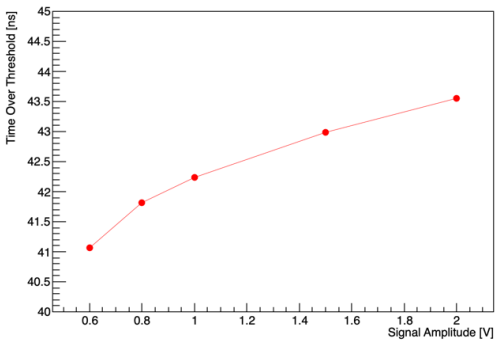

Fig. 6: *Plot of measured pulse amplitude (ToT) vs pulse generator set amplitude (absolute value) for negative fast (4 ns) signals and positive threshold. As clearly shown, with a positive threshold, the measured ToT increases as the signal amplitude (see Fig 2).*

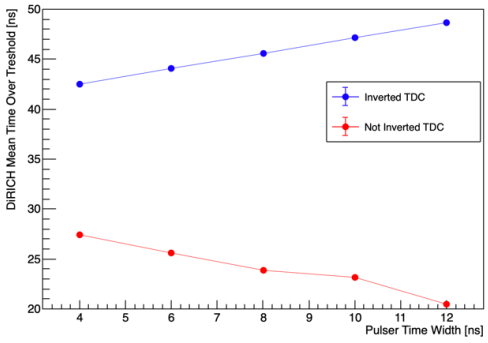

Fig. 7: *Plot of measured pulse width (ToT) vs pulse generator set width for negative signals and positive threshold. As clearly shown, with inverted TDC for longer signals the measured ToT increases as expected.*

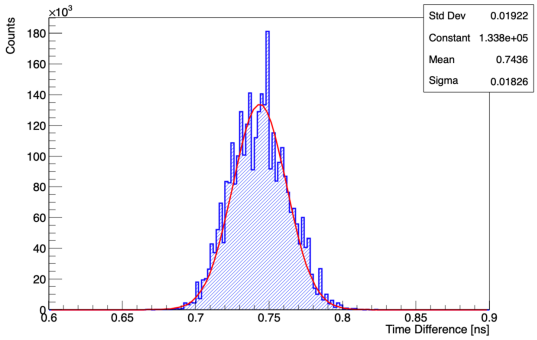

Fig. 8: *Distribution of time differences between the two pulser channels. The timing resolution for just the electronics itself is calculated as* $\sigma_{el} = \frac{\sigma_{dist}}{\sqrt{2}} = 12.91 \pm 0.01$ *ps. The fit line is in red.*

region around the ToT maximum ($|ToT - Maximum| < 10$ps). This sharp cut minimises the walk effect. The result is shown in Fig. 13 while in Fig. 10 the same 2D histogram is shown for the pulser channel. Here the shape of the graph is not affected by walk as the pulser has a constant amplitude. This results in a bi-dimensional Gaussian.

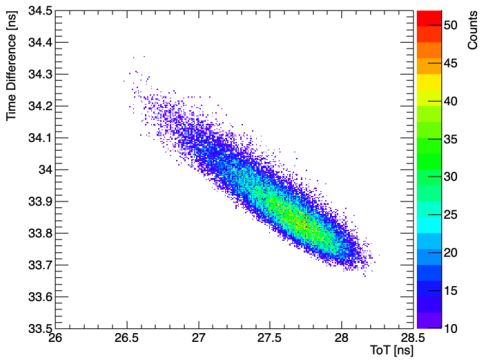

Fig. 9: *Two-dimensional histogram of time difference vs ToT for a particular pixel. Notice the "banana-like" shape of the graph caused by the walk effect.*

The final timing precision is given as the average over the channels as shown in Fig.11 giving as result a value of $\sigma_{system} = 73 \pm 14$ ps.

The two contributions to the final timing precision of the system (detector and electronics) can be separately seen in Fig. 13 and Fig. 8.

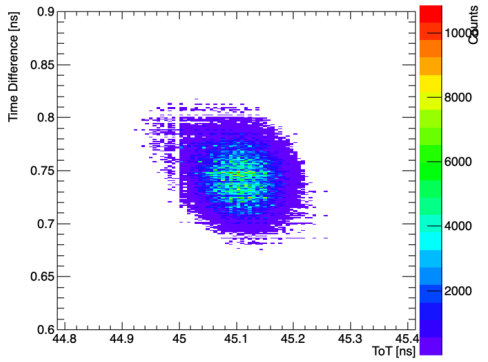

Fig. 10: *Two-dimensional histogram of Time Difference vs ToT for pulser channel. The shape of the graph is very different from the one in Fig. 9 because the pulser is less affected by time walk.*

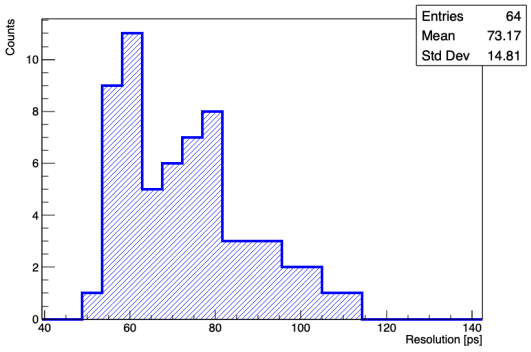

Fig. 11: *Distribution of the timing precision for each channel. The value shown for each channel is the Standard Deviation of the Gaussian fit of the Time Difference peak (see Fig.13). Source code in [7]*

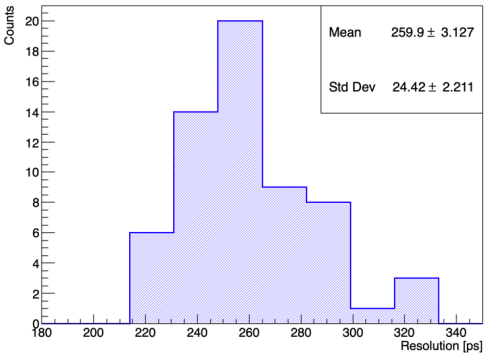

Fig. 12: *Distribution of RMS for each channel. The value shown for each channel is the RMS of the Time Difference distribution (see Fig.12).*

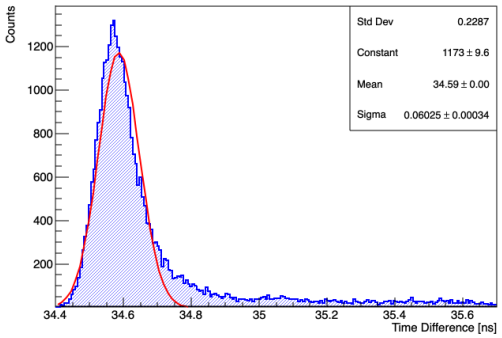

Fig. 13: *Distribution of time difference between the photon signal and the laser trigger signal for a particular pixel.*

As evident from Fig. 13 and Fig. 8 the timing precision for the MCP-PMT channels are spoiled by a right tail in the time difference distribution causing the RMS to be 228 ± 1 ps while the peak itself shows a timing precision of $\sigma_{ch} = 60.2 \pm 0.3$ ps.

5 Conclusions

The setting of a positive threshold together with the inversion of the LVDS signal as input to the FPGA line receivers has shown to produce a sensible improvement in the timing precision of the overall detector system.
In particular, the RMS has an average value of $RMS_{system} = 260 \pm 24$ ps and the average channel resolution of $\sigma_{system} = 73 \pm 14$ ps represents a significant improvement compared to the previous value between 150 ps and 215 ps [6] .
The electronics show a better timing precision of $\sigma_{electronics} = 12.91 \pm 0.01$ ps compared to the previous result of 32.31 ± 0.02 ps [6].

Acknowledgments

We want to express our heartfelt gratitude to our supervisor Carsten Schwarz for his infinite patience and for the vast experience and expertise he shared with us. We also want to thank Manuel Reyes, Yannic Wolf and Georg Schepers for their help and support.
We desire to extend our thanks to Ralph Averbeck and Pradeep Ghosh for the impeccable organisation of the Summer Student and GET_INvolved programs respectively. Finally, our biggest thanks go to our families and friends for their constant support and encouragement.

References

[1] PANDA Collaboration, https://panda.gsi.de/article/panda-physics, visited on September 2022.
[2] V. Patel and M. Traxler *JINST* **13** C03038 (2018)
[3] W.R. Leo, *Techniques for Nuclear and Particle Physics Experiments*, Springer-Verlag, Berlin (1987).
[4] H. Spieler, *Semiconductor Detector Systems*, OUP, Oxford (2005).
[5] PANDA Collaboration, *Technical Progress Report*,Darmstadt (2005).
[6] M. Salvan, *Picosecond Readout Electronics for a Cherenkov Detector*,Summer Student Report Book,Darmstadt (2019).
[7] DiRICH Fit Routine Source Code, https://github.com/UtkarshVerma/fit-hpd-gsi

Coincidence techniques for fast timing measurements

Stefanos Pelonis
Instituut voor Kern en Stralingsfysica, KU Leuven, Celestijnenlaan 200D, B-3001, Leuven, Belgium,
s.pelonis@gsi.de

A new setup for lifetime measurements in the picosecond region, utilising a $LaBr_3$ and βPlastic scintillator, has been developed and tested for the first time. The collection of the detector signal for leading-edge timing was achieved using the fast branch of the TAMEX4 module. Despite the picosecond precision of the Digitiser's internal clocks, the time precision of the scheme could only be limited to a few tens of ns, making it insufficient for the desired lifetime range. Additional investigation and testing is needed in order to reach the required level of granularity.

1 Introduction

The atomic nucleus is a multi-body system of protons and neutrons, bound together by forces with spin- and isospin-dependent components. While the shell model, which was introduced several decades ago, was largely successful for stable nuclei, as one moves to more exotic ones further away from the valley of β stability, shell evolution starts taking place [1]. In this regime, the importance of the components of the nuclear force shifts, creating a very strict test for the validity of up-to-date theoretical models. A particular observable is the B(E2) of a nuclear state, which not only heavily depends on its particular configuration, but also gives information about its collectivity. In order to calculate B(E2) values, the lifetime of the excited states of interest must be measured, since the two are connected via:

$$B(E2) = (8.156 \times 10^{-14}) E_{\gamma}^{-5} \frac{(1 - B_r)}{\tau} \quad (1)$$

where τ is the lifetime, B_r the transition branching ratio and E_γ the energy of the γ-ray depopulating the level in MeV.

Several experimental techniques suitable for different lifetime regimes exist, including Doppler Shift Attenuation Method (DSAM) [2], Recoil Distance Doppler Shift (RDDS) [3] etc. This work focuses on the Delayed Coincidence Counting (DCC) technique [4], wherein the lifetime of a level can be measured through the centroid shift in the time difference spectrum between the transitions feeding and depopulating the level of interest as:

$$\delta C \sim 2\tau \quad (2)$$

where δC is the centroid difference.

To this date, several successfully used versions of this technique have been employed, including $\gamma\gamma\gamma$ or $\beta\gamma\gamma$ coincidences. In these, the timing information of the level of interest are extracted from the γ-rays that populate and depopulate it. The third γ emission or β decay is used to isolate the selected cascade and reduce random coincidences. Nowadays, however, as one moves away from the region of β stability, it becomes increasingly important to study isomeric states that are populated directly by a β decay and deexcite through a γ emission. This more recently implemented technique has been known as $\beta\gamma$ coincidence.

2 $\beta\gamma$ Coincidence Measurement

In this method, a plastic scintillator with low Z is used for the detection of the β particle, while the delayed γ is registered in a large-volume inorganic scintillator. $LaBr_3$ ones are usually employed, due to their excellent timing characteristics and high light output. Despite that the main principle of this approach is simple, other complications quickly arise.

To date, thin plastic scintillators with uniform response to β radiation were mostly chosen. The problem with this approach is the low detection efficiency of the setup, which cannot be tolerated in cases where statistics are low.

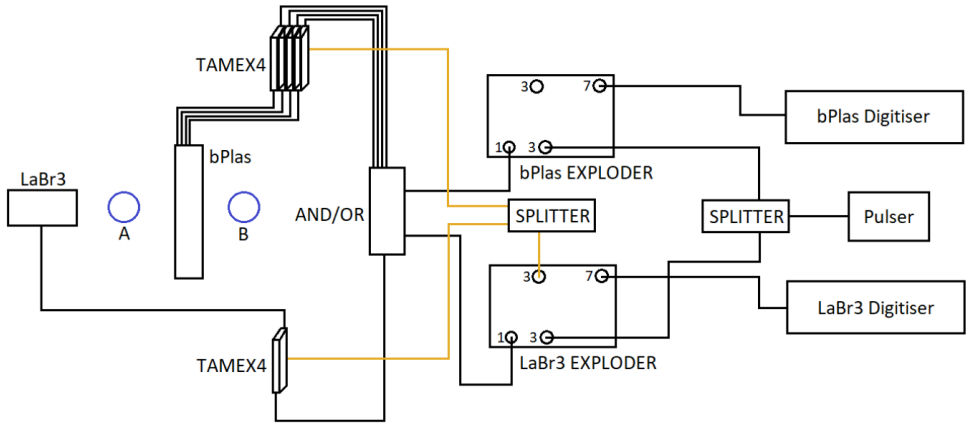

Fig. 1: *Schematic representation of the system designed for $\beta\gamma$ coincidence measurements. The orange cable indicates the $LaBr_3$ accepted trigger.*

The answer to this is a thick plastic scintillator, in which more β particles will be detected. However, the depth of the detector means that the interaction point inside it - and hence the time that it takes for it to be collected - has to be accounted for, especially when one is interested in ps lifetimes.

Another implication that is especially present in systems based on leading-edge timing is the Time-Walk effect. The idea behind this is that the registering of the leading edge time of a signal is affected by the energy of the event, especially in the low-energy regime. To account for these effects, Prompt Response Difference (PRD) curves are used in order to calibrate the time response of the detector. To provide data across a wide energy range, ^{152}Eu is usually chosen and the technique is applied to its 344 keV $2_1^+ \rightarrow 0_{gs}^+$ transition. The PRD curve is then fitted with a function of the form:

$$PRD\,(E_\gamma) = \frac{\alpha}{\sqrt{E_\gamma + \beta}} + \gamma E_\gamma + \delta E_\gamma^2 + \epsilon \quad (3)$$

and the centroid shift can finally be expressed as:

$$\delta C = 2\tau + PRD \quad (4)$$

3 Experimental Setup

To test the applicability of the $\beta\gamma$ coincidence method for the DESPEC setup at GSI/FAIR, a simple scheme comprising a $LaBr_3$ detector and a βPlastic detector was set up, as can be seen in Fig. 1. The former is a 5.5x5.5 cm^2 cylinder and utilises one SiPM. The latter is 24x8 cm^2 in dimensions and has 3-mm thick BC404 scintillating plastic. There are 48 3x3 mm^2 SiPMs along the long edges and 16 along the short edges, which are all coupled in pairs to give 24 (8) channels along the long (short) sides and 64 channels in total.

Two source positions were used, one between the two detectors referred to as A and the other behind the βPlastic one called B, so that γ radiation emitted from the source passed first through the βPlastic and was then incident on the $LaBr_3$ crystal. Five TAMEX4 TDC modules [5] were employed in the DAQ setup, one for the $LaBr_3$ scintillator and four for the βPlastic one. To read the output of the SiPMs, the specially designed analog front-end TwinPeaks was employed in conjunction with the TAMEX4 system. TwinPeaks has 16 inputs and 4 logic outputs. Each input is split into two channels, a slow one with a shaping amplifier and a discriminator for energy measurements and a fast one, with a fast amplifier and a discriminator for leading-edge timing. The outputs of the four cards for the βPlastic were connected with an OR condition and this output was then set with another OR condition with the output from the $LaBr_3$ TAMEX card. The final signal was split into two and fed as an input trigger to two EXPLODER modules [6], one for each detector

respectively. Finally, the OR accepted trigger from each EXPLODER was taken and sent to two Digitisers.

To synchronise them, two different schemes were used. In the first, the WhiteRabbit clock [7] was employed for the coincidence measurements, offering 1 ns precision. Going to sub-nanosecond precision, however, requires a method that utilises clocks with better timing precision. The Digitisers' internal clocks satisfy these requirements with their tens of ps precision and hence, they were chosen as the second approach. In it, an accepted trigger signal was taken from the $LaBr_3$ EXPLODER, split into two and then fed as input to the TAMEX4 modules of both detectors.

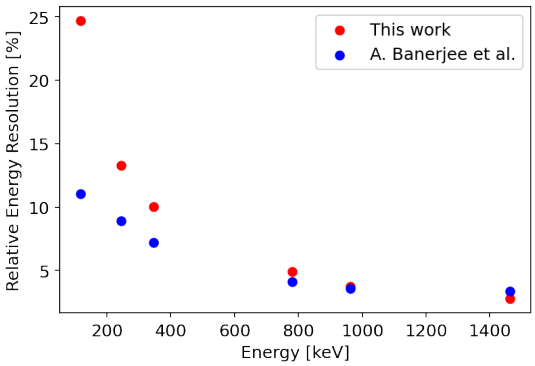

Fig. 3: *Relative Energy Resolution of the $LaBr_3$ scintillator with respect to the γ-ray energy. The data are compared with values from the FATIMA setup described in [5]. In both cases, the error bars are smaller than the data symbols.*

4 Results

4.1 Energy Calibration and Resolution using ^{152}Eu

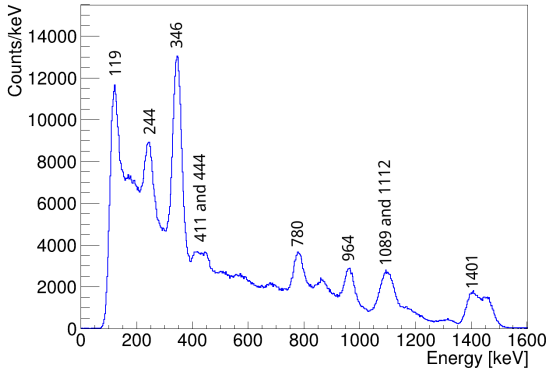

Fig. 2: *^{152}Eu decay energy spectrum obtained from the $LaBr_3$ scintillator, using the Slow Branch of of the TAMEX4 module.*

To perform an energy calibration of the $LaBr_3$ scintillator, a ^{152}Eu source was used, with the corresponding energy spectrum depicted in Fig. 2. The resolution of the detector was measured using six peaks that are not overlapping, as it can be seen in Fig. 3. The experimental data are compared with values from the FATIMA setup in [5], which consisted of 36 $LaBr_3$ detectors. The higher relative resolution in the low energy regime in our case is due to the coupling of the SiPM with the detector crystal.

4.2 Time Difference spectra using ^{22}Na

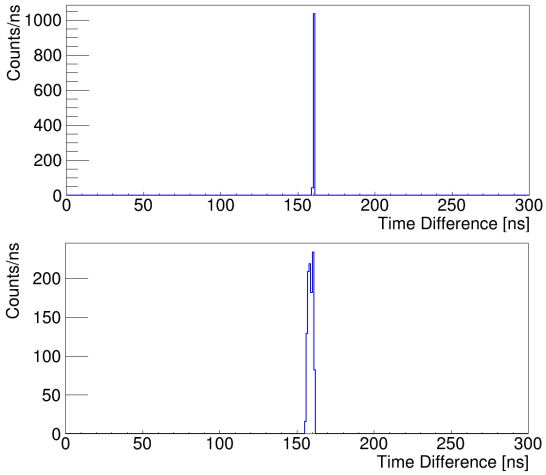

Fig. 4: *Top) ToT spectrum of the $LaBr_3$ accepted trigger, as registered by the $LaBr_3$ TAMEX4 module. Bottom) ToT spectrum of the $LaBr_3$ accepted trigger, as registered by the βPlastic TAMEX4 module.*

To test the precision of the two methods for fast timing measurements, a radioactive source of ^{22}Na was used and placed at source position A, since its 511 keV γ-rays are emitted in opposite directions and will be therefore detected simultaneously by the two detectors.

The first step in the analysis is to ensure that the Time Calibration for the system was correct. To this end, the Time over Threshold (ToT) spectrum of the $LaBr_3$ accepted trigger was measured in both detectors and found to

be around 160 ns, as it can be see in Fig. 4. This signal is a logic pulse with a fixed width around 160 ns, so the conversion factors were verified. A small variation in the mean position is due to the different thresholds set for the two detectors.

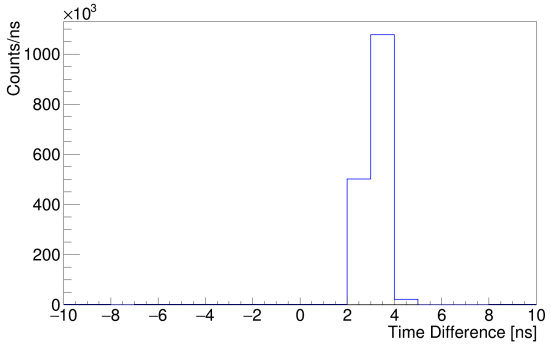

Fig. 5: *Time difference between the pair of the two detectors, using the WhiteRabbit clock.*

Since the Time Calibration was completed, one can now look on the 1 ns granularity offered by the WhiteRabbit clock between the two detectors. This is depicted in Fig. 5, where a FWHM of 0.8 ns was measured. Before moving to the second approach, it is important to emphasize again the complications of a thick scintillator, where the interaction area will shift the time difference between the events. Fig. 6 is a nice example of this, in which the time difference as a function of the channel number has been plotted for uncollimated ^{22}Na data, after gating on the 511 keV emitted γ. A physical oscillation of the average time difference can be easily observed.

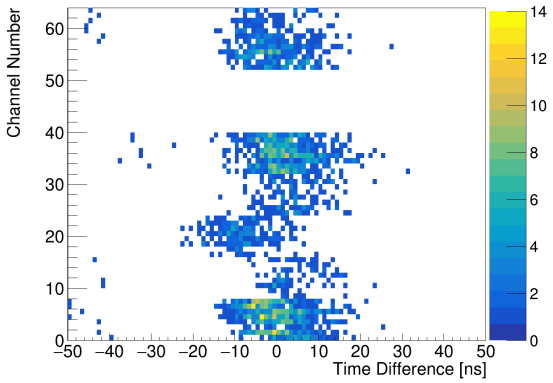

Fig. 6: *Time difference between the $LaBr_3$ and βPlastic detectors, as a function of the βPlastic channel number. The empty region between channels 42 and 54 is due to dead channels in the bPlas.*

To test the time resolution of the second approach, a single channel with a high light output was chosen from the bPlas. Thanks to this, no correction for the relative position of the channel had to be taken care of. The time difference between the two detectors was then obtained as:

$$TD = (bPlas - REF) - (LaBr_3 - REF) \quad (5)$$

where REF is the OR accepted trigger from the $LaBr_3$ EXPLODER. To better localise the interaction area and avoid ns delays due to signal propagation through the detector, a channel B opposing A was chosen, with their time difference spectrum given in Fig. 7. This spectrum corresponds to the ^{22}Na data. A gate was then set $\pm$ 5 ns around the centroid of the respective peak and used in the rest of the analysis.

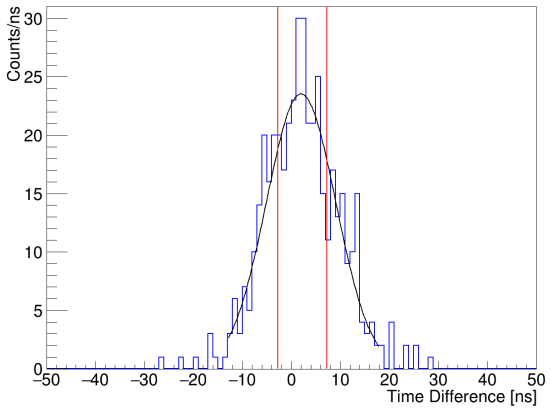

Fig. 7: *Time difference spectrum between two opposing channels in the bPlas. The red lines indicate the gating region around the centroid of the peak.*

The time difference between the two detectors for ^{22}Na data has been plotted in Fig. 8, after applying an energy gate on the 511 keV γ-ray in the energy spectrum of the $LaBr_3$ scintillator. The blue line corresponds to data before applying any gate on the time difference and the red after. A FWHM of 14.9 ns and 11.1 ns was measured for the two cases respectively. Although establishing a gate based on opposing channels in the βPlastic slightly increased the precision of the approach, the uncertainty remains too high, rendering the technique insufficient in the subnanosecond lifetime region.

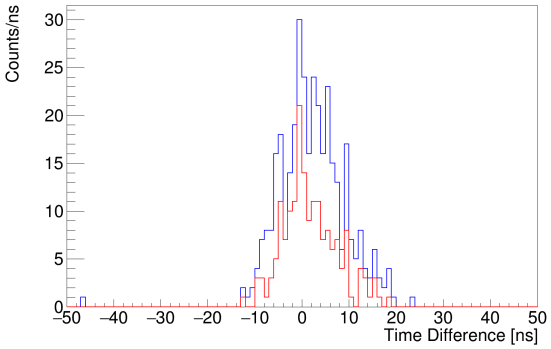

Fig. 8: *Time difference spectra between the two detectors for the ^{22}Na source. The data before the application of any time gate are depicted in blue, while the ones after in red.*

5 Discussion

A new scheme to measure picosecond lifetimes, utilising the TAMEX4 module and the internal clock of the Digitisers, was proposed and tested for the first time. The energy calibration and resolution was obtained with a ^{152}Eu source, while the conversion factors for the time resolution were verified using the EXPLODER's accepted trigger. A radioactive source of ^{22}Na was used in a non-collimated configuration, to test the time response of the setup. Although no possible flaw in the DAQ was observed, the time resolution of the proposed method proved to be inadequate for lifetime measurement below a few ns. Further investigation is needed to determine the reason behind the poor time resolution observed. Possible reasons could be a detector defect, incorrect signal processing, noise in the accepted trigger etc. However, this attempt can be used as a useful reference for future $\beta\gamma$ coincidence scheme.

Acknowledgments

I would like to thank my tutor Dr. Helena M. Albers, for her guidance and help during the course of the past two months and Dr. Biswarup Das, who assisted me in every step of the project and kept me company in the office. Finally, special thanks should go to H. Schaffner and G. Aggez for setting up part of the DAQ.

References

[1] Takaharu Otsuka, Alexandra Gade, Olivier Sorlin, Toshio Suzuki, and Yutaka Utsuno. Evolution of shell structure in exotic nuclei. Rev. Mod. Phys., 92:015002, Mar 2020.

[2] S Devons, G Manning, and D St P Bunbury. Measurement of -transition lifetimes by re- coil methods. Proceedings of the Physical So- ciety. Section A, 68(1):18–31, jan 1955.

[3] A. Dewald, O. M oller, and P. Petkov. De- veloping the recoil distance doppler-shift technique towards a versatile tool for life- time measurements of excited nuclear states. Progress in Particle and Nuclear Physics, 67(3):786–839, 2012.

[4] E. I. Rekhin, P. S. Chernov, and S. G. Basiladze. The coincidence counting method. Moscow Atomizdat, January 1979.

[5] A. Banerjee et al. Analog front-end for fpga- based readout electronics for scintillation de- tectors. Nuclear Instruments and Methods in Physics Research Section A: Accelera- tors, Spectrometers, Detectors and Associ- ated Equipment, 1028:166357, 2022.

[6] EXPLODER, a hardware board developed by GSI Experiment Electronics department.

[7] The White Rabbit project. www.ohwr.org/projects/white-rabbit.

Data analysis of Lattice QCD correlation functions

Tomáš Poledníček
Czech Technical University in Prague, poledto1@fjfi.cvut.cz

We analyse an ensemble of gauge filed configuration with pion mass $m_\pi = 287$ MeV with dynamical light and strange quarks. We calculate correlation functions from Lattice QCD methods. The simulations were performed with combined $(q\bar{q})$ and $(\pi\pi)$ basis with quantum numbers of the ρ resonance to extract the discrete energy spectrum in a finite volume. We present the resulting p-wave scattering phase.

1 Introduction

Quantum Chromodynamics (QCD) is a quantum field theory describing the interactions of quarks and gluons. Hadrons are a composite subatomic particle made of two or more quarks held together by the strong interaction.

In Lattice QCD, quark and gluon fields live on a space-time lattice of finite volume with finite spacing. The expectation value of the observable can be calculated in the Lattice QCD by averaging over a sampled set of gauge field configurations.

The discrete spectrum of interacting hadrons can be extracted from the correlation functions constructed from quark and gluon fields.

It serves to determine the infinite-volume scattering amplitudes from the discrete spectrum of QCD in a finite cube. This formalism was developed by Lüscher.

Most of the hadrons listed in the Particle data Group [3] are unstable. Most of them decay strongly are observed experimentally as resonances. In this report, we analyse correlation function to extract the ρ resonance in $\pi\pi$ scattering.

2 Lattice QCD

Lattice QCD is a well-established nonperturbative approach to perform calculation the QCD theory of quarks and gluons. It is a lattice gauge theory formulated on a lattice points in space and time.

The discrete space-time lattice acts as a nonperturbative regularisation scheme with the lattice spacing a providing a cutoff. Furthermore, renormalized physical quantities have a finite well behaved limit as $a \to 0$. It can be simulated on the computer using methods from statistical physics. These simulations allow us to calculate correlation functions of hadronic operators and matrix elements of any operator between hadronic states in terms of the fundamental quark and gluon degrees of freedom.

Like continuum QCD, Lattice QCD has the inverse coupling constant $\beta = \frac{6}{g^2}$ and the masses of the quarks up, down, strange, charm and bottom as unknown input parameters. The top quark is too short-lived and heavier than the other quarks, $m_{top} = 172 \pm 0.3$ GeV. The top quark is not included in the Lattice QCD calculations. Lattice QCD provides a well-defined approach to calculate observables nonperturbative starting directly from the QCD Langragian.

In this paper, we do not present the theoretical background. We present just the necessary equations. All theoretical derivations related to Lattice QCD, can be found in [2]. The basic tool for quantizing fields on the Lattice is the Euclidean path integral. The main building blocks are the two following equations. The first of them is

$$\lim_{T\to\infty} \frac{1}{Z_T} \mathrm{tr}[e^{-(T-t)\hat{H}} \hat{O}_2 e^{-t\hat{H}} \hat{O}_1] = \\ = \sum_n \langle 0|\hat{O}_2|n\rangle\langle n|\hat{O}_1|0\rangle e^{-tE_n}, \quad (1)$$

where Z_T is a normalization factor $Z_T = \mathrm{tr}[e^{-T\hat{H}}]$, the left-hand side of (1) is the Euclidean correlation function of operators $\hat{O}_1$, $\hat{O}_2$ and $\hat{H}$ the Hamiltonian of the system. The right-hand side of (1) is a sum of matrix elements of the operators $\hat{O}_1$, $\hat{O}_2$ taken between

vacuum state $|0\rangle$ and physical state $|n\rangle$. These matrix elements are weighted with exponentials containing the energy eigenvalues E_n. The second equation is the Euclidean correlator expressed via a path integral

$$\frac{1}{Z_T}\mathrm{tr}[e^{-(T-t)\hat{H}}\hat{O}_2 e^{-t\hat{H}}\hat{O}_1] = \\ = \frac{1}{Z_T}\int \mathcal{D}[\phi] e^{-S_E[\phi]} O_2[\phi(.,t)] O_1[\phi(.,0)]. \tag{2}$$

The left-hand side is formulated in the operator language of quantum field theory. The integral goes over all possible configurations of the field. The right-hand side contains functionals of the fields, no field operators and it can be evaluated numerically by using a space-time lattice. The quarks and antiquarks are massive fermions and as such are described by Dirac 4-spinors

$$\psi^f(f)_{\alpha c}, \bar{\psi}^f(f)_{\alpha c}, \tag{3}$$

where x is the space–time position, the Dirac index $\alpha = 1,2,3,4$, and the colour index $c = 1,2,3$. In general, Greek letters are used for Dirac indices and letters $a,b,c,...$ for colour. Each field $\psi^f(f)$ thus has 12 independent components. The quarks have flavors called up (u), down (d), strange (d), charm (c), bottom (b), and top (t). QCD contains gauge fields describing the gluons,

$$A_\mu(x)_{cd}, \tag{4}$$

where a space–time argument is denoted by x, a Lorentz index μ labels the direction of the different components in space-time. Since we are interested in the Euclidean action, the Lorentz index μ is Euclidean the gluon field carries colour indices $c,d = 1,2,3$. For given x and, the field $A_\mu(x)_{cd}$ is a traceless, hermitian 3×3 matrix at each space–time point x.

To construct the Euclidean correlators of QCD as a path integral, we need to construct the fermion $S_F[\psi,\bar{\psi},U]$ and gauge $S_G[U]$ field actions on the lattice. On the lattice one works with the so called link variables U which are related to the gauge field $A_\mu(x)$. The continuum analogue is the gauge transporter. The constructions are provided from the QCD action, but we skip this derivation. We can now write down the complete expression for the Lattice QCD path integral formula for Euclidean correlators. We write Euclidean correlators as a lattice path integral

$$\langle O_2(t)O_1(0)\rangle = \frac{1}{Z}\int \mathcal{D}[\psi,\bar{\psi}]\mathcal{D}[U]\times \\ \times e^{-S_F[\psi,\bar{p}si,U]-S_G[U]} O_2[\psi,\bar{\psi},U] O_1[\psi,\bar{\psi},U], \tag{5}$$

the partition function Z is given by

$$Z = \int \mathcal{D}[\psi,\bar{\psi}\mathcal{D}[U] e^{-S_F[\psi,\bar{\psi},U]-S_G[U]}, \tag{6}$$

and the corresponding path integral measures are products

$$\mathcal{D}[\psi,\bar{\psi}] = \prod_n \prod_{f,\alpha,c} = \mathrm{d}\psi^{(f)}_{\alpha c}\mathrm{d}\bar{\psi}^{(f)}_{\alpha c}, \\ \mathcal{D}[U] = \prod_n \prod_{\mu=1}^{4} \mathrm{d}U_\mu. \tag{7}$$

3 Hadron Spectrospocy

One of the simplest observables, that can be computed on a lattice, are the masses of hadrons. There exist many possibilities of hadrons. Proper reproduction of all their masses is already a powerful test for the accuracy of Lattice QCD.

Commonly in Lattice QCD calculation, the gauge configurations are generated according to the desired distribution. In order to calculate hadron masses, we need to perform the hadron spectroscopy calculation. In the analysis of the mass spectrum one studies the correlation function of an operator $\hat{O}$. Nevertheless, these operators usually do not create eigenstates of the Hamiltonian. The first step of such a spectroscopy calculation is the identification of hadron interpolators O and $\bar{O}$ corresponding Hilbert space operators $\hat{O}$ and $\hat{O}^\dagger$. Physically allowed states can be observed in the spectral decomposition of the propagators of these interpolators

$$C(n_t) = \langle O(n_t)\bar{O}(0)\rangle = \\ = \sum_k \langle 0|\hat{O}|n\rangle\langle 0|\hat{O}^\dagger|n\rangle e^{-n_t a E_k} \approx \\ \approx A e^{-n_t a E_H}(1+\mathcal{O}(e^{-n_t a \Delta E})), \tag{8}$$

where A is a constant, E_H is the energy of the lowest state $|H\rangle$ with $\langle 0|\hat{O}|H\rangle \neq 0$ and ΔE is the energy difference to the first excited state. From these correlators one can extract the corresponding hadron masses. For finite lattice size

the values E_k are discrete. The masses m_k of those particles will correspond to the low-lying energy values

$$C(n_t) = A_0 e^{-n_t E_0} + A_1 e^{-n_t E_1} + ... \quad (9)$$

One defines an *effective mass* as

$$m_{eff} = \ln \frac{C(n_t)}{C(n_t+1)}, \quad (10)$$

To extract the lowest two levels, we construct a matrix of correlators $C_{ij}(n_t)$ of the lattice interpolating fields. To be precise, we can improve the situation of the single correlator (8) by computing a matrix of cross correlators

$$C_{ij}(n_t) = \langle \tilde{O}_i(\mathbf{0}, n_t) \bar{O}_j(\mathbf{0}, 0) \rangle = \\ = \sum_k \langle 0|\hat{O}_i|k\rangle\langle k|\hat{O}^\dagger{}_j|0\rangle e^{-n_t E_k}, \quad (11)$$

for a set of N basis interpolators O_i, $i = 1, ..., N$, all with the quantum numbers of the state one is interested in. For the matrix (11), the generalised eigenvalue problem (GEVP) [8–10]

$$C(n_t)\vec{\psi}^{(n)} = \lambda^{(n)}(n_t) C(t_0) \vec{\psi}^{(n)}, \quad (12)$$

is solved for each time slices. For the eigenvalues $\lambda^{(n)}(n_t)$ one obtain

$$\lambda^{(k)}(n_t) \propto e^{-n_t E_k}(1 + \mathcal{O}(e^{-n_t \Delta E_k})), \quad (13)$$

where ΔE_k is the distance of ΔE_k to nearby energy levels. This method is often called *variational method*.

4 Results

The simulation is performed on an ensemble N451 from the CLS consortium [11]. We use 198 gauge configurations with with dynamical light and strange quarks. The pion mass m_π is 287.93 MeV, the lattice volume V is $48^3 \times 128$ and the spacial extent of the lattice is $L \simeq 3.7$fm [4].

In this report, we first present results from ensemble N451 compared with ensemble N401. The most crucial step is the statistical analysis of the measured data. Lattice QCD calculations are often really expensive. The number of configurations for our data set is too lower. In order to obtain robust results, we use statistics techniques for smaller data sets. There are two efficient and easy-to-use methods dealing with both problems - *Statistical bootstrap* and *JACKKNIFE*. For simplicity, we assume that the data are not correlated. We use *JACKKNIFE* for the sampling data. In principle, the *JACKKNIFE* is a resampling technique that is especially useful for bias and variance estimation. Given a sample of size n, a jackknife estimator can be built by aggregating the parameter estimates from each subsample of size $n-1$ obtained by omitting one observation.

Our data consists of irreducible representations on the lattice with different momenta for instance T_{1u}^+ with $P = (0,0,0)$. In this report, we show only two examples.

In Fig.1 the single correlator for the A_1^+ with momentum $P = (0,0,0)$ is shown. The obtained energy of the ground state is $E_0 = 287.93 \pm 2.32$ MeV. This energy corresponds to the pion in the rest frame and it is the value of the pion mass on the lattice. We also see contamination from higher energy levels. In the Fig.2 the matrix correlator for the T_{1u}^+ with momentum $P = (0,0,0)$ is shown. The obtained energies are $E_0 = 789.68 \pm 6.28$ MeV and $E_1 = 927.44 \pm 7.91$ MeV.

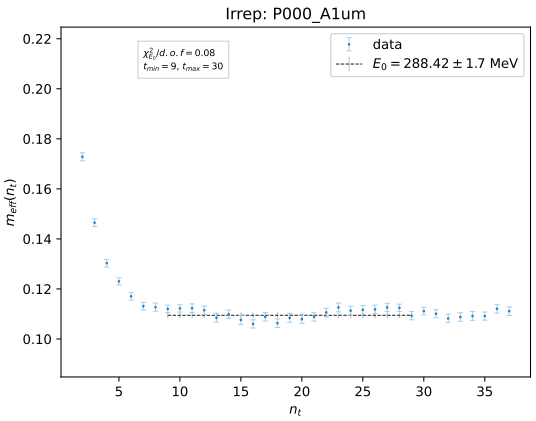

Fig. 1: *The effective energy for single correlator for irrep A_1^+ with momentum $P = (0,0,0)$.*

In Figs.3 and 4 the the energies in the centre of mass frame to pion mass ratio for different momentum compared to data from ensemble N401 are depicted. The energy E_{cm} with given momentum $\mathbf{P}$ is computed

$$E_{cm} = \sqrt{E^2 - \mathbf{P}^2}. \quad (14)$$

We implement the formalism relating elastic $\pi\pi$ scattering phase-shifts to the finite-volume spectrum. Here we repeat only the essential feature,

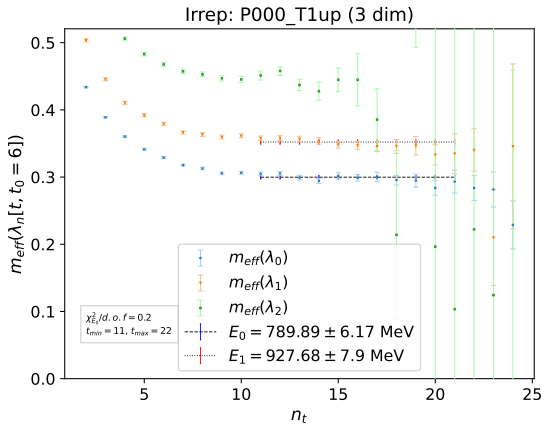

Fig. 2: *The effective energy for matrix correlators for irrep T_{1u}^+ with momentum $P = (0, 0, 0)$.*

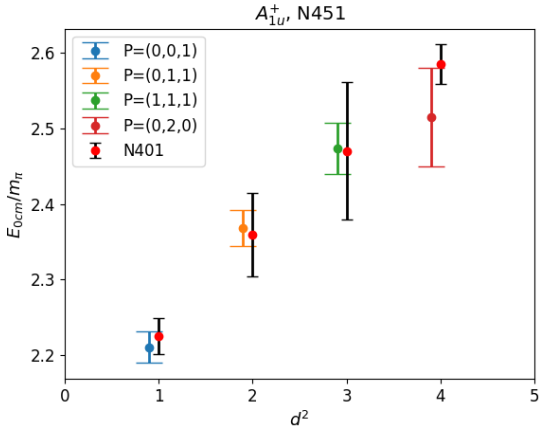

Fig. 3: *Comparison of energy E_{0cm} of irrep A_1^+ from ensemble N451 and ensemble N401 [1].*

that the phase shifts are related to the finite-volume energies by the Lüscher's quantization condition [6, 7]

$$\delta_1(k) + \phi\left(\frac{L}{2\pi}k\right) = n\pi, \qquad E_{cm}(k) = 2\sqrt{k^2 + m_\pi^2} \tag{15}$$

where k is momentum and m_π^2 is pion mass. The resulting phase-shift is related to the relativistic Breit-Winger form for the elastic p-wave amplitude in the resonace region

$$a_1 = \frac{-\sqrt{s}\Gamma(s)}{s - m_\rho^2 + i\sqrt{s}\Gamma(s)} = e^{(\delta(s))}\sinh\delta(s), \tag{16}$$

where $s = E_{cm}^2$ is the Mandelstam variable and the decay width $\Gamma(s)$ can be expressed in terms

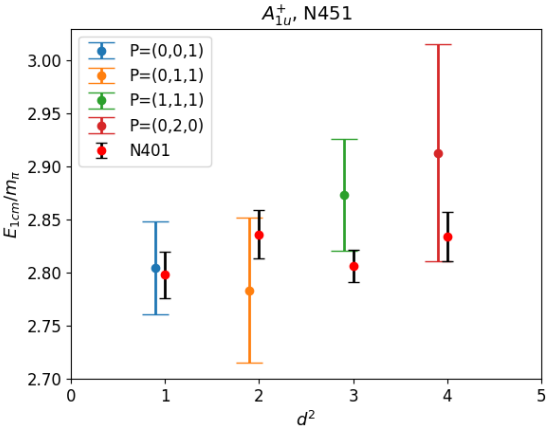

Fig. 4: *Comparison of energy E_{1cm} of irrep A_1^+ from ensemble N451 and ensemble N401 [1].*

of the coupling constat $g_{\rho\pi\pi}$

$$\Gamma(s) = \frac{p^3 g_{\rho\pi\pi}^2}{s6\pi}. \tag{17}$$

Fig.5 and Fig.6 show results of p phase-shift of the resonance region. We obtain

$$m_\rho = 792.47 \pm 0.01\text{MeV}, \qquad g_{\rho\pi\pi} = 6.25 \pm 0.18. \tag{18}$$

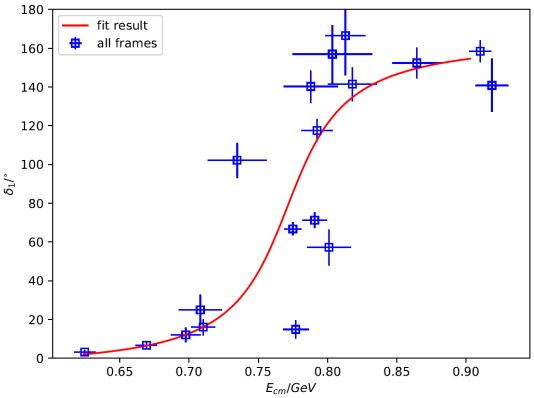

Fig. 5: *P-wave $\pi\pi$ elastic scattering phase-shift. The fit has χ^2/d.o.f = 2.35.*

5 Conclusions

Extracting scattering phase-shifts and resonance properties is one of the most challenging problems in hadron spectroscopy based on lattice QCD. We combine sophisticated tools to approach this problem: Lüscher's scattering

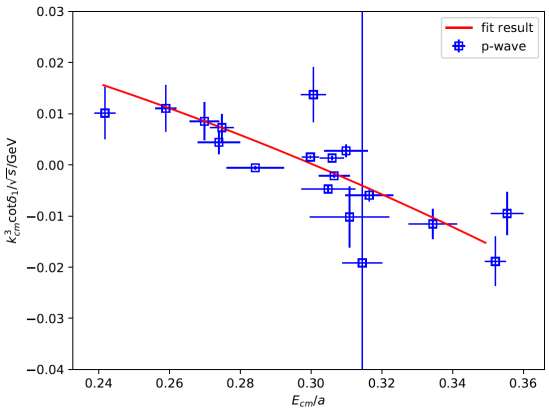

Fig. 6: *Our data for* $k^3_{cm}\cot\delta_1/\sqrt{s}$ $\pi\pi$ *as function of* E_{cm}/a*. The fit has* $\chi^2/\mathrm{d.o.f} = 2.35$.

phase-shift relations for finite-volume lattices, moving frames and variational analysis of correlation matrices.

We present the pion mass on the lattice $E_0 = 287.93 \pm 2.32$ MeV. We see that our results for scattering phase-shifts are not so good. For our pion mass we obtain the resonance mass and $m_\rho = 792.47 \pm 0.01$MeV and $\rho \to \pi\pi$ coupling $g_{\rho\pi\pi} = 6.25 \pm 0.18$, which is quite close to the experimental value $g^{exp}_{\rho\pi\pi} \approx 5.97$.

In the future, we plan data analysis with larger number of configurations.

Acknowledgments

It is my honourable duty to thank my supervisor prof. Daniel Mohler at the GSI facility for help in leading, compiling, patience, formulating tasks, providing professional materials and scientific guidance in solving the tasks of my summer project. Many thanks to Barbara Cid Mora for invaluable technical assistance and professional advice.

References

[1] C. Andersen, J. Bulava, B. Hörz and C. Morningstar, Nucl. Phys. B **939** (2019), 145-173 doi:10.1016/j.nuclphysb.2018.12.018 [arXiv:1808.05007 [hep-lat]].

[2] C. Gattringer and C. B. Lang, Lect. Notes Phys. **788** (2010), 1-343 Springer, 2010, ISBN 978-3-642-01849-7, 978-3-642-01850-3 doi:10.1007/978-3-642-01850-3

[3] R. L. Workman *et al.* [Particle Data Group], PTEP **2022** (2022), 083C01 doi:10.1093/ptep/ptac097

[4] M. Cè, A. Gérardin, G. von Hippel, R. J. Hudspith, S. Kuberski, H. B. Meyer, K. Miura, D. Mohler, K. Ottnad and P. Srijit, *et al.* [arXiv:2206.06582 [hep-lat]].

[5] J. J. Dudek *et al.* [Hadron Spectrum], Phys. Rev. D **87** (2013) no.3, 034505 [erratum: Phys. Rev. D **90** (2014) no.9, 099902] doi:10.1103/PhysRevD.87.034505 [arXiv:1212.0830 [hep-ph]].

[6] M. Luscher, Commun. Math. Phys. **104** (1986), 177 doi:10.1007/BF01211589

[7] M. Luscher, Commun. Math. Phys. **105** (1986), 153-188 doi:10.1007/BF01211097

[8] C. Michael and I. Teasdale, Nucl. Phys. B **215** (1983), 433-446 doi:10.1016/0550-3213(83)90674-0

[9] C. Michael, Nucl. Phys. B **259** (1985), 58-76 doi:10.1016/0550-3213(85)90297-4

[10] M. Luscher and U. Wolff, Nucl. Phys. B **339** (1990), 222-252 doi:10.1016/0550-3213(90)90540-T

[11] M. Bruno, D. Djukanovic, G. P. Engel, A. Francis, G. Herdoiza, H. Horch, P. Korcyl, T. Korzec, M. Papinutto and S. Schaefer, *et al.* JHEP **02** (2015), 043 doi:10.1007/JHEP02(2015)043 [arXiv:1411.3982 [hep-lat]].

DEGAS Electrical Cooling

Damiano Stramaccioni
Universidad de Sevilla, damianostramaccioni99@gmail.com

DEGAS crystals, like all the HPGe detectors, need to be cooled down to reduce electronic noise and obtain excellent energy resolution. Different cooling systems can be employed to perform this task, but so far only a Liquid Nitrogen dewar was used. Using an electrical cooler represents a possible upgrade, and its mounting and testing are described in this work.

1 Introduction

1.1 The DEGAS spectrometer

The DESPEC Germanium Array Spectrometer (DEGAS) [1] is a high-purity germanium (HPGe) γ-detector array for high-resolution spectroscopy of electromagnetic decays from exotic nuclear species. It is a key instrument of the Decay Spectroscopy (DESPEC) [2] experiment at FAIR [3]. At DESPEC, rare isotopes produced by the Super-FRS [4] will be stopped in an active implanter surrounded by DEGAS measuring γ rays from α, β, proton, neutron and isomeric decays. For this purpose, DEGAS must have maximal sensitivity to measure discrete transitions in the presence of prevailing background radiation. High sensitivity must be achieved by large solid angle coverage, large intrinsic full energy efficiency, large peak-to-total (peak-to-background) ratio, high granularity and high energy resolution. In particular, in order to obtain excellent energy resolution germanium detectors must be cooled down. Indeed, due to their small bandgap (0.7 eV), room-temperature operation of germanium detectors of any type is impossible because of the large thermally-induced leakage current that would result. Normally, the temperature is reduced to 77-110 K through the use of an insulated dewar in which a reservoir of liquid nitrogen (LN2) is kept in thermal contact with the detector. Alternatively, in cases where the required cooling power is low ($\lesssim$ 10 W), an electrical cooling system based on a thermodynamic cooling cycle (e.g. Stirling cycle) can also be used.

1.2 DEGAS cryogenic design

The DEGAS Triple Cluster is supposed to have an electrical cooling engine instead of the classic LN2 cooling. This type of cooling is rather simple: it does not need of any refilling or safety system and has significantly reduced sizes [5]. The Triple Cluster effective diameter is only 204 mm, which makes it difficult to find a suitable dewar vessel with a reasonable size. A too small vessel would require too frequent filling, which reduces the performance of the detector and potentially decreases its reliability. If the detectors are arranged in a spherical geometry this problem does not exist, the projection of the edges defines a much larger dewar vessel, but such an arrangement would exclude the box geometry chosen for the DEGAS array. The germanium crystals and the cold structure are installed in a vacuum cryostat where, as shown in Fig. 1, three processes determine the energy transfer between the room temperature cryostat walls and the low temperature assembly: heat radiation, thermal conductivity and residual molecular heating. A careful design of the components and appropriate materials choice is essential to reduce the heat absorbed by the germanium crystals sufficiently to enable electrical cooling. The HPGe detectors are typically operated within the range of 77-110 K which determines a temperature difference between the warm cryostat walls and the cold frame of about 200 K. The triple crystal assembly possesses a large surface of the detector cup surrounding the capsules hence predetermining an elevated radiative heating which may dominate even the overall heat transfer.

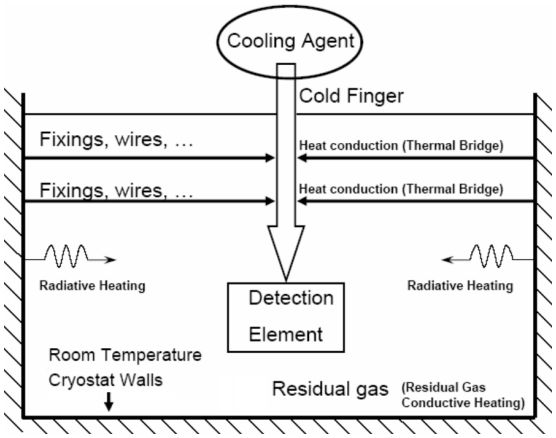

Fig. 1: *Scheme of the three energy transfer processes between the room temperature cryostat and the low temperature assembly: heat radiation, thermal conductivity and residual molecular heating.*

Beyond that, the warming impact of the thermal bridges, the mechanical components used for fixing the cold structure to the warm section of the cryostat and the internal cabling between the crystal housing and the vacuum feedthrough, play a substantial role. The fixing elements of the detector system under optimization, namely labyrinths and spacers, are critical parts and an accurate dimensioning is needed in order to achieve minimal heat transfer while preserving γ-spectroscopy properties and the functionality required. The space limitations impose a minimal gap between the capsules assembly and the cryostat walls. However, at some critical gaps width, the residual gas of the evacuated inner space contributes significantly to the detectors warming and this effect depends on the vacuum level. A comprehensive study of the heat transfer processes and their impact on the detector performance can be found in [6]. Here, the dominating heat transfer mechanisms have been identified and appropriate mathematical modelling has been applied. Temperature distributions within the detector structure were calculated for various environment and cooling conditions and the functional characteristics of the assembly needed to reach the operational temperature range, were determined. Different design solutions were compared and proper materials selected. In the last few years, many improvements were made to reduce heat transfer, leading to a cooling power of < 8 W for the DEGAS triple, small enough for electrical cooling engines. The cooling engine for the DEGAS Triple cryostat is supposed to be a Cryotel engine type CT or GT [7]. Both of them are sufficiently powerful – the type GT has 16 W cooling power, while type CT 11 W, compared to 6-8 W suggested by the study of the detector thermodynamics.
In the following, the installation and test of a Cryotel engine type CT will be presented and discussed.

2 Installation of the electrical cooling system

2.1 Mounting of the apparatus

The Cryotel engine type CT was mounted as shown in Fig. 2. This cooling engine was fixed to the “cold finger", a copper cylinder in turn connected to the Ge crystals. In this way, the heat can be transferred from them to the engine and their temperature kept low. As mentioned above, the low cooling power delivered by the engine requires extreme attention in reducing possible heat transfer from the external environment to the crystals. For this reason the cold finger was equipped with a “super insulation" system, consisting of metalized mylar and glass tissue foils wrapped around it. In this way, radiative and residual gas heating were greatly hindered.

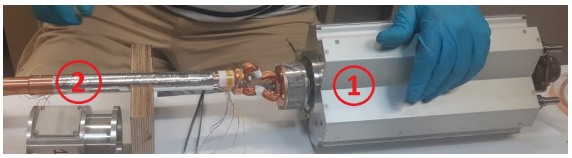

Fig. 2: *Mounting of the apparatus: 1) Electrical Cooling engine 2) Cold finger connected to the engine and equipped with “super insulation".*

2.2 Conditioning of the apparatus

After mounting the apparatus, it needs to be conditioned and tested. The conditioning consists in recreating the conditions in which the detector is supposed to work, namely in good vacuum and at low temperatures. To accomplish a good vacuum level (around 10^{-7} mbar), an important component of the system is the so-called “absorber". It consists of a metallic struc-

ture containing Zeolith spheres. Given the great internal porous structure of Zeolith, their role is to increase the vacuum level of the apparatus absorbing the gas particles trapped inside. In order to get the best performances from these spheres, the gas particles previously absorbed need to be freed. This is achieved heating up the system, making a DC current flow through a couple of resistors directly connected to the absorber while keeping a good vacuum level in the apparatus with a vacuum pump. In Fig 3 the temperatures reached at three points, namely at the cooler connection with the cold finger, at the absorber and on the cold frame connected to the Ge crystals, can be observed. These temperatures were obtained measuring the resistance of three resistors (two PT100 and a PT1000 [8]) mounted at the three points, given their well-known resistance dependence on the temperature.

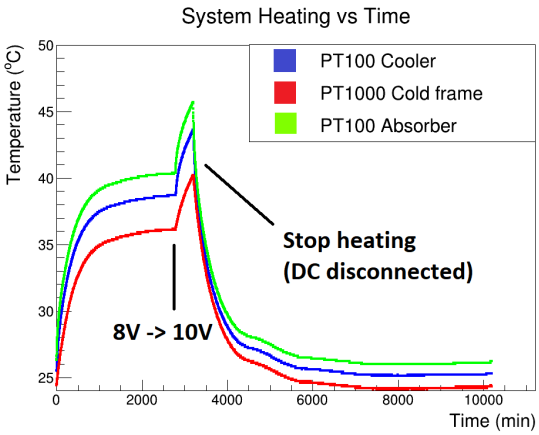

Fig. 3: *Heating of the system: temperatures versus time reached at the cooler connection with the cold finger, at the absorber and on the cold frame.*

After this stage, the crystals needed to be cooled down. This was achieved turning on the CT cooler and setting a target temperature. It was also important to keep the cooling water of the CT cooler at low temperature. This was done with the "TERMOTEK AG P1020-19409" heat exchanger, which consists in a closed system in which a refrigerant gas circulates in thermal contact with the water fed into it. To test the performances of the cooling system we set four different target temperatures (labelled as "TT") and recorded the cooling curves of the three points mentioned above, as shown in Fig. 4. In the same figure is highlighted the moment in which the PT100 connected to the cooler went out of range (T < -200 ^{o}C) and stopped recording the temperature.

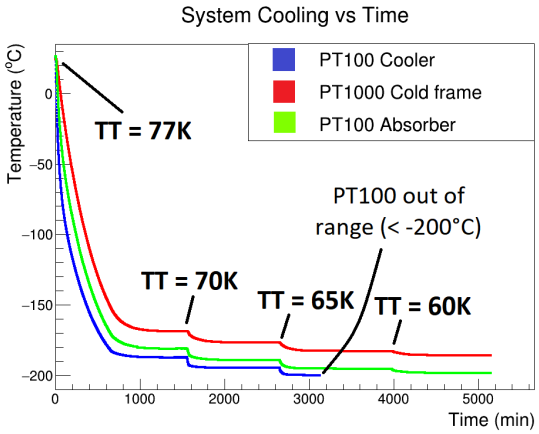

Fig. 4: *Cooling of the system: temperatures versus time reached at the cooler connection with the cold finger, at the absorber and on the cold frame.*

In particular, the temperatures reached in the cold frame with different cooler target temperatures is reported in Tab. 1. It is interesting to appreciate the non-linearity of the cold frame response, due to the cooler lower cooling power at low temperatures.

T Target	T Cold frame
-196.15 ^{o}C	-168.7 ^{o}C
-203.15 ^{o}C	-176.9 ^{o}C
-208.15 ^{o}C	-182.8 ^{o}C
-213.15 ^{o}C	-186.1 ^{o}C

Tab. 1: *Target temperatures and temperatures reached by the cold frame connected to the crystals.*

3 Test of detectors performances

Finally, after mounting the High Voltage filter and the preamplifier, the detector response was tested. The target temperature was set to 77 K and a source of ^{60}Co was used. As a first check the noise level of the signal was evaluated with an oscilloscope. As shown in Fig. 5, the signal was not affected by any important source of noise which might spoil its energy resolution significatively. Subsequently, the preamplifier output was connected to a shamping-amplifier NIM module and sent to an ADC to obtain the energy spectrum recorded by two different crystals (labelled as B and C) of the detector.

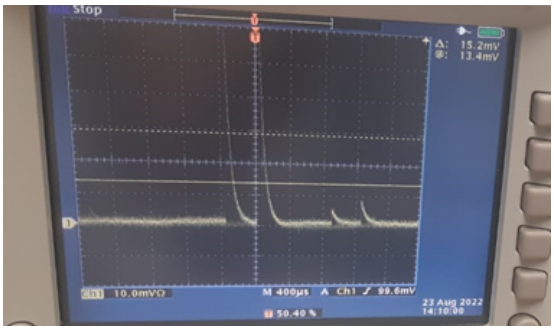

Fig. 5: *Signal from the detector visualized on the oscilloscope for noise evaluation.*

The energy resolution (FWHM) for the 1332.5 keV γ ray was measured to be 2.46 keV and 2.19 keV for the Crystals B and C, respectively. These values are reported in Tab. 2, along with the FWHM measured for the same crystals when using a Liquid Nitrogen cooling system. In both cases the energy resolution obtained with the Electical Cooling system resulted to be lower, but it should be considered that the noise due to the electronics and to mechanical vibrations of the system have not been optimized yet.

Cooling	FWHM Crys. B	FWHM Crys. C
LN2	1.98 keV	1.94 keV
EC	2.46 keV	2.19 keV

Tab. 2: *FWHM for the 1332.5 keV γ ray measured with the Crystals B and C when cooled with the Cryotel CT engine ("EC") and with liquid nitrogen ("LN2").*

4 Summary and perspectives

The Cryotel CT electrical cooling engine was mounted and proved to work properly. In fact, the temperatures reached by the cold frame

were even lower than the expectations. In addition, the DEGAS crystals performances with this cooling system were also tested. The raw signal obtained was not affected by any significant source of noise and the energy resolution, even if worse than the one obtained with the Liquid Nitrogen cooling system, was in agreement with the expectations. In the future, the main goal is to reduce as much as possible the noise due to the electronics and to mechanical vibrations of the system. It will then be possible to compare the energy resolution of the detector cooled with the cooling systems and choose the best performing one.

Acknowledgments

Thanks to my tutor Dr. Ivan Kojouharov and to Dr. Philipp Herrmann for their patience and availability in answering my questions and doubts. I also want to thank Dr. Ralf Averbeck and to Mrs Gabriela Menge for their help and great organization, without forgetting all the Summer Students who made my summer extremely pleasant.

References

[1] J. Gerl, et al., *Phys. Scr.* **91**, 103001 (2016).
[2] Z. Podolyák, *Nucl. Instrum. Methods Phys. Res.* B **266**, 19 (2006).
[3] G. Spiller, G. Franchetti, *Nucl. Instrum. Methods Phys. Res.* A **561**, 2 (2006).
[4] J. Äystö, K.-H. Behr, J. Benlliure, A. Bracco, P. Egelhof, A. Fomichev, S. Galès, H. Geissel, T. Grahn, L.V. Grigorenko, et al., *Nucl. Instrum. Methods Phys. Res.* B **376** (2016).
[5] I. Kojouharov et al., *GSI Scientific Report*, p. 235 (2008).
[6] I. Kojouharov et al., *IEEE Proceedings of Sixth UKSim/AMSS European Modeling and Simulation (EMS) Symposium*, p. 461-465 (2012).
[7] *https://www.sunpowerinc.com/products/stirling-cryocoolers/cryotel-cryocoolers/ct*
[8] *https://www.picotech.com/library/application-note/pt100-platinum-resistance-thermometers*

*

0pt0pt0pt

Innovative solution for upgrading the vacuum system in a cryogenic stopping cell

Lisa Suette
Technical University of Vienna, e11810035@student.tuwien.ac.at

This project has taken place in the group of the FRS (Fragment Separator) at GSI which specialises on producing and observing exotic nuclei and their nuclear structure by cooling the nuclei down to a very low Energy. Therefore, the CSC a cryogenic stopping cell is used which is an important part of this ion catcher experiment. To prepare the CSC for the next fission run, it was taken apart and some parts like the Teflon-plug, the RF-carpet and the fission sources were exchanged. Several calculations and adjustments that needed to be done to modify the Teflon-plug and check the RF-carpet as well as the execution and the results of the pumping test can be found in the following report.

1 Introduction

To be able to make high-precision measurements of the nuclei and their fission products coming from the FRS, the nuclei have to be cooled down to just a few eV/nuclei which happens in the ion catcher experiment.
The Ion catcher experiment consists of four main parts

- the FRS with the degrader system
- the cryogenic stopping cell (CSC) including the Teflon-plug and the RF carpet
- two diagnostic units (DU1 and DU2)
- the MR-TOF-MS which is a multiple-reflection time-of-flight mass spectrometer. [1]

Depending if there is beamtime available or not, the experiment can either be run online or offline. If a beam is coming from the Sis18, going through the FRS and the degrading systems before arriving at the CSC, the experiment is run "online". If there are specialised radioactive sources put into the stopping cell instead of an incoming beam, one can call it an "offline" run.

2 Experimental setup

For better understanding of the project the experimental setup is briefly described in the following.

2.1 FRS and degrading system – "online"

The beam coming from the Sis18 is led on a target and consequently interacts with it. This interaction leads to projectile fragmentation or fission and creates the exotic nuclei that are observed as part of this experiment. After these nuclei are produced, the beam is led to an energy buncher which compresses the range of the nuclei and then to the Super-FRS, where a pre- and main- separator separate the nuclei of interest from the abundant contaminants. Because of the huge number of different particles that are delivered in the beam, it is necessary to first decide which particles to study and then detect only the particles of interest by tuning the degrader in a way that just those can enter the experimental setup. Passing the degrader system, the nuclei are slowed down and reach the CSC with an energy of about 2MeV/nuclei. This still is too high for the experiment and therefore the nuclei are further slowed down the CSC.

2.2 Cryogenic stopping Cell

In the CSC, the nuclei coming from the ion beam are slowed down from 2MeV/nuclei to 10^{-5}MeV/nuclei within a range of 3m due to collisions with the cooled helium atoms located inside the cell. The CSC consists of three main parts. The DC-cage, the cold chamber and the outer chamber, whereby the DC-cage is located inside the cold chamber and the cold chamber is located inside the outer chamber. The DC-cage consists of many metal rings that are connected to a voltage supplier, which becomes less strong from the top to the bottom side due to a resistance chain connecting the rings. This way the electric field acts like a transport unit and forces the ions to travel along the cage to the RF-carpet (the so-called push field). The RF-Carpet is located at the end of the cold chamber and it generates an electric field (so-called focus field) but in the radial plane, which acts like a funnel for the ions and focuses them in radial direction. This way they are forced to travel through the central point of the RF-carpet where the carpet has a very small hole [ca. 1mm] and finally enter the acceleration line that leads to the two diagnostic units and the MR-TOF-MS. [1]

Using fission sources – "offline"

One big advantage of this experimental setup is that running an experiment does not rely on the beamtime. To be able to install several fission sources inside the chamber and to make experiments with the ions and fission products of those ions, provides the possibility to run experiments even when the linear accelerator and Sis18 are not running. Three different sources are installed inside the chamber for the next run, all of them being α -emitters:

Gd148 → Activity: 19.4kBq
Th228 → Activity: 4.3kBq
Cf252 → Activity: 37kBq

Where Cf252 will be the fission source and Th228 and Gd148 are used as calibration sources.

2.3 Transport line and diagnostic units

A RF-Quadrupole, which is located after the RF-carpet, again, focuses the ions on radial direction and ensures their transportation to the diagnostic units DU1 and DU2 and in further succession to the MR-TOF-MS. The path from the RF-carpet to the MR-TOF-MS consists of three segments which are driven by pumps and act like an accelerator unit for the ions. The first diagnostic unit (DU1) consists of three detectors and her main function is to control and check the position of the detectors and to adjust the detectors if needed. The second diagnostic unit (DU2) will contain an integrated laser in the future. Thanks to the interaction between particles from the beam and the laser one can create new nuclei to be used as calibrate for a certain mass range where one is measuring.

2.4 MR-TOF-MS

The main measuring unit of the experiment is the MR-TOF-MS which is a very strong mass spectrometer that can identify all ions of interest. [1] As soon as the ions leave the DU2, they get collected in a so-called "trap-system". The trap-system is an empty glass where the ions are collected in bunches. As soon as the glass is full of ions, the valve opens automatically and the bunch is further accelerated and transported to the detectors placed at the end of the MR-TOF-MS. The detection of the ions can be performed two different ways:

1. All the ions contained in the bunch that is released from the trap-system are accelerated to the detector and get detected at the same time. With this the masses of the isobars occurring on the detector can be measured, the resolution however is not very high.
2. Nuclei can be forced to do more than just one turn in the tracking system which leads to a slight change of the path for different isobars. This leads to the isobars hitting the detector at the same time but at different points, allowing their masses to be separated more precisely and to improve the resolution of the mass spectra.

3 CSC - Pumping system, Teflon Plug and RF-carpet

Pumping system

Figure 1 displays the CSC and the two pumping systems which are connected to it. Each pumping system first uses a pre-vacuum pump (Ebara PDV250 and Ebara Dry Pump) and then several turbo-pumps to further lower the pressure. The pre-vacuum pump is used for reducing the pressure from the atmospheric pressure of approximately 1013mbar to a pressure of 10^{-3}mbar before the turbo-pumps can further reduce the pressure down to 10^{-8}mbar. The first pumping system, illustrated in the lower left corner of Figure 1, uses two turbo-pumps additionally to the pre-vacuum pump. One is called Seiko, which is located on top of the CSC and is connected to the insulation vacuum - this is the space between the cold chamber and the outer chamber. The second turbo-pump is called Edwards pump, which is connected to the Cryostat and regulates the flow between the Cryostat and the CSC. Referring to the right upper corner of Figure 1, the second pumping system is illustrated. It is located on the side of the CSC that is connected to the DU1. It also consists of a pre-vacuum pump which in this case is attached to three turbo-pumps for the DU1, one turbo-pump for the DU2, three turbo-pumps for the MR-TOF-MS and one Pfeiffer turbo-pump. The Pfeiffer turbo-pump is connected to the inside of the cold chamber and is used to evacuate it. The whole reason of evacuating the inside of the cold chamber is to provide the cleanest environment possible so no collisions between the nuclei and the impurities existing in the normal air occur. When evacuating the chamber, it is very important to reduce the pressure in the cold chamber and in the space between the RF-carpet and the connection to DU1 simultaneously otherwise there would be a risk of breaking the RF-carpet due to the pressure gradient between both sides of the carpet. In this arrangement also the Teflon-plug is used, which acts as a valve between the cold chamber and the connection line and is completely vacuum-tight when closed but lets the vacuum escape when opened. Therefore, it is very important that the Teflon-plug opens and closes properly otherwise the whole vacuum system would not work and no vacuum could be held in the cold chamber.

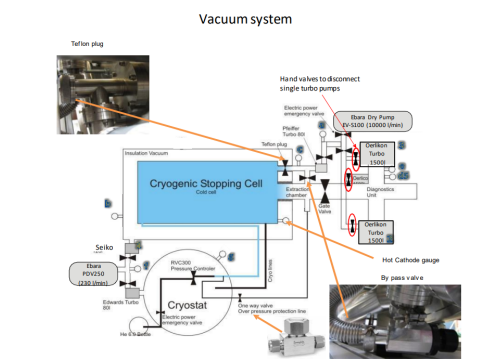

Fig. 1: *Pumping system of the CSC*

3.1 Teflon plug

A new feedthrough for the Teflon-plug had been ordered because tests showed that the old one did not work as expected anymore. The problem with the new feedthrough was, that the dimensions were different regarding the length and therefore some changes had to be made. In general, there were two major things to consider.

1. Dimensional changes of the regulation part
2. Elongation of the Teflon-plug

Dimensional changes of the regulation part The space between the L-flange and the bar of the outer framework wherein the CSC is fixed was just 60mm and the regulation part of the linear feedthrough itself was already 70mm so the setup needed to be adjusted in a way to fit everything within those 60mm.
Therefore, two things were changed:
Firstly, the part of the L-flange where the old linear feedthrough was fixed got cut off and instead a CF16-flange which was needed for the new feedthrough was welded on. Because the inner diameter of the L-flange is 35mm and the outer diameter of the CF16-flange is 34mm, the workshop was able to weld a one side-blinded CF16-flange inside the inner diameter of the L-flange. Modifying the flange this way saved about 10mm of space compared to the old setup but still provided complete vacuum-tightness. Before, the full length of the L-flange was 114mm and after the adjustment it was reduced to 104mm.
The second thing that was changed was the regulation part of the new feedthrough. Instead

of the small but quiet thick handle at the end, that is used to open and close the Teflon-plug, a screw system was built. With this system one should be able to open and close the Teflon-plug depending on how the nuts are fixed on the connecting screw. Because a system like this did not exist yet, a drawing of the parts had to be made. Figure 2 shows a sketch of the two screw plates and the long mounting plate which were needed for the screwing system and Figure 3 shows the whole system with all the parts fixed in their position.

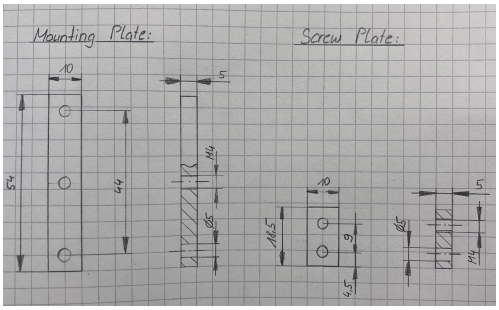

Fig. 2: *sketch of the mounting plate and the screw plates*

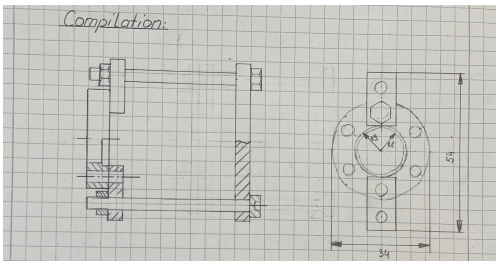

Fig. 3: *Compilation of the screwing system*

Elongation of the Teflon-plug

To make sure that there was enough space to open and close the Teflon-plug when mounted to the CSC, the new feedthrough was fixed in a position where it could still be moved back and forth. Only after this arrangement the measurements to calculate the final length of the elongation part were taken. These calculations revealed the total length of 196mm for the elongated part. Because the new feedthrough just had a length of 82mm, it was too short to be able to close the vacuum system properly and had to be elongated. Since in this case two cylinders with a diameter of 12mm (old feedthrough) and 4mm (new feedthrough) had to be connected, the most efficient solution was to cut off the original part including the Teflon plug and weld it to the small diameter of the new feedthrough, which was done by the workshop. Considering the full length of 196mm and subtracting the length of the new feedhtrough (82mm) yielded a length of 114mm, which needed to be cut from the old feedthrough. A detailed sketch can be seen in Figure 4.

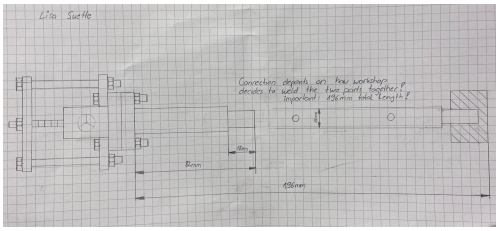

Fig. 4: *Sketch of the elongation part already connected to the new feedthrough*

3.2 The RF-Carpet

The RF-carpet consists of 500 concentric rings – starting with ring 1 in the centre, continuing with ring $2, 3, 4$ and so on. Every ring with an even number is connected to circuit 1 and every ring with an odd number is connected to circuit 2. This, in the end, leads to two circuits consisting of 250 resistances each, where every concentric ring is connected to a resistance. Each of the resistances has a value of 10kOhm and if measured over the whole circuit it sums up to 2.5MOhm. This is also the value that is needed to be measured to guarantee that the carpet is working properly.

Measurements and Testing

When the RF-carpet was dismounted, the cables and the PT100 were disconnected from the pins of the old carpet and connected to the new RF-carpet accordingly. The cable for the PT100 was soldered to the carpet as well for extra security. When all the cables were connected and soldered at the right position, the resonance could be measured. For the carpet to work properly, the resonance should at least be $-10/-11$ dB. The measurements taken delivered a value of -18dB at a frequency of 5.5MHz as seen in Figure 5, which indicated that the resonance was correct.

The RF-carpet itself creates an electric field which is run by an oscillating circuit. This circuit is excited with the resonant frequency

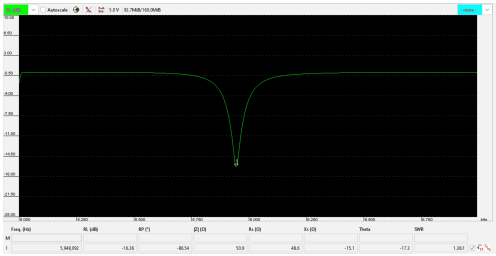

Fig. 5: *Measured resonance in dB at a Frequency of* $5.5MHz$

of 5.5MHz. To ensure an evenly distributed funnel-like electric field to focus the ions on the centre of the carpet, all the connections between the resistances have to work properly. Therefore, the total over every circuit was measured, which should yield a value of 2.5MOhm. The measurement of the first circuit (between R1 and R499) and the second circuit (between R2 and R500) each yielded a value 2.5MOhm which was very good. After getting the right values for both individual circuits also the resistance over both circuits from R498 to R499 was measured and the value was 5MOhm, as expected. After the right value for the PT100 was successfully measured too, the new carpet was ready to be connected back to the plateau of the cold chamber.

3.3 Pumping test

As soon as the modifications done by the workshop were completed, the Teflon-plug could be installed together with the L-flange as seen in figure 6 and with that the final test to confirm a proper function of the vacuum system could be executed, the pumping test.

In this test two functions could be obtained.

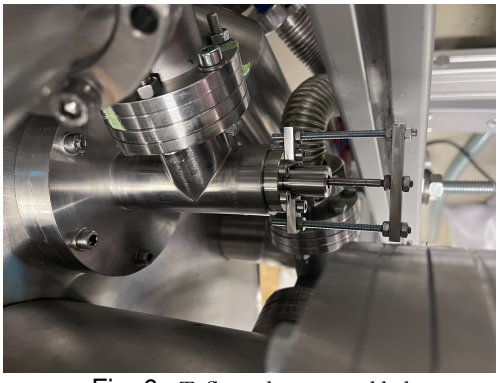

Fig. 6: *Teflon-plug assembled*

In the first run the bypass valve and the Teflon-plug remained open and an external pre-vacuum pump was connected to the gate valve. In this way one could check if the whole system including the cold chamber is closed properly and no leak exists. To verify the proper work one should be able to reduce the pressure in the cold chamber from 1013mbar (room pressure) to 5mbar within 30min and after activating the turbo-pump, one should reach 10^{-3}mbar following a graph comparable to the gray line in figure 7. In the second test, while having the vacuum inside the chamber, the Teflon-plug and the bypass valve were closed and then the pump was shut off. This way one could check if the Teflon-plug was able to be properly closed and to hold the vacuum inside the chamber. If in any case these values cannot be reached, there has to be a leak in the pumping system, either on the outside e.g. the Teflon-plug or any other flange connection or inside e.g. the cold chamber is not closed properly, which means that the whole CSC has to be opened again.

4 Results and Discussion

The new arranged Teflon-plug was installed and the pre-vacuum pump was attached to the gate valve after which several measurements were taken. Figure 7 shows a line diagram where the behaviour of the pressure in dependency of the time is plotted. The gray line shows the optimal behaviour that is observed when the pumping system is completely leak tight, which was measured directly at the pre-vacuum pump. After 30min at the latest, the pressure has to be reduced to 5mbar in order to be able to continue pumping with the turbo-pump. The blue line represents the first measurement taken, which failed. It shows a pressure of 183mbar after 30min. The great difference in the values between the blue and the gray line pointed out that the pumping system was not properly working and there had to be a leak in the system. Observing the whole vacuum system led to finding a leak in the Teflon-plug, which was fixed in the following. Furthermore, it was observed that handling a screw system in a place with very little space is not advantageous and there was enough space to use the

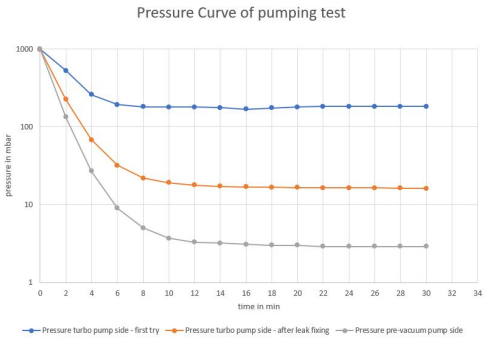

Fig. 7: *Teflon-plug assembled*

initial handle. Because of these reasons it was decided, that using the original configuration of the Teflon-plug with the wheel instead of the screwing system makes more sense. After adjusting the setup back, exchanging O-rings to make sure every part is assembled correctly and testing all flange connections that could possibly leak, another test was done - shown in Figure 7 by the orange line. Even though the pressure could be lowered way more, it still was not possible to reduce the pressure below 16mbar. This led to the assumption that the leak had to be caused by the not properly closed cold chamber inside.

To make sure that the failure really arised

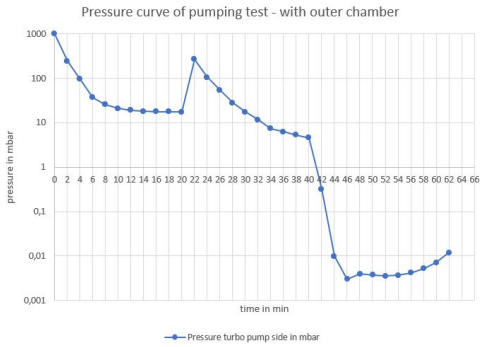

Fig. 8: *Teflon-plug assembled*

from the cold chamber, one last test was done - displayed in Figure 8. This time the pre-vacuum pump was connected to the turbo-pump to evacuate the cold chamber but also to the outer chamber to be able to evacuate the insulation layer too.

The pre-vacuum pump was started and after 20minutes the pressure was stagnating at 17.4mbar, as expected. This was when the connection between the pre-vacuum and the insulation layer was opened to evacuate that part too. The pressure instantly jumped to 267mbar because of the bigger volume, but started to decrease right afterwards. 20min later, at a total of 40min the pressure already reached the 5mbar mark and the turbo-pump could be activated. Just 6min later, at 46min, the needed pressure of 10^{-3}mbar, was reached. This test clearly pointed out that there was no leak in the Teflon-plug but for sure some kind of leak between the cold and the outer chamber, which proved the previous assumption.

5 Conclusion and outlook

The aim of this work was to develop convenient and properly operating solutions for the given problems in the vacuum system of the CSC regarding the Teflon-plug and the RF-carpet. Even though it was not possible to fix the main issue of the leak in the pumping system at the end because of the lack of time, the correct function of the new Teflon-plug and the RF-carpet could be proven. The next step will be the re-opening of the CSC and fixing of the leak in the cold chamber, after which the experimental setup can be re-assembled again for the next fission run in October.

6 Acknowledgments

I would like to thank my tutor Timo Dickel for giving me the opportunity to work in his group and the knowledge I have earned. I also want to thank Nazarena Tortorelli and my working group for supporting me throughout my project.

References

[1] W. R. Plaß u. a., „The FRS Ion Catcher – A facility for high-precision experiments with stopped projectile and fission fragments“, Nuclear Instruments and Methods in Physics Research Section B: Beam Interactions with Materials and Atoms, Bd. 317, S. 457–462, Dez. 2013, doi: 10.1016/j.nimb.2013.07.063.

Growth of Sb nanowires and investigation with x-ray diffraction and scanning electron microscopy

Julia Świątkowska
Faculty of Physics, Warsaw University of Technology, julia.swiatkowska1@gmail.com

Sb nanowires were fabricated via electrochemical deposition in polycarbonate ion track-etched membranes. In this work, we present how presence of a surfactant (Brij 58, Pluronic F-127 or Pluronic P-123) in electrolyte affects growth duration, as well as surface morphology and crystal orientation of the nanowires. The analysis was performed using scanning electron microscope images and x-ray diffraction data. We discovered that surfactants mentioned above have significant impact on duration of the deposition, along with preferred crystal orientation.

1 Introduction

Low-dimensional materials have been a subject of research for over 30 years now due to their unconventional characteristics and applications. Their main use can be found in optoelectronic, electric and medical devices as well as in chemical catalysis processes, although specific materials excel in different fields. [6] Antimony (or any other semimetallic, i.e. bismuth) nanowires are a topic of interest because of their small effective mass, energy overlap between conduction and valence bands and large mean-free path. [1] They could potentially be a great replacement for commonly used graphite in Li-ion batteries. [2]

Depending on the utilization, specific properties of nanowires surfaces are desired. For thermoelectric or optical use, it should be smooth and uniform, whereas in catalysis the imperfections and roughnesses are preferable, since they provide higher surface to volume ratio. We wanted to study the effects of three surfactants: Brij 58, Pluronic P-123 or Pluronic F-127 on the process by looking at the surface morphology and crystal orientation using scanning electron microscopy (SEM) and x-ray diffraction (XRD). There are many methods of fabricating Sb nanowires including chemical vapor deposition, focused ion beam induced synthesis, displacement reaction or hydrothermal reduction. [2] In this work, we present results of template-assisted electrodeposition using electrolytes with different surfactants and concentrations.

2 Experimental

The 30 μm thick polycarbonate (PC) foils were irradiated with Au ions having fluence of 10^8 ions/cm^2 and energy 11.1 MeV/n. Firstly, they underwent UV light treatment in presence of oxygen for 1 hour on each side to enhance and uniform the ion tracks. [3] Next, they were etched in 6M NaOH solution in 50°C to fabricate open pores. To obtain a diameter of around 180 nm, total etching time was 8 minutes. [5] After that, foils were immediately rinsed with deionized water and dried. On such samples thin Au layer ($\sim$ 100nm) was sputtered to provide electrical conductivity. It was then thickened using AuSF bath for 45 minutes in a two-electrode setup with the sputtered layer serving as the working electrode and Au counter electrode. The process was carried out by applying constant current of -2.4 mA.

Finally, for the process of antimony deposition a three-electrode setup with $Pt_{80}Ir_{20}$ counter electrode and a saturated calomel electrode (SCE) reference electrode was used. For all of the series 0.1M Sb electrolyte solution was used consisting of NaCl, HCl, tartaric acid, Sb(III)-chloride and glycerol as a base. [4] Additionally, three different non-ionic surfactants were tested (Brij 58, Pluronic F-127 or Pluronic P-123) in four different concentrations: for Brij 58 - 25, 18.75, 12.5, 6.25 g/L and for both Pluronics - 10, 7.5,

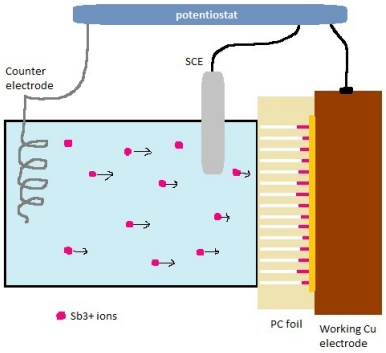

Fig. 1: *Scheme of experimental setup for Sb plating. The gold back electrode is in a contact with Cu ring.*

5, 2.5 g/L. The deposition was performed by pulsed plating, applying square waved potential $U_1 = -260$ mV vs. SCE for $t_1 = 20$ ms and $U_2 = -130$ mV vs. SCE for $t_2 = 100$ ms. At last the foil was cut and placed in dichloromethane overnight to remove the polymer template, in order to obtain samples suitable for SEM imaging. For the XRD the remaining part was taken. The analysis was performed from 20° to 80° with step of 0.04° and 10 seconds measurement time.

3 Results and discussion

3.1 Electroplating

During the deposition of antimony the curre of electroplating was recorded. The curve can b divided into 3 major stages. First an immedia increase is visible, followed by a steep decreas It corresponds to formation of the double lay on the electrode and the diffusion layer in th pores. After the current drops, it stabilizes a a certain value due to constant area antimor ions flow through, which signifies the nanowire growth. This phase is the longest one and vari vastly between the surfactants. At last, th end of the deposition process can be notice when the current increases again, as it is n longer constrained by the pores and antimor can freely accumulate on top of nanowires, form-ing so-called caps [6]. Fig. 2 shows the mean of ten pulses as the $I - t$ curves of all the samples with comparison to the sample without any surfactant. It is apparent, that the growth without the surfactant takes significantly less time than the others and involves higher current. Samples with Brij 58 required more, however Pluronics' platings took the longest - over three and up to even five hours. Additionally, for P-123 no increase in current was observed. It does not imply that the nanowires did not grown - they just have not reached the top.

3.2 SEM

Using the scanning electron microscope (SEM) images of the samples were taken to determine any irregularities or disproportions between the surfactants and examine the surface morphology. Fig. 3 shows close-up pictures of three samples with highest amounts of surfactants (b, c, d) and a reference one (a). It is clear that addition of any of the studied surfactants results in greater roughness on the exterior, as well as at the ends of the nanowires. Although not pictured here, in all the samples caps were present to some extent. This indicates, that the length of the majority of the wires is about the same and reaches 30 μm.

3.3 XRD

X-ray diffraction allowed to examine crystallinity of the wires, in particular their crystal orientation, which is particularly meaningful, as Sb demonstrates anisotrophic properties.

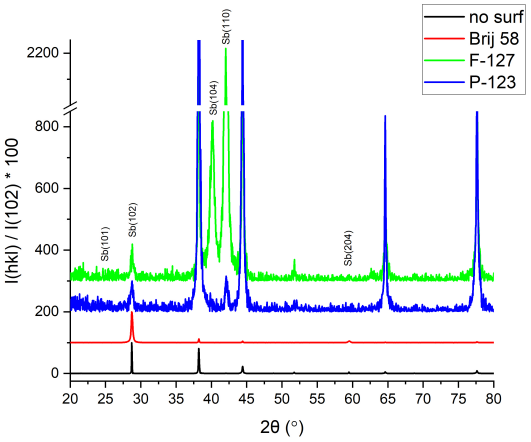

Fig. 4: *Joint x-ray diffractogram of four samples with the highest surfactant concentrations. Y-axis represents intensities normalized by the intensity of the (102) reflection multiplied by the factor of 100. Due to big differences between heights, some peaks appear less visible. Every subsequent diffractogram has an offset of 100 to improve clarity of the plot.*

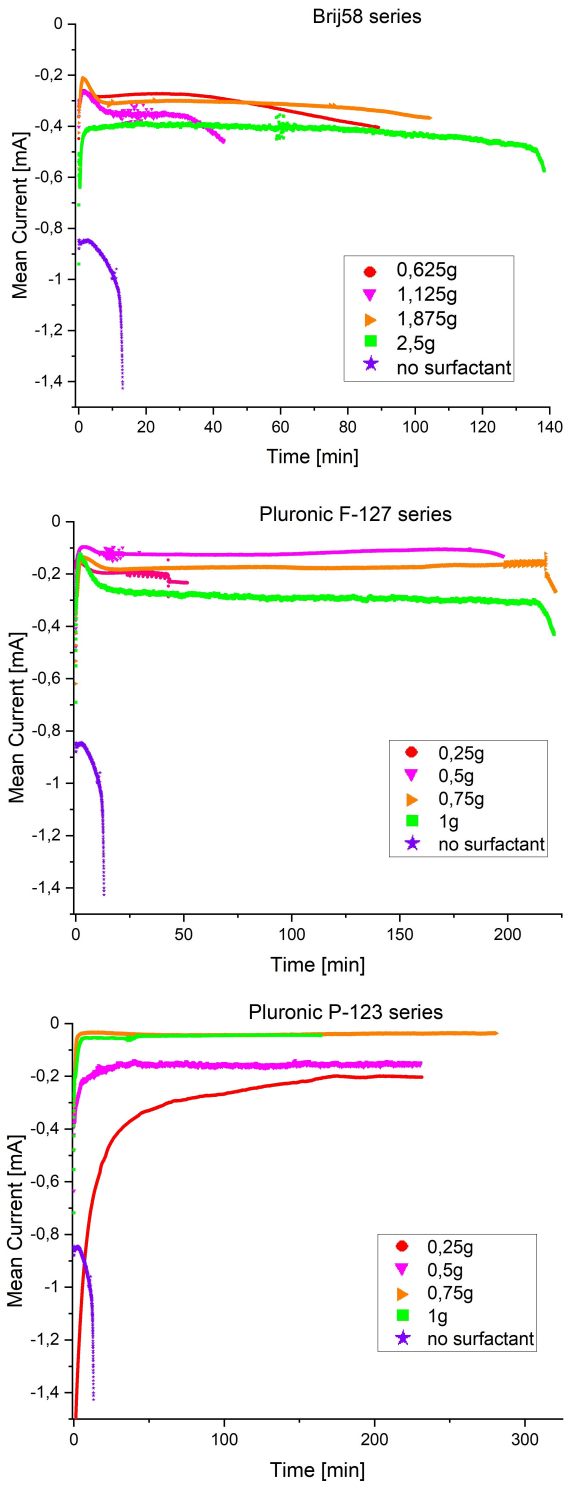

Fig. 2: *Plot of current averaged over ten pulses for samples with Brij 58, Pluronic F-127 and Pluronic P-123 surfactants in different concentrations respectively. Please note the negative axes as well as different time scales.*

(hkl)	No surf.	Brij 58	F-127	P-123
(101)	0.92	0.25	0.96	4.64
(102)	3.36	4.46	0.11	0.22
(110)	0.06	0,02	4.83	0.69
(113)	0.46	0.10	0.44	0.41
(202)	0.64	0.02	0.34	0.43
(204)	1.37	2.13	0.18	0.31
(212)	0.20	0.02	0.14	0.30

Tab. 1: *Texture coefficients for samples with zero and highest concentrations based on XRD results. Values above 1.0 are coloured to indicate predominant orientation.*

Fig. 4 presents diffractograms of the samples with highest concentrations of examined surfactants and a reference. For each, reflections coming from antimony were identified. Intensities were normalized by dividing every value with highest one, corresponding to approximately 28° ((102) plane). Additional reflections visible at 38°, 44°, 65° and 77° are associated with gold. From the peaks' intensities, the texture coefficient was calculated for each orientation using formula (1):

$$T_{c(hkl)} = \frac{I_{(hkl)}/I_{0(hkl)}}{(1/N)\left[\sum_N I_{(hkl)}/I_{0(hkl)}\right]} \qquad (1)$$

where $I_{(hkl)}$ is the measured intensity, $I_{0(hkl)}$ is the tabled intensity [7] and N is the number of reflections taken into consideration - in our case, 7. The values of $T_c > 1$ correspond to dominance of crystalline orientation for particular plane. The results are presented in Tab 1. While presence of Brij 58 makes nanowires grow with similar orientation as in the sample without any surfactant, that is (102) and (204), all three cases vary from each other. Nanowires grown with Pluronic F-127 have preferred (110) direction and P-123 - (101). Hence, addition of every surfactant results in crystals growing in a different direction, which is strongly defined.

4 Conclusions

The purpose of the experiment was to examine impact of three surfactants (Brij 58, Pluronic F-127 and P-123) on the process of growing Sb

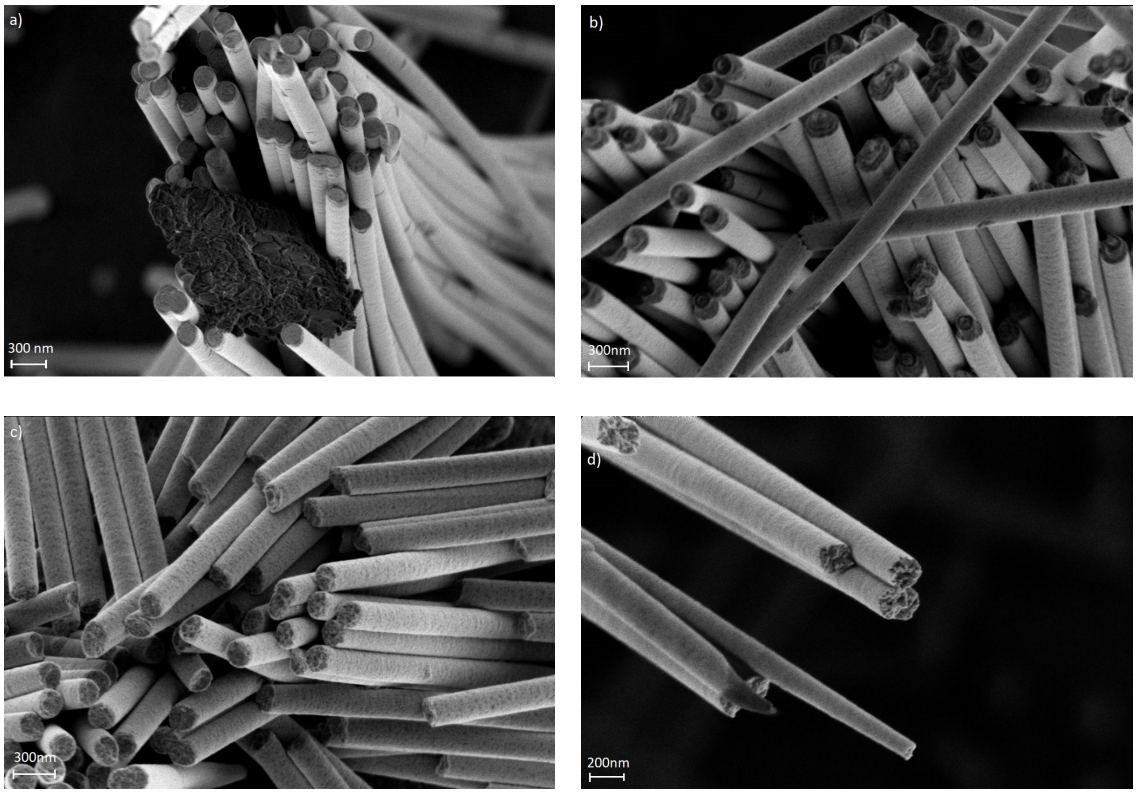

Fig. 3: *Pictures from SEM of nanowires grown in presence of a) no surfactant, b) 25g/L Brij 58, c) 10g/L Pluronic F-127 and d) 10g/L Pluronic P-123. On figure a) additionally, cap of grown antimony can be seen.*

nanowires. We looked into growth length by observing current, as well as the outside appearance by imaging with SEM and crystal structure of the final product by XRD analysis. The results showed, that deposition using electrolyte with Brij 58 takes least amount of time, while F-127 and P-123 need significantly more (over 3 hours). When looking at the surface slight roughness and porosity could be observed in all three samples in comparison with reference one. X-ray diffraction analysis revealed that crystallinity of nanowires depends on the sufractant used. All of the samples had different leading orientation, with texture coefficient higher than 4, although sample grown with Brij 58 resembled reference the most.

Acknowledgments

I would like to express my gratitude to Michael Wagner for the most pleasant introduction to nanoworld I could imagine, seeking answers to all of my questions and finally, for ever-lasting patience to all mistakes, accidents and mess ups I committed during my work here.

References

[1] Ye Wu Wang et al. *The Journal of Physical Chemistry B*, 108(43):16723–16726, 2004.

[2] R. Al-Salman, S. J. Sedlmaier, H. Sommer, T. Brezesinski, and J. Janek. *J. Mater. Chem. A*, 4:12726–12729, 2016.

[3] C. Trautmann. *Nuclear Instruments and Methods in Physics Research Section B: Beam Interactions with Materials and Atoms*, 105(1):81–85, 1995.

[4] Marco Cassinelli. *Thermoelectric Properties of Bi1-xSbx Nanowires Electrodeposited in Etched Ion-Track Membranes.* PhD thesis, Technische Universität Darmstadt, Darmstadt, June 2016.

[5] Gérard Pépy et al. *Journal of Applied Crystallography*, 40, 04 2007.

[6] M. Cassinelli et al. *Nuclear Instruments and Methods in Physics Research Section*

B: Beam Interactions with Materials and Atoms, 365:668–674, 2015

[7] A. V. C. et al. *Information-Calculating System on Crystal Structure Data of Minerals*, 1990.

Energy resolution of CVD-Diamond detectors

Sebastian Walch
University of Tuebingen, sebastian.walch@student.uni-tuebingen.de

In this experiment, the energy resolution of two different diamond detectors was investigated. The influence of the applied bias voltage, the signal amplifier and the gain voltage on the energy resolution was investigated.

1 Introduction

The goal of the nuclear physics community is to develop a unified model of the atomic nucleus. The Lisa Experiment by Kathrin Wimmer [1] aims to characterise collectivity and shape transitions in exotic nuclei. These are directly related to different components of the nuclear force, so that the general model underlying the nucleus could be improved. To achieve this goal, the LISA project will aim to improve the lifetime measurement of different states in the nucleus. In order to make a more accurate lifetime measurement, the energy of the photons emitted during the decay must be determined as accurately as possible. The gammas radiated by a nuclear decay in motion at the speed $\beta \cdot c$ at an angle α must be Doppler corrected with equation 1

$$E_0 = E_{lab} \cdot \frac{1 - \beta \cos(\alpha)}{\sqrt{1 - \beta^2}} \tag{1}$$

In order to carry out an energy correction of the measured gammas as accurately as possible, the parameters β and α have to be determined as precisely as possible. In standard in-beam gamma-ray experiments a single target is used. For the velocity correction the velocity is measured before and after the target. To determine the angle, the centre of the target is used as the position. The LISA project aims to reduce the inaccuracy of these parameters. For this purpose, several layers of solid active targets made out of CVD diamond will be used. These individual layers are significantly thinner than conventional targets. Since the CVD diamonds also function as detectors, if the energy deposited by the ions in the diamond material is measured with sufficient precision, the nuclear charge of the ions can be deduced. In this way, it can be determined in which diamond layer the reaction took place. Thus, the LISA project could improve the Doppler correction by both a more accurate α and β value. To achieve this objective, the energy resolution of the detectors must be precise enough, which is investigated in this project for two different CVD diamond detectors.

2 Experimental setup

Two different CVD-based diamond detectors are used for this test. The first detector (hereafter *DET1*) has an active area of $2 \times 2\ mm^2$ and a thickness of $0.09\ mm$. The second detector (hereafter *DET2*) has an active area of $3.23 \times 3.23\ mm^2$ and a thickness of $160\ \mu m$. Both sides of the detectors are used for the measurements (See Fig. 1). *DET1* is operated with a bias voltage between $-100\ V$ and $100\ V$. *DET2* is operated with a bias voltage of $-170\ V$ to $+170\ V$. The bias voltage is generated by a high voltage module and is applied to the detector through the amplifier. The detectors are mounted opposite a triple alpha source at various distances from 1 cm up to 6 cm. The source contains Am241, Cm244 and Pu239 and emits mainly at 5156 keV, 5486 keV and 5806 keV. The detector and source assembly is placed in a vacuum chamber with a pressure between $5 \cdot 10^{-6}\ mbar$ and $5 \cdot 10^{-7}\ mbar$ during the measurement. Two different generations of the current sensitive DBA preamplifier [2] are used to amplify the signal. For the amplifier of the third generation (hereafter *DBA3*) a fixed gain set by the gain voltage 3.5 V can be used.In contrast for the amplifier of the fourth generation (hereafter *DBA4*) gain voltages of 1 V, 2 V and 3.5 V are used. The signal generated by the alpha particles in the detector is then amplified using

the amplifier. The amplified signal is read out and stored using an oscilloscope. An overview of the setup is given in Fig.2 .

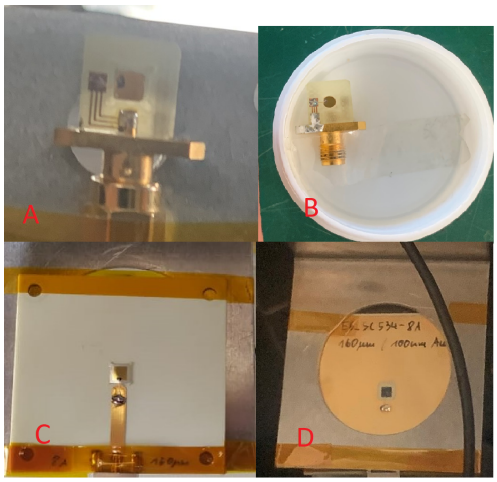

Fig. 1: *A: First side of DET1; B: Second side of DET1; C: First side of DET2; D: Second side of DET2*

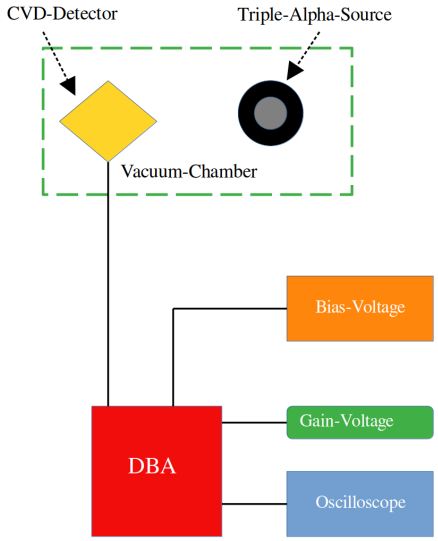

Fig. 2: *Experimental setup*

3 Data-Analysis

3.1 Preparation of the recorded data for further analysis

The measurements of the energy deposited by the alpha particles in the detector are carried out with the setup described. The highest energy resolution possible with this setup is thus determined. The release of energy from the alpha particles in the detector creates electron-hole pairs that drift to both contacts of the detector. The resulting signal is then amplified by the amplifier and recorded by the oscilloscope. The traces recorded in this way are evaluated with the C++ software package ROOT.
An example trace is given in Fig.3.

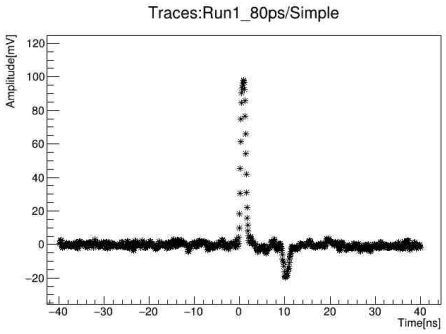

Fig. 3: *Example trace, measured with the first side of DET1 with DBA4 with 2 V gain and -170 V bias*

The signal generated by the alpha particle is the peak in the middle of the trace. The energy that can be assigned to a trace can be determined by the peak using various methods, these methods are described in section 3.2. During data acquisition, in addition to the signal generated by the alpha particles, a periodic signal is recorded that cannot be associated with the deposition of the alpha particles' energy in the detector. Fig 4 shows the superposition of 2560 recorded traces. Here, a periodic signal is clearly visible that extends over the entire recorded trace. This signal is classified as electronic noise and disturbs the measruement. The connecting cables from the detector to the amplifier and the amplifier itself are wrapped in aluminium foil, which acts as a Faraday cage to shield these externally collected signals. The periodic signals still occur during data collection. The periodic signals are removed offline using a ROOT macro which detects the periodic signals and suppresses them during further data analysis. An example of the superposition of the measured tracks after identification of the periodic signals is given in Fig. 5. In the following data evaluation, the periodic signals for all recorded data are filtered out using this method.

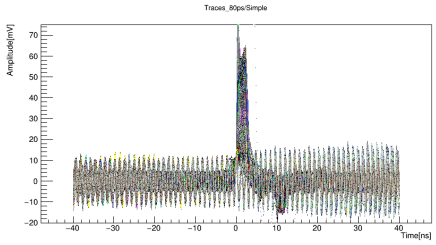

Fig. 4: *2560 traces including traces with periodic signals; measured with the second side of Det2 with DBA4 with 2 V gain and -170 V bias*

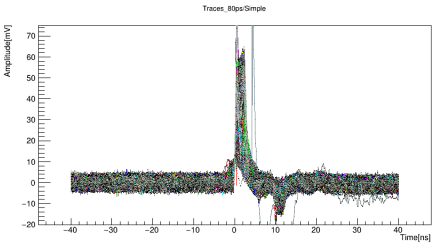

Fig. 5: *2400 Traces after suppression of the periodic signal; measured with the second side of Det2 with DBA4 with 2 V gain and -170 V bias*

3.2 Determination of the energy resolution based on the recorded traces

The evaluation of the traces is done with the C++ software package ROOT.
A measure of the energy deposited in the detector is the height of the measured peak [3]. Since the peak is very narrow in the measured data, the area under the peak is used as a measure of the height. Due to the discretisation of the measured data points, the sum of the data points belonging to the peak is used as a measure of the area under the peak. The energy can be determined in arbitrary units in this way.
This measure of the areas under the peaks shows an accumulation at three different values (Fig. 6). Since the alpha particles are completely stopped in the detector, they emit all of their kinetic energy. The accumulations found are consequently identified with the three energies that the alpha source primarily emits. Due to the spectrum of the alpha source, energies at 5156 keV, 5486 keV and 5806 keV are expected to be measured. The accumulations in the calculated areas underneath the peaks are then adjusted to the corresponding energies of the alpha particles with a ROOT macro.

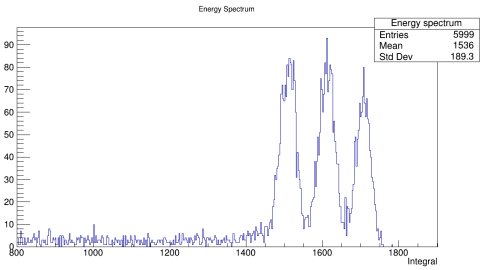

Fig. 6: *X-Axis: Calculated area underneath the peak in arbitrary units; Y-Axis: Counts for a prticular x-value; Representation of the calculated area by summing up the surfaces underneath the peaks of 6000 traces; traces measured with Det1, DBA4, 2V Gain, first side, Bias -100V*

It is possible that the rise time is energy-dependent [3]. To determine this rise time, the peak is fitted with a Gaussian function from its beginning to its maximum. A measure of the rise time is then determined by determining the time interval in which the Gaussian fit increases from 15% to 85% of its maximum value. Determining the rise time in this way does not work with the measured data. In Fig.7 the rise time values are plotted against the corresponding area underneath the peaks, which is determined by adding up the data points of the peaks. It can be seen that the areas under the peaks show three discrete accumulations, as can also be seen in Fig.6. For the method of determining the rise time via the Gaussian fit, there are no accumulations for three different values. An integral over the Gaussian fit of 15% to 85% of the maximum value as a measure of rise time shows similar results to using the time interval of the Gaussian fit (Fig. 8). The values determined by the integral over the fit are plotted in Fig.9 and show only a single accumulation, as can be seen from the y-axis in Fig.8. The direct use of the discrete data points instead of a fit to determine the rise time does not provide any meaningful results. The rise time is thus independent of the signal amplitude. This is of importance for the application of diamond detectors as timing detectors as well as the application in the LISA project.

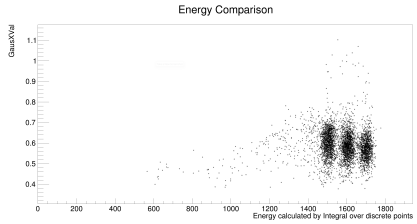

Fig. 7: *Comparison of the rise time method to the respective calculated area under the peak; X-Axis: Calculated area underneath the peak in arbitrary units; Y-axis: Rise time determined by the time interval of the rise interval of the Gaussian fit in arbitrary units; traces measured with Det1, DBA4, 2V Gain, First side, Bias -100V*

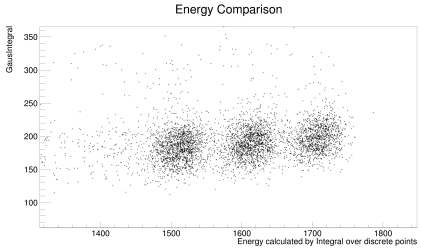

Fig. 8: *Comparison of the rise time method to the respective calculated area under the peak; X-Axis: Calculated area underneath the peak in arbitrary units; Y-axis: Rise time determined by the integration of the rise interval of the Gaussian fit in arbitrary units; traces measured with Det1, DBA4, 2V Gain, First side, Bias -100V*

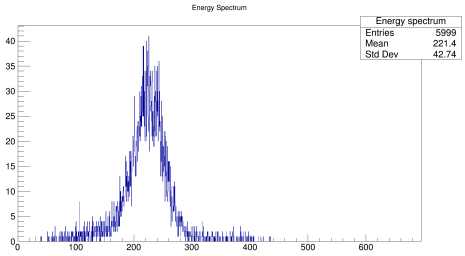

Fig. 9: *Representation of the determined rise time of the traces from Fig.8; X-Axis: Calculated area underneath the peak in arbitrary units; Y-axis: Number of traces; traces measured with Det1, DBA4, 2V Gain, First Side, Bias -100V*

The traces recorded for *DET2* have a very strong overlap in the associated area calculation (Fig.10) when compared to the peaks associated with *DET1* in the area calculation (Fig.6). Due to this overlap, the resulting energy resolution is highly inaccurate. The reason is unknown but this detector has been used in-beam and could suffer from damage. Therefore, only *DET1* is further analyzed.

A time shift occurs in some cases during the measurement. This can be seen in Fig.11 by the fact that some peaks occur at different time stamps. The resulting effects on the energy resolution are negligible for the measured data.

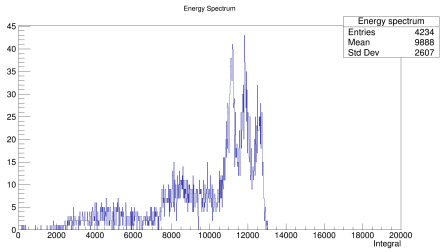

Fig. 10: *X-Axis: Calculated area underneath the peak in arbitrary units; Y-Axis: Counts for a particular x-value; 4234 traces measured with Det2, DBA4, 3.5V Gain, first side, Bias -170*

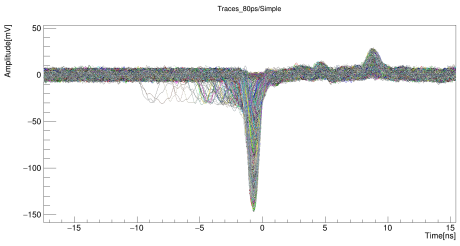

Fig. 11: *Representation of the time shift; traces measured with DET1, DBA4, 2V Gain, First Side, Bias +100V*

4 Results

The energy resolution for both sides of *DET1* for different gain voltages determined by the area underneath the peak (Sect. 3.2) are listed in table 1. Due to the vacuum magnitude of $6 \cdot 10^{-6} mbar$, the alpha particles lose an amount of energy up to the detector that cannot be detected in this experiment. The distance between the source and the detector does therefore not influence the results. The DBA3 amplifier shows worse results than the DBA4 with otherwise the same setup, so no measurements with DBA3 are listed. The results using a gain voltage of 1V are significantly worse than those at 2V and 3.5V. Therefore, these are not listed. The noise of the

Amplifier - Gain-Voltage	Noise [mV]	Amount of traces	Energy resolution	Side	Bias [V]
DBA4 - 3.5 V	48.70 ± 10.02	1500	Energy resolution at 5156 KeV: 3.57% Energy resolution at 5486 KeV: 3.35% Energy resolution at 5806 KeV: 3.16%	1	+85
DBA4 - 3.5 V	47.85 ± 10.79	2000	Energy resolution at 5156 KeV: 3.10% Energy resolution at 5486 KeV: 2.89% Energy resolution at 5806 KeV: 2.38%	1	−100
DBA4 - 3.5 V	105.59 ± 14.50	12000	Energy resolution at 5156 KeV: 4.32% Energy resolution at 5486 KeV: 3.76% Energy resolution at 5806 KeV: 3.22%	1	+100
DBA4 - 2 V	5.54 ± 0.97	6000	Energy resolution at 5156 KeV: 3.10% Energy resolution at 5486 KeV: 2.87% Energy resolution at 5806 KeV: 2.35%	1	−100
DBA4 - 2 V	9.40 ± 1.63	12000	Energy resolution at 5156 KeV: 3.62% Energy resolution at 5486 KeV: 3.30% Energy resolution at 5806 KeV: 2.89%	1	+100
DBA4 - 2 V	5.32 ± 0.94	2000	Energy resolution at 5156 KeV: 3.61% Energy resolution at 5486 KeV: 3.30% Energy resolution at 5806 KeV: 3.16%	2	−100
DBA4 - 3.5 V	47.63 ± 8.09	2000	Energy resolution at 5156 KeV: 3.26% Energy resolution at 5486 KeV: 3.14% Energy resolution at 5806 KeV: 2.38%	2	−100

Tab. 1: *Data evaluation for DET1*

traces is displayed. This allows the comparison of different settings with the same absolute value of gain and bias voltage.

5 Conclusion

With the setup used here, the first detector, with the first side opposite the source in connection with the DBA4 amplifier, a gain voltage of 2V or 3.5V and a bias voltage of -100V, shows the best energy resolution. This energy resolution is not sufficient, as a resolution of around one percent is required for the LISA project. Using a charge sensitive amplifier instead of a current sensitive amplifier might enhance the results. The rise time is independent of the signal amplitude. The occurrence of the time shift during the measurement (Sect. 3.2) should be investigated to ensure the reliability of the results of the detectors in longer measurements for the LISA project.

Acknowledgments

I would like to thank Kathrin Wimmer, Zhiqiang Chen, Jelena Bardak and Bellona Bles

very much. I am really grateful for all the support I have received. I was very fortunate to be able to work with you! I would also like to thank Ralf Averbeck and Gabi Menge for the great organisation of the summer school. Thank you to all the summer students, I had a really good time with you. (BB)

References

[1] K. Wimmer, LISA-ERC Consolidator Grant 2020 Part B2

[2] Information about DBA preamplifier, http://www.micronsemiconductor.co.uk/wp-content/uploads/2018/08/DiamondPreAmpDatasheets.pdf, 2022

[3] KNOLL, G.F.(2020), 4. General Properties of Radiation Detectors, In Radiation detection and measurement, 978-0-470-13148-0

File Report Marcos.aux

Axial resonators of the non-destructive detection system in ARTEMIS

Marcos Quintas Pérez
University of Santiago de Compostela, marcos.quintas.perez@rai.usc.es

The resonators are the basis of the non destructive detection systems in Penning Traps experiments such as ARTEMIS, performed in GSI. They act as RLC circuits attached to the ion trap. In this article we focus in the study and test of the axial resonators. This kind of resonators are the most difficult to build.

1 Introduction

1.1 Fundamental of Penning Traps

Some Penning Traps experiments, like ARTEMIS (Asymmetric Trap for the measurement of Electron Magnetic moment of Ions) in GSI, are designed to perform precise measurements of the magnetic moment of the bound electrons in heavy ions. This provide a test for the QED theory and lead to more accurate fundamental constants.

A Penning Trap consist in a device used to confine a charged particle. Due to the fact that is not possible to confine a charged particle using only a electric field, is necessary the use of a magnetic and a electric field to carry it out. This kind of ion trap use a strong vertical homogeneous magnetic field (axial direction) and a quadrupole harmonic electric field.

A particle in a electric and magnetic field experiences the Lorentz force

$$F = q(\vec{E} + \vec{V} \times \vec{B}). \tag{1}$$

In a real Open-Endcap Penning Trap with Cylindrical Electrodes, such as the ARTEMIS Penning traps, this force lead to the ion to have different types of oscillations. One is the axial oscillation with frequency

$$\omega_z = \sqrt{\frac{qU_0C_2}{md^2}}, \tag{2}$$

and other is the radial oscillation caused by the homogeneus magnetic field, with a cyclotron frequency

$$\omega_c = \frac{|qB|}{m} = \sqrt{\omega_-^2 + \omega_+^2 + \omega_z^2}. \tag{3}$$

Actually the radial motion is the superposition of two circular motions, one with frequency w_+ and other with frequency w_-. The last term of the equation above have into account that the electrodes are not perfect, and therefore the trapping potential is not ideal.

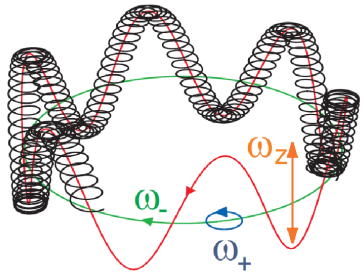

Fig. 1: *Ion motion in a Penning trap*

1.2 Electronic detection system

The motion of the ion inside the Penning trap induce in the elecrodes a small electric current I_p. To amplify the electic signal, a RLC paralell circuit (or resonator circuit) is conected to the electrodes is used. The ion may be regarded as another RLC circuit itself.

The quality factor Q is the ratio between the stored and dissipated energy per angular cycle. It is given by

$$Q = \frac{\omega_0}{\delta\omega}. \tag{4}$$

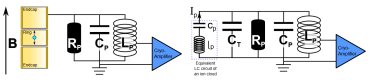

Fig. 2: *Electronic system:a)Ion in the trap and resonator circuit; b)Considering the ion as a RLC circuit*

The higher the quality factor, the lower the energy loss and higher the efficiency. ω_0 is the resonance frequency of the resonator circuit. In a helical resonator, if L is the inductance of the resonator, C_p his self-capacitance and C_T the capacitance of the trap, then we have that

$$\omega_0 = \frac{1}{\sqrt{L(C_p + C_T)}}. \tag{5}$$

when the resonance frequency of the RLC-circuit is the same as the frequency of the ion motion, then there is a voltage drop

$$U_P = R_P I_p = \omega_0 L Q I_p. \tag{6}$$

Where $R_P = \omega_0 L Q$ the paralell resistor. At its resonance frequency the resonator behave like a resonator with resistance R_P.

A resonator is building in such a way that his frequency resonance tune with the frequency of the ion motion. In order to maximize the voltage drop, the inductance and quality factor Q of the resonator should be maximized.

In the experiment ARTEMIS, there are three different types of resonator. One is a axial resonator whose resonance frequency should tunes with the axial frequency motion of the ion, cyclotron resonator to measure the cyclotron frequency of the ion. They are located at the spectroscopy trap. The another one is other axial resonator located at the creation trap. The connection with the trap add a resistor and a external capacitance C_T that reduces the quality factor and change the resonance frequency of the resonator.

2 Experimental process

In our project we focus on the building and study of axial helical resonators. In order to maximize the quality factor and the inductance, the axial resonator is built using a core of Polytetrafluoro Ethylene (PTEF) that have a low dielectric constant, resulting in a low capacitance of the coil, and winding a thin copper oil around this core. Each layer of coil should be shielded with teflon tape for mechanical stability and better thermalisation of the wire. The device is surrounded by a housing of OFHC copper. The base plate is also made up of this material, which reduces the resistance and improve the heat conduction at cryogenic temperatures.

Two kind of resonators were built. First one resonator of a single layer coil and posteriorly other resonator of two and a half layer coil.

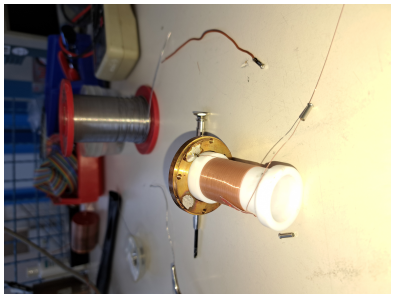

Fig. 3: *Building process of one of the resonators*

For each complete coil layer, it is necessary to reduce the external noises. The method to do this in the resonators of ARTEMIS is the inductor tapping. It consist of soldering the inductor coil in a position with a winding ratio of 2/3 for the primary coil and 1/3 for the secondary coil. The end part from the side where the coil have the larger number of windings is named hot end while the end part of the other side is referred as the cold end.

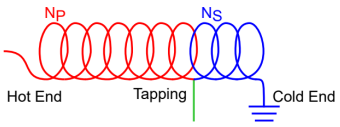

Fig. 4: *Inductor tapping*

Being V_P and V_S the voltages through the primary and the secondary coil respectively, then we have

$$\frac{V_P}{V_S} = \frac{N_P}{N_S}, \tag{7}$$

where N_P and N_S are the number of turns in the primary and secondary coil.

The test of the resonators was made sending harmonic electrical signals (harmonic electrical currents) of different frequencies in a specific range like input to the resonator and measuring what frequencies the resonator let pass at the output (resonance peaks). This measurements were repeated for different capacitors (each one

with their capacitance C_T). The device that performed this task was the spectrum analyser. The measurements were make at room temperature.

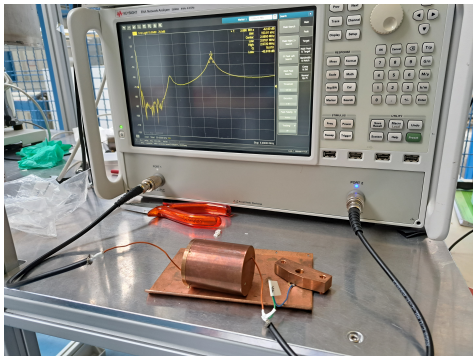

Fig. 5: *measurement process of one resonator with one capacitor attached using the spectrum analyser. Notice that the capacitor should be grounded*

During the building process of this second one, it was realized that the resonator didn't work. This was due to any resonance peak were observed as output in the spectrum analyser. After disassembled the resonator it was realized that the coil had broken at the first layer. The break of the coil is the only reason because of any resonator doesn't work. Then other resonator of two and a half layer coil was built.

3 Results

The error of the frequency was taken as the bandwidth of the resonance peak for each measurement. With the measurements of the resonance frequency of the resonator versus the external capacitance C_T attached to the resonator, the representation of the square inverse frequency for each capacitance C_T should be a linear relation according to (5).

From a linear fit $y = a\dot{x} + b$ where $y = 1/w^2$, $x = C_T$, we have, using (5), that

$$L = a \qquad C_p = \frac{b}{a} \tag{8}$$

where C_p is the self-capacitance of the axial resonator.

Then for the resonator of one single coil layer the results are the following

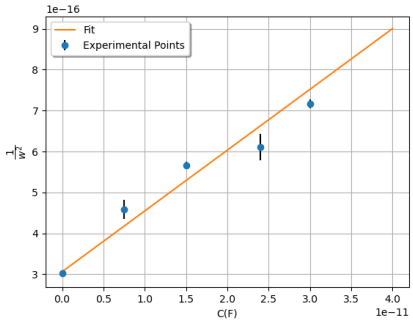

Fig. 6: *linear fit-resonator with a single layer coil*

$$a = 1,455710350(12) \cdot 10^{-5} \quad F^{-1}s^2$$

$$b = 3,061616001097557000000(12) \cdot 10^{-16} \quad s^{-2}$$

$$r = 0.9776$$

where r is the Pearson correlation coefficient. Te experimental inductance a self-capacitance of this resonator are

$$L = 1,455710350(12) \cdot 10^{-5} \quad H$$

$$C_p = 2,060708536(16) \cdot 10^{-11} \quad F$$

and the resonance frequency without any capacitance is

$$w_0 = 9,16(11) \quad \text{MHz}$$

Meanwhile for the resonator with two and a half layer coil the results are

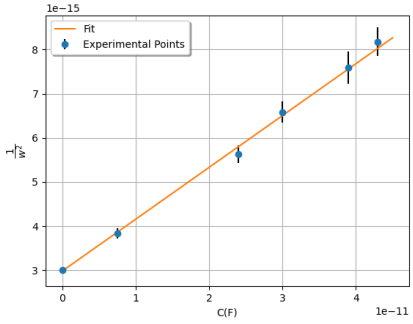

Fig. 7: *linear fit-resonator with two and a half layer coil*

$$a = 1,17511664(23) \cdot 10^{-4} \quad F^{-1}s^2$$

$$b = 2,9771423300000000000(52) \cdot 10^{-15} \quad s^{-2}$$

$$r = 0.9989$$

and therefore

$$L = 1,17511664(23) \cdot 10^{-4} \;\; H$$

$$C_p = 2,5334866588222256000(61) \cdot 10^{-11} \;\; F$$

and the resonance frequency without any capacitance is

$$w_0 = 2.908(72) \;\; \text{MHz}$$

The linear fits were made with the python module scipy.optimize and the function $curve_fit$ from that module. This function make linear (and no linear) fits using the least square method.

4 Conclusions

It was showed that the builded axial resonators behave according to the theoretical equation (5). In the case of the resonator of two and a half layer coil the experimental behaviour is more close to that equation.

For the case of the resonator of two and a half layer coil the result for the self-capacitance make sense due to the large number of turns (between 280.300). In the case of the resonator of a single layer coil the result for the self-capacitance is a bit big for the number of turns considered. If we see with

Also from the previous section we can see that the more the external capacitance C_T attached to the resonator is, the lower is the resonance frequency of the resonator and therefore lower the quality factor, according to (4). That is exactly what happens when the resonator is connected to the Penning Trap.

The next step should be study the resonator in cryogenic conditions, similar to the conditions inside of the Penning Trap, and check the change in the frequency resonance and the quality factor. This can be done using a vacuum chamber. It couldn't be done for lack of time.

Acknowledgments

Special gratitude to all GSI Summer Students for your support and kind messages after my unfortunate accident. Also thanks to Manassa for being with me at the lab.

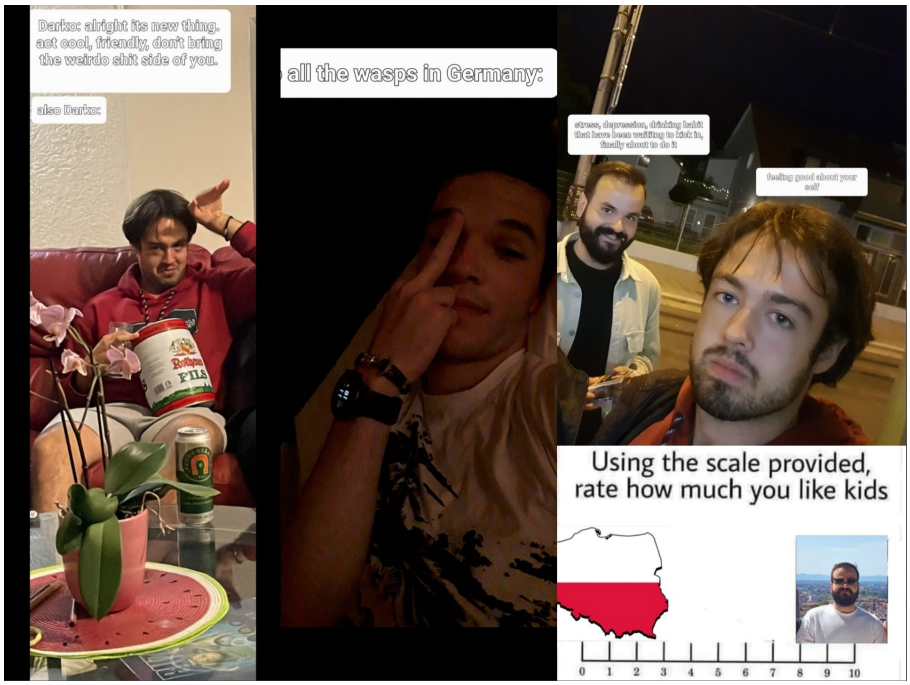
Darko: alright its new thing, act cool, friendly, don't bring the weirdo shit side of you.
also Darko:
all the wasps in Germany:
Using the scale provided, rate how much you like kids
0 1 2 3 4 5 6 7 8 9 10


when you at work checking the time it's says 3:00pm den you check again 3hr later and it's says 3:15
When you hear that a country has oil
When you and your bestie can finally celebrate finishing the reports after having many breakdowns for 2 months :
demons of the underworld cheering for me when I commit harams

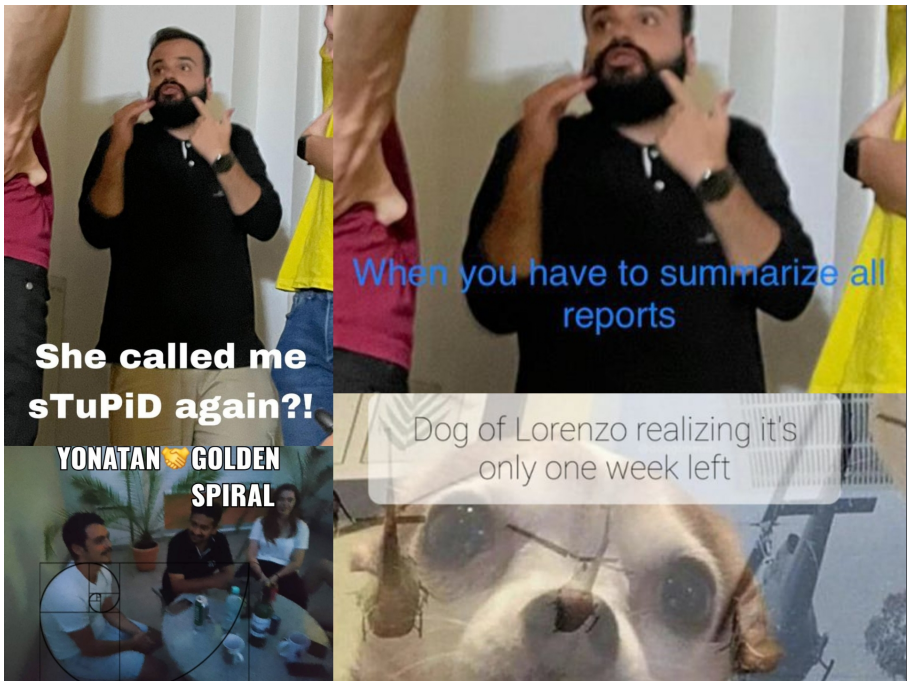
She called me sTuPiD again?!
YONATAN 🤝 GOLDEN SPIRAL
When you have to summarize all reports
Dog of Lorenzo realizing it's only one week left


Corporate needs you to find the differenc between this picture and this picture.
They're the same picture.
HARAM!!
DARKO WITH A SWISS KNIFE
UKRANIAN KIDS

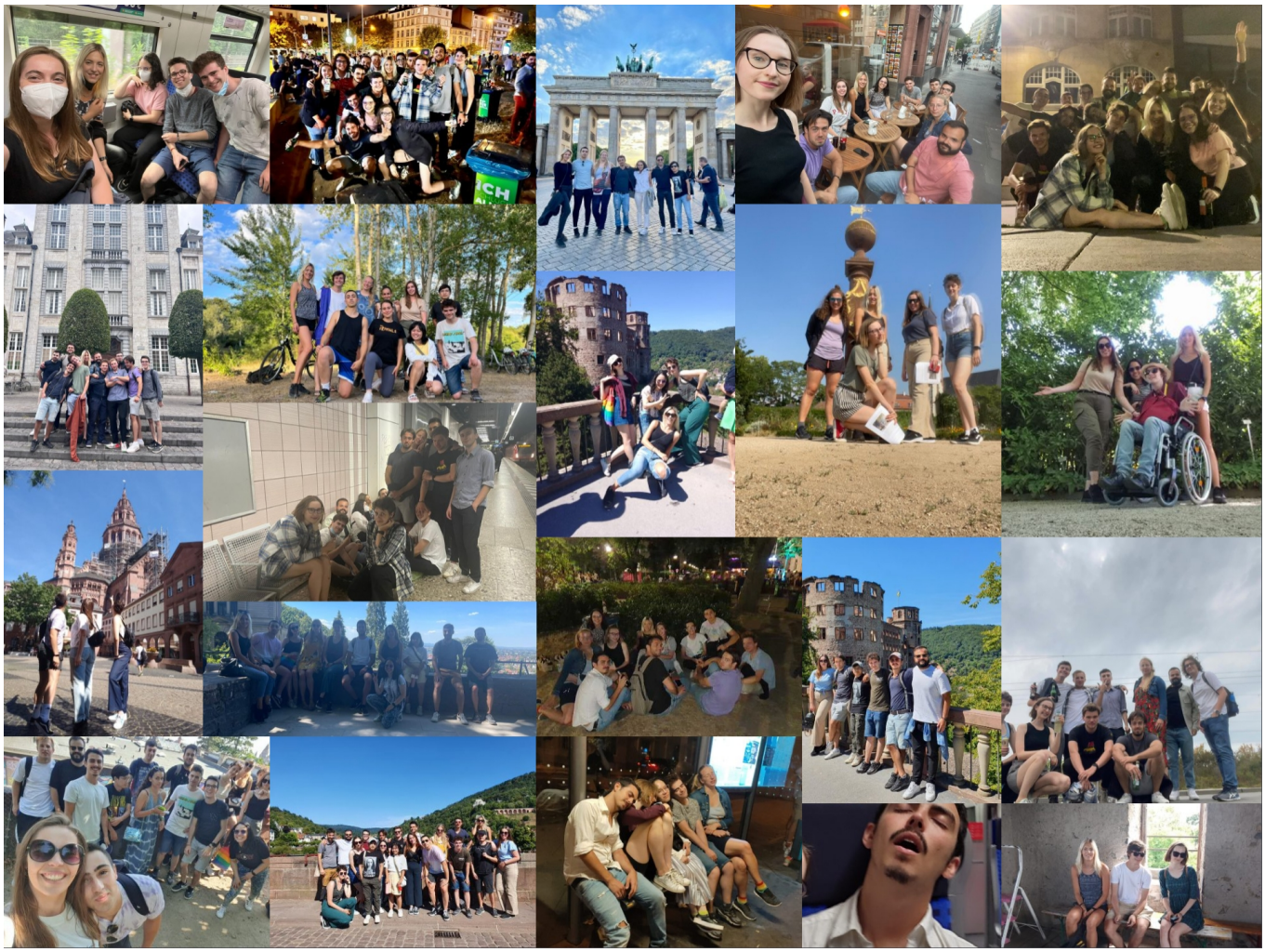

Notes


GSI Helmholtzzentrum für
Schwerionenforschung


FAIR


HGS-HIRe for FAIR
Helmholtz Graduate School for Hadron and Ion Research